GKSS
FORSCHUNGSZENTRUM
in der HELMHOLTZ-GEMEINSCHAFT

Friction Riveting: development and analysis of a new joining technique for polymer-metal multi-materials structures

(Vom Promotionausschuss der Technischen Universität Hamburg-Harburg als Dissertation angenommene Arbeit)

Author:

S. Amancio

ISSN 0344-9629

HELMHOLTZ
| GEMEINSCHAFT

wissen
schafft
nutzen

GKSS 2007/18

GKSS 2007/18

Friction Riveting: development and analysis of a new joining technique for polymer-metal multi-materials structures

(Vom Promotionausschuss der Technischen Universität Hamburg-Harburg als Dissertation angenommene Arbeit)

Author:
S. Amancio
(Institute of Materials Research)

GKSS-Forschungszentrum Geesthacht GmbH • Geesthacht • 2007

Die Berichte der GKSS werden kostenlos abgegeben.
The delivery of the GKSS reports is free of charge.

Anforderungen/Requests:

GKSS-Forschungszentrum Geesthacht GmbH
Bibliothek/Library
Postfach 11 60
D-21494 Geesthacht
Germany
Fax.: (49) 04152/871717

Als Manuskript vervielfältigt.

ISSN 0344-9629

GKSS-Forschungszentrum Geesthacht GmbH · Telefon (04152)87-0
Max-Planck-Straße 1 · D-21502 Geesthacht / Postfach 11 60 · D-21494 Geesthacht

GKSS 2007/18

Friction Riveting: development and analysis of a new joining technique for polymer-metal multi-materials structures

(Vom Promotionausschuss der Technischen Universität Hamburg-Harburg als Dissertation angenommene Arbeit)

Sergio Amancio

145 pages with 73 figures and 21 tables

Abstract

The increasing demand on environmental consciousness, cost savings and high performance end-products has been guiding scientists and engineers to a constant development of new materials and technologies. Results from these efforts are for instance the so called multi-material structures, where mechanical performance is enhanced by combining the positive features of each single material partner. An important class of lightweight multi-materials structures specially used in industrial fields such as transportation and modern civil engineering, is the polymer-metal multi-materials structure. Due to problems associated with component size, fabrication capabilities or material physical-chemical incompatibilities, joints frequently exist in these multi-material structures. Currently available joining methods for polymer-metal multi-material structures are usually application-specific, presenting high operational costs, limited mechanical performance or are not environmental friendly. A new Friction Riveting technique for polymeric-metallic joints was developed, demonstrated and characterized in this work, as an alternative, reliable, environmental compatible and economically viable spot joining process. In the simplest process variant a rotating cylindrical metallic rivet is inserted in a thermoplastic base plate. The high rotation speed and pressure increase friction and heat is generated. The local increase in temperature induces the formation of a softened/molten polymer layer around the tip of the rotating rivet. When a certain penetration depth is achieved the heat input rate becomes higher than heat outflow (owing to the low polymer thermal conductivity), temperature highly increases and the rivet tip plasticizes. At this point rotation is stopped and the forging pressure applied, so the plasticized rivet tip is deformed by the opposite reactive forces of colder polymeric volumes, assuming a paraboloidal pattern; after cooling it becomes anchored in the polymeric base plate. In this work case-study joints on commercially available polyetherimide (PEI) and aluminium 2024-T351(Al-Cu-Mg alloy) were chosen for demonstrating proposed theories, models and mechanisms, as well as an analytical heat input model. Sound friction riveted point-on-plate and single-rivet overlap joints with elevated joint efficiencies in terms of base materials strength were obtained (joint efficiencies for point-on-plate joints: 60 %–93 %; for overlaps: 70 %) through tensile and lap shear testing at room temperature. The influence of process parameters (rotational speed, total time and total pressure) on process variables and joint properties were evaluated by thermometry, infrared thermography, microscopy, Vickers microhardness, X-ray microtomography and by gel permeation chromatography. Temperature (average maximal temperatures $\approx$ 500 °C) was directly proportional to rotation speed, total time and total pressure. Volumetric flaw formation was directly proportional to total time and total pressure but appeared to be independent of rotational speed. Molecular weight results showed low amount of thermal degradation in the polymeric portion; thermal degradation presented an inversely proportional behaviour to these parameters. Average microhardness in the rivet decreased and in the polymeric portion increased, due to annealing phenomena and physical ageing and/or water elimination, respectively. Generally, heating time (associated with heat input and material plasticizing), burn-off (related to rivet insertion/consumption and material plasticizing), and burn-off rate (considered as the average joining speed) were found to increase with rotational speed, total time and total pressure. Torque, an important variable providing information on the plasticizing level of both rivet and softened/molten polymer, was found directly proportional to total pressure and inversely proportional to rotational speed and total time. The proposed analytical heat input model, which initially included the frictional and normal force contributions on heating, was demonstrated. Since results showed that heating due to normal force (axial pressure) is only about 0.1 % of total heat input, it can be disregarded for practical calculation purposes. Calculated heat input results showed a good correlation with experimental heating time results, increase with rotational speed and total time and remain almost unchanged with total pressure. The scientific and technological results of this work have provided a complete approach on the joining mechanisms, microstructure, temperature history and mechanical behaviour of friction riveted joints. Additionally, the proposed heat input model offers a starting point for more complex modelling as for instance, temperature, microstructural and forging regime models. Results from this work suggest that friction riveting has the potential to be established as a reliable, simple, cost effective and environmental friendly joining technique for polymer-metal multi-materials. It also offers the research community a vast field of scientific-technological exploitations, opening up possibilities for further improvements accelerating the technology transfer of friction riveting to industry.

Reibnieten: Entwicklung und Untersuchung einer für Polymer-Metall-Multimaterialstrukturen geeigneten neuen Fügetechnik

Zusammenfassung

Die wachsende Anforderung an Umweltbewusstsein, Kosteneinsparung und hochleistungsmäßigen Endprodukten hat Wissenschaftler und Ingenieure beeinflusst, neue Materialien und Technologien zu entwickeln. Beispiele resultierender Ergebnisse sind sogenannte „Multi-Materialien-Strukturen“, wobei mechanisch positive Verbindungseigenschaften durch die Kombination der einzelnen Fügepartner erhalten werden. Die insbesonders in Transport- und moderner Bauindustrie angewandten Polymer-Metall-Verbindungen sind eine wichtige Klasse leichtgewichtiger Multi-Materialien-Strukturen. Verbindungen in solchen Strukturen sind normalerweise vorgesehen wegen Komponentgröße, Prozessfähigkeit oder physikalisch-chemischer Inkompatibilität. Geeignete herkömmliche Fügeverfahren dafür sind üblicherweise entweder teuer, mit beeinträchtigter Festigkeit und Anwendung oder nicht umweltfreundlich. Die im Rahmen dieser Arbeit neue Reibnieten-(Friction Riveting)Methode für Polymer-Metall-Mischverbindungen wurde hierdurch als alternative, zuverlässige, umweltfreundliche und potenziell sparsame Punktverbindungstechnik entwickelt, beschrieben und nachgewiesen. Im grundsätzlichen Prinzip des Reibnietens dringt die in Rotation versetzte zylinderförmige metallische Niete in die Oberfläche eines Kunststoff-Grundwerkstoffs ein. Aufgrund der hohen Rotation bzw. des hohen Axialdruckes wird Reibungswärme erzeugt, und es formt sich eine dünne Schicht aus aufgeschmolzenem/aufgeweichtem Kunststoffmaterial um die Spitze des Niets. Mit Erreichen einer bestimmten Tiefe erhöht sich die Temperatur signifikant, bedingt durch die geringe thermische Leitfähigkeit des Kunststoffes und der höheren Wärmeeinbringung im Vergleich zur Wärmeabfuhr. Dadurch wird die Spitze des Niets plastifiziert; in diesem Moment wird die Rotation abgebrochen und der Reibdruck in die Fügepartner aufgebracht. Als Folge wölbt der Niet sich entsprechend der Temperatur und des Druckverhältnisses auf. Nach der Abkühlungsphase wird die aufgewölbte (paraboloid) Nietspitze formschlüssig im Kunststoff verankert. Die in dieser Arbeit vorgeschlagenen Theorien, Modelle, Mechanismen und analytisches Wärmeeinbringungsmodell wurden bei Verbindungen von Polyetherimid (PEI) und Aluminium 2024-T351 (Al-Cu-Mg-Legierung) nachgewiesen. Punkt- und Überlappverbindungen mit hohem Festigkeit-Wirkungsgrad unter Raumtemperatur wurden reibgenietet. Der Zugfestigkeit-Wirkungsgrad der Punktverbindungen betrug 60 % bis 93 %. Der Scherzugfestigkeit-Wirkungsgrad betrug circa 70 %. Darüber hinaus wurde der Einfluss von Prozessparametern (Rotationsgeschwindigkeit, Zeit und Axialdruck) auf Prozessvariablen und Verbindungseigenschaften mittels Thermometrie, Infrarotthermographie, Mikroskopie, Vickers-Mikrohärte, Röntgen-Mikrotomographie und Gelpermeationschromatographie untersucht. Gemessene Temperaturen (durchschnittliche Werte um 500 °C) waren direkt proportional zu Rotationsgeschwindigkeit, Zeit und Axialdruck. Volumetrische Einschlüsse im Polymer waren auch direkt proportional zu Zeit und Axialdruck, andererseits anscheinend unabhängig von Rotationsgeschwindigkeit-Zunahme. Geringe thermische Degradation im Polymerteil der Verbindungen wurde durch die Ergebnisse der Molekulargewicht-Untersuchung festgestellt; der Zusammenhang zwischen Rotationsgeschwindigkeit, Zeit, Axialdruck und thermischer Degradation zeigte sich umgekehrt proportional. Wegen der Erholungsmechanismen nahm die durchschnittliche Mikrohärte im Niet ab, während die Mikrohärte im Polymervolumen wahrscheinlich aufgrund der physichen Alterung oder der Wasserabnahme zunahm. Die Prozessvariablen Erwärmungszeit bzgl. Wärmeeinbringung und Materialplastifizierung, Nietverkürzung bzgl. Nieteindringtiefe, aber auch Materialplastifizierung und Verkürzungsrate bzgl. Verfahrensgeschwindigkeit stiegen hauptsächlich mit steigender Rotationsgeschwindigkeit, Zeit und Axialdruck. Das Drehmoment, dessen Interpretation sowohl mit dem Niet- als auch Polymer-Plastifizierungsverhalten verknüpft werden kann, nahm mit steigender Rotationsgeschwindigkeit und Zeit ab und mit Axialdruck zu. Im Wärmeeinbringungsmodell wurde festgestellt, dass der Beitrag der Axialkraft geringer als 0,1 % war, so dass dieser Beitrag angesichts praktischer Wärmeeinbringungskalkulationen ignoriert werden kann. Zudem waren die berechneten Wärmeeinbringungen der experimentelle Ergebnisse sehr ähnlich, wobei steigende Zeit und Axialdruck größere Wärmeeinbringung verursacht, während steigende Rotationsgeschwindigkeit die Wärmeeinbringung kaum veränderte. Die im Laufe dieser Arbeit enstandenen wissenschaftlichen bzw. technischen Ergebnisse wiesen auf die Machbarkeit des Reibnietens hin. Nebenbei bietet das vorgeschlagne Wärmeeinbringungsmodell die Möglichkeit, komplexere Temperatur-, Gefügeänderungs- und Stauchmodelle neu zu entwickeln. Darüber hinaus bietet sich das Reibnieten als potenzielle zuverlässige, sparsame und umweltfreundliche Fügetechnik für Polymer-Metall-Verbindungen an. Durch die Entwicklung dieses innovativen Fügeverfahrens öffnet sich der Wissenschaft eine Tür zur technischen Weiterentwicklung, deren Beiträge den Technologie-Transfer des Reibnietens in die Industriefelder beschleunigen und vereinfachen können.

Manuskripteingang in TKP / Manuscript received: 4. September 2007

ACKNOWLEDGEMENTS

The author would like to gratefully thank the following people for their support and contribution to this work:

- Professor K.-H. Schwalbe (GKSS-TUHH), Professor K. Schulte (TUHH) and Dr. J. F. dos Santos (GKSS) for the supportive orientation of this work.

- Dr. J. F. dos Santos (GKSS) for the encouragement and unconditional professional and personal support, by giving me full autonomy in my research pathway at GKSS Forschungszentrum on one hand, and on the other hand by giving me valuable guidance.

- The CNPq-Brasil for sponsoring me with a PhD scholarship and the DAAD Germany for the intensive German language course stipend.

- V. Leiser (GKSS), for his support and friendship during the course of this work.

- P. Fischer (GKSS) for her support with metallographic etching and microscopy and for her friendship.

- V. Ventzke (GKSS) for the scanning electron microscopy photographs.

- J. Lohmann and A. Schilf (GKSS) for the technical support and sample preparation.

- S. Riekehr (GKSS) and H. Mackel for their support with mechanical testing.

- Professor S. P. Nunes and Dr. J. Roeder (GKSS) for the differential scanning calorimetry and infrared spectroscopy analysis and valuable discussions regarding the thermal degradation mechanisms of thermoplastics.

- Dr. F. Beckmann (DESY-GKSS) for carrying out the experimental X-ray microtomography testing and providing full access to the HASYLAB Synchrotron Light Lab facilities in Hamburg.

- My mummy, daddy, Sara and Daniel for their love and patience and prayers, during the good and hard times of my life. I can not find enough words to thank you for all you have done to me.

- My family and friends in Brazil for the unconditional faith in the success of my work.

- My beloved, beautiful, intelligent, wife and best friend Gisele, for smiling me when I was sad, for pushing me forward when the difficulties tried to stop me, for her love and full comprehension during the long days, nights and weekends that I spent in front of my computer. I love you!

Finally I would like to thank the Lord for given me health and intelligence to complete this work. Without His strength and protection I would never be able to reach my objectives.

TABLE OF CONTENTS

LIST OF ABBREVIATIONS

ABS	Acryl-butadiene-styrene
AZ	Anchoring Zone
BO	Burn-off
BOR	Burn-off Rate
BP	Failure on polymeric base plate
BSE	Back Scattered Electrons
CF	Carbon-Fibre
CTE	Linear Coefficient of Thermal Expansion
DB	Deformation Band
FOP	Forging Pressure
FOT	Forging Time
FP	Friction Pressure
FT	Friction Time
GF	Glass-Fibre
GPB	Guinier-Preston-Bagaryatskii Zone
GPC	Gel Permeation Chromatography
HDT	High Deflection Temperature
HT	Heating Time
LSS	Lap Shear Strength
MHAZ	Metal Heat Affected Zone
MTMAZ	Metal Thermo-Mechanically Affected Zone
MW	Molecular Weight
MWD	Molecular Weight Distribution
PEI	Polyetherimide
PHAZ	Polymer Heat Affected Zone
PPS	Polyphenilenesulfide
PTMAZ	Polymer Thermo-Mechanically Affected Zone
PVC-U	Unplasticized Polyvinylchloride
RE	Failure on extern rivet-shaft portion

RI	Failure on intern rivet-shaft portion
RS	Rotation Speed
SFE	Stacking Fault Energy
TT	Total Time
TP	Total Pressure

LIST OF SYMBOLS

A	Rubbing Area
A_S	Screw tensile testing fictive area
E(t)	Stress Relaxation Modulus
F_M	Maximum Tensile Force
F_N	Normal Force
h	Rivet insertion depth
H	Width of polymer molten film beneath rivet
HR_{L01}	Average Infrared Heating Rate
HV	Vickers Microhardness
M_n	Average Numeric Molecular Weight
M_w	Average Molecular Weight
M_Z	Frictional torque
n	Polymer Power Law Coefficient
Q	Heat Input
RE	Failure on extern rivet-shaft portion
RI	Failure on intern rivet-shaft portion
R_m	Tensile Strength
R(t)	Time-dependent Stress
$R_{2,0\%}$	2,0% Off-set Stress (in Bearing Testing)
T_a	Polymer Physical Ageing Temperature
T_{drying}	Polymer Processing Drying Temperature
T_g	Polymer Glass Transition Temperature
T_{L01}	Infrared Average Peak Temperature

T_m	Material Melting Point
T_{mold}	Polymer Processing Mould Temperature
T_{proc}	Polymer Processing Temperature
T_{td}	Polymer Thermal Degradation Temperature
V_d	Microtomogr. Polymer Volumetric Defects
V_{PEI}	Microtomographic. PEI Volume
V_{Riv}	Microtomographic Rivet Volume
w	AZ-width
α_K	Impact Resistance
β	Coefficient of pressure-dependent Viscosity
γ	Shear Rate
ε	Strain
ε_o	Constant Strain (in Stress Relaxation Testing)
ε_m	Strain at R_m
ε_r	Fracture Strain
η	Viscosity
η_o	Polymer Zero-Shear Viscosity
μ	Coefficient of Friction
µCT	X-ray Computer Microtomography
τ^*	Newtonian Shear-Thinning Coefficient
ω	Angular Speed

INTRODUCTION

Since man realized in the early 20th century that steels were strong and tough but heavy, and ceramics strong but brittle, the efforts in materials science became focused on developing new materials, which could offer the same mechanical features of metals and ceramics but with low density and easier workability. These efforts led to the development of the first synthetic polymers and polymeric composites in the 1910s [1] and the first lightweight alloys, such as aluminium. Nowadays polymeric materials are as strong as or even stronger than some metallic alloys exhibiting not only improved mechanical performance, but also chemical and corrosion resistance plus increased design freedom to manufactured products. On the other hand, lightweight alloys have become mechanically more reliable and also cheaper owing to the processing and fabrication advance supported by the fast development in some industrial sectors, particularly in the transportation industry. The growing necessity of human beings for moving faster but with less fuel consumption, plus the need of cheaper and lighter structures yet strong and durable, has helped accelerating the development of lighter materials.

Nevertheless, polymeric materials and lightweight alloys cannot always individually fulfil design requirements of new products. In order to solve these problems research and industrial communities have started developing combinations of different classes of lightweight materials, such as fibre-reinforced thermoplastics and aluminium alloys, giving rise to so called multi-materials structures. Multi-materials are also known as macrocomposites; they are designed aiming at improving properties or reducing weight and costs [2]. This family of materials is characterized by the presence of solid interface(s), normally with a sharp gradient of properties, in other words interfacial heterogeneity. The use of multi-material structures in industrial products has been raised, mainly due to the coupled properties enhancement. Particularly polymer-metal multi-material structures are being increasingly selected to be applied in real products within industry sectors such as automotive [3-7], shipbuilding [8, 9], aerospace [10, 11], railway [12, 13] and civil engineering [14, 15].

A specific growing class of multi-material structures is the high-temperature thermoplastic/thermoplastic composites-lightweight alloys structure. High-temperature thermoplastics are often associated with their performance under high temperature, i.e. high thermal decomposition temperature ($T > 450\ ^{o}C$), good short- and long-term strength under high temperatures ($T>177\ ^{o}C$) and high softening temperatures (glass transition temperature, $T_g > 200\ ^{o}C$) [16]. When reinforced with fibres high-temperature thermoplastics are called composites and display not only the characteristics related to their parent matrix but also higher toughness, formability and delamination resistance comparing to thermoset matrix composites [17]. The 10% global market growth of this polymer class in the last decades [18] is mainly regarded as the industry response to the environmental legislation and concerns, such as processing emissions and end-of-life recycling [19]. On the other hand lightweight alloys, such

as aluminium, are being ever more used as substitute to traditional commercial alloys, due to their strength/specific weight ratio and corrosion resistance [20]. The consumption of aluminium in Europe and USA has experienced an elevated annual growth rate like for instance in the automotive industry [21, 22]; it is mostly thanks to lower gas emissions and reduced fuel consumption associated with weight savings brought by the substitution of traditional alloys by aluminium.

In theory, an ideal component should not include joints, which can deteriorate its mechanical strength. Nevertheless, the size of a component is usually limited by its production process, and in the case of multi-materials a “joint-free” concept is unrealistic. Hence, joints frequently exist in a multi-material structure. After an extensive literature review on current joining techniques for polymer-metal, presented in Section 1.1 it was identified that these methods are usually application-specific, presenting usually high operational costs related to pre- and post-joining procedures, or environmental threatening owing to post-joining chemical disposals. Furthermore, present techniques are still searching for their market niches, though without complete success. This lets the research & development market open for innovative joining techniques, such as the new friction riveting spot joining method developed and presented in this work, in a comprehensive technical and scientific way.

In Chapter 1 a literature review on current joining techniques for polymer-metal multi-material structures, on used base materials polyetherimide (PEI) and aluminium 2024 and on heat input modelling of similar available joining technique is presented. Chapter 2 presents the experimental approach used in this work. In Chapter 3, used equipments, methods and base materials are described. Chapter 4 provides the experimental results and discussions on the chosen case study materials combination PEI/AA2024-T351, including the description of proposed process theories, mechanisms and models (Section 4.1), the analysis of process parameters (Rotational Speed (RS), Total Time (TT) and Total Pressure (TP)) influence on process variables and properties of point-on-plate joints (Section 4.2) and the additional investigation of features and mechanical properties of overlap joints (Section 4.3). A summary of results, conclusions and final remarks containing the main achievements in this work are presented in Chapter 5. Finally Chapter 6 provides proposed scientific and technical recommendations for future work.

MOTIVATION AND OBJECTIVES

Considering the issues regarding the increasing market development for polymer-metal multi-material structures (particularly high-temperature thermoplastics and aluminium) and the current demand for more reliable, environmental friendly and economically viable joining techniques, as previously discussed in the Introduction, a novel spot joining technique is hereby introduced. The joining technique Friction Riveting, developed and patented in the course of this work [23, 24], has the potential to fulfil these technology and market needs by offering strong joints obtained in a simple, fast and more environmentally correct way. The feasibility of the technique was demonstrated in this work through the evaluation of joints on the commercially available materials polyetherimide (PEI) and aluminium AA 2024-T351. PEI was selected due to its application in flooring, lightning, seating and other secondary and tertiary transportation structures [25, 26], as well as due to its inherent transparency, which facilitates visual inspection of the joint. Aluminium AA 2024-T351, was chosen for its well spread use in fuselages and other aircraft structures [27, 28].

The following objectives in this work have been defined:

- To further develop and demonstrate this new technology by means of joining currently available commercial materials.
- To understand the bonding mechanisms through investigating thermal history and local mechanical phenomena.
- To propose an analytical heat input model for friction riveting, as a tool for process optimization.
- To investigate the influence of process parameters on temperature, microstructure, mechanical properties and process variables.
- To study the mechanical behaviour of overlap joints.

With the accomplishment of these objectives it is aimed to offer the industry a new alternative, simple, fast and cost effective joining technique for a wide range of polymer-metal multi-material structures.

1. LITERATURE REVIEW

1.1. Joining techniques for polymer-metal multi-materials

Although the first investigations on joining of multi-material structures are dated back to the second half of the 1950's, such as the North American patent in joining tubes [29], joining of polymer-metal multi-materials is still a new research topic. While many studies have been carried out on reviewing available joining techniques for thermoplastics and thermoplastic matrix composites, and for lightweight alloys, little information is available on joining of polymer-metal multi-materials. Niu [17] and Messler [30, 31] recently reported that the joining methods used for multi-material structures are mechanical fastening, adhesive bonding, and some welding processes (the latter only for similar joints within the structure, e.g. metallic cover plate of a polymer-metal sandwich panel joined to a metallic stringer). Furthermore, other techniques like hybrid joining methods (adhesive bonding combined with mechanical fastening or welding) and plastic injection moulding into perforated metallic parts are currently being exploited [32-35]. The main features of the current joining techniques for polymer-metal multi-materials are discussed in the next section.

1.1.a. Adhesive bonding

Adhesives are materials used to bond two or more joining surfaces. Two important definitions to understand the adhesive bonding theory are adhesion and cohesion. "Adhesion" is the intimate contact force between two pieces, where the "adhesive" is placed between two joining pieces or "adherends". "Cohesion" means the internal force to keep the body or structure together. Considering this, the ideal failure type of an adhesive bond should be 100 % cohesive, that is, the adhesive is stronger than the adherends.

Adhesive bonding has proven to be a very effective method for joining dissimilar materials. The primary function of adhesive-bonded joints is the transfer of load by shear [36]. The overall mechanical strength of adhesive-bonded joints is, in its majority, dependent on the adhesive properties (strength and ductility), but the joint configuration also plays an important role. Adhesive shear stress distribution in an overlap bonded joint is uneven, where the edges will experience the loading peak values, while the central regions will be less affected [17]. The most used industrial adhesives are cyanoacrylates, silicons and polyurethanes [37].

The main advantages of this joining method in comparison to mechanical fastening and welding are [17, 48, 57]: (a) Bonding of dissimilar materials. (b) No induction of stress concentration. (c) Improvement of fatigue resistance. (d) Sealing. (e) Weight reduction. (f) Good surface finish. (g) Assembly of thin or flexible substrates. (h) Lower stress concentration (no holes required) and

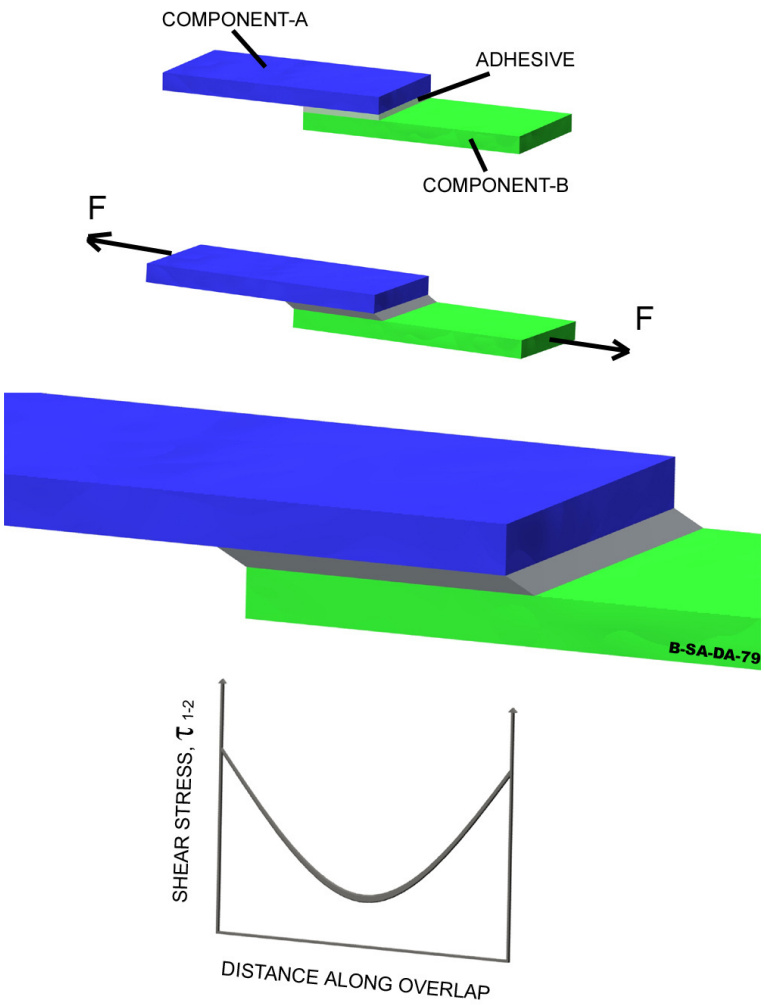

Figure 1. Adhesively bonded single lap joint loaded in tension (F). On the bottom of the figure the distribution of elastic shear stress in the adhesive layer. Adapted from A.J. Kinloch [46].

(i) Good as repair method. The major disadvantages are summarized as [17, 48, 57]: (a) Difficulty of disassembling. (b) Good surface preparation is required. (c) Engineering design confidence is not so high compared with fasteners. (d) Resistant only to shear loading. (e) Difficulty in predicting bond failure. (f) Temperature sensitivity. (g) High purchase and disposal costs. (h) Assembly rate limitations. (i) Special handling (hazardous chemicals and solvents). (j) Emission control, and (k) Adhesive may suffer thermal and environmental degradation.

Adhesive bonding is a technique often used in industrial applications. Basically the process consists of the following steps: 1. surface preparation of adherends by either degreasing, grinding, etching or by applying a primer layer for increasing adhesion [38]; 2. joining partners are firmly clamped and adhesive applied; 3. joining surfaces are brought in contact and kept under pressure; 4. adhesive cures and joint is formed; cure can either take place at elevated or room temperatures. Figure 1 provides a schematic representation of a single lap joint loaded in tension and the distribution of elastic shear stress in the adhesive layer.

In the aircraft industry, adhesive bonding is used to customize and repair primary (critically loaded) and secondary (non-critically loaded) structures, as well as interior pieces made of engineering plastics, polymeric composites and metallic parts [17, 39-41]. In the automotive and railway industries, its application includes the range from decorative to structural parts in polymers, composites and light alloys. A current application example is the Lamborghini Murcièlago, which has carbon/epoxy parts bonded to metals such as steel and lightweight alloys (bumpers, fenders, hood) [42]. Figure 2 shows a scheme of body-in-white structure of the Lamborghini Murcièlago, where composite body panels are adhesively bonded to the steel

frame. These joining parts are firmly clamped during the bonding process (work duration about 30 min.) and cured at room temperature for about 2h. Polymer-metal multi-material structures in cars [43] and in trains [44] are also adhesively bonded nowadays. Shipbuilding is another example of joining with adhesives, where composites ship structures are bonded with metallic parts [45].

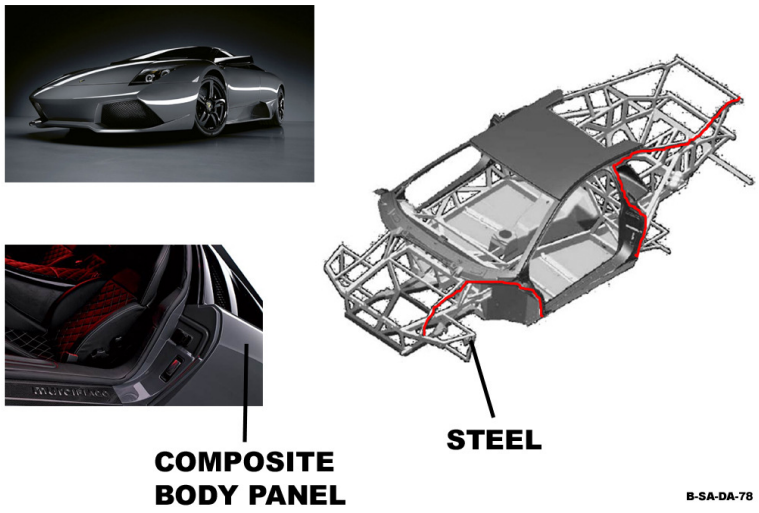

Figure 2. Composite-to-metal adhesive bonding in the Lamborghini Murcièlago. The frame-rails, which are the bonding sites for the composite panels are indicated by red lines. Photos: www.lamborghini.com. Body-in-white drawing: Feraboli und Masin [42].

Further details in fundamental theories of adhesive bonding, which are not aimed to be described in this review, can be found elsewhere [46-49]. Complementary literature on theory and properties of metal-polymer bonds is presented in [50-55]; for recent literature reviews on adhesive bonding theories for polymer-metal multi-materials please refer to [56, 57].

1.1.b. Mechanical fastening

Stress concentration related to the hole in mechanical fastening is a major concern in this technique. However, when disassembly is required this method offers significant advantages. Disassembly and recycling of fastened parts and fasteners are easier in comparison to other joining techniques. For polymer-metal multi-materials, it is a technique, which easily enables several structures to be assembled independently of the joining partners' properties. Mechanically fastened polymer-metal joints frequently fail under loading by the same failure modes as those observed in metallic joints (shear-out, net-tension, bearing, cleavage, bolt pulling through the coupons and bolt failure) [39]; but they show higher susceptibility to hole stress concentration because of the greater polymer notch sensitivity; fabric reinforced joints even display lower joint efficiency (about 50% of the weaker joining partner) [54]. Further studies on the theory and technology aspects of mechanical fastening and mechanical fastening of polymer-metal multi-material structures are presented in [58-61].

When utilizing mechanical fastening the key advantages are [17,48, 60]: (a) Re-openability of the assembled pieces. (b) Easy technology and machinery. (c) Controllable volume capability. (d) Joint of dissimilar materials. (e) Ease of joint inspection. (f) Assurance of structural integrity by well known prediction methods and analysis. (g) Little surface preparation and cleaning is required, and (h) repair or replacement of pieces is facilitated. On the other hand there are also disadvantages [17,48,60]: (a) Augmented Stress Concentration. (b) Loosening of fasteners due to creep, moisture and stress relaxation. (c) Notch sensitivity and Crazing (beginning of cracking) of the polymeric partner. (d) Reclosure limitation (polymer does not withstand torque from inserted fasteners). (e) Differences between thermal expansion coefficient of plastics and metallic partners may increase residual stresses. (f) Loss of properties due to moisture. (g) Need to access both sides of the part. (i) Increased number of process steps, and (j) Weight penalty due to thicker sections (for reducing effect of hole stress concentration) and fasteners.

The selection of fastener type is dependent on the properties of joining partners, such as strength and corrosion resistance. Fasteners for polymeric composites can be metallic or non-metallic. In order to prevent galvanic corrosion, metallic fasteners are typically made of titanium, incomel and A286 steel, which are galvanic compatible materials. Stainless steels, and monel, are standard fastener materials [48]; aluminium and alloy steels are usually chosen in order to reduce weight, however only if environment or coating are not aggressive [62]. Non-metallic fasteners (typically made of fibre-reinforced plastic composites) are not common but still finding their niche. Due to their lower elastic modulus, they are only applied in secondary or tertiary structures. Still they are lighter than metallic counterparts, are electromagnetically transparent, corrosion resistant and minimize radar signature [17]. A typical non-uniform distribution of local peak bearing stress (stress

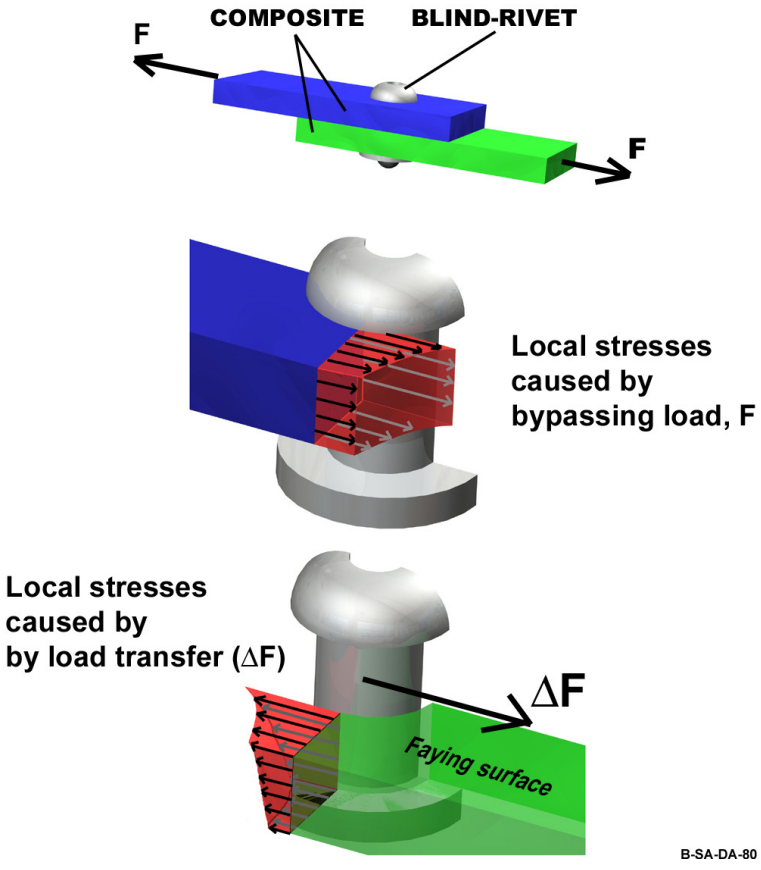

Figure 3. Schematic representation of non-uniform local peak stresses in a tensile-loaded blind-riveted overlap joint. Adapted from Niu [17].

formed in the region around the rivet hole due to interaction with rivet) for blind-riveted composite plates is presented in Figure 3.

There are many variations of mechanical fastening methods for joining multi-material structures. The most used ones are press-in-fasteners, where some sort of device is protruded from a shaft creating an interference fit with the hole into the plastic and self-tapping screws, which comprise the group of re-openable fasteners without female-threaded part. Other types of fasteners are inserts, boss caps, press-on fasteners and panel fasteners [48, 63]. There are also other sorts of mechanical joining techniques for metal-polymer, such as clinching, where sheet materials are fixed between a punch and a die, the punch is moved downwards into the sheets partially pushing through material from the sheet plane inside the die; the continuous action of the punch induces material flow to die edges forming an undercut [64]. It is a flexible and fast process (1,8 s cycle-time) but limited by the thickness and formability of the sheets [65].

Another newly developed mechanical joining process for metal and polymers is the Collar Joining Method [66, 67]. In this method two steps are taken. Firstly, a standard metal-shaping punch projects annular “collars” by perforating the metal sheet; finally, the produced annular collars are cold-pressed into the plastic piece, so a mechanical interlocking is created. It is argued that the process produces strong joints, quickly and without crazing or fracturing the plastic piece. Nevertheless, the nature of this process may suggest that brittle polymers (the case of the majority of thermoset matrix composites and some engineering plastics) would undergo crazing (stress concentration due to cold pressing of metal collar), decreasing mechanical performance. Moreover this process is still limited by the thickness of metallic sheets.

Applications of mechanical fastening are numerous and well established in the market. Some examples involve assembly of automobile body-in-white structures [30] as for instance the rear door of Audi A3 assembled by clinching [65] and automatic gear boxes of several vehicles mounted with aluminium screws [62]. In aircraft, fuselage aluminium panelling, joining of pultruded sandwich composite laminates, and other sandwich structures are also good examples of consolidated applications [39,68,69].

1.1.c. Welding

Welding is not currently wide spread in the field of polymer-metal multi-materials structures for a simple reason: weld formation relies exclusively on the natural attraction tendency between atoms, ions and molecules to physically bonding [31]. In the case of metal-polymer combination, physical interaction takes place only seldom due to the so extremely dissimilar nature of the materials.

While polymers are constituted of large macromolecules formed by a repetition of thousand covalently bonded units (monomers) and held together by secondary forces like van der Waals forces, which in turn leads to amorphous or semi-crystalline open structures [70], metals are materials with high cohesive energy having in general a densely packed crystalline structure [71]. This means that the solubility of metals in polymers is very low; metals tend to form round clusters when embedded in polymers instead of mixing themselves up [72]. Since the cohesive energy of metals is usually two orders of magnitude higher than the one found in polymers, it has correspondingly higher surface Gibbs free energy than polymers (the round cluster shape is the most stable format when no wetting conditions are assumed, in order to minimize energy [73]). Furthermore, necessary plasticizing temperatures for allowing mixing flow of the harder material (metal) during welding are generally too extreme for the softer polymer, which tends to degrade before metal is plasticized or molten. For this reason direct welding of polymer-metal multi-materials structures is not possible without selecting joint design modifications, as for example by covering the surface of the metal component with a polymeric film and welding it with another polymeric component.

Joining by welding in metals is a well known research area and the description of the employed processes is not intended in this work; further information on this matter can be found elsewhere [74, 75]. On the other hand, polymer welding is still a matter of research and development and is worth of reviewing. Welding techniques for polymers are described in detail in several documents and technical publications [37, 76-81]. They are basically divided into three classes regarding the sort of heat generation source: *Conductive, Electromagnetic* and *Frictional*.

Conductive Heating welding processes rely on the transfer of heat by contact between the joining partners and an external heat source. *Hot tool welding* is a representative of this class, where two abutting pieces are put in contact with a heated tool until a thin molten or softened layer is created on the contact surfaces; following that, the heated tool is retrieved and pieces are pressed together under constant pressure, until joint consolidation [48, 77, 78]. Other examples of conductive heating welding processes for polymers are *Hot Gas* and *Extrusion Welding*, the latter being an improved variant of the former [37, 80]. Those techniques were inspired by the traditional oxy-acetylene metal gas welding, where the external heat source consists of a heated gas. In these techniques, two abutting pieces are put in contact and a plastic rod is placed either over or stuck between them. The hot gas is then used to soften the joint area and the rod filler, in order to achieve the softening temperatures of the polymers. The parts are kept together under pressure until the joint is consolidated [48]. The main difference in extrusion welding is that molten polymer, in form of rod or pellets is fed into an extrusion machine, and deposited at the joint, which is pre-heated by a hot gas device in order to increase weldability [79].

Welding techniques based in *Electromagnetic Heating* rely on heating transferred by convection or conduction, which are resultant of molecular interaction with magnetic fields, microwaves, or photon energy. In *Resistive Implant welding* melting heat is generated by the insertion of a metallic wire in the joint region. The wire is connected to electricity and through electrical resistance generates heat. Insert stays entrapped inside the joint after weld consolidation [82]. The *Induction Welding* [48] consists in installing a magnetic insert between the welding pieces and then, by placing them in an alternating current electromagnetic field produced by a coil. This will cause the magnetic insert to heat up, through influence of ferromagnetic electron-spin orientation, melting the welding pieces' surfaces. In *Microwave Welding* [37] a metal part or a conductive polymer is inserted between two welding pieces and submitted to a microwave energy field (2,5Ghz), inside a microwave oven. Since the polymers to be joined are transparent to microwave radiation, only the insert heats up by internal atomic/molecular vibration due to microwave energy absorption [83]. Other recently exploited welding techniques based on photon energy are *Laser Welding* and *Infrared Welding*. With these techniques foil or thin sheet polymers, which are non-transparent to these radiations, are heated by internal molecular vibration incited by radiation absorption, achieving their softening points [84,85].

Frictional Heating based processes have their heat source as a result of relative movement of joining surfaces maintained under pressure. The principal welding techniques within this family are *Spin Welding* (Rotary Friction Welding), *Vibration Welding* and *Ultrasonic Welding*. In *Spin Welding* [86], symmetric joining pieces are placed in contact and rotated against each other, in order to accomplish heating by friction (internal friction by molecular shearing). Spin welding can be performed either by inertia or direct-drive welders, in the same manner as for metals [87-89]. In *Vibration Welding* heat also arises from the friction between welding pieces. In this process, also known as linear vibration welding, two pieces are placed in contact under pressure and set up in relative motion. The relative movement between pieces happens under controlled frequency and amplitude. After accomplishing melting of the joint area, relative movement is stopped and pieces are kept under pressure until the joint consolidates [88,90]. In the case of *Ultrasonic Welding* frictional heating is generated by applying ultrasonic sound waves (from 20 to 40 kHz) in the welding pieces [87]. The pieces are kept together and pressure is exerted by a vibrating horn. Vibrations create surface and intermolecular friction, which in turn melt the polymer. After cooling under clamping, the joint is formed [78].

The field of thermoplastics composites welding is still a new area in joining technology. Ageorges et al. [91], recently carried out a review of fusion-based joining methods for thermoplastic matrix composites. They found that almost all welding methods for plastics are also adequate for thermoplastic composites, with the exception of friction welding methods, which may cause composite's microstructural deterioration, through fibre breaking or realignment. One of the most utilized welding techniques for composites is resistance welding.

McKnight et al. [92] studied carbon-fibre reinforced polyetherketone resistance welded composites parts by ultrasonic evaluation, mechanical testing, microscopy and fractography. Ageorges et al. [93, 94] in their two-parts study, studied the weldability and the process variables influence on glass-fibre and carbon-fibre reinforced polyetherimide composite laminates by investigating mechanical and microstructural weld features. Other works on composite welding can be found in [95-97]. The main advantages and disadvantages observed in welding of polymers are summarized in Table 1 [37,48, 80-82, 85].

Table 1. Main advantages and disadvantages of current welding techniques for polymers [37,48, 80-82,85].

Conductive Heating Processes	
Advantages	Disadvantages
Several Joint Geometries	High Energy Consumption
Cheaper Equipment	Slow Welding Cycles
Low Emissions	Induced Residual Stress
Assembly of large parts	
Electromagnetic Heating Processes	
Advantages	Disadvantages
Improved Heat Input Control	Expensive Equipment
Low Emissions	Low welding Speed
High Joint Strength	Induced Residual Stress
Assembly of large parts	High Energy Consumption
Frictional Heating Processes	
Advantages	Disadvantages
Ease of Assembly	Only Symmetric Geometries
Energy Efficiency	Inferior Mechanical Properties
High Welding Cycles	in Composite Materials
Low Emissions	
Assembly of large parts	T-SA-DA-01

The field of applications of welding of thermoplastics is large and found in several industrial sectors. The main applications of *Hot Tool Welding* are in the automotive, construction and pipework industries. In automotive, hydraulic reservoirs, fitting/filter pipes and battery cases are hot tool welded. Extruded PVC doors and window frames hot tool welded are examples of civil construction articles as well as polyethylene pipes for gas distribution [82]. Examples of *Hot Gas* and *Extrusion* welded products are chemical storage tanks, car bumpers and other applications where thickness is up to 50 mm [79]. For *Resistive Implant Welding* and *Induction Welding* typical applications are joining of sailing hulls, automotive parts and domestic appliances [79,

82]. Applications of *Microwave Welding* are also found in automotive and domestic appliances, where ultra high molecular weight polyethylene, ABS and PC are examples of current joining materials [83]. *Laser Welding* applications are mainly in food and medical packaging, as well as electronic and micro-components [37,81]. In the case of *Infrared Welding,* end-uses are in piping, window frame assembly, biomedical products and laminates [79]. *Spin* and *Vibration Welding* applications are PVC-pipes and fittings, PP ball floats for WC-cisterns, transmission shafts, and aerosol bottles as well as car intake manifolds [48, 79]. Applications of *Ultrasonic Welding* normally fall into domestic (white goods) and medical appliances [48].

1.2. Literature survey on the base materials used in this work

1.2.a. Polyetherimide, PEI

Polyetherimides (PEI) are high-performance amorphous thermoplastic polymers developed in the 1970s by Wirth et al.[98] and first commercialised in 1982 by General Electric under the brand name Ultem [99]. Their chemical structure consists of repeating aromatic imide, propylidene (isopropylidene) and ether groups, as seen in Figure 4. While the aromatic imide groups are responsible for polymer stiffness and high thermal resistance, the ether groups provide PEI good processability associated with low melting viscosities (good melt flow) [100]. PEI is synthesized through a condensation polymerization of diamines and dianhydrides [63]. The polymerisation reagents are N-phenyl-4-nitrophthalimide and di-sodium-salt of bisphenol-A, which are catalysed by NaCl or $Fe_2(SO_4)$ in the temperature range of 200°C to 290°C [101].

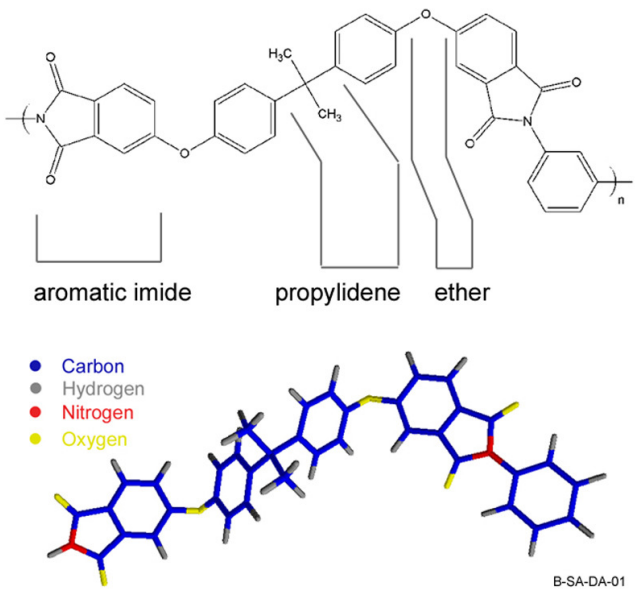

Figure 4. Polyetherimide molecular structure; at the top the 2D-PEI scheme; at the bottom the 3D-PEI stab-model with real bond-angle distributions.

PEIs are generally characterized by high mechanical strengths and rigidity at room and elevated temperatures, good long-term heat resistance, excellent dimensional stability, and good resistance to a broad range of chemicals including most hydrocarbons, non-aromatic alcohols, and fully halogenated solvents. They also offer good resistance to mineral acids and tolerate short-term exposure to mild bases [99,101]. Due to its amorphous structure, the natural polymer

is transparent and amber in colour [102]. It also displays good ultraviolet radiation resistance without extra incorporation of additives. The polymer is transparent to infrared light and microwave radiation [99].

PEI resins can be processed on most conventional thermoplastic equipments. In order to achieve good processing results, resin granulates must be dried prior to melt processing, because of their relative high water absorption [99,103]. High melting processing temperatures are needed, ranging from 350°C to 425°C, for injection moulding [102]. PEI also shows a low moulding shrinkage of 0,005-0,007 cm/cm, which results from its low coefficient of thermal expansion [25]. Extrusion, thermoforming, and compression moulding are also processes used in the fabrication of PEI components [101]. Typical joining methods for PEI and PEI-composites include hot tool [104,105], resistance [94, 106-109], ultrasonic [99], vibrational [110], and induction welding [99]; mechanical fastening, adhesive bonding [99,111] are also alternative joining methods.

PEI is one of the strongest available commercial engineering thermoplastics [25,111]. Its mechanical behaviour is in accordance to Hooke's law, with a linear stress-strain relationship below the proportional limit (about 69 MPa for unreinforced resin) and an ultimate tensile strength usually over 100 MPa at room temperature [100, 112-115]. The high-temperature mechanical strength of this material is very good. At a range of 170 to 190 °C, where temperature is generally far beyond the useful range of engineering plastics; tensile strength is about 50% of room temperature values [100,116,117]. PEI is replacing metals in several structural applications because of the exceptionally good long-term resistance to creep at high temperatures (35 to 160 ^{o}C) and stress levels [99,112, 118]. There is little literature information on fatigue properties of PEI resins. However, a study [119] has shown that PEI fatigue S-N curves presented endurance limits of about 38 MPa (testing conditions: 5 Hz, 20 ^{o}C, bending mode, R= 0,1, sinusoidal wave shape), below which fatigue failure occurred for a range of cycles between 10^{7} to 10^{8}. Due to the fact that PEI is a brittle amorphous polymer impact resistance is highly affected by notch sensitivity [120]. Charpy Impact figures showed an average decrease of circa 95 % for notched samples in comparison to un-notched samples (13,3 J/cm for un-notched samples and 0,67 J/cm for notched samples) [99].

One remarkable thermal property of PEI resins is their high softening point, represented by the glass transition temperature in the order of 215 to 220 ^{o}C [99-101] , which allows the polymer to be intermittently used at 200°C. PEI's high heat performance, elevated heat deflection temperature (about 200 ^{o}C at 2 MPa) and excellent flame resistance characterizes it as plastic for high-temperatures applications [102]. PEI's high limiting oxygen index, LOI, of 47% and low smoke generation (ASTM E-622) [111], allows it complying with the hard flammability and heat-release aircraft interior applications requirements [25]. Table 2 presents the main properties of polyetherimides.

Table 2. PEI main mechanical, physical, thermal and processing properties [25, 99-101].

Mechanical / Physical		Thermal		Processing	
Rm (MPa)	105 (1)	CTE, linear at 20 ºC	45 (3)	Tproc (ºC)	335-375
ε% @ Yielding	7-8 (1)	(µm/m-ºC)		Tmold (ºC)	114-149
εR (%)	10 (1)	Tg (ºC)	215 -220	Tdrying (ºC)	135-149
E (Gpa)	3,4 (1)	HDT (ºC)	190 (4)	(1) DIN 53455 and DIN 53457-B4 for E-values (2) DIN 53453 for notched Charpy specimens (3) DIN 53752-A (4) DIN 53461 - ISO/R75 method A, 1,8 MPa (5) DIN 52612	
αK (kJ/m^2) (3)	3,5 (2)	Conductivity	0,22 (5)		
µ Fric	0,18 - 0,42	(W/m-K)			

T-SA-DA-02

The world market for polyetherimides is in expansion. In 2000, market figures have shown a production volume of approximately 14500 tons, about 7% of the whole production volume for high-performance polymers [16]. PEI polymers are primarily used in the automotive, electrical/electronic, medical, packaging, aircraft and industrial markets [100,121, 122]. PEIs are used as sheet and moulded parts in aerospace applications, due to their inherently flame retardant behaviour, low smoke emission, chemical resistance against most fuels and fluids. Examples of application in primary structures in helicopters are the thermoplastic tailplane of the Westland 30-300 [123]. In this component thermoset matrix composites were substituted by CF-PEI matrix composites, leading to a cost reduction of around 17% and weight savings of 22% [124]. In order to assembly those components different joining technologies were adopted, from mechanical fastening to adhesive bonding and ultrasonic welding [125]. Recent applications of this material are found in the Fokker 100 aircraft cargo flooring (GF-PEI), in the floor panes of Gulfstream G400 and G500 business jets and in the Airbus Beluga airplane [126].

1.2.b. Aluminium 2024-T351

Aluminium 2024 is a wrought heat treatable alloy member of the 2000 aluminium series, where the main alloy elements are Cu and Mg, and first introduced in the 1930s [127]. The nominal chemical composition of this Al-Cu-Mg ternary alloy is presented in Table 3.

Table 3. Nominal chemical composition of aluminium 2024 alloys [128].

Wt%	Cu	Mg	Si	Mn	Fe	Zn	Cr	Ti	Al
ASM (nominal)	3,8-4,9	1,2-1,8	≤ 0,5	0,3-0,9	≤ 0,5	≤ 0,25	≤ 0,1	≤ 0,15	bal.

T-SA-DA-03

The atomic formula of aluminium 2024 is $AlCu_4Mg$. The T351 temper designation means that the alloy was solution heat-treated (at ≅ 495 °C), cold-worked, naturally aged to a substantial stable condition, and than stress relieved. Moreover, it does not undergo further straightening or stretching. The T351 temper is commonly used for plates, rods, forged parts and rolled rings

[128]. 2024-T351 alloy generally exhibits fair corrosion resistance, medium to good stress corrosion cracking resistance and workability, and good machinability [127,128]. Their major mechanical, physical, thermal, and processing properties are shown in Table 4.

Table 4. Main mechanical, physical, thermal and processing properties of 2024-T351 aluminium alloys [127-130].

Mechanical / Physical		Thermal		Processing	
Hardness (HV0,2)	137	CTE, linear at 20 ºC	23,2	Annealing Temp. (ºC)	256
Rm (MPa)	425	(µm/m-ºC)		Sol. Heat Treating Temp. (ºC)	495
R0,2 (MPa)	324	Conductivity	130 - 150		
εR (%)	8 - 20	(W/m-K)			
E (GPa)	70	Melting Point (ºC)	518 - 548		

T-SA-DA-04

For this precipitation hardenable alloy, the nature of the major hardening particles is closely dependent on the Cu/Mg ratio. For lower ratios (Cu/Mg 2,2 to 2,7) hardening is attained in the sequence GPB zones (Guinier-Preston-Bagaryatskii) through a coherent phase S' to Al_2CuMg or S-particles, while for higher ratios through the GPB-zones sequential precipitation of coherent phase θ' to Al_2Cu or θ-particles [129, 131-133]. For the former case the precipitation sequence leading to the equilibrium phase S is still a matter of discussion [134]. It is believed that these particles are formed by a complex precipitation sequence summarised as following,

Solid Solution, SS → GPB zones → S' (Al_2CuMg) → S (Al_2CuMg)

Even more complex is the precipitation sequence for the latter case, where the equilibrium phase θ is formed.

Solid Solution, SS → GPB 1 zones → GPB 2 zones → θ' → θ'' → θ ($CuAl_2$)

For further information on the sequences of precipitation described above, as well as on precipitate geometries and properties for alloy 2024, please refer to [129,134, 135].

Currently, dominant joining methods for aircraft alloys such as the aluminium 2024 are mechanical fastening and adhesive bonding. Only few elements in an airplane are joined by welding [136]. The reason for that is directly related to the low weldability (by conventional fusion methods) observed for aircraft alloys, like for instance the 2024 [74]. The major issues dictating the weldability of aluminium alloys are the presence of oxide layers with much higher melting points and electrical isolation in comparison to aluminium bulk material, high hydrogen

solubility in the molten state, which leads to solidification porosity, poor electrical conductivity (associated with the oxide layer) and high thermal conductivity, which requires larger heat inputs in order to keep up with heating [128]. Friction welding, flash welding, gas metal arc welding (GMAW), gas tungsten arc welding (GTAW), plasma arc welding (PAW), laser beam welding (LBW), electron beam welding (EBW), diffusion welding (DB), and friction stir welding (FSW) are examples of welding processes used in joining aircraft aluminium alloys [137]. Although 2024 alloys are also used in other transportation applications, machine parts, screws and fasteners, among others, the major application of these alloys is still within the aircraft industry. It is used mainly for fuselage skins clad with a layer of pure aluminium for corrosion protection. This alloy is found in most in-service civil and military airplanes [27,127].

1.3. Review on analytical heat input modelling of friction and spin welding

In this section, an introductory survey on heat input modelling of friction and spin welding is provided in order to support the proposed heat input model for friction riveting (Section 4.1.g), which principles were based on the current thermal modelling of these two similar welding techniques.

Although friction and spin welding are consolidated processes, the thermal modelling of these processes is still in constant development due to the physical complexity of the processes. Analytical thermal models are normally simplified tools in comparison to more complex mathematical models. Even though, they are very attractive for process optimization, considering that they are usually semi-empirical, in the case of these two joining processes. The use of experimental data as model input facilitates the calculation of theoretical data, which in turn accelerates the interpretation of calculated results. On the other hand, this sort of modelling provides normally only global average data, letting the study of local behaviour data apart. They also usually involve physical and mathematical simplifications, which for more refined mathematical thermal modelling are a key factor for success.

Rykalin et al. [138] presented one of the first analytical heat input models for friction welding. In their model, heat input and temperature distribution in the rubbing area for low carbon butt-welded rods were studied. The calculation of heat input (Q) was assumed to exclusively arise from the frictional forces. For simplification they assumed the friction force at a given instant to be constant and proportional to the distance (r) from the centre of the rubbing area. Additionally, pressure (P) and friction coefficient (μ) were considered constant over the whole cross section of the rubbing area due to the difficulty in measuring them. The Equation (1) for Q was:

$$Q = M \cdot \mu \cdot v_0 \cdot P \qquad [cal/s] \tag{1}$$

where:

M = 2,34 x 10-2 is the heat equivalent of the mechanical work.

μ is the friction coefficient.

V_0 is the peripheral speed of rotation of the rod.

Vill [139] following the assumptions of Rykalin [138], based its model on the friction forces contributions involved in the friction welding of low carbon steels. In addition the author tried to taken into account the influence of rotation speed (RS) in the friction coefficient, resulting in Equation (2):

$$\mu = \frac{k}{(RS \cdot r)^2} \tag{2}$$

where :

k is a constant coefficient equal to the square of the linear speed (mm2/min2). For low carbon steels k = 8 x 107 mm^2/min^2.

r is the distance to the center of the joining partner.

Q (in W/mm^2) is obtained by Equation (3):

$$Q = 2 \cdot P \cdot \left(\frac{k}{RS \cdot R} \right) \cdot 10^{-3} \qquad [W/mm^2] \tag{3}$$

where:

R is the radius of the rod.

Schaefer [140], Schober [141] and Neumann [142] proposed similar approaches for modelling heat input of friction welding of metals. In their models they additionally considered the contribution of the axial load in the heat generation. From the assumption that almost the whole mechanical energy is transformed in thermal energy (a transformation efficiency equal to 1,0) they assume that, the mechanical work (W_{mech}) due to rotation and axial load was equal to total

heat input (Q_{total}) in the welding area. Q_{total} is equal to the sum of heat input due to friction contribution (Q_{fr}) and heat input due to the axial load contribution (Q_{ax}). Q_{fr} and Q_{ax} were calculated from the instantaneous power, which take into account the contributions of frictional torque (M_z) and the axial load (F) respectively. Q_{total} is obtained from Equation (4):

$$Q_{total} = Q_{fr} + Q_{ax} = \left(M_Z \cdot \omega\right) + \left(F \cdot v_0\right) \qquad [W] \tag{4}$$

where ω is the angular velocity of the rotating joining partners.

The experimental validation of this model in friction welding of steels provided the information that the contribution of axial load on heat generation is less than 1,0%, so for practical calculation purposes it could be discarded [140, 141].

Crossland [143] in his work also chose to consider only the influence of friction forces on heat generation of friction welding of metals. Although the author recognized that there is a correlation between μ and the temperature (T), he also assumed μ to be equal to the quotient between shear strength and yield pressure of the softer material. As those two quantities, which are related to strength, will vary together with temperature, he considered μ as a constant. In the same fashion as Rykalin [138] and Vill [139], the calculated Q involved the contribution of the friction forces. However, the author tried to incorporate the pressure distribution over the rubbing area in his model:

$$P(r) = \frac{P}{2 \cdot \pi \cdot R^2} \tag{5}$$

The resultant Q-model of Crossland for the whole rubbing area is given by the Equation (6):

$$Q = \frac{2}{3} \cdot P \cdot \mu \cdot RS \cdot R \qquad [W] \tag{6}$$

Another heat input model for friction welding of metals, which shares the same assumptions of the models presented in Equations (1), (3) and (6), was presented by Na [144]. In contrast to these models the author preferred representing the influence of friction forces by using frictional torque (M_z) ($M_z = 2 \times \pi \times n$) so Q is obtained by the Equation (7):

$$Q = \frac{3 \cdot M_Z \cdot RS \cdot r}{R^3} \qquad [W/mm^2] \tag{7}$$

Midling and Grong [145] used a similar approach as by Vill [139] and Crossland [143] as a base for the development of a more complex temperature model in friction welding of aluminium and

aluminium metal matrix composites (MMC). Their experiments showed that this heat input theoretical approach firstly developed for steel could also be successfully extended for other metallic materials.

Considering the geometric similarities of friction welding and spin welding of thermoplastics [86], the initial efforts in thermal modelling of the latter were based on the available thermal models for friction welding of metals. Although both joining techniques are geometrically similar, the physical phenomena taking place during welding are different. Firstly, friction welding is a solid-state welding method (temperatures bellow the melting point of the alloys), while spin welding is a fusion welding method. The friction coefficient of polymers has a different behaviour in comparison to metals with singular wear mechanisms dictating friction. However, the most important physical difference between both techniques is the flow behaviour of the molten polymer. The viscosity of the polymers is strongly dependent on temperature and strain rate, so a sharp drop in viscosity can occur within a slight increase in temperature [146]. This in turn leads to changes in friction conditions and heat generation, and this viscosity plays an important role in heat input modelling of spin welding.

Potente and Reinke [147] provided a mathematical description of spin welding of plastic tubes made of polyolefins. They considered only the contribution of friction forces in their modelling, dividing the heat input into heat input during the solid-phase (Q_{solid}) and during the molten phase (Q_{molten}). Q_{solid} was calculated from the work of friction, in the same manner as for friction welding, while Q_{molten} from viscous dissipation per unit of volume. Q_{total} can be calculated by Equation (8):

$$Q_{total} = Q_{solid} + Q_{molten}$$

$$\Leftrightarrow \left(\frac{P \cdot \omega \cdot \mu}{3} \cdot \frac{r_2^3 - r_1^3}{r_2^2 - r_1^2} \right) + \left[\eta \cdot \left(\frac{r_m \cdot \omega}{H} \right)^2 \right] \qquad \left[W / mm^3 \right] \qquad (8)$$

Where:

r_1 and r_2 are intern and extern radius of the tube

r_m = (r1 + r2)/2 is the average radius of the tube

η is the molten viscosity of the polymer

H is the thickness of the molten polymeric layer on the rubbing area region.

Tappe and Potente [148], Stokes [149], and Stokes and Poslinski [150] modelled the spin welding process in a rheological approach in the way like other polymer processing techniques involving melting of polymer are described. In these treatments no direct values of heat input

are provided. On the other hand, the process is separately studied in its different phases (solid to molten state) and quantities such as melting and local temperatures, among others, are modelled. However, all these three models showed that viscosity (η) is strongly influenced by the parameters of the process, only the thermal modelling of Stokes and Poslinski [150] was able to account for the strong dependence of η on process temperature. They succesfully modelled the temperature-strain rate behaviour of η in the molten state of spin welded PEI-parts, by zero-shear viscosity theory by Willians-Landel-Ferry (WLF) associated with the shear-rate dependence theory described by the generalized Cross-equation. This approach on determining η in the molten state was adopted in the heat input for Friction Rivet and is further discussed in Section 4.1.g.

2. EXPERIMENTAL APPROACH

The experimental strategy behind this work consisted of an initial exploratory development of the friction riveting technique and its patent application. In this initial phase several combinations of materials were joined and different joint geometries were tested (not described in this work; for further information see references [151-153]). Additionally the main properties, process parameters and variables were identified and described through a physical and microstructural approach.

The second experimental phase consisted of selecting adequate base materials for the main experimental investigation. Based on commercial importance, mechanical, thermal and optical properties (transparency of the polymer base material), two aircraft materials, Polyetherimide (PEI) and aluminium AA2024-T351 were chosen.

Following that a feasibility study on the joinability of these base materials was carried out for two different joint geometries, the point-on-plate (where the rivet is inserted into a polymeric plate) and the overlap geometries.

The fourth and the main experimental phase consisted of the investigation of the bonding mechanisms, the influence of process parameters on properties and process variables, the development of an analytical heat input model and the microstructural characterization of overlap joints. The investigation of the bonding mechanisms was carried out through microstructural analysis of the joint region with special attention to the polymer-metal interface (by microscopy and X-Ray microtomography), analysis of the temperature history (thermography and infrared-thermography), investigation of thermal degradation of the polymer (gel permeation chromatography) and the study of the local mechanical properties (Vickers microhardness).

The study of the influence of process parameters on joint formation was done by individually varying rotation speed, joining time (total time) and joining pressure (total pressure), and interpretating the associated results of joint formation (microstructure and material flow), temperature history, local and global mechanical behaviour (microhardness and tensilie testing, respectively) and process variables (heating time, burn-off, burn-off rate and frictional torque). Parallel to that, an analytical heat input model based on available models for friction and spin welding was developed and demonstrated. To close phase four, a microstructural investigation and the evaluation of static and creep mechanical properties (lap shear tensile testing and stress relaxation testing) of single-riveted overlap joints was carried out.

The analysis and conclusions obtained from the experiments helped further understanding this new technique, pointing out potential scientific and technical improvements, which were

suggested as future work. Finally, this experimental approach provided an alternative joining technology for a wide range of polymer-metal multi-materials structures. Figure 5 presents the summarized flow-chart with the experimental approach of this work.

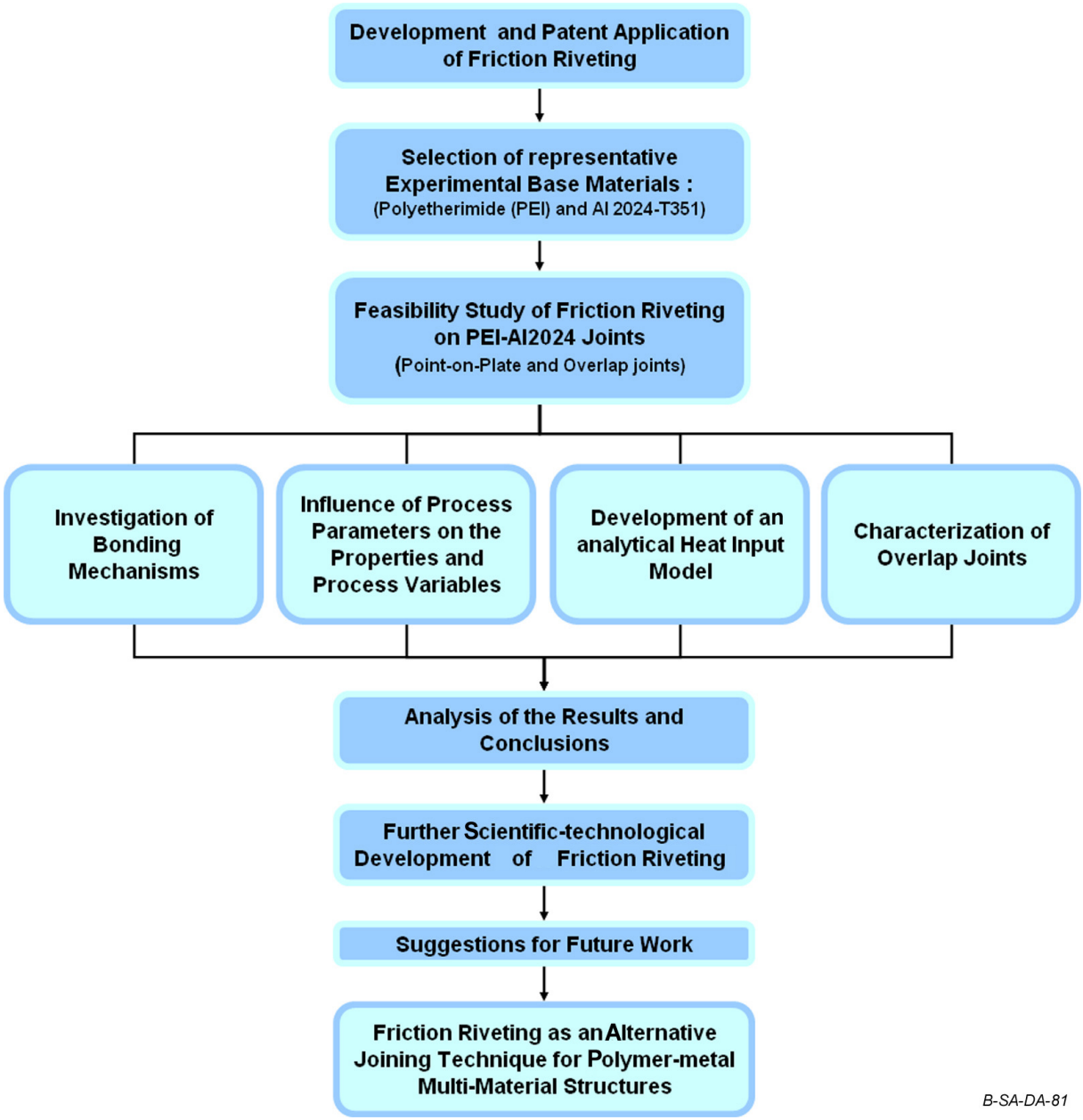

Figure 5. Summarized experimental approach of current work.

3. EQUIPMENTS, METHODS AND MATERIALS

3.1.a. Friction riveting joining equipment

The equipment used at GKSS for friction riveting consists of a friction welding system RSM200 manufactured by Harms & Wende GmbH & Co. KG [154]. The machine was developed for joining steel, aluminium and non-ferrous alloys. The system is suited for flexible applications and for automation. Owing to the possibility of applying a pneumatic operated chuck the welding system is prepared for fully automatic installations [154]. The summarized technical data regarding the friction riveting equipment used in this work is presented in Appendix 1. The modular friction welding system RSM200 consists mainly of three components, the modular welding head RSM20, the switch cabinet RSMS20 and the control panel RSMP20, which are presented in Figure 6.

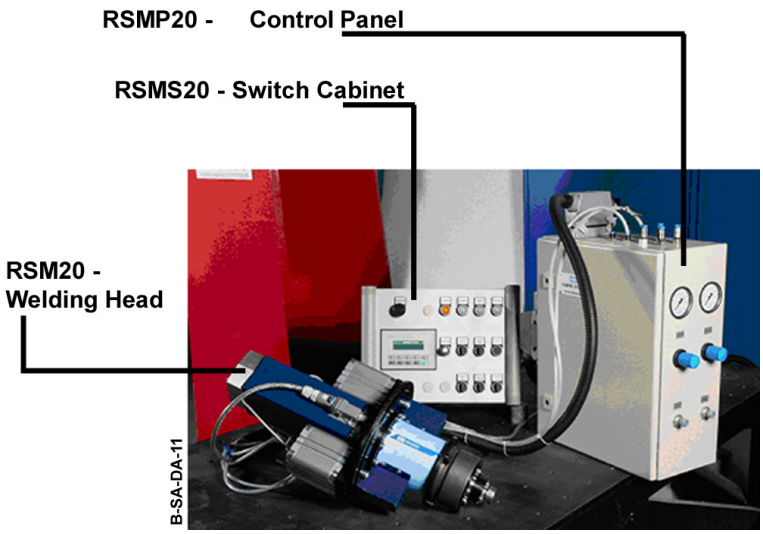

Figure 6. RSM 200 friction welding machine used for friction riveting.

The RSM200 experimental setup frame was specifically designed for GKSS Forschungszentrum by Witte GmbH, Germany, in aluminium profiles. This set-up includes the welding head and all necessary cabinets. The welding head is placed horizontally in a fixed position, while the clamping-table can be moved backwards and forwards in 20 mm stages. Various sample clamping devices can be used, making possible the joining of different sample geometries. Due to the possibility of using high rotational speeds and the good flexibility of the set-up system the machine has been found adequate to the development of the friction riveting method.

In addition to the RSM 200 system, a force measuring system was used for recording the frictional torque during friction riveting joining. The system was composed of a table supported

by four quartz force sensors (mod. nr. 9366AB, Kistler Instrumenten AG) controlled by a multi-channel charge amplifier specially designed for force and torque measurements (mod. nr. 5017B, Kistler Instrumenten AG) which were connected to a PC with controlling/evaluation software Dynoware (Kistler Instrumenten AG). For technical information regarding this force control system, please refer to [155]. The torque measuring system was fixed vertically on the RSM 200 clamping-table in alignment with the centre of the spindle, so measured torque values could be direct translated to frictional torque (M_z) at the rivet tip. Figure 7A and B show the torque measuring system coupled on the RSM200 joining equipment.

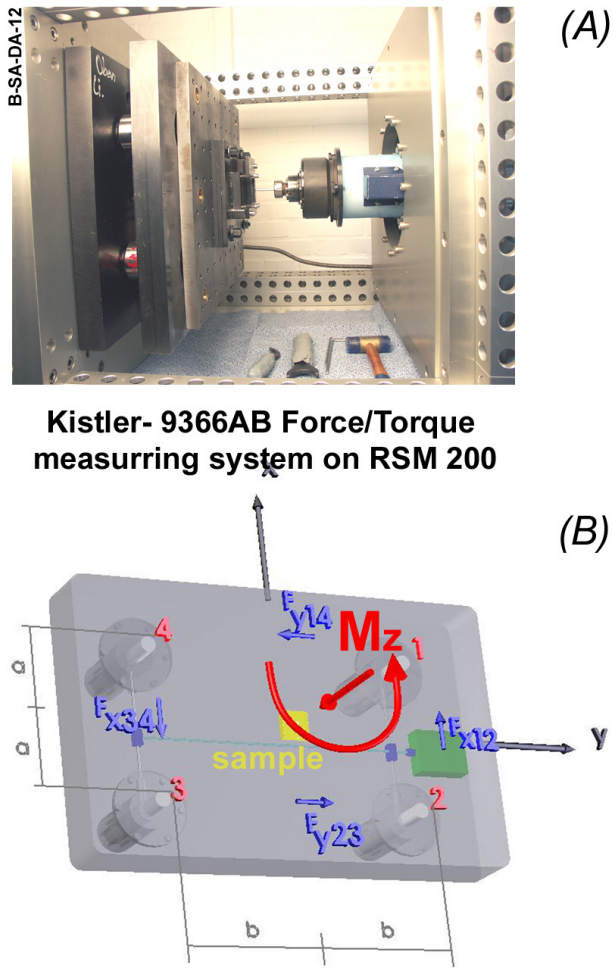

Figure 7. A) Major components of the torque measuring system in this work. B) Scheme of main forces and frictional torque (M_z) evaluated by the system.

Friction riveting joining parameters are controlled by software (RQ-Fuzzy, Harms & Wende). This software is capable of graphically recording four analogue variables (rotational speed, time, pressure and axial displacement); it is also possible to export the experimental data as ASCII-files for further analysis in statistics software. In association with the M_z control data, the joining system is able to supply a complete set of process information, which is very important for identifying possible process issues and equipment mal-function. A schematic example of a graph with major controlled joining parameters and variables is seen in Figure 8. As the RSM 200 equipment is a time-controlling direct-drive friction welding machine, the friction riveting is

consequently time-controlled in this work. Prior to joining, the duration of the application of the experimental rotation speed and pressure (joining time) is set up and axial displacement plus frictional torque are recorded.

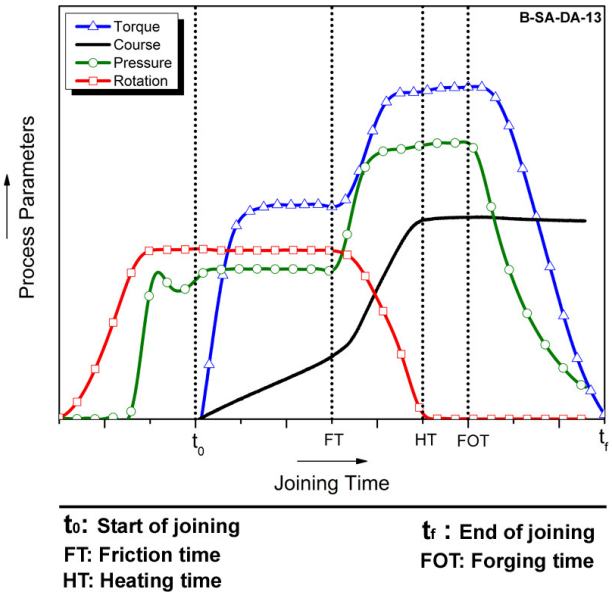

Figure 8. Scheme of a friction riveting joining diagram.

3.1.b. Joining procedure

A typical friction riveting joining procedure used in this work consists of the following steps: prior to joining, base materials are cleaned with acetone for removing machining fluids. The polymeric base plate is then firmly fixed over the Kistler force control table placed in the RSM 200's clamping table. Besides, the rivet is fixed in the spindle adapter. Joining parameters (rotation speed, time and pressure) are set in the RSM 200 equipment panel and both RQ-fuzzy and Dynoware control software is manually started. Following that, the machine is turned on, whereby the rotating spindle is moved forward, when programmed rotation speed is achieved. The rotating rivet touches down on the polymeric base plate, starting the joining process plunging. When the pre-set friction time is accomplished, rotation is stopped and forging pressure is applied up to the end of the joining time. Subsequently, the forging pressure is released and the joint removed from the clamping system. Finally, the samples are labelled and control data exported for further statistical treatment. In this study, all produced joints had their control data stored.

3.1.c. Microscopy

In order to analyse the macrostructure, microstructure and fracture surfaces from base materials and joints, light optical microscopy (LOM) and scanning electron microscopy (SEM),

were chosen. LOM-samples consisting of cross-sections (from the centre of the rivet, across the whole thickness for joints, and perpendicularly to extrusion direction for polymeric base plates) and longitudinal sections (only for the metallic rivet) were cut off with a diamond disc low speed cutter (ISOMET, Buehler); cut offs were embedded in low cure-temperature thermoset epoxy-resin (Epoxihart, Buehler) for avoiding structural thermal alteration of polymer-metal interface. Embedded LOM-samples were ground and polished in a semi-automatic metallographic sample preparation machine (Phoenix 4000, Buehler) with diamond and silica solutions down to 0,05 µm adopting standard metallographic procedures [156].

In addition, etching was carried out to reveal metallic microstructural features on the samples. LOM-samples of base materials and joints were electro-etched in Barker anodic solution (200mL distilled-H_2O plus 5 g of fluoboric acid 35%) during 120 s, with 30 V DC/0.9 A at 20 ℃; Kroll etching solution (100 mL distilled H_2O, 6 mL nitric acid 65% and 3 mL hydrofluoric acid 40%) was also used for some samples. The macrostructure of LOM-samples was investigated in a stereo-microscope (Olympus), the microstructure in a polarised light microscope (PMG 3, Olympus). Fracture surfaces were examined by stereo-microscopy (Olympus), and by secondary electrons mode (SE) in a SEM-microscope (DSM 962, Zeiss).

3.1.d. Microhardness measurements

Microhardness investigations were carried out on LOM-samples preceding (for polymeric areas) and following etching (for metallic areas); this test is important in providing information on the local mechanical properties of base materials and joints. Vickers microhardness measurements were carried out according to ASTM E384-992e1 [157] for the metallic areas and in accordance to procedures [158] described in the literature for the polymeric areas. The microhardness equipment used in this evaluation was a UT 100 microhardness tester (BAQ GmbH) [159], which utilizes ultrasonic frequency for measuring indentation depth and to calculate hardness. The machine operates with control/evaluation software, which allows obtaining microhardness profiles and maps.

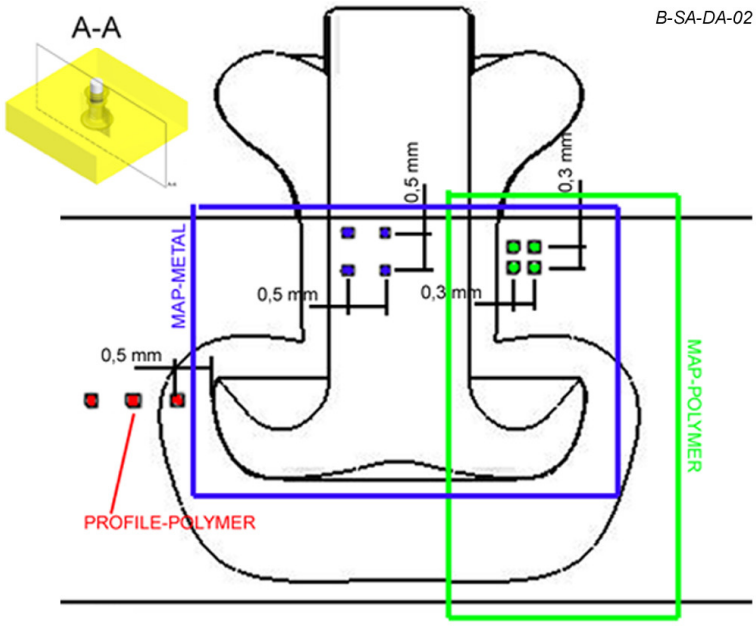

Figure 9. Scheme of microhardness measurements in a cross section A-A from a friction riveting joint.

Microhardness maps for the metallic areas were automatically obtained by scanning an area of approximately 400 mm^2 with an indentation force of 1,96 N (200g) during 5 s with a distance between indentations of 0,5 mm. An example microhardness-map for the polymeric area of a joint was generated by scanning an area of roughly 300 mm^2 with an indentation load of 0,98 N (100g), during 15 s with a distance between indentations of 0,3 mm, calculated manually by measuring the indentation diagonals in a optical microscope and applying it in Equation (9) [158]:

$$HV = \frac{1{,}854 \times P}{d^2} \tag{9}$$

where:

P is the force.

d is the mean indentation diagonal

Horizontal polymer microhardness profiles (3,5 mm long) positioned approximately 0,5 mm away from the rivet centre in joint's cross-sections, were produced by following the procedure described above, for studying the influence of variable process parameters on joint properties. Figure 9 presents the schematic representation of microhardness measurements in a friction riveted joint.

3.1.e. Tensile testing

Flat tensile testing specimens for the polymer base material were machined parallel and perpendicular to the extrusion direction from the whole thickness of 13,4 mm PEI-plates, in accordance to geometry type 3 of DIN 53455 [160]. Round tensile specimens for the metallic profiled M5-rivets (threaded) were machined from drawn rods down to a nominal diameter of 5 mm and length of 60 mm; this geometry was adapted from DIN EN ISO 898 [161] for tensile testing of metallic screws. For evaluating tensile strength of joints, T-pull tensile specimens were designed based on the concept behind tensile testing for determining the critical length of engagement (number of internal threads in complete engagement with a nut or boss) of threaded bolted joints [162]. Point-on-plate joints were used as T-pull tensile specimens, where the rivet had the geometries and dimensions of a half of a DIN EN 10002 [163] round-tensile bar and the polymeric base plate dimensions were 70 x 70 x 13,4 mm (L x W x T). Figure 10 illustrates the tensile samples used in this work.

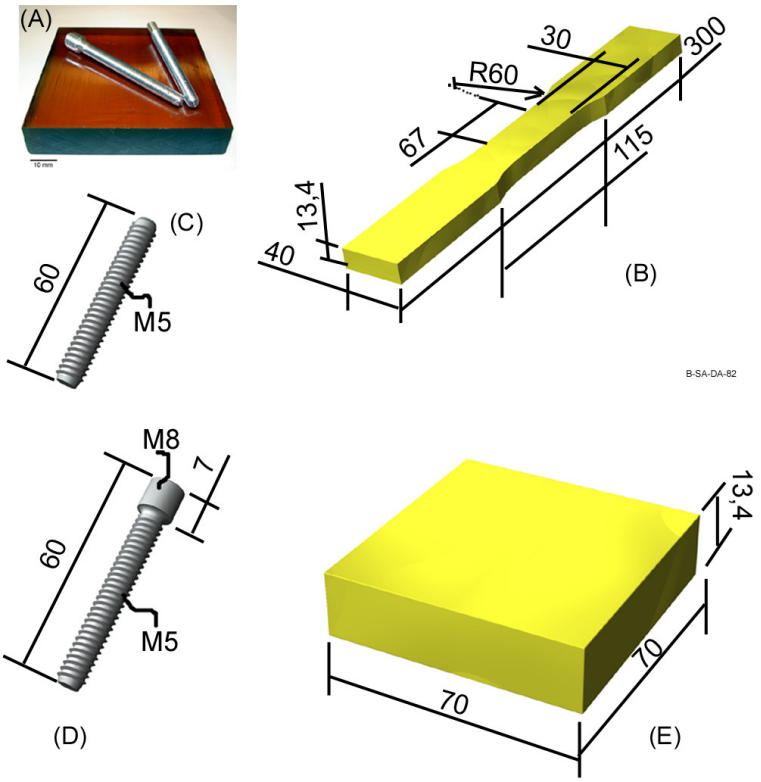

Figure 10. Tensile specimens used in this work. A) photo of the PEI-base plate and Al 2024 for T-pull tensile testing. B) DIN 53455 type-3 flat tensile specimen. C) M5-rivets tensile test specimen adapted from DIN EN ISO 898. D) Rivet for T-pull specimen based on DIN EN 10002. E) Polymer plate for T-pull specimens.

Tests were carried out in a universal testing machine (Instron 1195) with 50kN load capacity. Laser extensometry (FOE WS 180; 3,3 mW, 25 Hz, 0,4 s, λ= 671 nm, Fiedler Optikelektronik) was chosen for measuring elongation through placing white stripes in the gage length (L_0= 20 mm) positions. Metallic profiled rivets were held by adapters generally used for testing aluminium screws [164,165]. Testing traverse speed was 1,0 mm/min at room temperature (21 °C). A sample holder for the joined samples was specially fabricated for fixing the polymeric base plate, whereas the rivet was screwed in a sample holder for round tensile bars. The tensile testing assemblies are shown in Figure 11A and Figure 11B.

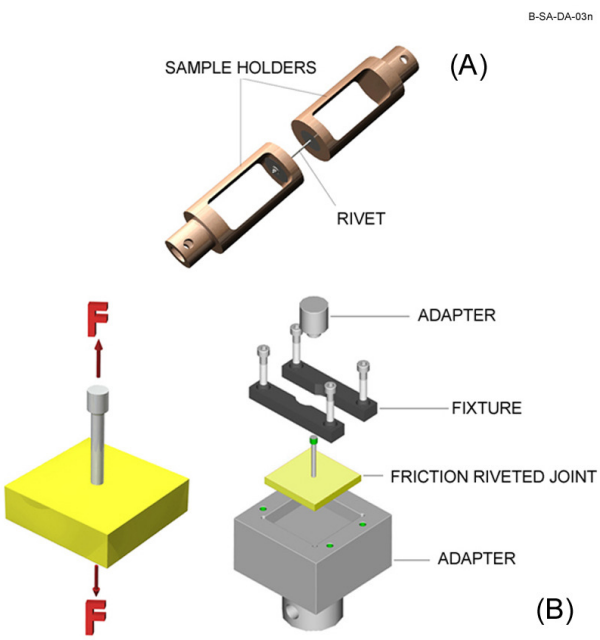

Figure 11. A) Schematic representation of tensile testing in M5-metallic rivets. B) Scheme of T-Pull tensile testing in friction riveting joints.

3.1.f. Lap shear testing

Lap Shear testing was carried out using a Zwick/Roel 1484 servo-electric testing machine with 200 kN load capacity. Tests were performed at room temperature with traverse speed of 2mm/min. Elongation measurement was obtained by using a mechanical extensometer (ZWICK) as the principal data collecting system and a laser extensometer (same used system as described in Section 3.1.e) as a secondary control source for evaluating possible "xy" in-plane rotations. ASTM–D–5961/D-5961M-05 [166] lap shear samples (dimensions: 342 x 36 x 10 mm, overlap of 36 mm; free rivet length of 20 mm and ϕ 5 mm rivet diameter) were extracted from coupons of single-rivet overlap joints (coupon's dimensions: 402 x 96 x 10mm, overlap of 36 mm). Figure 12 presents the dimensions of overlap joints coupons, lap shear samples, as well as the testing assembly with used extensometers.

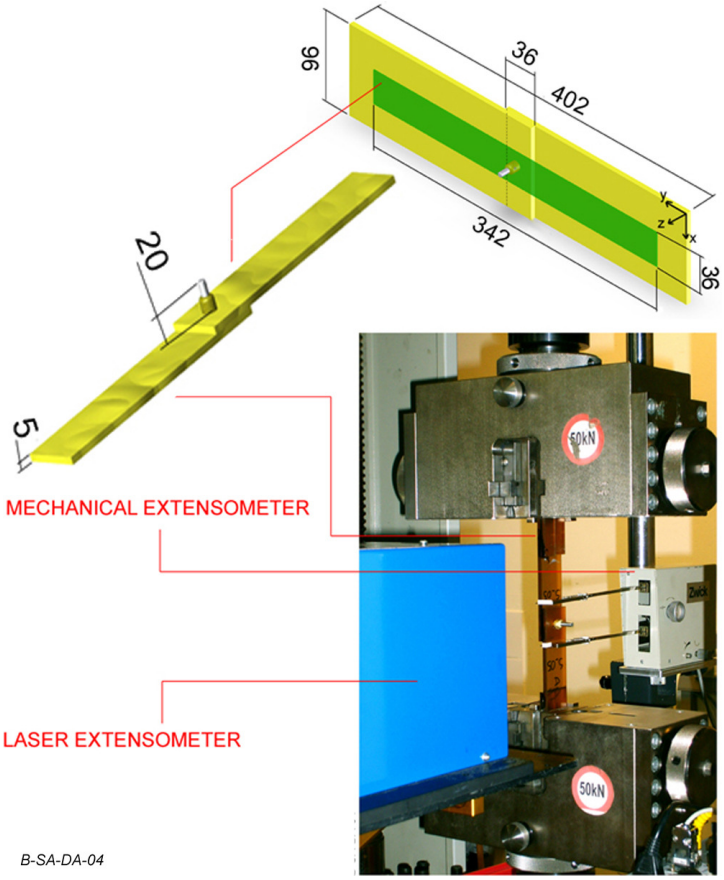

Figure 12. Lap shear testing of friction riveted joints. On the top right-hand side, the overlap joint coupons from where the lap shear specimens (on the top left-hand side) were extracted in accordance to ASTM-D-5961/D-5961M-05.

3.1.g. Lap shear stress relaxation testing

Lap shear relaxation tests were carried out by adopting the sample geometries, measuring systems, and testing machine used for lap shear testing [166]. Testing parameters and results evaluation were based on DIN 53 441 [167] for plastic stress relaxation testing. Tests were carried out with three different constant strain conditions, (ε_0 = 4%, 6% and 8.5%), by firstly loading the sample with a 2 mm/min traverse speed up to the desired ε_0-value and then measuring the time-dependent stress decay during an interval of about 24 h, at room temperature. Results were presented as time dependent stress, R(t) and stress relaxation modulus, E(t), calculated by Equation (10) [167]:

$$E(t) = \frac{\sigma(t)}{\varepsilon_0} \qquad (10)$$

where:

E(t) is the stress relaxation modulus

$\sigma(t)$ is the time-dependent stress relaxation

ε_o is the constant strain

3.1.h. X-ray- computer microtomography (μCT)

Microtomographic testing was performed at GKSS Forschungszentrum´s high-energy synchrotron beamline (HARWI-2) at Hamburger Synchrotronstrahlungslabor, HASYLAB, of the Deutsches Elektronen-Synchrotron, DESY.

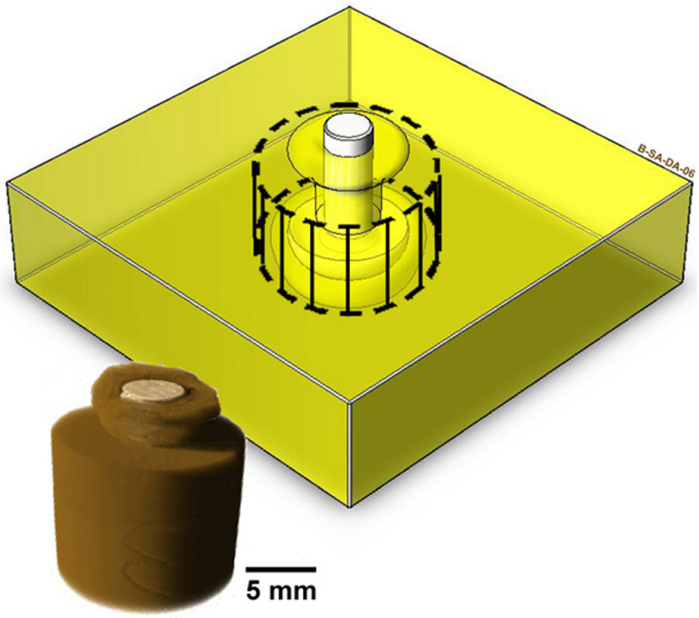

Figure 13. μCT-specimen used in this work.

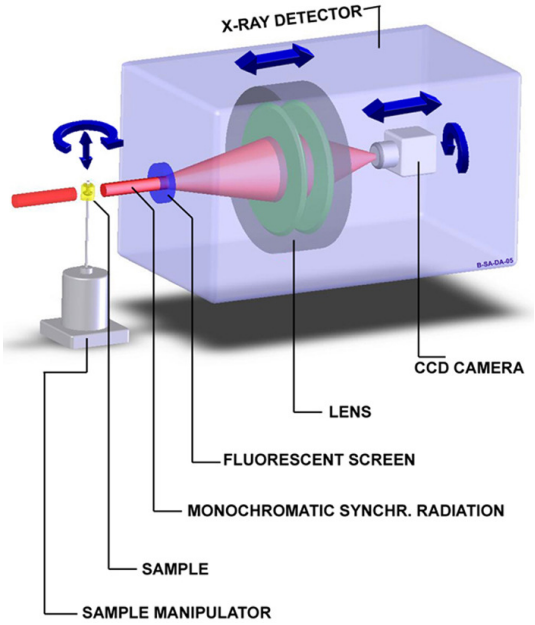

Figure 14. μCT-experimental setup used in this work (HARWI-2, HASYLAB-DESY, Hamburg)

Cylindrical μCT-samples were machined from the centre of the joint, as represented in Figure 13. Friction riveting samples were scanned by using 36 keV photon energy. A simplified description of the used μCT set-up is given in Figure 14. It is mainly divided into a sample manipulator and a two-dimensional X-ray detector. The specimen is placed on the sample manipulator, which provides both rotation and x/y translation movements, allowing a full body scanning. A CCD-camera captures the diffracted and collimated (by a lens set) beam from the specimen, which is previously transformed by the fluorescent screen from monochromatic X-ray in visible light. The complete description of this set-up is found elsewhere [168]. Slices reconstruction, volume rendering and measurements were performed with VGstudiomax software (Volume Graphics, Heidelberg, Germany).

3.1.i. Gel permeation chromatography (GPC)

GPC is a very powerful technique for determining the molecular weight of the polymer and molecular weight distribution, which in turn can be directly associated with mechanical properties and polymer processability. In this technique, polymer molecules or chains are separated by their single effective size (herein related to molecular weight) [169]. A dilute solution (called "dynamic phase") containing the material to be analysed as its solute is continuously injected into a separation column filled with little porous gel particles (named "stationary phase"). Separation of chains happens by preferential chain's penetration into the porous gel particles. Chains with small size ("low molecular weight") will readily penetrate pores while big chains (high molecular weight) will be eluted faster, so the detectors will measure at first chains with higher effective size and finally chains with lower effective size. In this way a normal distribution of molecular weight, as well as the mean molecular weight values can be obtained [170-172]. Figure 15 illustrates schematically a GPC-setup.

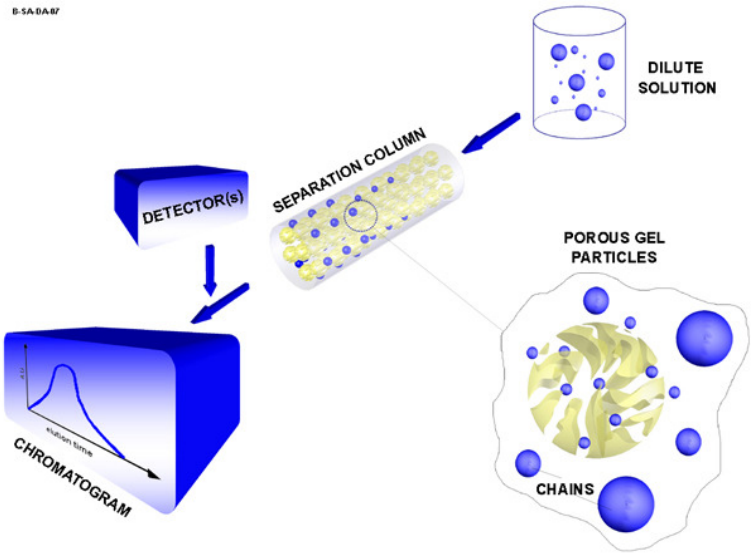

Figure 15. Schematic view of a GPC-system.

GPC-experiments were carried out in an equipment composed by a HPLC-pump 515, autosampler 717 plus a vertical heating furnace, a dual λ absorbance detector 2487 and dual refractive index detector 2414 (Waters); a polystyrene-divinylbenzene 5 µm column (mod. Styragel HR 5, 4, 3, Waters) and a PC-based evaluation software (Empower, Waters) completed the system. Samples of approximately 8 mg extracted from polymeric flash produced during joining were diluted in 4 mL of dimethylformamide, DMF (Nr. D/3846/PB17, Fisher) with 0,05 M LiBr (Nr. 13008, Riedel-de-Haën) under agitation at room temperature during

Table 5. Summarized experimental GPC-parameters used in this study.

GPC - Parameters	
Temperature (°C)	80
Eluent	DMF + 0,05 M LiBr
Flow rate (mL/min)	1
UV-Wavelength (nm)	280
Calibration Standard	PMMA

24hs, and finally filtered (0,45 μm polyamide filter). GPC-system calibration was performed with polymethylmetacrylate, PMMA, standards (Polymer Lab). Table 5 shows the summarized GPC-experimental conditions in this study.

3.1.j. Polymer base material analytical techniques

In order to determine structural and thermal features of the polymer base material, two techniques normally used in polymer science and analytical chemistry were selected: Fourier Transform Infrared Spectroscopy (FT-IR) and Differential Scanning Calorimetry (DSC). *FT-IR* is a technique, which relies on the capacity of some molecules in absorbing and vibrating in the same frequency of incident IR-radiation. It is not intended to present the complex theory of molecule vibration under infrared absorption; for a comprehensive approach in this area, refer to [173]. As for X-ray diffractometry of polycrystalline materials, an infrared spectrum of a substance can be considered as its fingerprint, whereby absorption peaks are correspondent to stretching and bending vibration frequencies from atomic bonds constituting the molecular structure [169, 171].

For polymers the most important IR-spectrum range is the middle infrared (wavelength range: $3x\ 10^4$ to $2{,}5x\ 10^3$ nm, or as typically used, wavenumber range: 4000 to 300 cm^{-1}) [174]. In a FT-IR equipment, infrared energy is emanated from a radiant black-body source; the IR-beam crosses an interferometer, which carries out a “spectral encoding”, so an interferogram signal is obtained. After that, the IR-beam interacts with the sample being either transmitted or reflected off the sample’s surface. At last the IR-beam passes through a detector, which sends the signal to a computer, where mathematical Fourier transformations are calculated and spectrograms generated. In this experiment spectra were recorded in a FT-IR ATR spectrophotometer (Bruker Equinox IFS 55) in the range of 4000-400 cm^{-1}, using sample pieces (≅ 2 mg/piece) cut off from the base material plates. Evaluated spectra peaks were within the wavenumber range of 3500–500 cm^{-1}.

DSC is a thermal analysis technique widely used for measuring the amount of absorbed or released heat when a material undergoes chemical or physical changes, such as glass transition temperature (T_g), melting, crystallization, cure, deterioration, oxidation, etc. [175]. From this technique the change of enthalpy (or internal energy) is obtained by measuring heat flux (heat per unit of time and mass), which in turn is directly proportional to specific heat capacity [176]. DSC-results are presented as thermograms (heat flux vs. temperature) where peaks and valleys and changes in curve inclinations represent different exothermic or endothermic reactions. For that, DSC-samples are placed in little metallic pans and evaluated against a reference sample in a test chamber consisting of two small furnaces, which are independently controlled, under defined heating routine. If a reaction leads to a change in the

furnaces' temperature difference, power is applied or taken in order to re-establish furnace "thermal-null" equilibrium state, during testing time. The change in heat influx is then calculated from the difference in thermal power between sample and reference [169,176].

In this study, temperature-scanning DSC-experiments were performed in order to determine the glass transition temperature of the polyetherimide, with 13 g base material samples prepared in the same way of the one described earlier for IR-samples, in a Netzsch DSC 204 equipment. A temperature range of 20-350 ^{o}C plus a heating rate of 20 K/min were chosen; samples were placed in Al pans and scanned in N_2 inert atmosphere (55 mL/min) within a 500 μV range. T_g values were calculated based on ISO 11357-1 [177].

3.1.k. Temperature measurement

The measurement of the temperature cycle developed during friction riveting joining was carried out by thermometry and infrared thermography techniques. The *thermometry* system consisted of chromium-nickel aluminium type K 0.5 mm-thermocouples (Thermocoax) connected to a data acquisition system (thermocouple multiplexer/amplifier SCXI 1102 from National Instruments) and controlled by software (Labview) on a PC-based system. This system is further described elsewhere [178].

In this work data was collected at 50 Hz. Thermocouples were positioned inside the PEI base plates in fixed positions close to the joining centre. This positioning was chosen so as to let the metallic rivet penetrating and passing as close to thermocouples as possible without damaging them (although avoiding thermocouples damaging was sometimes impossible). For that ϕ1mm wide guiding bores were drilled and ϕ0,8 mm capillaries were used as insertion media to thermocouples. This helped on the right thermocouples placement and a more precise data acquisition. Four individual measurement points (in some cases five points) were chosen in the PEI-plates: thermocouples H1 and H2 were placed respectively 2 and 4 mm deep, and 4 mm far from the joint centre, while H3 and H4, 9,5 mm and 11,5 mm deep and 7 mm away from the joint centre, respectively. When required a fifth thermocouple, H5, was placed right in the middle of the joining centre in a depth of approximately 6,5 mm. Furthermore, an extra thermocouple was set for recording room temperature data. The schematic view of thermometric setup and thermocouple positioning is found in Figure 16.

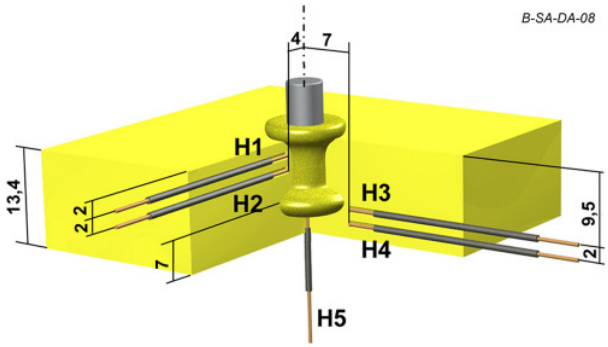

Figure 16. Positioning of thermocouples inside PEI-base plates. Dimensions are given in mm.

The infrared thermography system used in this work was basically constituted of an infrared thermo-camera (VarioTHERM, Jenoptik GmbH) connected to a computer with own data acquisition and processing software. This infrared camera is a mobile device capable of operating within the temperature range of –25 °C to +1200 °C in the spectral range of 3,4 to 5 µm. It is not only able to record films but also to capture 256 x 256 bits snapshots [179]. In this study a 25X-magnification objective was selected. Snapshots were taken at 50Hz in order to compare thermographic with thermometric results. The measuring temperature range of the camera was set within 200 °C to 500 °C. Aluminium rivets were painted with black paint and PEI plates were covered with a black painted cardboard-shield in order to minimise interference related to aluminium low emissivity, ε, and PEI semi-transparency. Temperature data was collected during joining from the expelled molten polymer flash. The measuring working distance was about 260 mm (distance from the measured area to the centre of objective) and an incidence angle of roughly 15°.

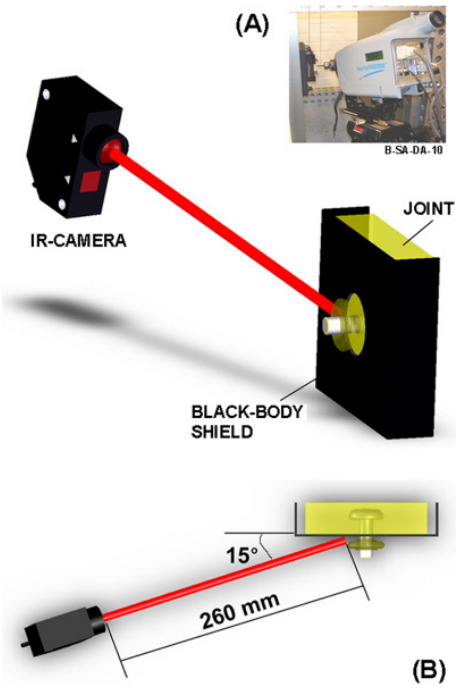

Figure 17. A) Thermography equipment. B) Schematic view of infrared temperature measurements of friction riveting samples.

Figure 17 presents the thermometry equipment and the measuring scheme. Temperature calibration was done prior to joining for determining the adequate emissivity and working distance as well as incidence angle. For that, type-K thermocouples were embedded in the samples (approximately in the mid-thickness of the PEI base plate and about 5 mm deep in the centre of axial direction for metallic rivets); samples were induction heated in a furnace up to 200 ^{o}C and temperatures were collected during cooling. Temperature results were compared and the infrared system calibrated.

3.2. Materials

3.2. a. Aluminium AA 2024-T351 drawn rods

This alloy was used for producing threaded rivets for point-on-plate friction riveting joints investigated in Section 4.2. The material supplied as ϕ10 mm rods had its chemical composition determined, as presented in Table 6. Tensile properties were obtained from manufacturer's certificate and no re-testing was carried out with rods, considering that tensile properties of machined rivets (the most interesting tensile results) were performed. Table 7 shows the tensile properties of this material.

Table 6. Measured chemical composition of AA 2024-T351 drawn rods.

Wt%	Cu	Mg	Si	Mn	Fe	Zn	Cr	Ti	Al
AA 2024-T351, drawn rod	4,2	1,6	0,15	0,8	0,25	0,033	0,011	0,01	bal.

T-SA-DA-06

Table 7. Tensile properties of AA 2024-T351 drawn rods.

Tensile Properties	Rm (MPa)	Rp0,2 (MPa)	εR (%)
AA 2024-T351, drawn rod *	425	310	8

* MANUFACTURER'S CERTIFICATE T-SA-DA-08

Figure 18 presents the main microstructural features and microhardness distribution of this material in the longitudinal direction. As it can be observed, grains are very flattened and oriented in the drawing direction; dark spots mainly seen inside grains (Figure 18B) are related to intermetallic and secondary particles. These particles were identified [180] as the intermetallic Al_2Cu-θ and AlMgCuC secondary particles (0,93% Mg; 0,73% Cu; 0,20% C).

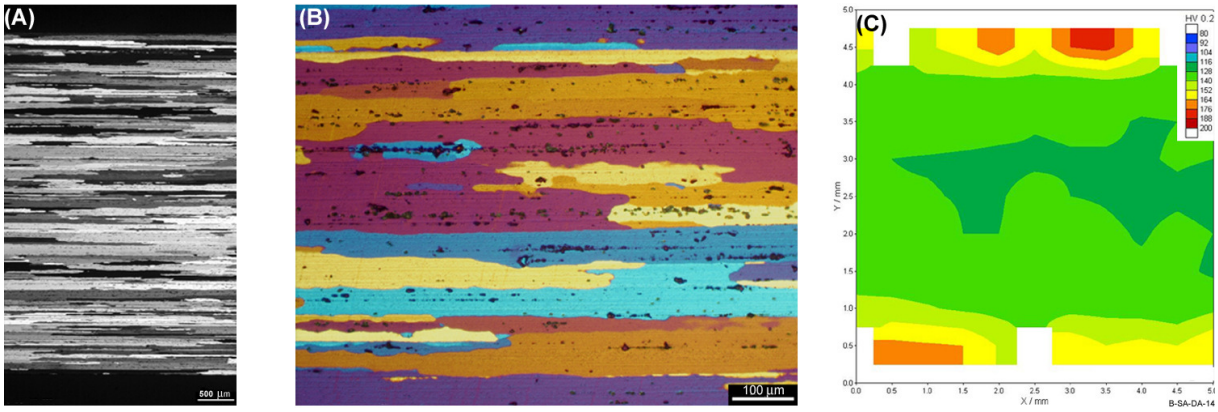

Figure 18. Microstructure and microhardness distribution of AA 2024-T351 drawn rods in the longitudinal section. A) Barker, 50X. B) Barker, 200X. C) Vickers microhardness map.

Hardness testing on the cross section of the rods (Figure 18C) has indicated that the outer regions of the rod (on the top and bottom of the picture), are slightly harder than the inner regions. This is probably related to the higher strain rates experienced by the surfaces in contact with the draw die. The calculated average microhardness is HV= 141,5.

3.2. b. Aluminium AA 2024-T351 extruded rods

Extruded rods of aluminium AA 2024-T351 (diameter: 10 mm) were used for fabricating rivets used in overlap joints (Section 4.3). Extruded rods were additionaly evaluated due to their industrial importance as an alternative fabrication process for rivets. The chemical composition is presented in Table 8. For the same reason as for drawn rod base material, tensile properties presented here were obtained from manufacturer's certificate (see Table 9).

Table 8. Measured chemical composition of AA 2024-T351 extruded rods.

Wt%	Cu	Mg	Si	Mn	Fe	Zn	Cr	Ti	Al
AA 2024-T351, extruded rod	3,9	1,2	0,19	0,55	0,23	0,22	0,001	0,02	bal.

T-SA-DA-07

Table 9. Tensile Properties of AA 2024-T351 extruded rods.

Tensile Properties	Rm (MPa)	Rp0,2 (MPa)	εR (%)
AA 2024-T351, extruded rod *	450	310	8

* MANUFACTURER'S CERTIFICATE

T-SA-DA-09

The microstructure of this alloy (Figure 19A and B) is formed by grains oriented to the extrusion direction; however they are not so flattened by processing as the grains from the drawn alloy and are also visually smaller. Intermetallic and secondary particles are believed to be the same as for the drawn material. The microhardness distribution (see Figure 19C) is also similar to the drawn material, displaying an average value of HV= 142,2.

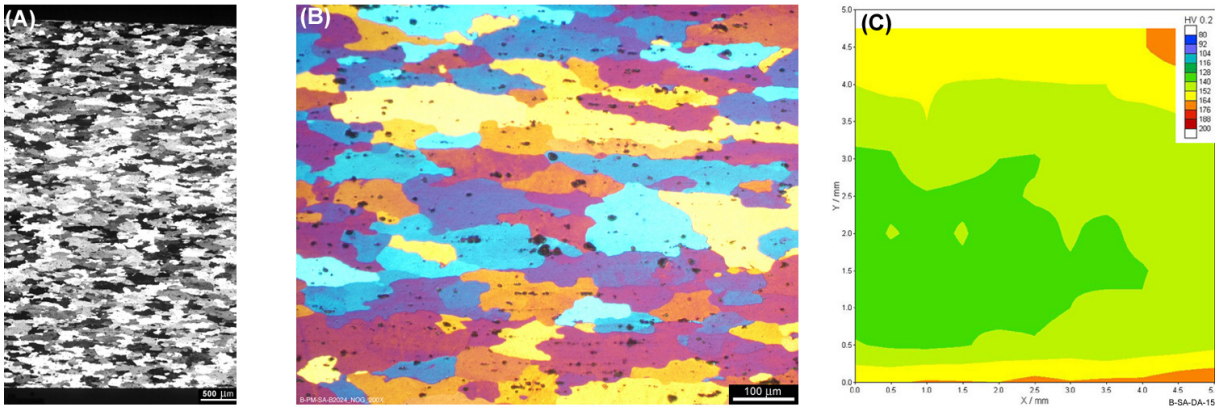

Figure 19. Microstructure and microhardness distribution of AA 2024-T351 extruded rods in the longitudinal section. A) Barker, 50X. B) Barker, 200X. C) Vickers microhardness map.

3.2. c. Polyetherimide (PEI)

Polymeric base plates for friction riveting were produced out of extruded 13,4 mm PEI-plates (GE Plastic's ULTEM 1000 polyetherimide). Due to PEI's intrinsic semi-transparency and low visual contrast, only a featureless and dull microstructure (characteristic of amorphous polymers) is obtained under LOM or SEM. When needed there are other microscopy techniques [181], which allow solving the microstructure of amorphous polymers; however they are very laborious and out of the scope of this work. In this work structure and properties of PEI were determined by ATR FT-IR, DSC, GPC, tensile and Vickers hardness testing. Figure 20A and Table 10 presents a tentative assignment of the main infrared peaks of this base material. The experimental IR-spectrum was in accordance with available data in literature [182-184]. The experimental DSC-thermogram shown in Figure 20B presents the glass transition temperature range for this polymer, which was found in accordance with literature [182,185] with an average value of $T_g \cong 221,0\ ^oC$.

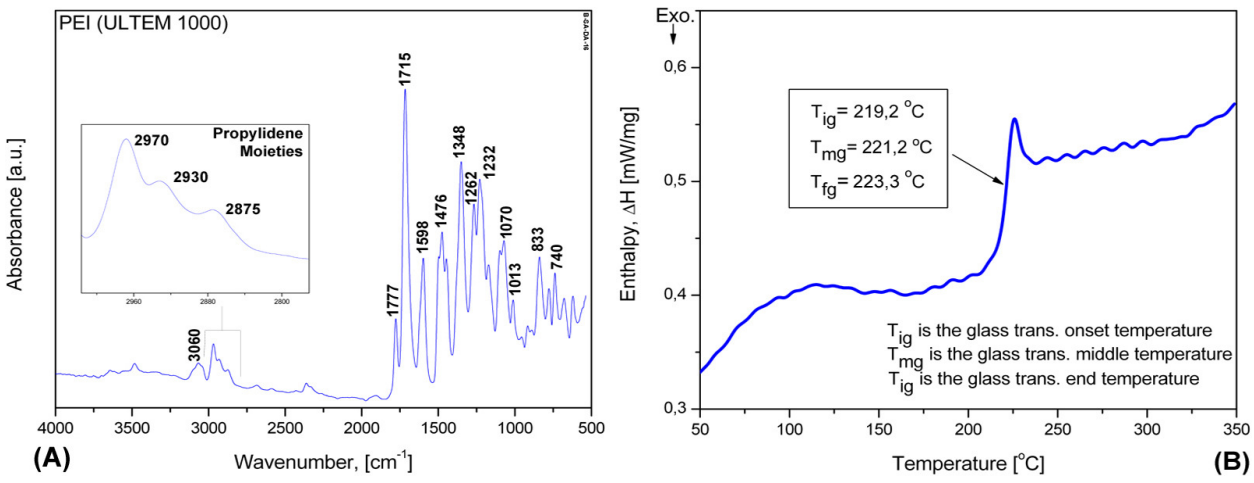

Figure 20. A) Experimental infrared spectrum of PEI (ULTEM 1000) base material with major peaks marked. B) experimental DSC-thermogram showing T_g-range.

Table 10. Major IR-absorbance peaks of the base material PEI ULTEM 1000.

Wavenumber [cm^{-1}]	Peak Intensity	Tentative Assignment
3060	weak	C-H, stretching (aromatic rings) [186, 187]
2970, 2930, 2875	weak	C-H stretching (propylidene moieties) [183, 186, 188]
1777, 1715	medium to strong	C=O, carbonyl stretching (in phthalimide rings) [182-184, 186, 188-194]
1598	medium	C=C or C-N stretching [187, 195]
1476	medium	Aromatic ring stretching[195, 192]
1348	strong	C-N stretching (in phthalimide rings) [183, 184, 188, 190-193, 195, 196]
1262, 1232, 1070, 1013	strong to medium	Ar-O-Ar stretching (aryl (Ar) ether bonds) [182, 183, 187, 190, 192-195]
833	medium	Aromatic ring deformation vibrations [195, 197]
740	medium	Phthalimide ring bending vibrations [186, 191, 193, 196, 197]

PEI-tensile properties and molecular weight averages obtained from GPC-measurements are presented in Table 11. Parallel and transverse to extrusion direction tensile strengths, R_m were similar, although slightly higher in the direction parallel to extrusion direction. The elongation at rupture, ε_r, in the case of specimens extracted perpendicularly to extrusion, was much smaller; this mechanical property anisotropy is due to preferential chain orientations caused by extrusion, where strength and strain are higher in the orientation directions. Calculated average Vickers microhardness (each indentation measured three times) was 284 ± 4,5 MPa.

Table 11. Tensile and colligative properties (molecular weight) of PEI base material

Tensile Properties			Molecular Weight, GPC **	
	// to Extrusion *	⊥ to Extrusion *		
Rm (MPa)	113,0 ± 1,4	111,6 ± 0,5		
εR (%)	16,8 ± 1,4	6,5 ± 1,0	Mn (Daltons)	26332 ± 2010
E (Gpa)	28,7 ± 3,0	29,0 ± 0,2	Mw (Daltons)	52234 ± 161

*** Mean Values of at least 3 specimens**
**** Mean Values of 4 specimens**

T-SA-DA-10

4. RESULTS AND DISCUSSION

Preamble

The presentation of results and main achievements of this work was intentionally divided into three main sub-sections in order to provide the document with a logical structure. Firstly, Section 4.1 covers the technique description, theories and models, for an initial familiarization with this new joining technique. Secondly, Section 4.2 presents the experimental part of the results, where the analysis of the influence of main process parameters on joint features helped further understanding of the process, theories and models proposed in Section 4.1. Finally, Section 4.3 covers the mechanical behaviour of friction riveted overlap joints, so the most important characteristics of the friction riveting and contributions to the state-of-the-art in joining technology for polymer-metal multi-material structures were delineated.

4.1. The friction riveting technique: proposed theories, mechanisms and models

4.1.a. Introduction

In order to create an alternative technique to current methods for joining polymer to metals, a new methodology is hereby proposed. The Friction Riveting technique is a new spot joining method based on mechanical fastening and frictional heating joining methods, invented and developed by the author [23, 24]. It was developed intending to reduce limitations related to traditional mechanical fastening and adhesive bonding methods, such as, high loss of strength associated with high stress concentration (e.g. riveting), reduced tensile strength performance (e.g. adhesive bonding) or elevated production costs (e.g. hybrid-joining methods). In this technique, the joining partners are divided into metallic rivets (profiled or flat) and base elements. Base elements can be made of polymeric materials or metallic alloys. They can be for instance plates, sheets, and rods, among others. Examples of profiled metallic rivets are seen in Figure 21, where threads (A) and interference elements (fitments) (B), which protrude from the shaft, are used so as to improve anchoring (rivet's pull-out strength).

There are various possible joint geometries in friction riveting. For instance in the simplest configuration (point-on-plate joints), either one or more base elements can be joined by a metallic rivet. Other possible hermetic sealed joint geometries are found in Figure 22. In this schematic picture a point-on-plate insert-joint is seen where a rivet with a threaded hole in its body serves as a connecting point for screws (Figure 22A); in Figure 22B an overlap joint between two plastic parts is shown, while in Figure 22C a sandwich-like joint between two thin

metallic base plates and a polymeric core is illustrated. In this last configuration a bore on the upper metallic plate is placed prior to joining for allowing the rivet to pass through and penetrate the polymeric core, finally generating a weld seam with the lower metallic plate.

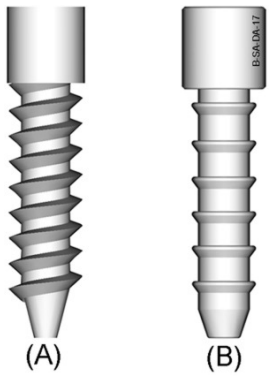

Figure 21. Examples of possible rivet geometries A)threaded. B) with interference-elements.

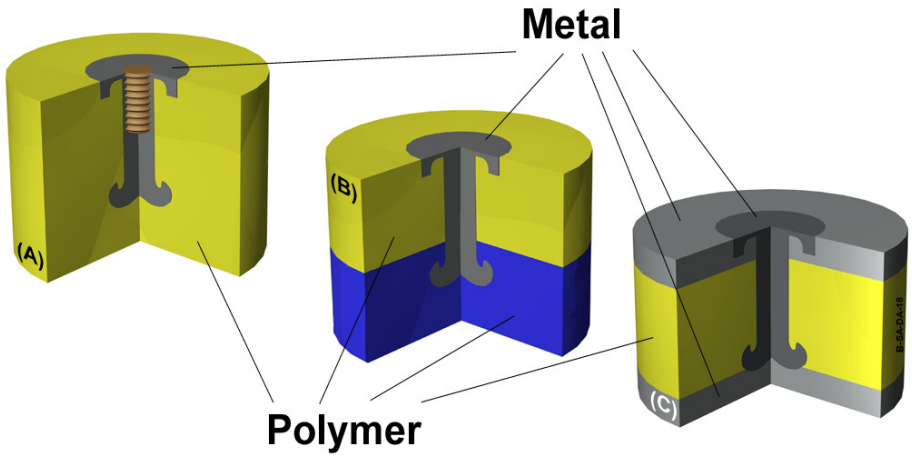

Figure 22. Possible configurations of hermetic sealed friction riveted joints. A) point-on-plate insert-joint. B) overlap joint. C) sandwich type joint

4.1.b. General process principles

In order to better explain the process, the simplest joint configuration, the “point-on-plate” joint, has been chosen, where a flat or profiled metallic cylindrical rivet (or a stud) is mechanically anchored into a polymeric base plate. Firstly, the joining partners are firmly clamped, the base plate onto a backing plate, while the rivet in the machine spindle, as represented in Figure 23A. Subsequently the rotating rivet is moved downwards touching down on the base plate (see Figure 23B). Rotation combined with pressure generates frictional heat locally increasing the temperature. This in turn leads to the formation of a very thin film of molten polymer underneath and around the tip of the rivet. With the continuous feeding of the rivet into the base plate, molten polymer material is expelled upwards outside the base plate as a flash.

At a certain insertion depth, heat input becomes larger than the heat outflow due to increasingly thermal insulation effect associated with the low thermal conductivity of the polymer. This elevates the local temperature to the plasticizing temperature range of the metallic rivet, whereby the tip of the stud becomes softened. At this point rotation is stopped and forging pressure is applied as shown in Figure 23C. Here the plasticized tip of the rivet is forged backwards to the feeding direction by the opposite forces associated with higher viscosity of colder regions. The forging phase leads to the formation of paraboloidal pattern on the rivet’s tip, resembling an inverted screw inserted in the polymer. During forging some of the remaining amount of molten polymeric film is pushed out to flash, whereas the rest stays and cools down

inside the joint. After cooling under constant pressure the joint consolidates and a strong rivet anchoring is achieved (see Figure 23D).

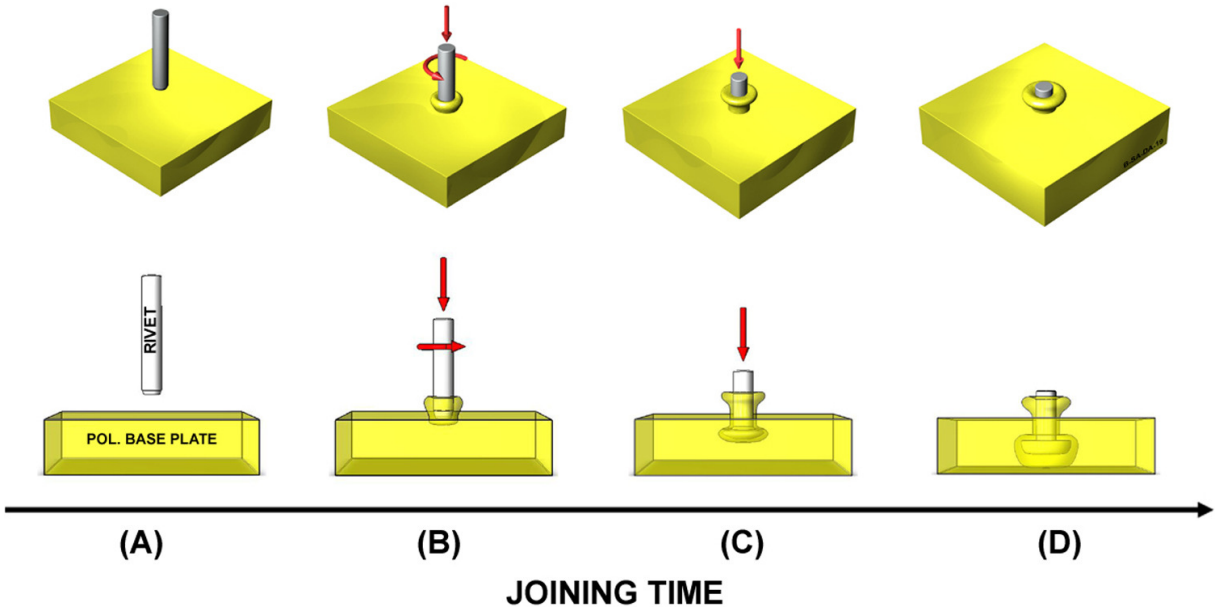

Figure 23. Friction riveting process scheme as illustrated for "point-on-plate" joints. A) Positioning and clamping of joining partners. B) Insertion of rotating rivet into the polymeric base plate. C) Rotation braking and subsequently rivet forging. D) Cooling and joint consolidation.

4.1.c. Physical description

Friction riveting is physically comparable to spin welding of plastics and friction welding of metals. In this fashion friction riveting can be analysed in terms of axial displacement and frictional torque over joining time, in a similar way to both processes. The process can be dived into five main phases as schematized in Figure 24A. In *Phase-I* solid friction, also known as *Coulomb Friction* or external friction [198], takes place; Coulomb friction is also found in the initial phases of other friction joining methods [139, 149], however in friction riveting the friction/abrasion mechanisms are similar to those observed in polymer-metal systems such as metallic parts of polymer processing machines [199], rather than the ones known for metal-metal interfaces. In polymer-metal friction the harder asperities of the metal penetrate the softer polymer, instead of being smeared off. Normally the dynamic friction coefficient decreases with rotation and time due to polymeric film transfer on the metal surface (normally for ductile polymers) or because of tiny split polymeric particles, which will act as lubricant [182] (normally for glassy polymers); so it actually turns to be a polymer-polymer solid friction type [198]. During this very short phase axial displacement is zero and torque increases slightly, being approximately constant for a couple of milliseconds and then decreasing with friction coefficient up to the end of this phase (see P-I, in the detail-view of experimental data in Figure 24B). Temperature increases herein mainly by plastic deformation in the polymeric part.

When frictional heating is high enough for temperature to achieve the softening point of the polymer (glass transition temperature for amorphous, T_g, and melting point, T_m for semi-crystalline polymers) the friction regime changes from solid to molten state, characterising the beginning of the *Unsteady State Viscous Dissipation or Phase-II*. From that point on frictional heating is mainly due to internal shearing in the molten polymer owing to chain disentanglement [70]; it induces scission of secondary weak bonds between chains releasing thermal energy. At this moment the rivet starts penetrating the base plate, whereby axial displacement and torque start increasing with time (see P-II, Figure 24A).

On the other hand during *Phase-III*, or *Steady State Viscous Dissipation* phase, there is a balance between polymer melting and molten material outflow rates (flash formation rate). Therefore, the axial displacement increases linearly with time. Torque stays constant up to the end of this phase where a slight drop (see $M_{z\text{-}III}$ in Figure 24A) is often observed as a result of a decrease in viscosity associated with increasing temperature, time and deformation. This time-temperature-deformation viscosity drop is known as *thixotropic behaviour* [146] or *shear thinning effect* [73] and is often found in polymeric molten systems. At this point the desired level of plasticizing in the rivet tip is achieved and the process is ready for the forging phase.

During the following step the *Rivet Forging Phase*, *Phase-IV*, rotation is stopped (motor braking) and forging pressure applied. The plasticized tip of the rivet is then deformed leading to the paraboloidal pattern. The thickness of molten polymer is strongly reduced underneath the rivet's tip and flash volume is increased by the amount of extra squeezed material. There is a sharp increase in axial displacement rate (see P-IV in Figure 24A, where forging pressure is set higher than friction pressure in order to increase forging) and torque, the latter achieving an equilibrium up to the end of the set forging time (see $M_{z\text{-}IV}$ in Figure 24A).

In the *Consolidation Phase* or *Phase-V*, the joint cools down under constant pressure. The frictional torque drops tending to null and the displacement reaches its maximum becoming constant (see P-V, Figure 24A). Molten polymer consolidates around the rivet creating a bonded polymer-metal interface. In this way, a joint is obtained by mechanical interference, enhanced by polymer-metal adhesion.

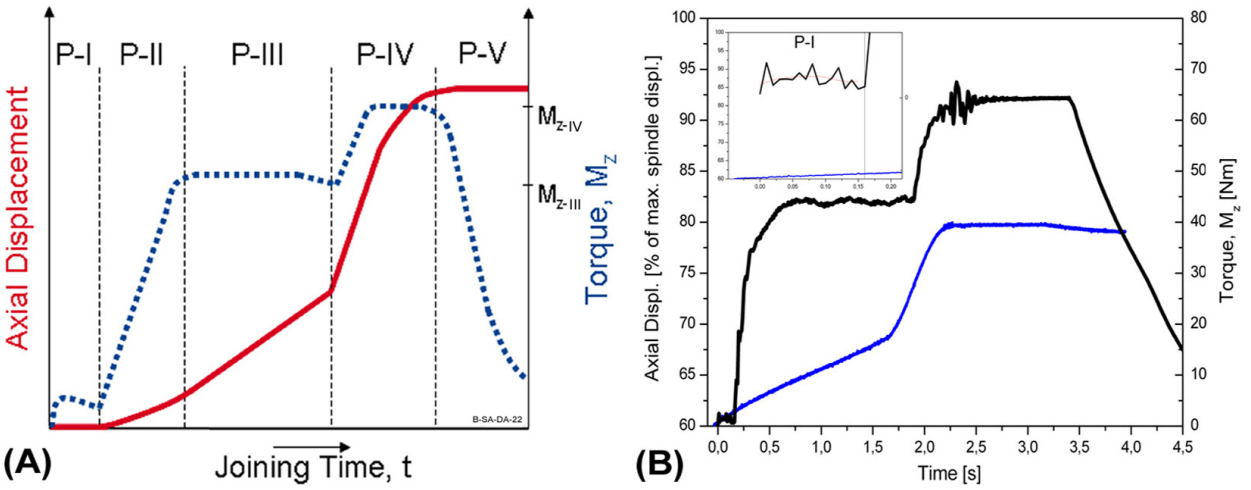

Figure 24. A) Schematic representation of Friction riveting process phases in terms of axial displacement and torque. B) An exemplary experimental control torque and axial displacement data for a friction riveting joint on PEI-aluminium. On the upper left-side corner a detailed view of torque in Phase-I, P-I.

4.1.d. Process parameters and variables

Process parameters and variables in friction riveting technique are analogous to the ones found in friction welding [200,201] and spin welding [149,202], due to their intrinsic process similarities. The main friction riveting process parameters are *rotation speed (RS), joining time (TT),* and *joining pressure (TP)*. Other important parameters are the rivet geometry and spindle distance to base element surface. *RS* is the angular velocity of the rotating rivet. It is important to the temperature development and associated phenomena (rheology of molten polymer, defect formation, etc.) taking place in the joint region assisting on the friction heating generation. Besides, *RS* influences indirectly the joining speed, by directly acting on the axial displacement. *TT* comprises the sum of the friction time (FT), plus forging time (FOT) (set time including Phases-I, -II and -III, and set time for Phase-IV and -V, respectively). Besides of being a joining speed control factor, *TT* also influences the level of volumetric defects related to thermal degradation, volatiles development and post-joining shrinkage, by controlling the temperature and exposure time in the molten polymeric film. The *joining pressure, TP is* the addition of the friction pressure (FP) (in Phases-I, -II and –III) and the forging pressure (FOP) (in Phases-IV and –V). These are the normal pressures applied on the rotating rivet and consequently related to the faying surfaces normal pressure distribution, P(r). Equally to *RS* and *TT*, *TP* contributes to heating of faying surfaces and joining speed, although its main role lies on controlling rivet forging and consolidation phases (Phases-IV and –V).

The major process variables observed in this process are the *heating time (HT), burn-off (BO), burn-off rate (BOR), temperature* of the faying surfaces and *frictional torque (M_z)*. *Heating time (HT)* is the interval related to the initial contact between rivet and the base element (touch down), and the moment when RS equals null. It is obtained from the joining diagram (see Figure

8, Section 3.1.a). *HT* is a representative of the heat input regime and provides an estimate of the degree of the thermal cycle, plasticizing level, thermal deterioration as well as aging. The *burn-off (BO)* is associated with the insertion level of the rivet and its consumed length. *BO* is also computed from the axial displacement in the joining diagram (see Figure 8, Section 3.1.a), by subtracting the maximum value of the axial displacement from the initial value. The analysis of this variable provides a good estimate of how deep and how deformed was the rivet tip inside the base plate and indirectly the level of rivet's plasticizing achieved during joining. Joining speed, on the other hand, is calculated from the quotient between *BO* and *HT*, the *burn-off rate (BOR)*. Although this variable is only an approximation of real conditions (actually there is an increase of axial displacement rate when applying *FOP*, which is normally higher than *FP*), the use of *HT* in calculating *BOR* gives a good approximation of the actual joining speed.

Temperature and M_z, are variables measured by external controlling systems (see Sections 3.1.k and 3.1.a). Temperature can be related to rheological properties of molten polymer, amount of thermal deterioration, material plasticizing level (viscosity) and other defect formation. This is also a variable associated with heat input. However, the temperature is more sensitive to parameter variation than HT, owing to the very low thermal conductivity of polymers. This can sometimes induce a deviation of the temperature behaviour in comparison to heat input behaviour with the variation of process parameters (i.e. temperature may display a greater increase in comparison to heat input increase). Compared to other joining processes [203] M_z represents not only the rheological behaviour of molten polymer and plasticizing of rivet-material, but also supplies a way of identifying process anomalies and defects regarding equipment mal-function, dirty surface of joining partners prior to joining, among others. Other important variables indirectly associated with the process are mechanical and physical properties of base materials. Young's Modulus, thermal conductivity, coefficient of linear expansion and surface finishing (rugosity, cleanness, etc.) often dictate joint formation. Further analysis on the influence of main process parameters on process variables is given in Section 4.2. Table 12 and Table 13 provide a summary of the main process parameters and variables.

Table 12. Summary of the main process parameters involved in friction riveting.

Parameter	Abrev.	Function
Rotation Speed	*RS*	Contributes to the frictional heating. Influences the joining speed.
Joining Time	*TT*	Contributes to controlling of joining speed and frictional heating. Influences the level of thermal degradation, volatiles development and post-joining shrinkage in the polymeric partner.
Joining Pressure	*TP*	Controls the distribution of pressure on the joining area. Contributes to frictional heating and joining speed. Controls the forging phase.

Table 13. Summary of the main process variables involved in friction riveting.

Variable	Abrev.	Significance
Heating Time	*HT*	Is a representative of the heat input; provides estimates of thermal cycle, plasticizing level, thermal degradation and aging.
Burn-off	*BO*	Indicates the level of rivet penetration and deformation (consumption).
Burn-off Rate	*BOR*	Provides an approximation to the actual joining speed.
Temperature	*T*	Influences the rheological properties of the polymer (plasticizing, degradation, viscosity). Associated with heat input.
Frictional Torque	M_z	Associated with material plasticizing. Identification of process mal-functioning and anomalies.

4.1.e. Microstructural zones

Due to the intrinsic structural complexity involving polymer-metal multi-materials joints, one would also expect complex microstructures in friction riveting joints. There are five microstructural zones in a typical friction riveting joint: the *polymer heat affected zone (PHAZ),* the *polymer thermo-mechanically affected zone (PTMAZ)*, the *metal heat affected zone (MHAZ)*, the *metal thermo-mechanical affected zone* (*MTMAZ)* and *anchoring zone, (AZ)*. These are schematically shown in Figure 25.

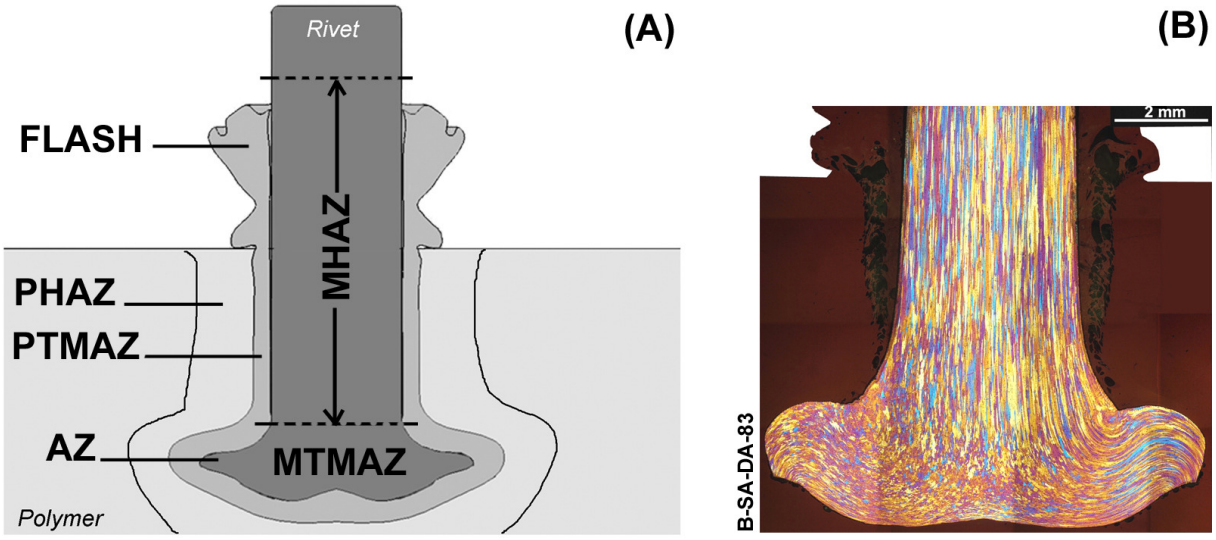

Figure 25. Proposed microstructural zones of a typical friction riveting joint. A) schematic representation of a cross-section. B) A LOM-micrograph of a polyetherimide-aluminium friction riveted joint. In this LOM-micrograph the PHAZ and the PTMAZ can not be well defined visually, due to the amorphous character of the polyetherimide.

The *PHAZ* consists of the polymeric volume around the rivet, whose temperature during joining did not reach the polymer softening point (T_g or T_m). Although this zone may not be visually identified, the polymer structure is affected by heat and consequently local mechanical properties. Examples of these changes are: induced crystallization/growth of crystallites in the case of semi-crystalline polymers, and physical ageing (or increase in strength and decrease in creep/stress relaxation rate) for amorphous polymers [204,205]. The *PTMAZ* is formed by the thin molten layer around the rivet; it is an interlayer between the *PHAZ* and the metallic rivet and is usually visually identified under *LOM*. In this zone temperature is well above T_g or T_m, frequently achieving or overcoming thermal degradation temperature (T_{td}) it is also a region where severe plastic deformation takes place.

At the interface between *PHAZ* and *PTMAZ* one finds the formation of weld lines originated by the encounter of the polymer molten front with the colder front leading to a bonded line. Weld lines might result in decreased mechanical performance particularly under dynamic loading [206]. They will always exist in the joint area, however their mechanical performance can be improved by selecting appropriate process parameters, in other words by creating right thermal conditions. For additional information of weld line formation theories, refer to [207-210]. The interface between *PTMAZ* and the metallic rivet is also characterized by a bonded line. In this case bonding happens by one or more adhesion mechanisms typically observed on adhesive bonding of polymer to metal: mechanical interlocking, chemical bonding, electrostatic bonding, and weak boundary layer [47,46]. The analysis of metal-polymer adhesion mechanisms is not the aim of this work. For further information on the theory of bonding mechanisms in polymer-metal joints refer to [51,52, 56, 211-215].

Still in the *PTMAZ* one observes the formation of voids and flaws associated with high temperatures and deformation (see results presented in Section 4.2.c). Voids can be originated from the expansion of volatiles, such as absorbed water, from entrapped air due to high molten viscosity of some polymers, from cooling shrinkage related to differences in linear coefficient of thermal expansion, *CTE*, between metal and polymer, and from thermal degradation. These flaws are detrimental to mechanical strength and should be reduced by optimizing the process [70]. An extensive study on thermal degradation of friction riveting joint is presented in Section 4.2.d. Finally, local mechanical properties in the *PTMAZ* can be slightly altered by some preferential chain orientation due to deformation.

In the *MHAZ*, metal is heat treated by frictional heat. In this region, different annealing phenomena can take place, e.g. recovering, recrystallization and overaging, as well as some hardening mechanisms such as ageing and re-precipitation, depending on alloy type, heating time and maximum temperature. Visually, the microstructure may not change, although the structure is rather modified. This is observed in changing joint microhardness values in comparison to the base material (see Section 4.2.d). *MTMAZ* microstructure and local

mechanical properties are influenced by heating and severe deformation. In this area material can undergo dynamic recovery and/or recrystallization, or even re-precipitation depending on whether critical temperatures and deformation are attained for a given period [216]. Large scale melting is usually not observed, although it might occur at the faying surfaces. The metallic element is only plasticized considering that measured temperatures are under T_m (see Section 4.2.b). Microstructure is normally characterized, respectively, by some grain refinement, and grains with sub-grain patterns characteristic of dynamic recrystallization and recovery.

The *AZ* is the zone, where the deformed tip of the rivet is located. Due to plastic deformation it generally assumes a paraboloidal format, whose external diameter is bigger than the original rivet diameter. This region mainly bears the applied mechanical requirement through mechanical interference (anchoring) with the polymeric base element. For alloys having higher melting points, frictional heating may not be enough to induce plasticizing for tip forming. In this case, one should choose rivets with fitments or protrusion elements in their shafts (see Figure 22, Section 4.1.a) in order to increase anchorage. Microstructurally, the *AZ* has mainly rotated grains, but some refined grains and/or polygonized sub-grain structures may also be found. *PTMAZ* is embedded in this zone.

4.1.f. Microhardness distribution

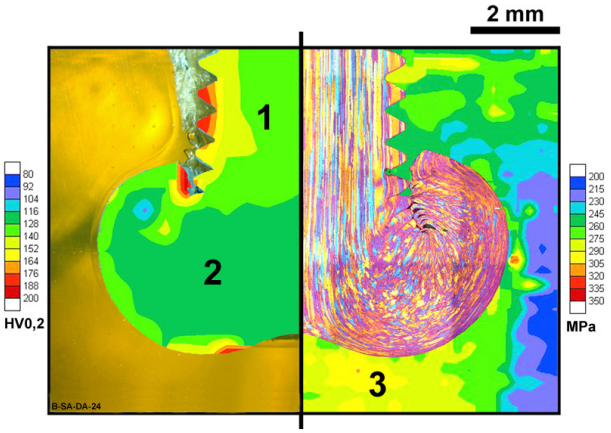

Figure 26. Schematic overlaying of micrographs and microhardness maps of a friction riveting point-on-plate joint (PEI/2024-T351). On the left-hand side, the non-etched LO-micrograph of the polymeric base plate and the microhardness map of the metallic rivet; on the right-hand side, an etched LO-micrograph of the metallic rivet plus the microhardness map of the polymeric base plate. Only the interior volume of the joint is shown.

The microhardness distribution in a friction riveted joint is dictated by structural changes associated with the thermal and mechanical processing as discussed in the previous section. For illustration, Figure 26 presents a schematic overlaying of experimental results on microhardness mapping of a friction riveting point-on-plate joint.

Generally speaking, one finds an overall decrease in microhardness in comparison to the base material in the metallic rivet portions inserted in the polymer, and an overall increase in the polymer volume around the rivet. The decrease in microhardness at *MHAZ*, is usually smaller than at *MTMAZ* ($HV_{MHAZ} \cong 95\%$ and $HV_{MTMAZ} \cong 85\%$ of base material AA2024-T351 average hardness value, as shown in see Figure 18, Section

3.2.a), as presented on the left-hand side microhardness map of Figure 26, locations 1 and 2. While in the MHAZ no visual changes in microstructure are seen, in the *MTMAZ* there is some grain refinement, or dynamically recrystallized grains. This supports the lower measured microhardness, where annealing was more extensive in rivet regions near to the faying surfaces.

When looking at the microhardness map of the polymer on the right-hand side of Figure 26, position 3, one observes that regions around the rivet suffered an increase in microhardness in comparison to the PEI base material ($HV_{PHAZ} \cong 110\%$ of base material PEI average hardness value of 284 ± 4,5 MPa given in Section 3.2.c). Although the Vickers microhardness test was not totally successful in determining *PTMAZ / PHAZ* interface values, it was sufficient to reveal overall changes in the *PHAZ*. Those changes are probably associated with physical ageing and/or hardening due to loss of water. *Physical ageing or structural relaxation* is a typical reversible phenomenon of glasses. Glasses are amorphous, so polymers are either fully or partially amorphous materials under their glass transition temperatures are thermodynamically instable [204]. It means that their enthalpy and entropy are larger than they would be in equilibrium. Molten plastics have a high entropic entangled chains structure. When they solidify, there is not enough time for the structure to organize so they can be considered as supercooled liquids, which seek the equilibrium state to decrease structural entropy (to improve structural ordering) towards a more compact structure. Chain mobility under T_g is very small, so physical ageing is slow. Increments in temperature under T_g accelerate structural relaxation, increasing compactness, or decreasing structural free volume [70]. A representation of physical ageing [217] is illustrated in Figure 27, where under a certain constant ageing temperature, T_a (i.e. $T_a < T_g$), free volume, V_f, and T_g, decrease with time, t.

As already mentioned, physical ageing elevates polymer strength, which can be detected by hardness measurements. For almost all plastics, hardness increases with increasing ageing temperature (T_a) and t [158]. Considering that measured temperatures at PHAZ of the PEI-2024-T351 joints were under T_g (see Figure 34, Section 4.2.b) and other physical reactions, such as crystallization, are excluded (PEI is amorphous), the most probable explanation for increased microhardness is that, PHAZ underwent physical ageing. On the other hand, *loss of water* can also cause a raise in

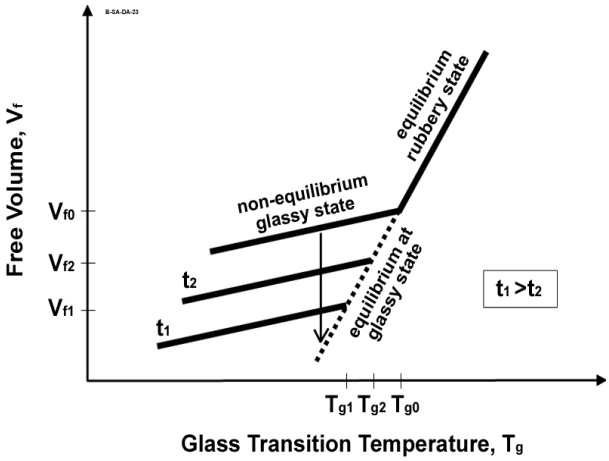

Figure 27. Physical ageing of amorphous polymers as regarded to free volume and T_g under constant ageing temperature, T_a. (Adapted from D´Amore et al [217]).

hardness, because structural water acts as plasticizer [158]; consequently, progressive disorption of water by increasing temperatures can contribute to materials hardening.

4.1.g. Analytical heat input model

The heat input generated during the friction riveting technique can be described through a simplified analytical model based on available thermal models for friction welding of metals and spin welding of polymers. The current model predicts heat per unit of area related to process parameters and variables as well as to geometrical singularities of the joint and base materials physical properties. M_z, *TP, RS, BOR*, and molten polymer viscosity, η are examples of key input parameters in the proposed heat input model.

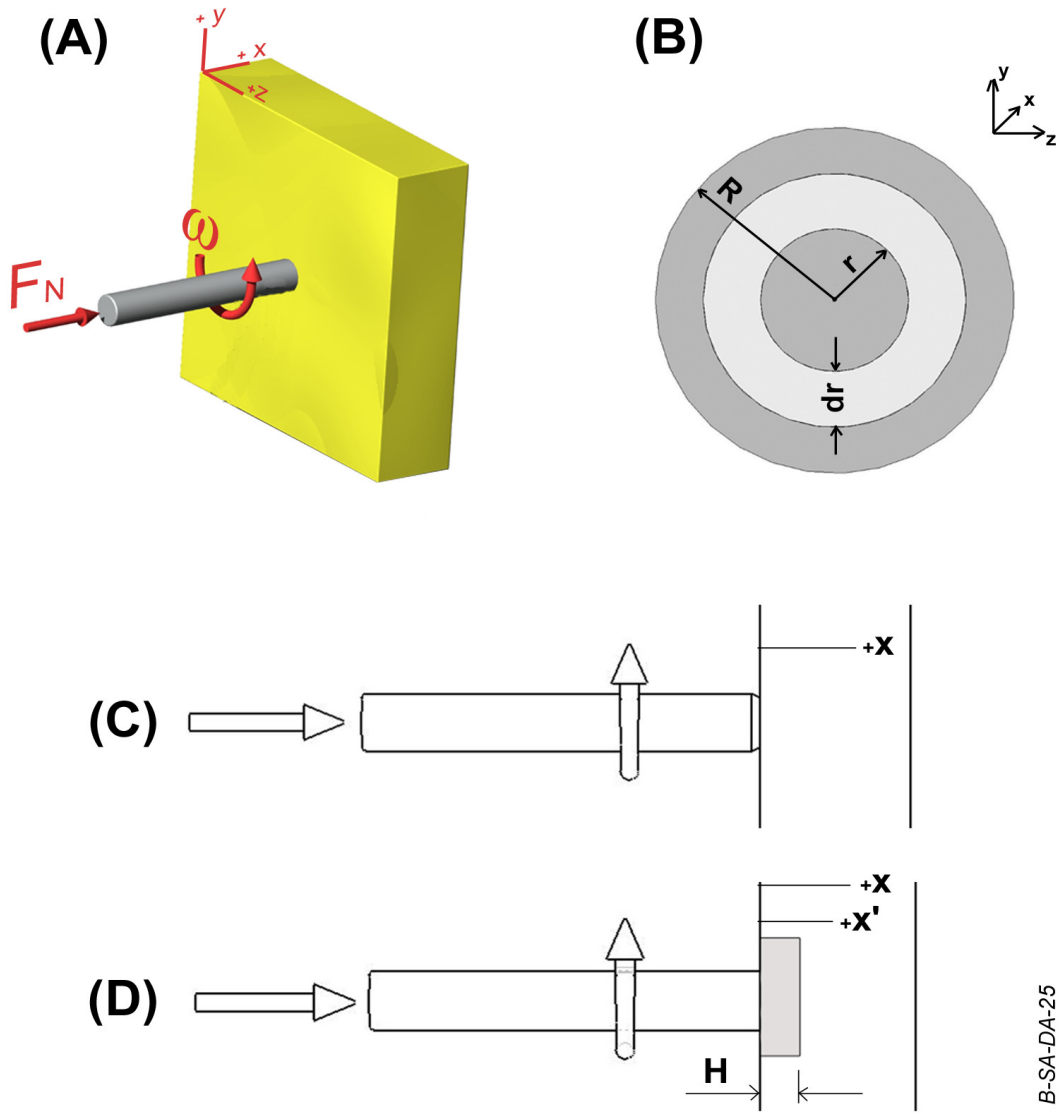

Figure 28. Schematic representation of a friction riveting joint for the proposed analytical model. A) Point-on-plate joint. B) The rubbing area, A*, with the annular element of* r *radius and* dr *radial width. C) Lateral view showing Phase-I (Solid Friction) condition. D) Lateral view presenting the case of Viscous Dissipation Phases-II and –III.* H *represents the height of the molten zone (painted in grey), herein simplified as a cylinder for the mathematical calculations.*

The thermal friction riveting problem can be represented by the scheme shown in Figure 28A, where a cylindrical rod with a radius, R, an angular speed, ω and normal force, F_N, rubs a macroscopically planar surface on the polymeric base plate, creating a rubbing area, $A = \pi \times R^2$, much smaller than the length of the rod. Friction and normal force will create mechanical work (W_{mech}), which is mostly converted in heat energy (Q), while a small amount is lost. If the heat generated by friction is taken as uniform over the whole rubbing area, and assuming a semi-infinite solution (i.e. $0 \leq x \leq -\infty$, as represented in Figure 28A), where the rod is initially at room temperature, one can say that [140,141]:

$$W_{mech} = Q_{total} = Q_{fr} + Q_{ax} \qquad (11)$$

where:

W_{mech} is the mechanical work.

Q_{total} is the total heat input per unit of area on the rubbing area.

Q_{fr} is the heat input per unit of area due to friction.

Q_{ax} is the heat input per unit of area due to normal force, F_N.

Considering that Q_{fr} and Q_{ax} are given by Equations (12) and (13) respectively,

$$Q_{fr} = Q_{fr}^{sol} + Q_{fr}^{visc} \qquad (12)$$

and

$$Q_{ax} = Q_{ax}^{sol} + Q_{ax}^{visc} \qquad (13)$$

where:

Q_{fr}^{sol}, Q_{ax}^{sol} are the heat input per unit of area due to friction and F_N, in the Solid Friction Phase-I.

Q_{fr}^{visc}, Q_{ax}^{visc} are the heat input per unit of area due to friction and normal force, F_N, in the viscous dissipation Phases-II and-III.

The estimation of Q_{fr}^{sol} can be carried out in the same way as calculated for friction welding of metals [138,143, 145] and spin welding of polymers [147]. In these approaches, Q_{fr}^{sol} is calculated from the integration of friction power (P_{fr}) for the whole rubbing area (A). P_{fr} is obtained from the known formulation *P = torque x angular velocity*. For solving this formulation, frictional torque (M_z) has to be determined. Considering now the annular element with radius *r* and radial width *dr* shown in Figure 28B, the instant frictional torque (dM_z) is obtained as follow:

$$dM_Z = dF_T \cdot r \tag{14}$$

$$F_T = \tau \cdot A \tag{15}$$

$$\mu = \tau \cdot P(r) \tag{16}$$

where:

F_T is the tangential force in *r* , at the rubbing area, *A.*

τ is the shear stress.

μ is the kinematic friction coefficient.

$P(r)$ is the normal pressure distribution on *A*.

When re-arranging Equation (16), the so called Amonton's law [218], and substituting it in Equation (15), Equation (14) becomes,

$$dM_Z = 2\pi \cdot \mu \cdot P(r) \cdot r^2 \tag{17}$$

Q_{fr}^{sol} is calculated with Equation (18),

$$Q_{fr}^{sol} = \frac{1}{A} \cdot \int_0^R d\,P_{fr} = \frac{1}{A} \cdot \int_0^R \omega \cdot dM_Z$$

$$\Leftrightarrow Q_{fr}^{sol} = \frac{2}{3}\pi \cdot \omega \cdot \mu \cdot P(r) \cdot R^3 \tag{18}$$

If applying $\omega = V_{\max} / R$ in equation (18), with $V_{\max}$ being the maximal tangential speed at *R,* it will result

$$Q_{fr}^{sol} = \frac{2}{3} \cdot V_{\max} \cdot \mu \cdot P(r) \quad \left[W / m^2 \right] \qquad (19)$$

The approach proposed by Potente and Reike [147] was chosen for calculating the heat input of spin welding during the steady state viscous dissipation phase. This choice is reasonable considering the rheological similarities of both processes. For the Q_{fr}^{visc} calculation, where heating takes place by internal viscous dissipation (internal shearing) in the molten polymer, shear deformation must be considered. This approach provides heat input per unit of volume, under simple shear conditions defined by Equation (15). In order to obtain heat input per unit area this equation has to be modified and its new format becomes

$$Q_{fr}^{visc} = (\eta \cdot \gamma^2) \cdot \frac{Vol}{A} \qquad (20)$$

where:

η is the viscosity in the molten state and

γ is the shear rate.

Vol is the volume of molten element in the rubbing area, A

The assumed simple shear condition [146] establishes that the shear rate is the quotient between tangential velocity in the *x* direction (v_x), and the distance in direction *x'*, in Figure 28D, so Equation (20) turns into

$$Q_{fr}^{visc} = \left[\eta \cdot \left(\frac{dv_x}{dx'} \right)^2 \right] \cdot \frac{Vol}{A} \qquad (21)$$

Since $v_x = V_{\max} \cdot \frac{x'}{H}$, and considering a linear velocity profile in the molten zone *H* (in Figure 28D, represented as a rectangular volume for simplification), then its substitution in Equation (20) after rearranging it in terms of angular velocity (ω) gives

$$Q_{fr}^{visc} = \left[\eta \cdot \left(\frac{\omega \cdot R}{H} \right)^2 \right] \cdot \frac{Vol}{A}$$

$$\because \quad Vol = \pi \cdot R^2 \cdot H \quad and \quad A = \pi \cdot R^2$$

$$\Rightarrow \quad Q_{fr}^{visc} = \eta \cdot \frac{V_{\max}^2}{H} \qquad \left[W/m^2 \right] \qquad (22)$$

The next step for completing the model is the determination of Q_{ax}. Firstly, Q_{ax}^{sol} is given by the definition of power (*P = Torque x angular velocity*) redefined in terms of force and linear velocity (*P = force x velocity)*, and calculated for the annular element in Figure 28B

$$Q_{ax}^{sol} = \frac{1}{A} \cdot \int_0^R dF_N \cdot \int_0^{V_{ax}^{\max}} dV_{ax}$$

$$\because \quad dF_N = P(r) \cdot 2\pi \cdot r \cdot dr$$

$$\Rightarrow \quad Q_{ax}^{sol} = P(r) \cdot V_{ax}^{\max} \qquad \left[W/m^2 \right] \qquad (23)$$

where:

$V_{ax}^{\max}$ is the maximum axial velocity.

Secondly, for determining the F_N contribution to heating, one should considerer the dependence of molten polymer viscosity (η) on normal pressure, *P*, which is given by [146]

$$\eta = \eta_0 \cdot e^{(\beta \cdot P)} \qquad (24)$$

where:

η_0 is the zero shear viscosity (a variable tending to constancy when low strain rate values, γ, are applied).

β is the coefficient of pressure dependence of η, with estimated value in order of 2 x 10^{-8} m^2/N, for thermoplastics [146].

In the same manner, by taking the power equation, Q_{ax}^{visc} can be obtained

$$Q_{ax}^{visc} = \frac{1}{A} \cdot \int_0^R dF_N \cdot \int_0^{V_{ax}^{\max}} dV_{ax}$$

$$\because \quad dF_N = \ln\left(\frac{\eta}{\eta_0}\right) \cdot \frac{1}{\beta} \cdot 2\pi \cdot r \cdot dr$$

$$\Rightarrow \quad Q_{ax}^{visc} = \ln\left(\frac{\eta}{\eta_0}\right) \cdot \frac{1}{\beta} \cdot V_{ax}^{\max} \qquad \left[W/m^2\right] \qquad (25)$$

With the values of Q_{fr}^{sol}, Q_{fr}^{visc}, Q_{ax}^{sol} and Q_{ax}^{visc}, the total heat input per unit of area can be calculated, if η is previously defined. Due to the high dependence of viscosity η on shear deformation, several approaches in trying to predict this behaviour are available in the literature [73,146]. The modified Cross-formulation used by Stokes and Poslinski [150] to determine molten viscosity in spin welding is a comprehensive model and was chosen in this study because it is able to predict well the behaviour of engineering plastics in their molten state:

$$\eta = \eta_0 \cdot \left[1 + \left(\frac{\eta_0 \cdot \gamma}{\tau^*}\right)^{\alpha}\right]^{\frac{n-1}{\alpha}} \qquad \left[N \cdot s/m^2\right] \qquad (26)$$

where:

τ^* is a material constant related to the Newtonian shear thinning behaviour transition.

α is the curves' breadth index.

n is the power law coefficient of polymer rheological behaviour.

η_0 can be calculated from the Willians-Landel-Ferry, WLF, equation [73]

$$\eta_0 = C_1 \cdot \exp\left[\frac{-C_2 \cdot (T - T_g)}{51{,}6 + (T - T_g)}\right] \quad \left[N \cdot s/m^2\right] \qquad (27)$$

where:

C_1, C_2 are experimental material constants

T is the temperature in the molten state.

By substituting and rearranging Equations (19) and (22) in Equation (12), and Equations (23) plus (25) in Equation (13), and subsequently taking the rearranged Equations (12) and (13) and applying it in Equation (11), the proposed analytical heat input model for friction riveting is given by

$$Q_{total} = \left[\left(\frac{2}{3} \cdot \mu \cdot P(r)\right) + \left(\frac{\eta \cdot V_{\max}}{H}\right)\right] \cdot V_{\max} + \left\{\left[P(r) + \left(\ln\left(\frac{\eta}{\eta_0}\right) \cdot \frac{1}{\beta}\right)\right]\right\} \cdot V_{ax}^{\max} \qquad \left[W/m^2\right] \qquad (28)$$

where, η and η_0 are computed from Equations (27) and (28). The model is demonstrated experimentally and further analysed in Section 4.2.g.

4.2. Influence of process parameters on joint formation, microstructure and mechanical properties

4.2.a. Case study PEI/AA2024-T351 point-on-plate joints: experimental design.

Friction riveted point-on-plate joints on AA2024-T351 and PEI, where produced in order to evaluate the influence of joining parameters on joints properties. The working parameter envelope defined by *RS x TT x TP* was within the range of 6000 rpm to 23000 rpm (*RS)*, 0,3s to

6s (*TT)* and 6 bar to 20 bar (*TP)*. The envelope, where joints formed (although in some cases with a high density of voids in the polymeric portion) was large with limits varying between 10000 rpm to 21000 rpm, 0,6 s to 5 s and 8 bar to 19,5 bar. Out of these limits, it could be observed that, either the joints did not hold at all, or the presence of flaws was so high that joint tightness was very poor. Appendix 2 shows a schematic view of the process parameters envelope for this case study joints. The 2D-views (TT vs. RS, TP vs. RS and TT vs. TP) with the LOM-macrographs of formed joints are also found in Appendix 2A, B and C. The green marked area of each graph limits the approximate area where the combination of parameters resulted in formed joints. Examples of defective joints (outside of the working envelope) owing to inadequate choice of process parameters are presented in Figure 29.

Four different levels of RS, TT and TP were selected and varied, while other process parameters were kept constant, to investigate the individual influence of these parameters on joint formation and properties. RS-samples were varied in the range 15000 to 21000 rpm; TT-samples in the range 0,6 to 4,0 s; and the TP-samples from 8,0 to 13 bar. Table 14 presents the detailed joining parameters for the investigated samples. Figure 30 presents the top-view from examples of produced samples. For each condition at least 9 samples were produced; for tensile testing (5 samples), microstructural and microhardness testing (1 sample), for temperature analysis (2 samples) and for 3D-µCT testing (1 sample).

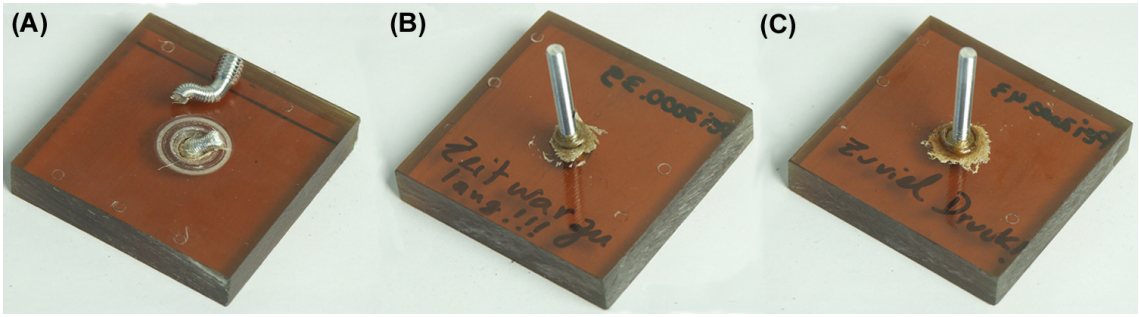

Figure 29. Defect point-on-plates joints on PEI-AA2024-T351. A) Too high RS. B) Too high TT. C) Too high TP.

Table 14. Summary of selected process parameters for the comparison samples.

Sample	RS (rpm)	FT (ms)	FOT (ms)	FP (bar)	FOP (bar)
15000 rpm	15000	1500	1500	4	7
17000 rpm	17000	1500	1500	4	7
19000 rpm	19000	1500	1500	4	7
21000 rpm	21000	1500	1500	4	7
0,6 s	21000	300	300	4	7
1,2 s	21000	600	600	4	7
3,0 s	21000	1500	1500	4	7
4,0 s	21000	2000	2000	4	7
8,0 bar	21000	1500	1500	2,5	5,5
9,0 bar	21000	1500	1500	3	6
11,0 bar	21000	1500	1500	4	7
13,0 bar	21000	1500	1500	5	8

T-SA-DA-11

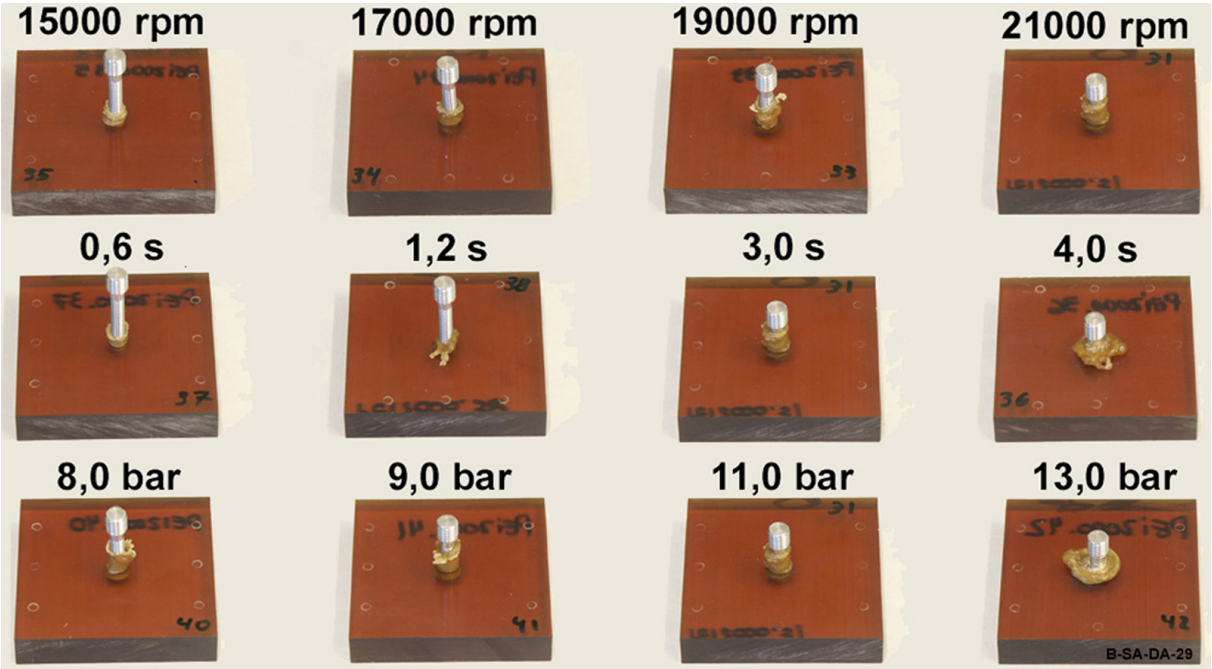

Figure 30. Surface photographs of samples in this investigation study on PEI/AA2024-T351 point-on-plate friction riveted joints.

4.2.b. Temperature development

In the temperature comparison, at least 2 samples were analysed by thermometry and IR-thermography. The thermometric results for the RS, TT and TP comparisons were collected by thermocouples H1, H2, H3 and H4, embedded in the polymeric base plate, whose positioning

was presented in Figure 16, Section 3.1.k. Results from thermocouple H5 were dismissed in this analysis because in most of the samples it has been damaged by contact with the rotating rivet, stopping instantly data collection. Figure 31 presents the results of thermometric assessment for RS, TT and TP series. As it is known, the principle of thermocouple measurement is based on direct contact of bodies, or in other words, on thermal conduction. Considering that, thermocouples were embedded into the polymeric base plate with lower thermal conductivity than aluminium (about only 0,2% of the aluminium conductivity, see Table 2, Section 1.2.a and Table 4, Section 1.2.b), measured results were highly dependent on the thermocouple distance to the heat source. The highest peak temperature values were observed for H2 thermocouples in Figure 31B (maximum T_{H2} values at about 370 ^{o}C for RS , TT and TP samples), where a general trend in increasing temperature with increasingly RS, TT and TP was observed. The highest temperatures recorded by H2-thermocouples were due to their positioning, which is the nearest to the rivet, at the PTMAZ close to the top of the AZ.

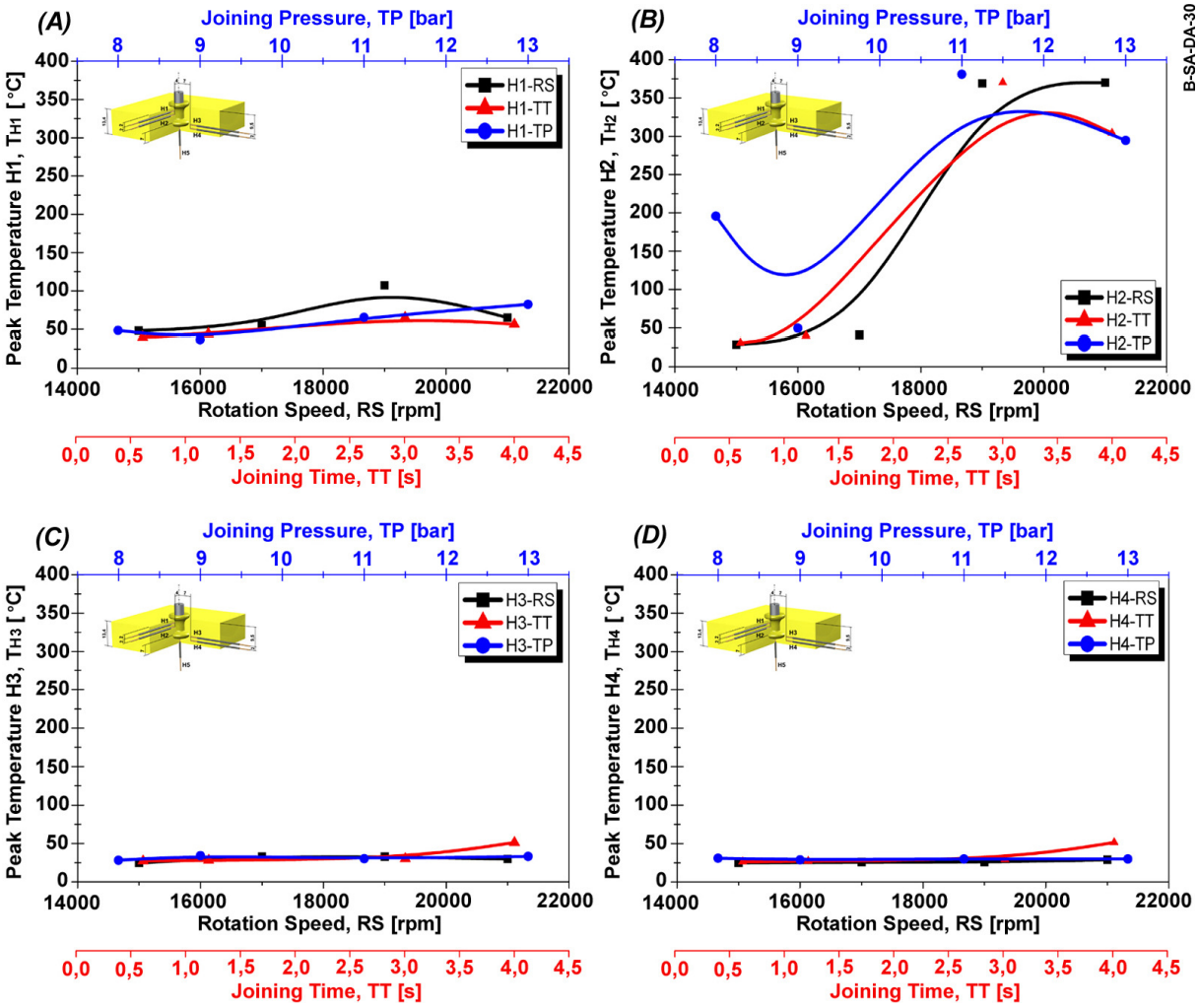

Figure 31. Thermometric results for PEI/AA2024-T351 point-on-plate comparison joints. A) Peak temperatures of H1-thermocouples (depth= 2 mm; distance to joint centre= 4 mm). B) Peak temperatures of H2-thermocouples (depth= 4 mm; distance to joint centre= 4 mm). C) Peak temperatures of H3-thermocouples (depth= 9,5 mm; distance to joint centre= 7 mm). D) Peak temperatures of H4-thermocouples (depth= 11,5 mm; distance to joint centre= 7 mm).

A weak trend of increasingly temperature with increasing parameter values was also seen for H1-thermocouples placed at the PHAZ. The maximum measured H1-temperatures (T_{H1}) were approximately only 17,5% of T_{H2} ($T_{H1} \cong 65$ °C for all samples, as shown in Figure 31A). This considerable difference in values is explained by the position of H1-thermocouples. Although they were located near to H2-thermocouples (about 2 mm) and only 4 mm to the rivet shaft, temperatures in the PHAZ are much lower than temperatures in PTMAZ, where molten polymer is directly in contact with the heat source. The same temperature dependence on the distance to the metallic rivet and low thermal conductivity of PEI was confirmed in the case of thermocouples H3 and H4 (see Figure 31C and D). With the exception of the slightly higher results for TT-sample 4 sec, there was almost no variation of maximum temperatures with increasing parameter values ($T_{H3} \cong 32$ °C and $T_{H4} \cong 30$ °C).

Prior to thermographic measurements, the IR-camera and software were calibrated. Appendix 3 presents the calibration procedure and examples of snap-shots with maximum temperature measured by thermocouples and by the infrared camera. For the PEI plates there was a variation of about 1,5 °C, and for the aluminium rivet a difference of about 13 °C. The higher difference in values for the aluminium rivet can be explained by its low surface emissivity.

The temperature of the flash is a good indicator of how high is the temperature of the softened polymer layer in the rubbing area. Due to the low thermal conductivity of the polymer, it is assumed that the polymer softened through friction and internal shearing action and pressed off as flash will not have enough time to cool down before it leaves the polymer base plate. In other words, the average temperature measured in the softened flash is nearly the same as in the molten layer inside the polymer plate. Joints had their temperature measured by Infrared thermography, following the procedures reported in Section 3.1.k.

IR-thermographic comparison results are presented as peak average temperature, T_{L01} calculated from a line, L01 (90 x 90 pixels) traced in a fixed position on the polymeric flash, parallel to rivet's axis. The curves of T_{L01} versus time for RS, TT and TP are presented in Figure 32A, Figure 32B and Figure 32C. Figure 32D compares the charts of maximum T_{L01}-values for RS, TT and TP samples. Figure 33A illustrates the average heating rate values, HR_{L01} for comparison samples, calculated from linear curves fitted within the time range between initial and maximum T_{L01} values in the curves of Figure 32A, Figure 32B and Figure 32C. An example for this linear fitting of a T_{L01} versus time curve for heating rate calculation is given in Figure 33B. HR_{L01} is an important parameter for the study of void formation in the PTMAZ during joining.

T_{L01}-results on Figure 32D indicated the same trend as for the thermometric measurements (see Figure 31A and B), where increasing RS, TT and TP led to a roughly logarithmic increase in temperature. These results were within the order of estimated experimental 10%-error; for the studied parameter range, infrared maximum TL_{01} was within 300 °C to 500 °C in the flash

molten material and less than 200 °C on the extern surface of the rivet, since it appeared in black colour on the IR-snapshots.

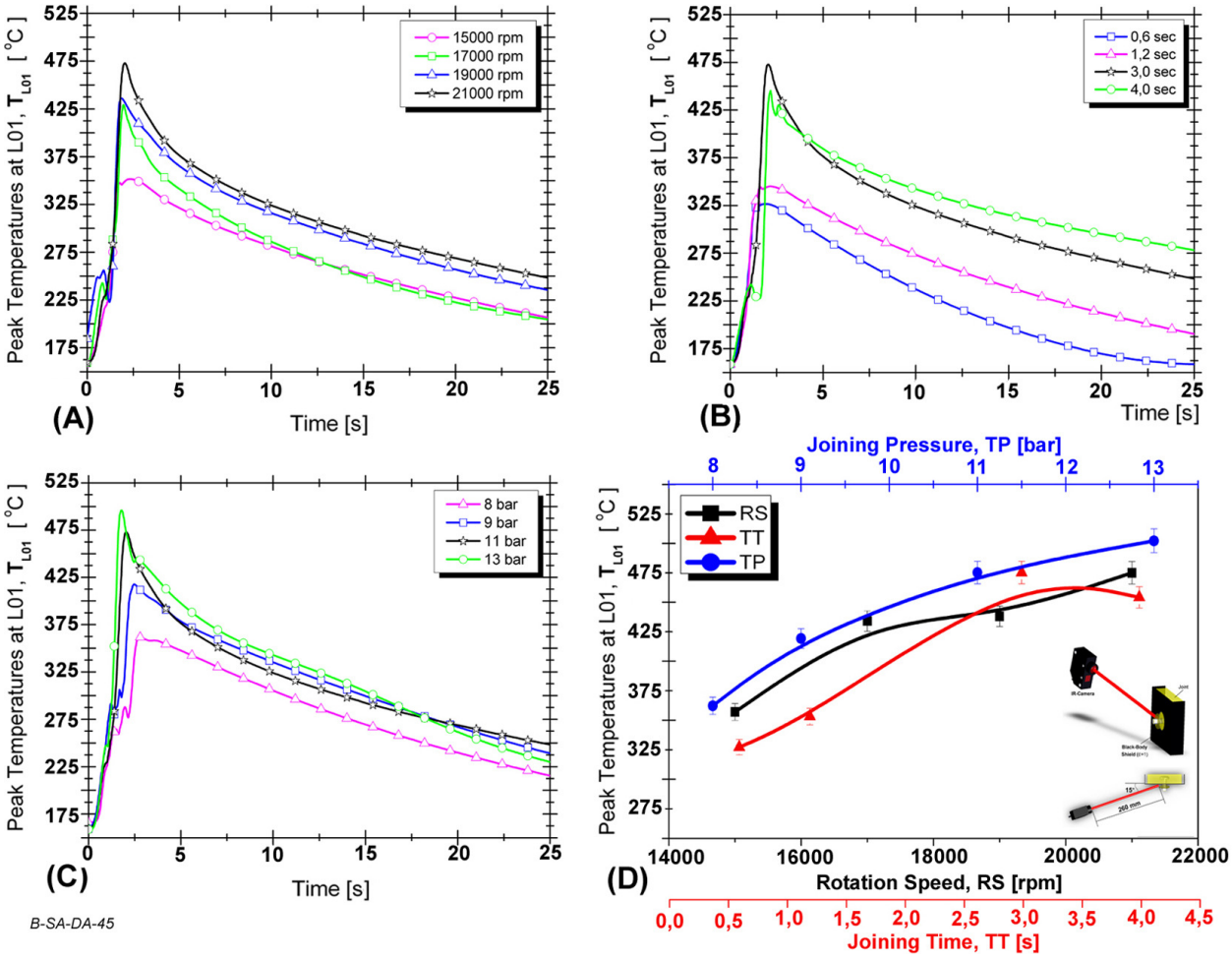

Figure 32. Charts of IR-temperature, T_{L01} versus time for RS (A), TT (B) and TP (C) comparison samples. In (D) the maximum values of T_{L01} extracted from charts in A, B and C.

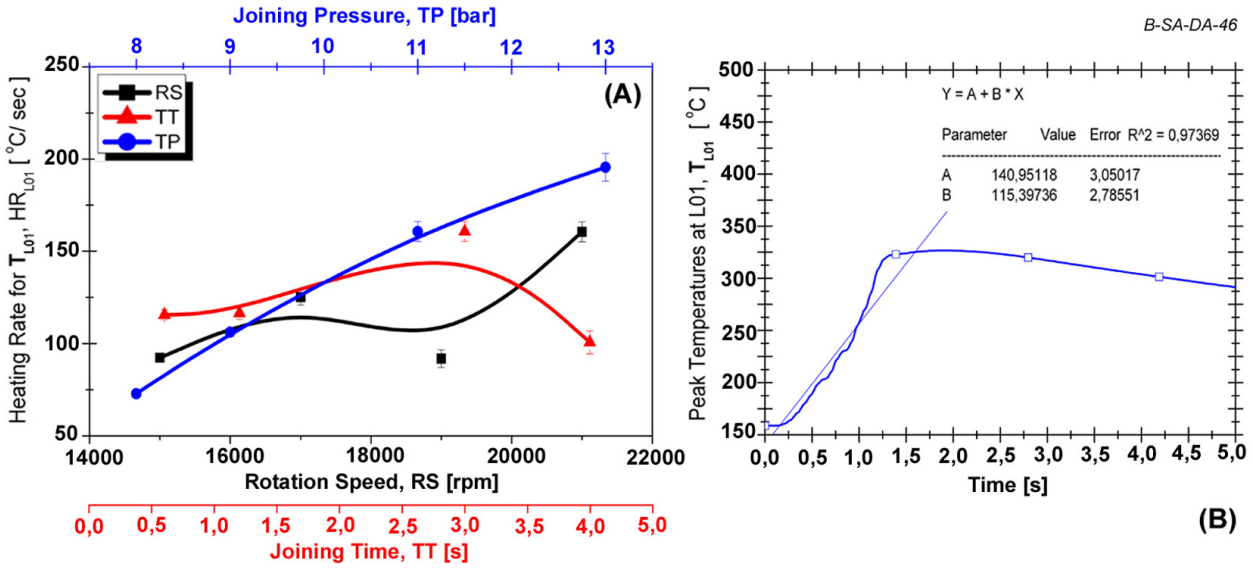

Figure 33. A) Average heating rates, HR_{L01}, for comparison samples. B) Exemplary calculation of HR_{L01} with linear fitted curve from beginning to maximum T_{L01}. The inclination of the line curve, B, is the estimated HR_{L01} value.

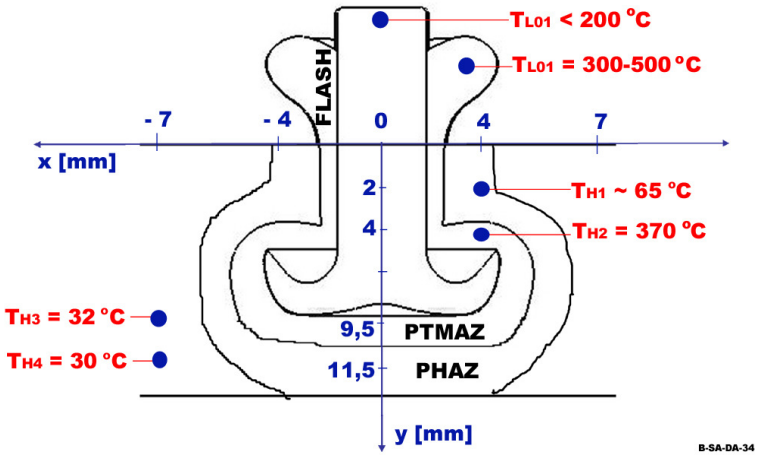

Figure 34. Schematic representation of experimental maximum temperature profile for friction riveted point-on-plate joints in this comparison study.

For TP-samples there was an almost linear increase of HR_{L01} with the parameter, while for RS-samples this increment was not so marked. In the case of TT-samples this increase with parameter took place up to 3 seconds and then HR_{L01} drops, as observed in Figure 33A.

This decrease in HRL_{01} in addition to the decrease in T_{L01} identified for the TT-sample 4,0 sec (see Figure 32D) is an indication of a change in frictional conditions. This phenomenon will be discussed later in this section for the frictional torque evaluation. With thermometric and thermographic results a schematic picture of the temperature profile for PEI/AA2024-T351 friction riveted point-on-plate joints could be conceived and presented in Figure 34. This evaluation has shown that the distance to the heat source is a dictating factor on controlling temperature due to the low conductivity of the polymer. High peak temperatures (around 500 ^{o}C) were observed during joining. A general trend of increasing temperatures and HRL_{01} with RS, TT and TP has been observed as well.

4.2.c. Microstructure

The influence of RS, TT and TP on microstructure formation and features was evaluated through X-ray µCT and LOM techniques. The X-ray µCT experiments were carried out as described in Section 3.1.h, where samples were scanned, and rendered in order to allow 3D volume measurements. Cylindrical samples (diameter ≈ 15 mm) had their full volume rendered and divided into 3 main volume units, by using the VGstudiomax graphics software (see schematic representation in Figure 13, Section 3.1.h): the volume of the PEI polymeric base plate (V_{PEI}) containing the PHAZ and PTMAZ, the volumetric defects (V_d) in the PTMAZ, and the volume of the metallic rivet inside the base plate (V_{Riv}) including part of MHAZ, the whole MTMAZ and AZ. Figure 35 presents an example of a µCT-sample, with a mid-cross section in the rivet's axial direction.

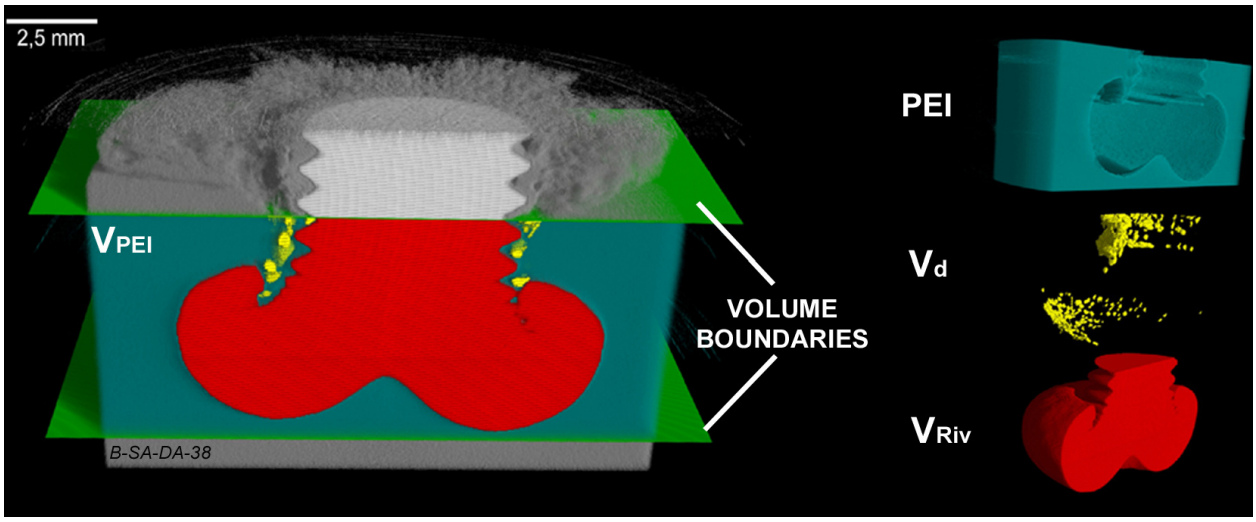

Figure 35. Example of an X-ray μCT friction riveting sample with its volume segmented and coloured for facilitating visualization.

The green horizontal plates define the volume of interest. This volume is then subdivided in V_{PEI}, V_d and V_{Riv} by image segmentation, based on grey tone differentiation. With the purpose of facilitating visualization, volume segments were coloured. In this volume analysis 1 pixel^3 = 9,96 x 10^{-7} μm^3. Figure 36 shows the μCT volume rendering of the friction riveted PEI/AA2024-T351 samples in this study. V_{PEI} was partially sectioned for revealing the microstructural characteristics of the joint. From Figure 36 one observes a visual increase in deformation on the tip of the rivet (the AZ), and a general rise in volumetric flaw density with increasing TT, and TP, while flaws look like to be unaltered for increasing RS. A visual trend in increasing rivet penetration with RS and TT was also identified. However, for TP this could not be visually observed. For clarifying these visual trends, V_d and V_{Riv} were separated from the whole volume and quantified. V_d-samples are found in Figure 37; V_{Riv} samples in Figure 38; V_d and V_{Riv} calculated volumes are found in Appendix 4.

When analysing Figure 37, it is possible to see that flaws primarily tend to be concentrated around the non-deformed rivet portion, for smaller values of RS, TT and TP (15000 rpm, 0,6 sec, and 8,0 bar plus 9,0 bar), while for higher values (21000 rpm, 4,0 sec and 13, 0 bar) they are found distributed in the polymeric volume around the whole rivet body. For the former case, volumetric defects can be related to a high amount of trapped air created by the unsteady rivet forging, probably due to the insufficient temperature leading to inhomogeneous rivet plasticizing. This in turn induces instability and bending during rivet feeding, which help create pockets of trapped air. On the other hand, volumetric defects for the later case were most likely thanks to volatile formation plus some thermal degradation, considering the high temperatures measured in the molten polymer from the PTMAZ (see Figure 34, Section 4.2.b).

It has been reported that PEI has a significant affinity for atmosphere moisture [219]. While for the majority of the polymers it would negatively affect short-term mechanical properties,

moisture does not considerably affect PEI strength [118]. Nevertheless, under high temperatures ($T > T_g$), high heating rates, HR_{L01} and increasing joining time, desorption of moisture and other volatiles in the polymer structure will lead to nucleation and growth of voids [220]. These flaws can drastically reduce short- and long term mechanical performance of the polymer and should be avoided. Unfortunately, in the case of a process where high temperature regimes are present, such as hot-tool welding, resistance welding, induction welding and friction riveting, voids will be inherently present [105, 220] , so one can only reduce their density but not fully eliminate them.

V_{Riv}-results from Figure 38 also seem to support the initial assumption of increasing deformation on the tip of the rivet with increasing RS, TT and TP. For smaller joining parameter values rivet tips were less deformed, while for larger values they were wider and more deformed. This growth in AZ-deformation with RS, TT and TP is an indication of higher amounts of metal plasticizing, which in turn is directly associated with higher temperature. Nevertheless, it can be observed that, for the highest values of TT and TP, the AZ presented cracks. This phenomenon is also connected with unsteady rivet forging (forging phase, P-IV, in Section 4.1.c) linked to high temperatures. This causes the shear thinning effect to grow causing a sharp drop in viscosity in the molten polymer layer around the rivet. Lower viscosity molten material is easily pushed off to the flash during the forging phase. As the forging phase goes on, the plasticized tip of the rivet suddenly runs into colder and harder polymeric regions, which makes the metallic material flow unsteady, leading to cracking of the AZ.

The determination of V_d and V_{Riv} has been performed through the calculation of ratios among V_d and V_{PEI}, (V_d/V_{PEI}) and V_{Riv} and V_{PEI} (V_{Riv}/V_{PEI}). This sort of volume normalizing allows direct comparison between different segmented volumes. Figure 39A illustrates the V_d-quantitative analysis in the PTMAZ and Figure 39B the V_{Riv}-quantitative analysis in the polymeric base plate. TT and TP resulted in induced growth of volumetric flaws (V_d/V_{PEI}) in the PTMAZ; for TT-samples, one observes that this increase happened only at higher levels of the parameter, while for RS-samples, flaw formation was not substantially altered. It may suggest that two situations can originate such behaviour: Firstly, RS at most and TT somewhat less may not strongly influence volatile void-formation and thermal degradation.

Additionally, the RS-range chosen for this study may not be the severest one in terms of heat input for this combination of materials, so less thermal degradation took place. Moreover, by examining Figure 32D and Figure 33A in Section 4.2.b, it is possible to observe that TP-samples had the highest temperature values, T_{L01}, plus the highest heating rates, HR_{L01}, among all samples, so the presence of defects related to higher thermal deterioration and volatile formation regimes should also be larger, as it was confirmed in Figure 39A. Finally, in the case of V_{Riv}/V_{PEI},-quantitative results showed an increase with increasing RS, TT and TP (see Figure

39B) owing to the increase in insertion depth (see results presented below) and metal plasticizing with these parameters (see burn-off results in Section 4.2.f).

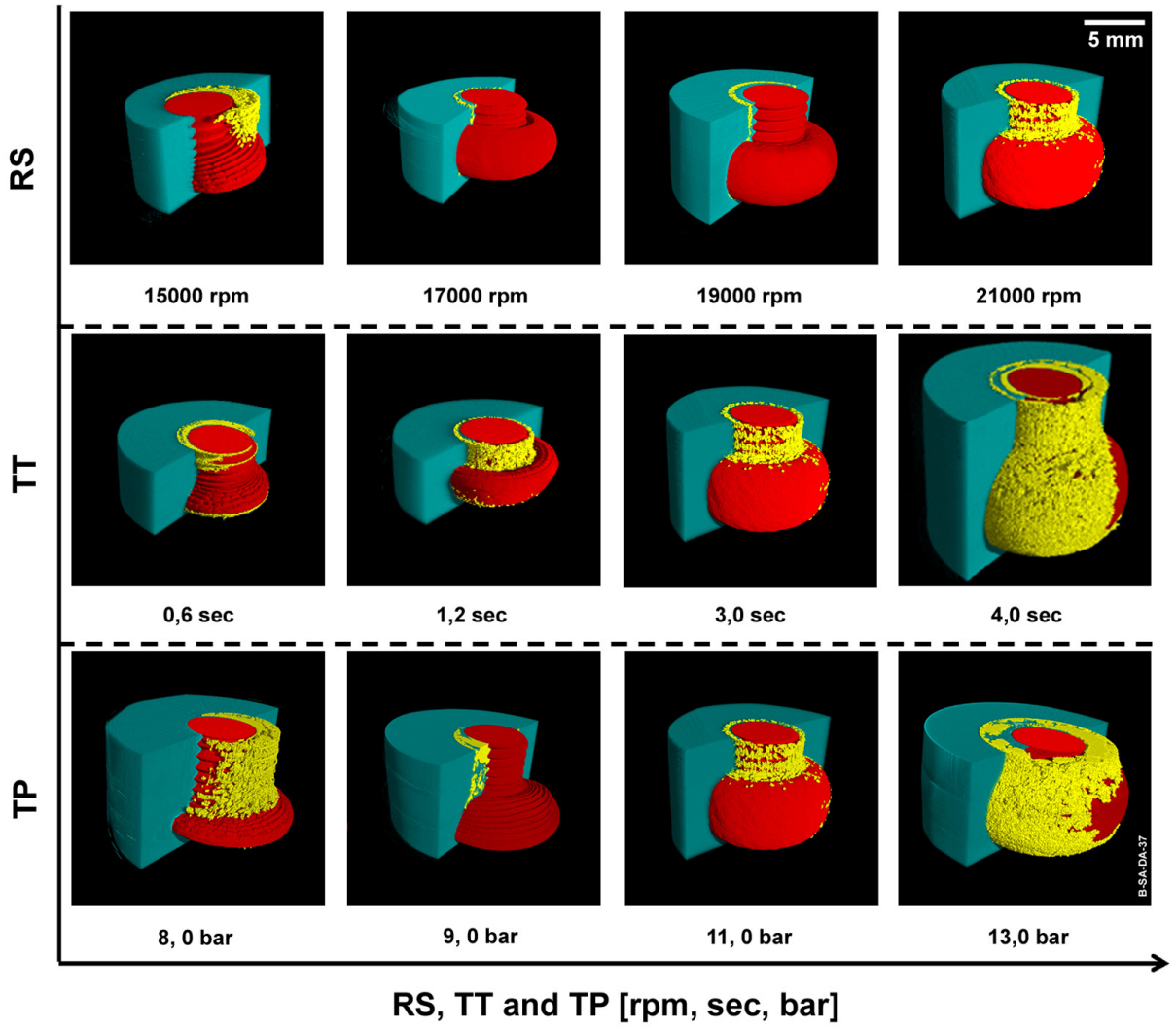

Figure 36. Microstructural appearance of point-on-plate joints on PEI/AA2024-T351, obtained by μCT-volume rendering. Rivet is presented in red, the volumetric defects in yellow and the polymeric base plate in green.

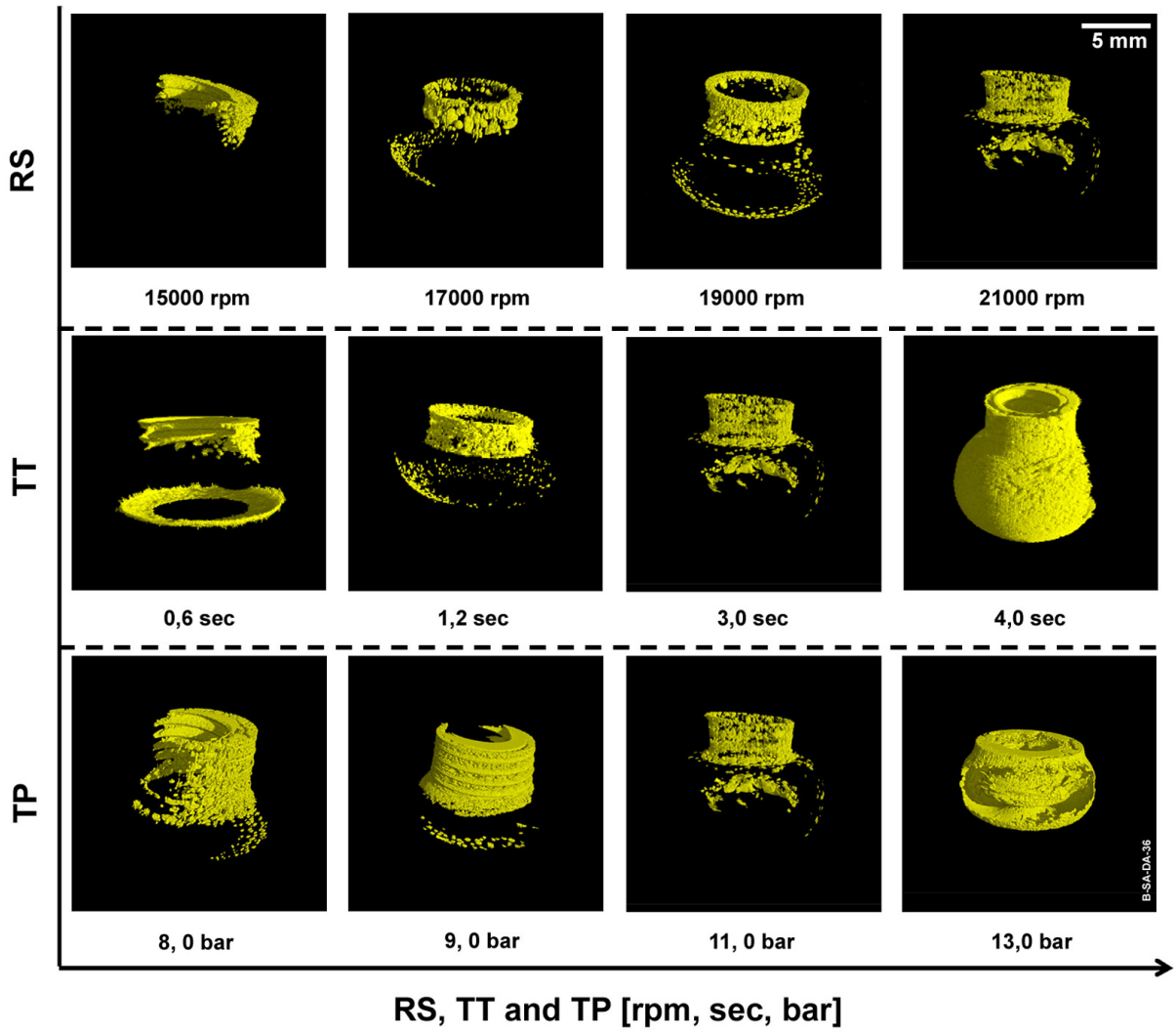

Figure 37. Isolated volumetric defects, V_d, of RS, TT and TP samples from Figure 36.

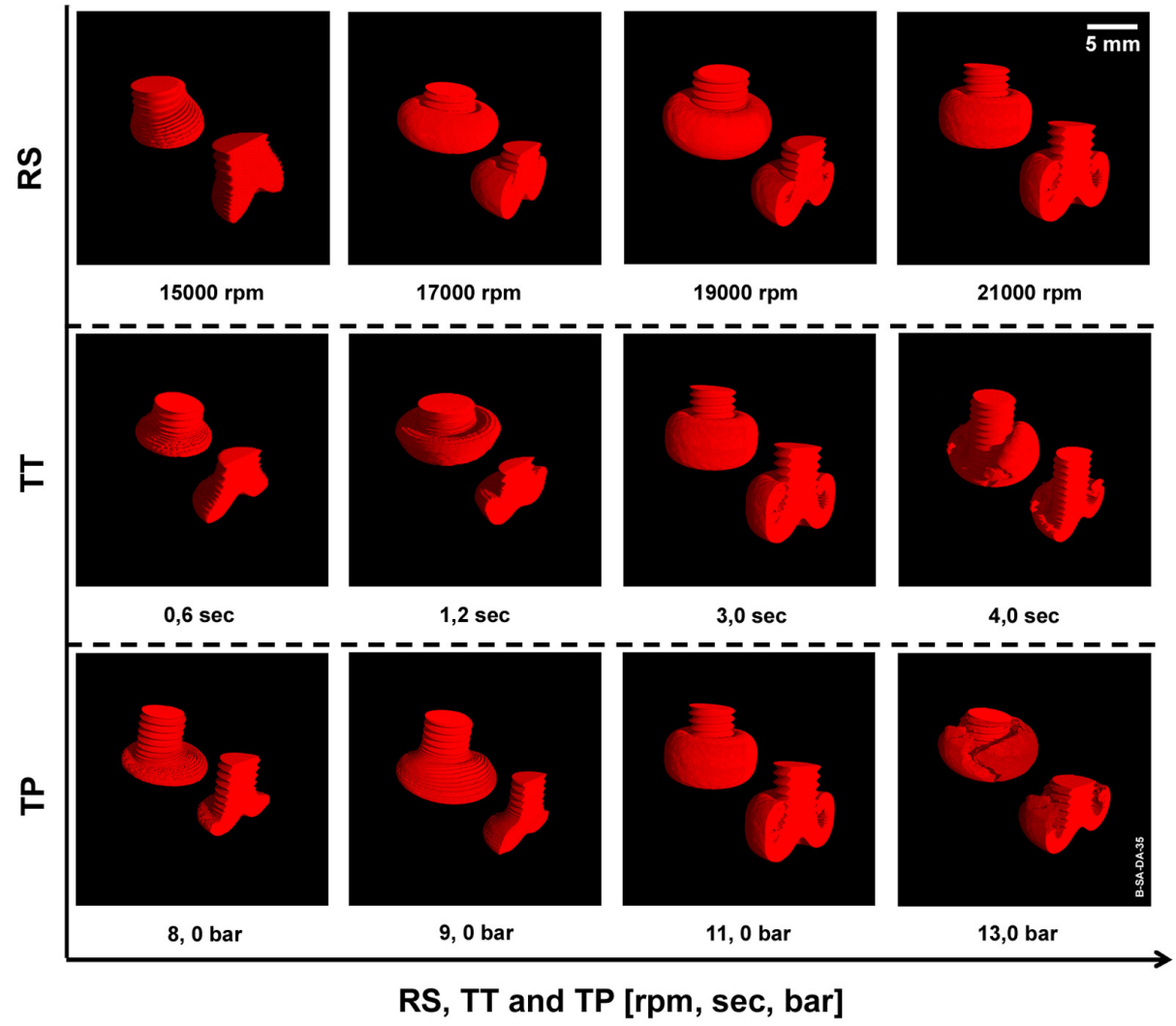

Figure 38. Isolated rivet-volume, V_{Riv}, of RS, TT and TP samples from Figure 36.

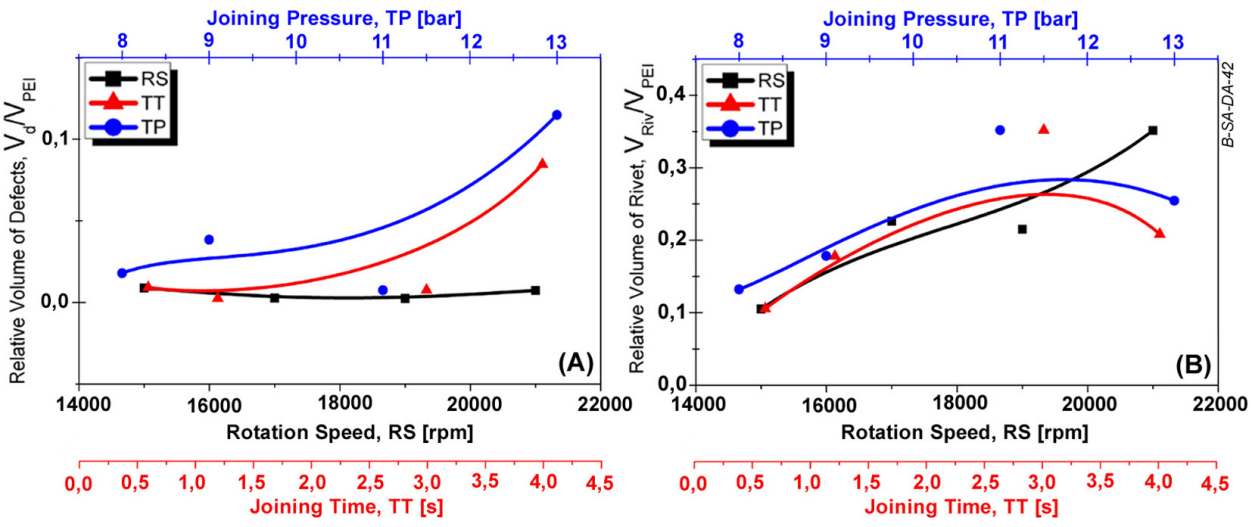

Figure 39. A) Relative volume of defects (flaws), V_d/V_{PEI} for RS, TT and TP comparison study. B) Relative volume of rivet inside the polymeric base plate, V_{Riv}/V_{PEI}, for RS, TT and TP comparison study.

The influence of process parameters on rivet insertion depth (*h*) and width of AZ (*w*) were also investigated by image analysis of LO-macrographs. Figure 40 presents the non-etched LOM-cross sections of friction riveting samples (LOM-investigation performed in separate joints). The *h*-values were computed by tracing a vertical line from the upper surface of the polymeric plate to the bottom of the AZ in the middle of thejoint, while the *w*-values where measured from a line placed on the greatest width of the AZ. This is schematically represented in the cross section from sample 21000 rpm in Figure 40.

The numerical results of measured *w* and *h* are presented in Figure 41A and Figure 41B. The width of AZ seems to increase with RS, TT and TP until a certain level where it becomes constant (see regions at 19000 rpm, 11,0 bar and 3,0 sec, Figure 41A). The rivet insertion depth on the other hand clearly increases with these parameters. Nevertheless, this increment rate seems to behave differently for each joining parameter, where the TT appears to have the strongest influence of all (see Figure 41 B).

Another singular macrostructural feature readily identified in macrographs of comparative samples in Figure 40, is the V-shape (actually a conical notch) at the bottom of AZ, a feature associated with plasticized metal flow. At the rubbing surfaces, inner regions will have lower tangential linear velocities than outer regions. This means that central regions of rubbing surfaces will experience lower frictional regimes and consequently lower heat generation than outer regions considering that, tangential speed plays an important role on heat input (see heat input model Equations (28) in Section 4.1.g). Lower heat generation will lead to lower local temperatures and viscosities. In this manner the central region on the rivet's tip will become less plasticized. During forging, the plasticized metallic material of outer regions will flow downwards easier than the somewhat harder plasticized material at the inner regions, until they reach the colder polymeric areas and are pushed backwards (see process description in Section 4.1.b). This differential flow gradient in the AZ will cause the left and right legs of the V-shape to form.

The preferable annealing mechanism in face-centred cubic metals (FCC) with high stacking fault energy (SFE), such as aluminium, is recovery instead of recrystallization, where dislocation annihilation happens through cross-slip and climbing, and subgrain structures are formed [216]. Nevertheless, recrystallization can also take place in alloyed FCC-metals with high SFE. The stacking fault is a planar defect in the material lattice in form of a sheet, controlling the dislocation dissociation into partial dislocations. As the partial dislocations repel themselves with a force proportional to the shear modulus, G, of the crystal, SFE can be defined as the energy to keep the partials in an equilibrium distance (d_e) [221].

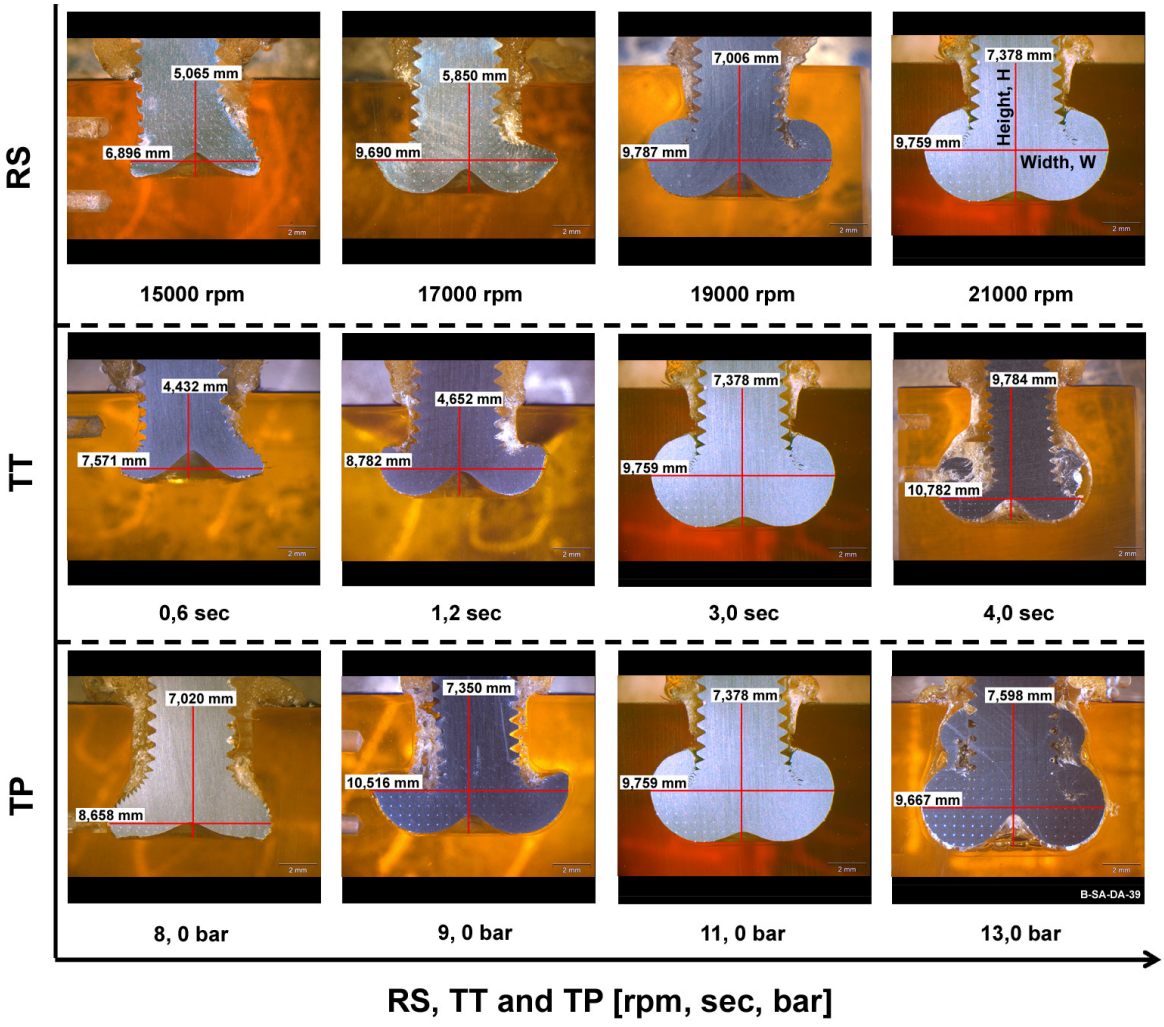

Figure 40. Non-etched LOM-macrographs of cross sections took from the middle of the joint. h-values are related to vertical lines and w-values to horizontal lines, 25X. Horizontal cylindrical holes near to rivet's shaft in samples 15000 rpm, 0,6 sec, 4,0 sec, 8,0 bar and 9,0 bar *are the holes for thermocouple temperature measurements.*

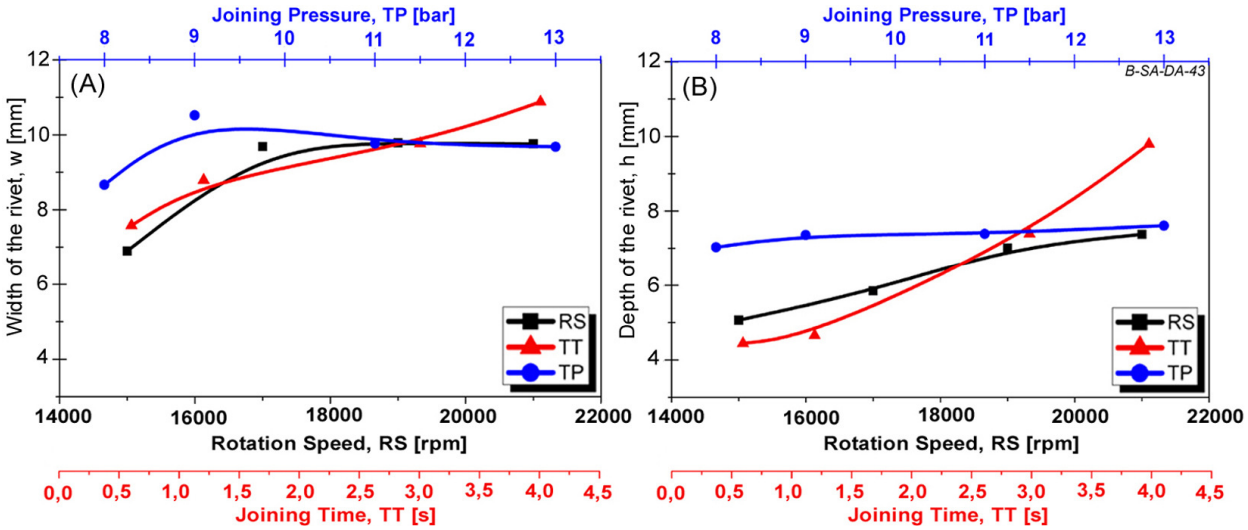

Figure 41. Rivet geometrical features from samples in Figure 40. A) Width of AZ, w. *B) Rivet insertion depth,* h.

Addition of solute in a pure FCC alloy will lead to a decrease in G and consequently in SFE, plus an increase in d_e, considering that SFE is directly proportional to G and inversely proportional to d_e [222], so recrystallization can take place in those metals. There are also other ways of supporting recrystallization. Addition of insoluble particles may prevent the redistribution of dislocations without changing SFE, so recovery is decelerated [223], while temperature combined with high strain rates will facilitate dynamic recrystallization [222, 224].

For Al-Cu aluminium alloys it has been shown that, during hot working, CDRX is the mandatory grain refinement mechanism [225-227]. An important mechanism of grain subdivision in aluminium alloys under severe plastic deformation, happening concomitantly with dynamic recovery, is the deformation banding. Deformation banding is normally the source of CDRX high angle boundaries [226, 228-232]. Deformation Bands (DB), are highly elongated banded or ribbon-like structures formed during severe deformation as a result of lattice rotation from adjacent regions inside a grain to symmetric final orientations [230-232]. The origination of DB is directly connected to the level of deformation and strain rate as well as the size of initial grains; coarse initial grains under high straining, like for example during hot rolling, are more prone to deformation banding [233]. Presence of solute, finely distributed precipitates and second phase particles may also support deformation banding [229,232].

The microstructure in the rivet was revealed by polarized light LOM of electrolytic-etched samples. In the joints examined in this work both partially CDRX and DB structures were detected. The initial microstructure of Al-Cu-Mg AA2024-T351 drawn rods presented coarse grains oriented in the draw direction with coarse $CuAl_2$-θ intermetallic particles and AlMgCuC secondary particles (see Figure 18, Section 3.2.a). In addition to this the high levels of strain and strain rates brought by elevated RS and TP, plus high temperature, contribute to these two restoring metallurgical mechanisms. It has been reported [234] that, DBs can be formed at temperatures starting at $0,4*T_m$, while at temperatures higher than $0,5*T_m$ dynamic recrystallization can be started [235]. Considering that $T_{m\text{-}2024\text{-}T351}$ = 502 - 638 ^oC [236] and the measured temperatures on the PTMAZ near to MTMAZ were within a range of 300 – 500 ^oC (see Figure 34, Section 4.2.b) which represents an approximate interval of 0,5- $0,95*T_{m\text{-}2024\text{-}T351}$, process temperatures were high enough for allowing DB and CDRX to go on. Figure 42 and Figure 43A confirm these assumptions where examples of DB in the MTMAZ are shown.

In Figure 42 one finds a magnified picture of deformation banded grains at the AZ of a point-on-plate PEI/AA2024-T351 joint. Figure 43A illustrates an example of multiple deformation banding (indicated by arrows) in the MTMAZ. CDRX-grains can be seen in Figure 43B and C; note that grains are much finer and equiaxed in comparison to initial coarse and flattened grains from the drawn rod (see Figure EE, Section). Indication of CDRX induced by DB is found in Figure 43B and C-4, where grains with DBs indicated by arrows, are found mixed with CDRX-grains.

The etched cross sections from comparative samples are illustrated in Figure 44. From a visual observation of this figure, it is possible to see that no fully CDRX-AZ was formed in the studied parameter ranges. Only partial grain refinement is observed on each leg of AZ, probably the regions with the highest strain rates. In the case of RS-samples it appears that percent of CDRX-grains tends to increase with the joining parameter, although only few CDRX-grains are observed at 15000-17000 rpm. On the other hand the amount of CDRX grains for TT- and TP-samples does not seem to be strongly influenced by these increasingly joining parameters. The level of CDRX appeared to be constant for the parameter ranges in this study. A quantitative analysis of grain size could not be carried out due to the highly flattened grains of the drawn base material on one side, and on the other side due the partially CDRX-structure which makes an interpretation of results very difficult.

Other metallurgical phenomena not resolved by LOM technique occur concomitantly with deformation banding and CDRX, such as dynamic recovery, DR (for AA2024 $T_{DR} \cong 400\ ^{o}C$ [236]), solutioning of hardening particles, SHT (for AA2024 $T_{SHT} \cong 250\ ^{o}C$ [236]), coalescence of precipitates (which are examples of softening processes) and dynamic precipitation/re-precipitation (hardening mechanism). Nevertheless, the investigations of these phenomena are out of the scope of this work and are not further discussed; for a complete approach in these metallurgical phenomena refer to [127, 216, 221].

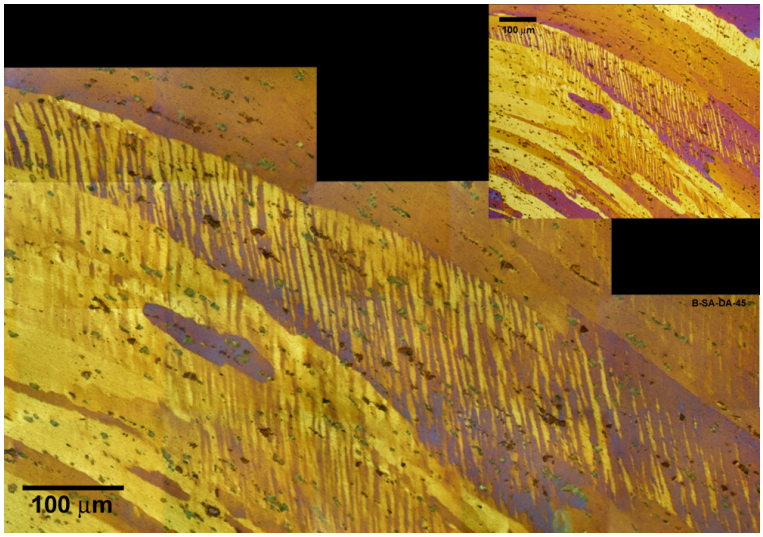

Figure 42. Deformation bands in the AZ of PEI/AA2024-T351 of friction riveted joint, 200X (smaller photo) and 1000X (bigger photo).

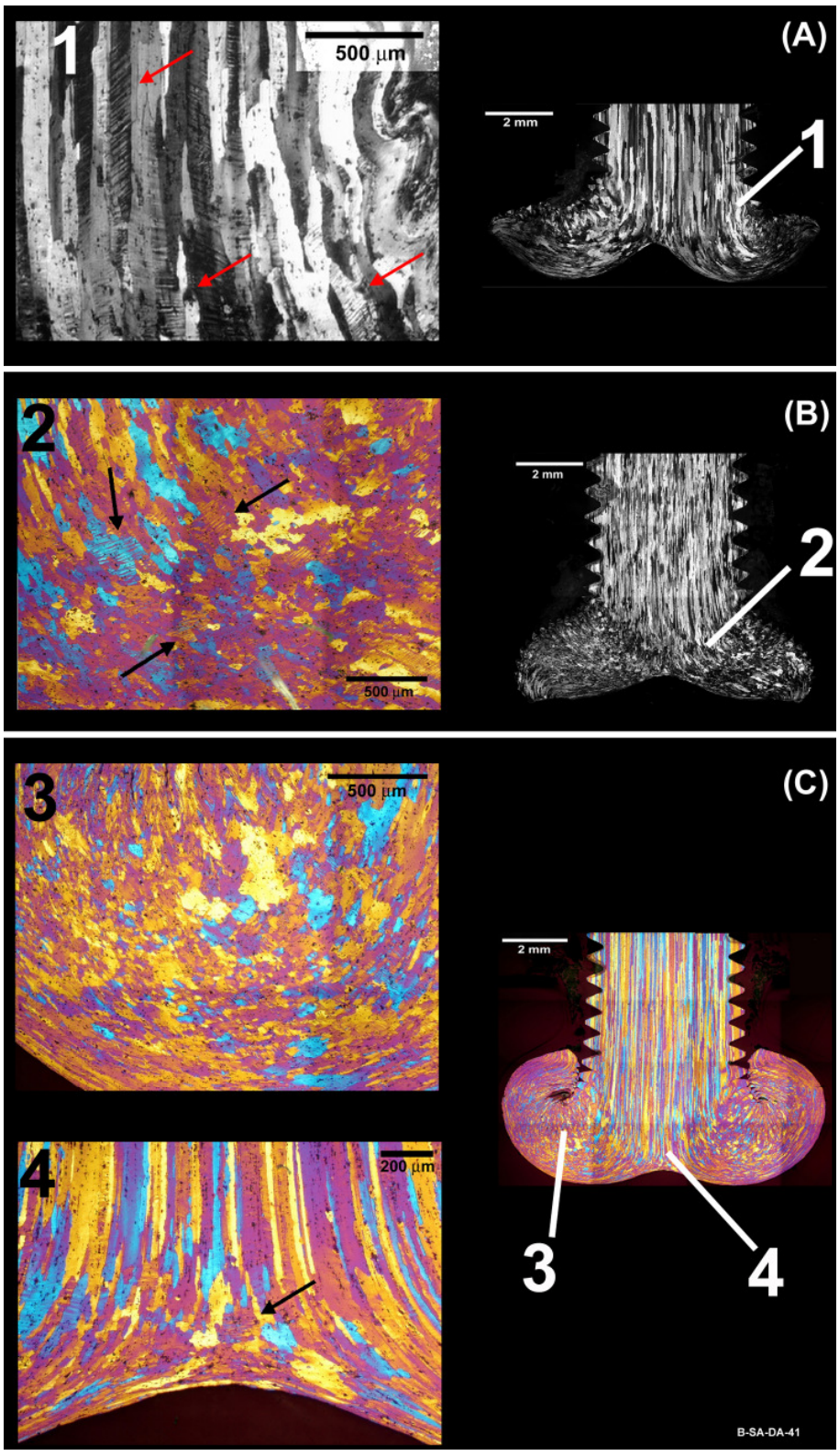

Figure 43. Example of microstructural transformation in the metallic rivet from comparison samples. A) Deformation bands, DB, in the MTMAZ. B) Partially continuous dynamic recrystallized (CDRX) grains nucleated by DB (marked with arrows), in the AZ. C) Nr.3 shows fine CDRX-grains and Nr. 4 the CDRX-initiation area at AZ in the middle of the joint. Detail pictures were originally taken with 200X and the macrographs with 50X.

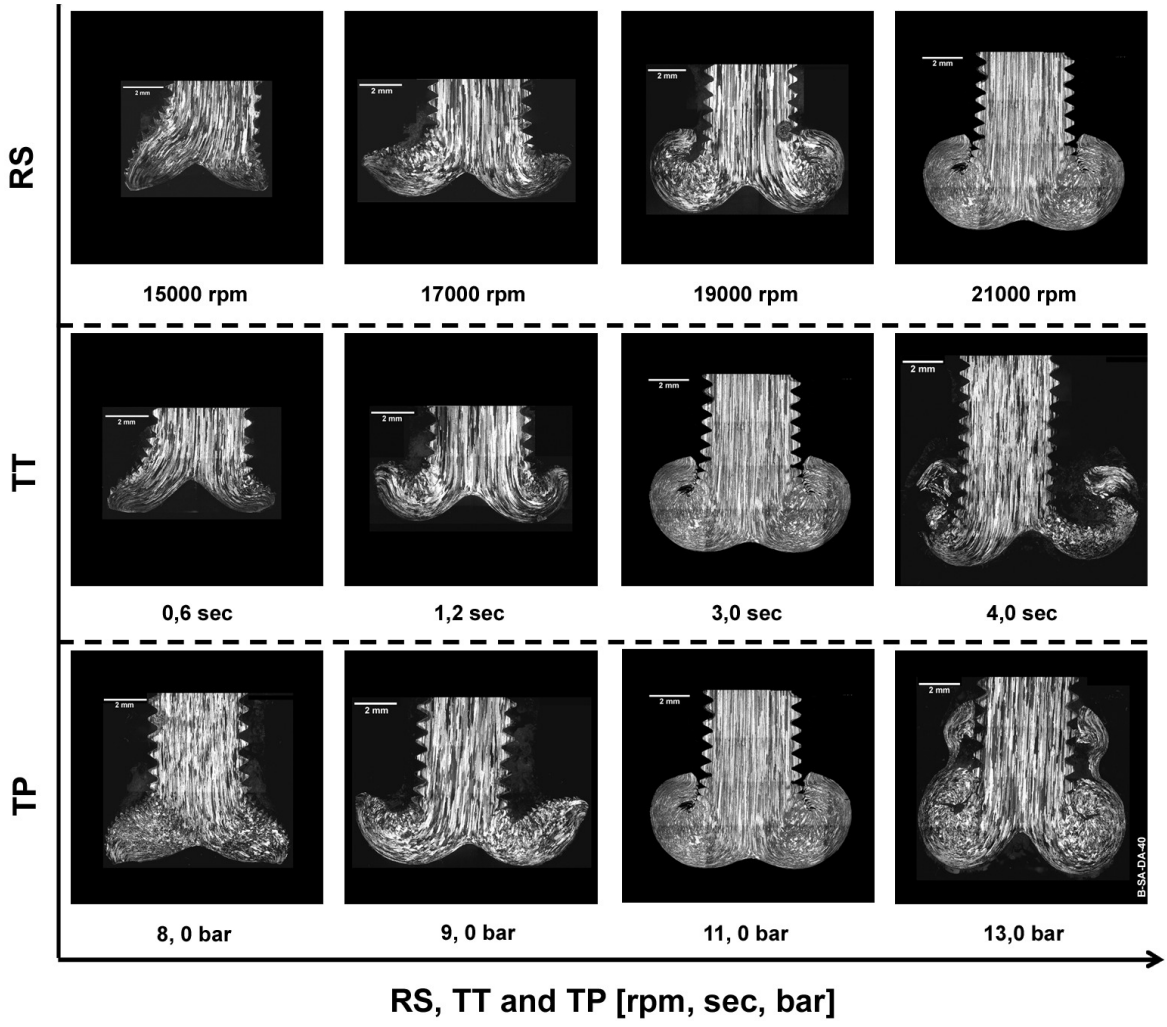

Figure 44. Electrolytic etched cross-section macrographs of comparative samples, 50X, Barker etching.

4.2.d. Local mechanical properties

The local mechanical properties of the friction riveting comparative samples were evaluated by microhardness and by GPC following the procedures presented in Sections 3.1.d and 3.1.i. The microhardness results for the metallic rivet were obtained in the form of hardness maps, while for the polymeric portion in the form of line-profiles. Figure 45 illustrates the microhardness results for metallic rivets. Vickers-maps are given in this picture for the rivet portion inside the polymeric plate, for macrographic cross-sections presented in Figure 44. It is important to keep in mind that friction riveting is an inhomogeneous thermal process, where physical factors such as temperature history, plasticizing regime and microstructural changes are not fully comprehended yet. Material properties like for instance thermal conductivity and joint geometry may directly influence the way the joint is formed.

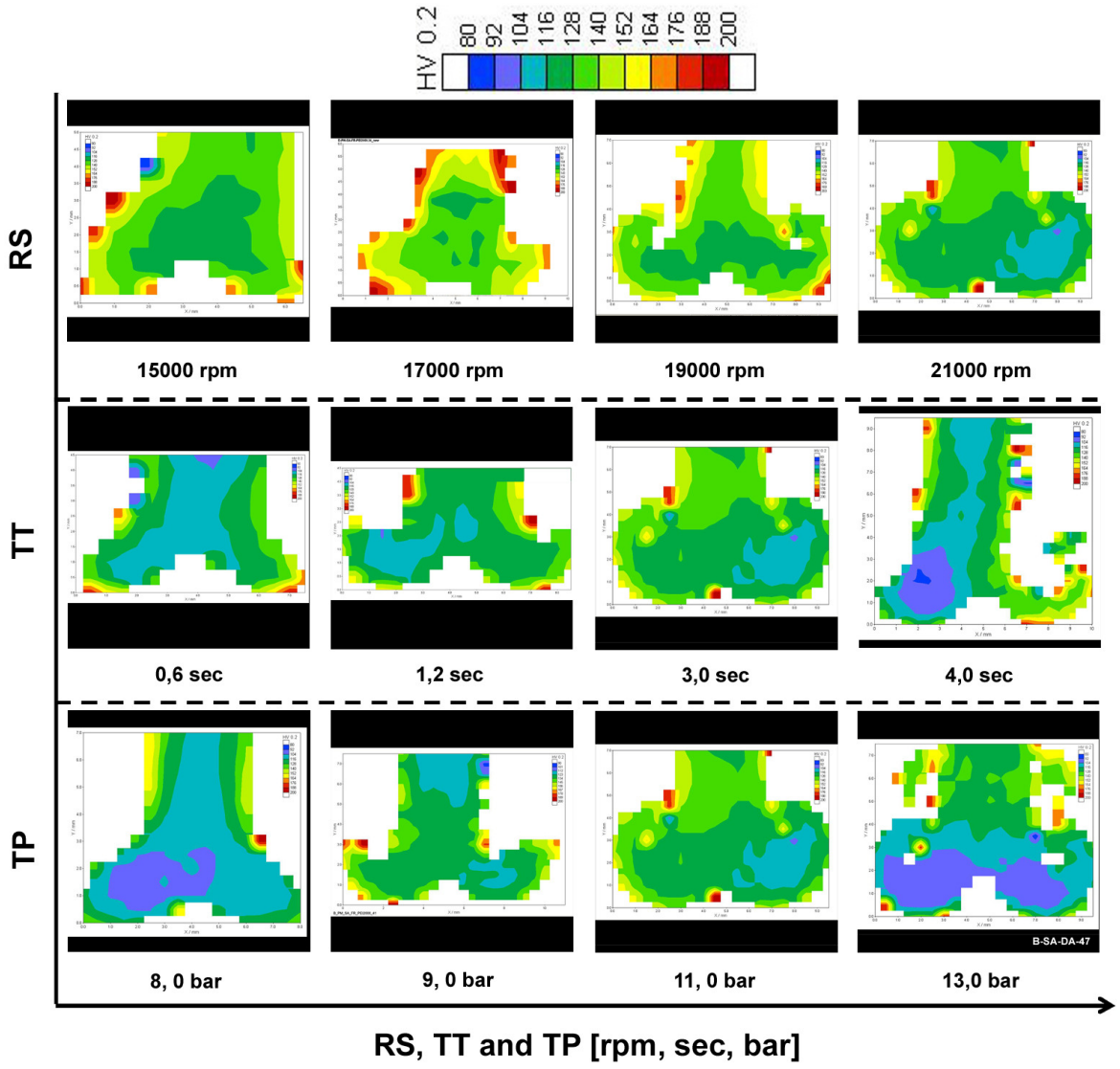

Figure 45. Vickers microhardness maps from the metallic rivet of comparative friction riveting joints.

From a first observation of Figure 45, one sees that for all conditions, there was a decrease in joint microhardness levels in comparison to the base material (see Figure 18C); the softest area was predominantly in the paraboloidal-AZ, in the MTMAZ. This microhardness drop is associated with the dynamically recovered and partially recrystallized microstructure found in this region, owing to higher temperatures near the rubbing area on the tip of the rivet. Secondly by individually examining the different sample groups, it seems that the range of RS led to lower levels of microhardness drops comparing to TT- and TP-samples; however a tendency in decreasing microhardness with increasing RS could be observed, which was in accordance with the visual increase of CDRX-grains for these samples (see Figure 44). Nevertheless, a clear trend in microhardness behaviour for TT- and TP-samples could not be delineated; it can be roughly associated with the practically unchanged microstructure of these samples, as presented in Figure 44.

The microhardness evaluation of the polymeric portion was carried out with reduced indentation load and longer times to compensate for the lower modulus and the viscoelastic behaviour of polymers. Vickers microhardness line profiles (3,5 mm wide) were obtained from indentations placed upright to polymeric base plate thickness, and microhardness results calculated from manual measurements of indentation diagonals. The profiles were positioned near to the top surface of the right side leg of AZ, as schematized in Figure 46D. Average microhardness results (three-time measurement of each diagonal/indentation), are found in Figure 46A, Figure 46B and Figure 46C. The yellow curves correspond to the measured average microhardness of PEI (HV0,1 $\cong$ 284,0 $\pm$ 4,5 MPa).

It was expected that microhardness testing of the polymeric areas would allow the accurate positioning of PHAZ and PTMAZ in the joint area, which was not the case. The PTMAZ should always display microhardness values either similar to or smaller than the original base material because at melting temperatures, all prior thermo-mechanical history is destroyed. The PHAZ should lead to higher hardness values than the base material thanks to the temperatures below T_g, leading to physical ageing and/or hardening by water elimination. Results presented in Figure 46A, Figure 46B and Figure 46C indicated alteration in microhardness in comparison to PEI average values, where hardness levels for profiles show bigger mean microhardness values suggesting structural hardening. Yet a well defined behaviour of microhardness with the distance to AZ and temperature (compare with Figure 34) could not be identified. For amorphous materials at temperatures under T_g [158], physical ageing (increasing hardness) and structural hardening related to water elimination are accelerated by increasing temperatures and/or residence times. However samples displaying higher temperature and/or dwelling time values did not follow this dependence.

Therefore, polymeric microhardness results in this study are only qualitative. Possible effects acting over microhardness behaviour of polymers are the indentation load and indentation distance. High loads can create greater plastically deformed volumes around the indentation in comparison to metals, due to the low modulus and work-hardening coefficient of polymers. On the other hand, if the distance between indentations is less than the length of one diagonal, the plastically deformed zones of indentations will superimpose each other [158]. The analysis of the distance between indentations in this study (0,5 mm) pointed out that the minimum distance among indentations was respected, as shown in the example of Figure 47. Thus the most likely explanation for the results limited to a qualitative character is the adopted force (force = 0,98 N), which was certainly too high for this polymer. No comparison data for Vickers-microhardness on PEI could be found in the literature. This may suggest that nanohardness testing with much smaller indentation forces (in micro Newton scale) and resultant indentation size, would provide improved hardness data and precise identification of polymeric microstructure for this new joining technique.

In an attempt to further clarify the local mechanical properties in the polymeric portion of the joints, the evaluation of molecular weight (MW) was carried out by GPC. Several polymer properties are known to be dependent on MW, such as tensile strength, toughness and creep-resistance [70, 237], because higher MW means more available chain entanglements and anchoring points to be overcome under loading. Sanner et al. [238] studied the effect of different MWs in the PEI ULTEM's tensile, impact resistance and brittle-to-ductile behaviour properties. They investigated a MW-range varying from M_w = 36640 – 52300 g/mol and M_n = 15660 – 22820 g/mol under tensile testing at temperatures ranging from 23 - 140 °C, conditions similar to the PEI-polymer in this work (Mw = 52234 ; Mn = 26332, Table 11, Section 3.2.c).

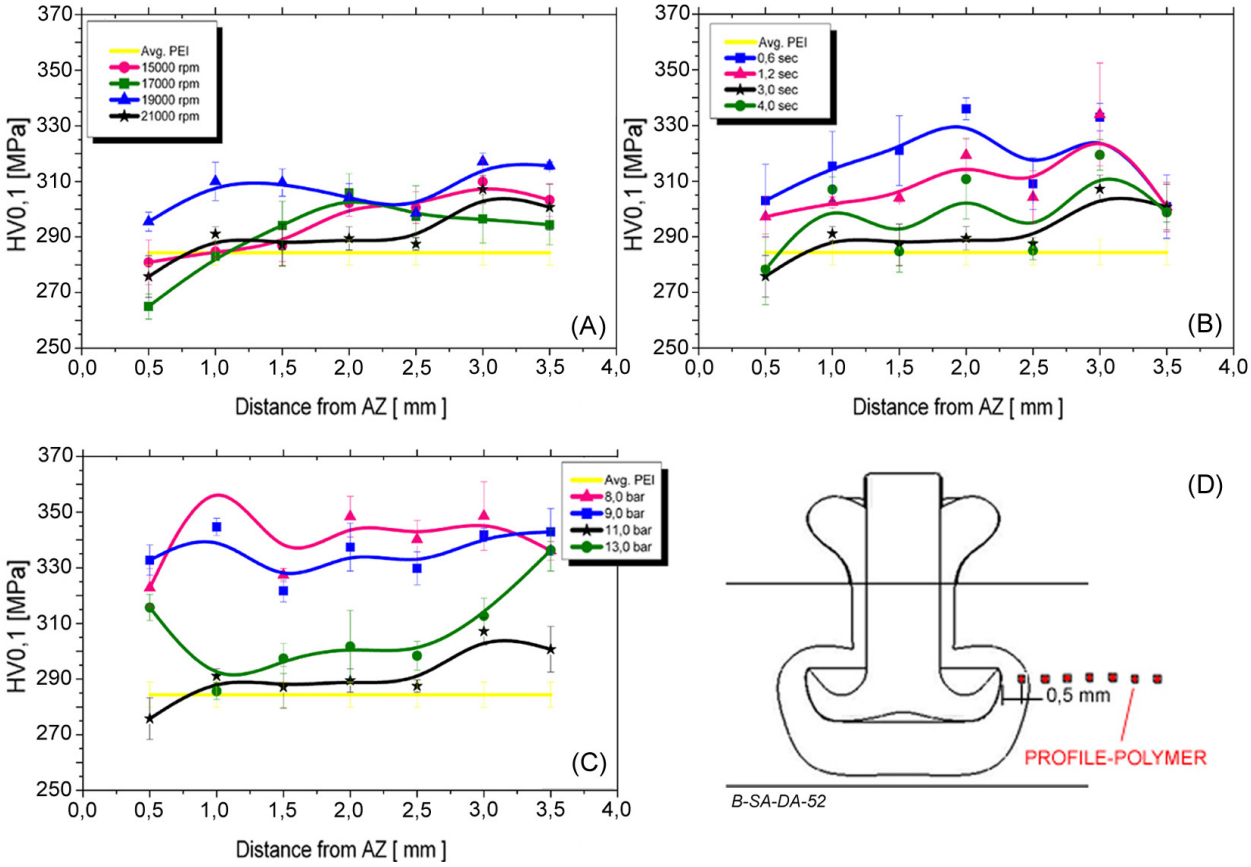

Figure 46. Microhardness results for the polymeric portion of comparative friction riveting joints. A) RS-samples. B) TT-samples. C) TP-samples. D) Scheme of line-profiles for HV0,1 Vickers measurements.

It has been observed that in these experimental ranges, the global yield strength remained unaltered for the different MWs within the testing temperature range; on the other hand, impact resistance increased and ductile behaviour was raised by increasing MWs. Those results show how robust the PEI polymer is in terms of mechanical performance. Bearing these assumptions in mind, one can associate MW with local mechanical properties in the polymeric base plate. A strong decrease in MW resulting from thermal degradation during joining could indicate a deterioration in properties of the PHAZ/PTMAZ (weld line formation) and PTMAZ/AZ bonded interfaces.

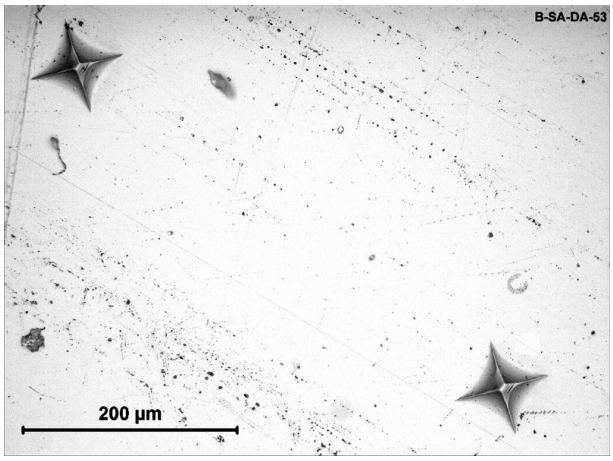

Figure 47. Example of indentations obtained from Vickers HV0,1 microhardness testing in the polymeric base plate of PEI/AA2024-T351 friction riveting joints.

In this way it is important to understand the thermal degradation mechanisms and their relationship to MW. The thermal degradation of PEI has been extensively studied in the last decades in face of its increasing commercial importance [239-246]. PEI's MW can undergo thermal degradation in two ways: by random scission or by crosslinking. While the former leads to a decrease in MW due to a decrease in chain size, the latter increases it [247]. As previously discussed, decreasing MW may result in inferior polymer strength, i.e. by chain scission. Conversely, crosslinking will augment polymer strength. While these effects from elevation in MW will improve yield strength, they can promote brittleness and increase molten viscosity [243]. Crosslinking in PEI was reported to occur in temperatures ranging from 320-380°C [239, 243], whereas chain scission above 400 °C shows a maximum rate of decomposition (rate of weight loss) around 510-540 °C [239-244]. Hence, neither high amounts of chain scission nor crosslinking are desired in friction riveting.

Carrocio et al [241, 246] and Kuroda et al. [239] are examples of works on describing the thermal degradation of PEI ULTEM 1000. Chain scission happens in two stages for PEI: an early stage at 520 °C where the isopropyledene moieties, ether linkages and phenyl-phthalimides rings are broken, and in a less markedly stage above 600 °C, producing CO_2 and water by heat-induced hydrolysis of phthalimide rings [241]. As the range of interest in this study is within the early stage of degradation, it is herein described in more detail in Figure 48.

From Figure 48, reactions T_1 and T_2 represent the scission followed by C-H hydrogen-transfer reactions at the ether linkages. This results in compounds containing phthalimide units with the phenyl rings substituted with H/OH and/or bisphenol-A. Reaction T_3 consists of the disproportion of the isopropylidene moieties in the bisphenol-A units, followed by hydrogen transfer reactions. This results in the formation of compounds containing intact phthlimide rings with ether linkages, hydrogen, methyl, ethyl, isopropylidene and isopropyl end-groups (R) (R

equals to H, CH_3, C_2H_5, C_3H_5, C_3H_7). If the working atmosphere is rich in oxygen, T_3 reaction may follow complex thermo-oxidative reactions leading to the formation of compounds such as alcohols, acetones and acids [246, 248]. Finally, reaction T_4 corresponds to scission of phenyl-phthalimide bonds followed by hydrogen transfer resulting in compounds with N-H and or N-phenyl end-groups.

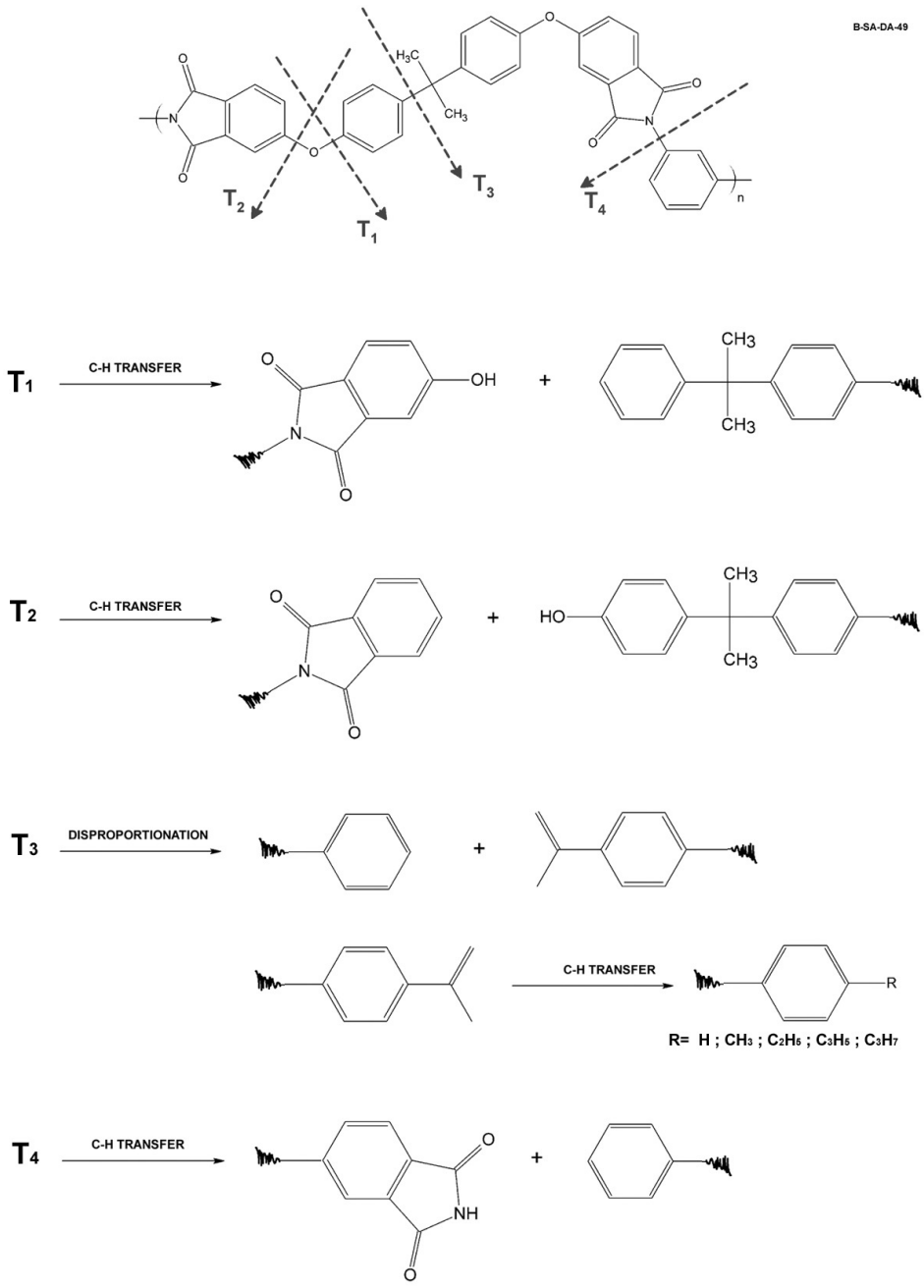

Figure 48. Mechanisms of thermal random chain scission degradation of PEI ULTEM 1000 (GE Plastics). Reactions T1 to T4 are related to early stage of chain scission. Adapted from Carrocio et al. [241].

The crosslinking mechanisms of PEI ULTEM 1000 are currently not well understood. Kuroda et al. [239] have proposed that links between chains are probably formed by combination of two radicals resultant from the chain scission (β-scission) of isopropylidene moieties followed by the substitution of phenyl radical into benzene. A schematic representation of a crosslinked region originated by such mechanisms is found in Figure 49.

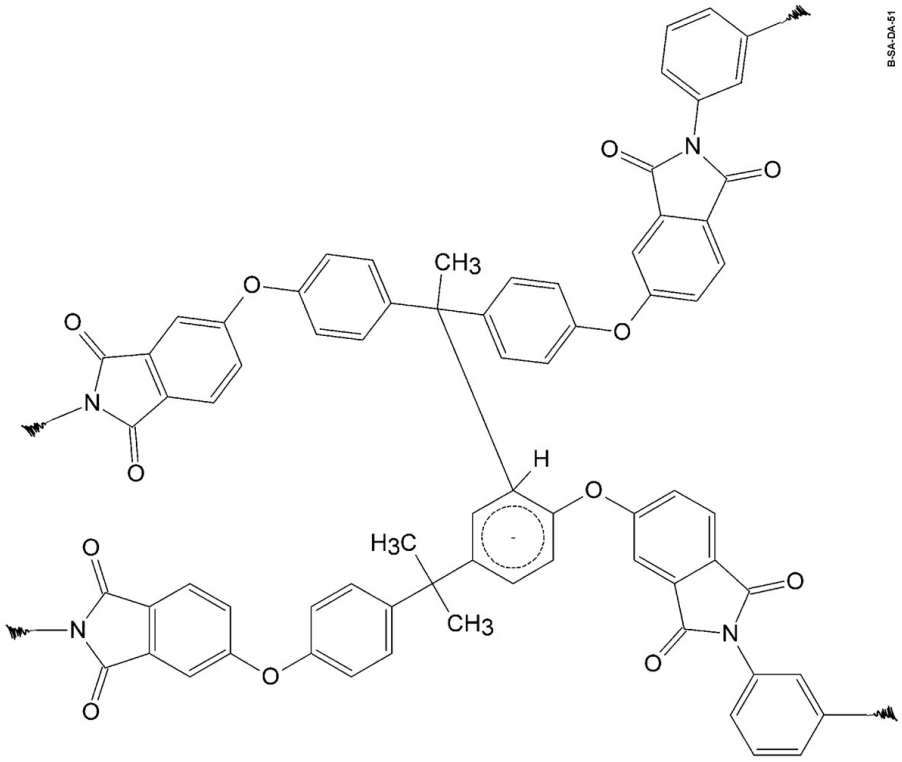

Figure 49. Schematic example of crosslinking between two chains in a thermally aged polyetherimide by the combination of two radicals as proposed by Kuroda et al. [239].

The results of GPC-experiments of the polymeric flash taken from joined samples are presented in Figure 50. The polymeric flash material is a good representative of the molten film in the PTMAZ, considering that it comes straight from the rubbing area, and was chosen for GPC analysis due to easier collecting in comparison to the remaining very thin PTMAZ-layer. Figure 50A, C and E illustrated the elugrams representing the molecular weight distribution (MWD), in terms of chain size normal distribution, where arbitrary units (AU) were selected to simplify comparison of different eluted volumes. The MWD-curves show the changes in MW regarding chain scission or crosslinking. Chain scission is identified when the MWDs evolve broader to the right-hand side of the base material curve, with a small drop in the normal peak in comparison to the polymer base line, because scissioned chains are smaller. On the other hand, crosslinking (chain size is elevated) would broaden the distribution to the left-hand side of the base material curve, and rise the normal peak [243].

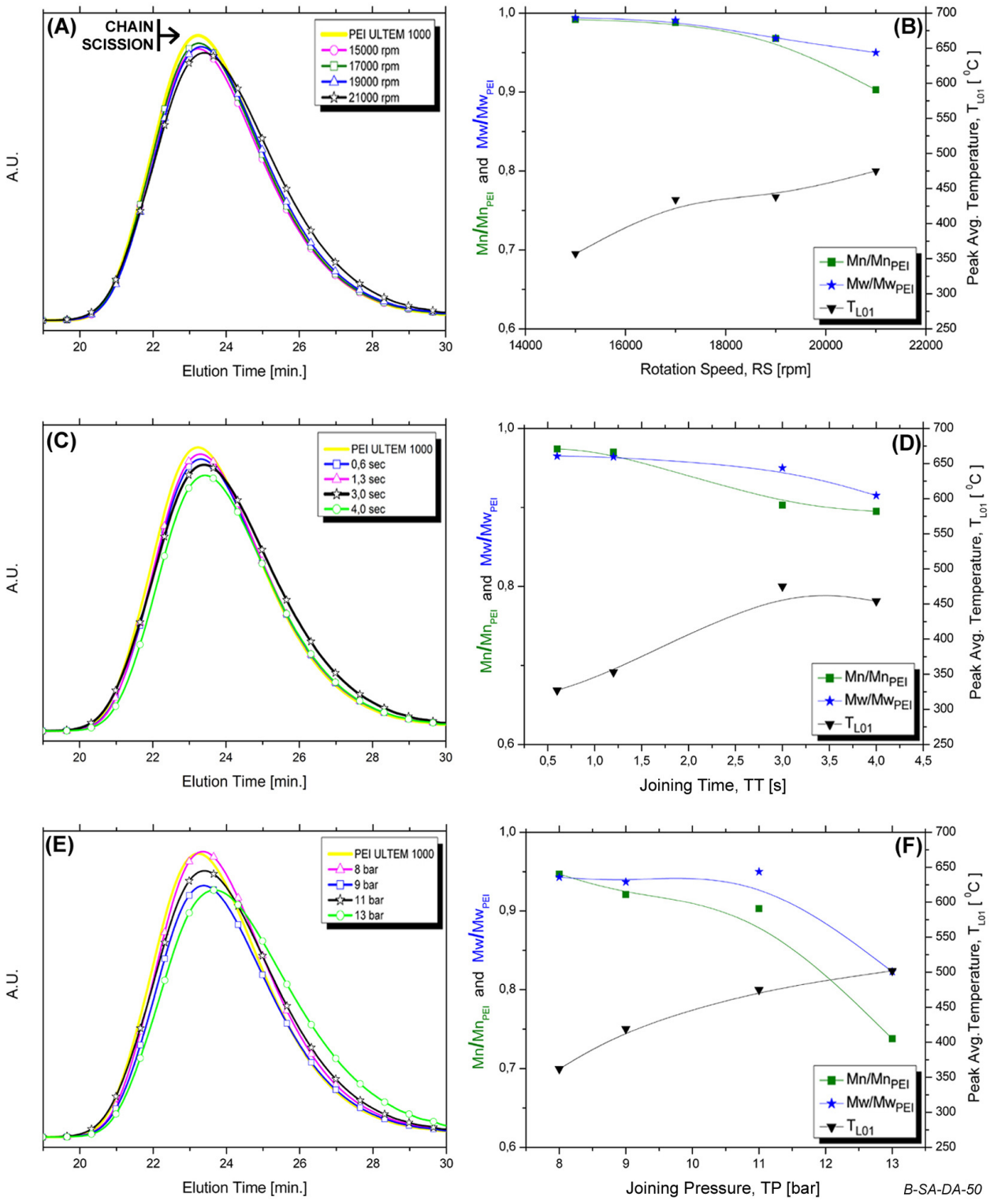

Figure 50. GPC results of polymeric flash material from friction riveting PEI/AA2024-T351 comparison joints in DMF. A), C) and E) presents the MWDs of RS-, TT- and TP-samples respectively; B), D) and F) shows the normalize molecular weight variation with RS, TT and TP in that order, plus their average peak temperatures measured by IR-thermography, T_{L01}.

By looking at the MWD distributions of comparative RS-, TT- ant TP-samples in Figure 50A, Figure 50C and Figure 50E one observes a tendency in broadening to the right-hand side of PEI ULTEM 1000 base line, when increasing the parameters, indicating that chain scission was

the most probable mechanism happening during thermal deterioration of PTMAZ. In order to confirm this assumption, the relative variation of average molecular weight (M_w) and number molecular weight (M_n) two typical representative figures for MW calculations, were evaluated by comparing the M_n and M_w normalized ratios between samples and PEI base material (M_w/ $M_{w\text{-}PEI}$ and M_n/ $M_{n\text{-}PEI}$) with the evolution of joining parameters and average peak temperatures, T_{L01}. These results are found in Figure 50B, Figure 50D and Figure 50F.

The trend in reducing MW observed for all conditions with increasing process parameters supports chain scission as the main thermal degradation mechanism for PEI in friction riveted joints. This behaviour can be clearly associated with increasing T_{L01}. For RS-samples (Figure 50B and D) this declining in MW was very low (less than 5% MW decrease) in the temperature range of 350-450 ^oC (15000 rpm to 19000rpm) and 5,0 % for M_w plus 10,0% for M_n at 500 ^oC (21000 rpm). TT-samples resulted in final values of MW roughly lower than RS-samples (Mw-drop of 8,5% and Mn-drop of 10,5% at 450-475 ^oC), while MW did not significantly decrease in the interval of 325-370 ^oC (0,6 sec and 1,2 sec). The highest drops in MW among comparison samples were observed for TP-samples (see Figure 50F). Decreases as high as 18,0% for M_w and 26,0% for M_n at ≅ 500 ^oC (13,0 bar) could be identified; in the interval of 350-450 ^oC (8 bar and 9,0 bar) MW did not markedly decrease too, although this behaviour was more accentuated than RS- and TT-samples in their initial parameter intervals.

The decrease in MW is in accordance with the volumetric flaw formation behaviour at the PTMAZ, as presented in Figure 39. TP samples have shown both the highest level in flaw formation and decrease in MW, indicating that flaws are mostly due to thermal degradation and not from volatile formation (MW would remain unchanged). On the other hand, RS and TT samples presented the lowest level of flaw formation, with TT samples resulting in slightly higher values than RS samples. This trend in flaw formation for these samples was in accordance with the MW results analysed in this section. The lower dropping levels at MW values of RS and TT samples may suggest that volatile void formation is the most likely mechanism of flaw formation. The accentuated thermal degradation of TP samples can be explained by the higher thermal regimes observed in this pressure range than for RS and TT ranges. Maximum average heating rates in order of 200 $^oC/s$ (see Figure 33) and maximum peak temperatures above 500 ^oC contributed to this drop in MW.

Thermal degradation results varying from 5,0% up to 18,0% for M_w (49622 – 42989 g/mol) and 10,0% to 26,0% for M_n (23778 – 19433 g/mol) might not be a big deal in the case of deterioration of global mechanical properties, since MW average values remained in the range where tensile properties are independent of MW (see prior discussion on the effect of MW in the PEI-ULTEM in this section). Nevertheless, for local mechanical properties of friction riveting joints it will remain always a matter of discussion. Round volumetric flaws are stress concentrators leading to a decline in quality of PHAZ/PTMAZ and PTMAZ/PHAZ interfaces and

should be avoided. As previously discussed, these effects owing to the intense thermal regime can not be totally eliminated but can be reduced by means of further optimization of the process and/or selecting materials with improved thermal resistance.

4.2.e. Global mechanical properties

The influence of joining parameters on the global mechanical properties of point-on-plate friction riveted joints was evaluated by T-pull tensile testing (see Section 3.1.e. for testing procedure). For this kind of tensile samples, strength may be influenced by the following factors: the strength of the weakest joining partner, the geometrical features of the AZ represented by rivet's depth, "h", the width, "w", the presence or absence of cracks on its deformed tip, the quality of the polymer-metal and polymer-polymer interfaces represented by the amount of volumetric defects/thermal degradation in the PTMAZ. Additionally, stress concentration associated with notch effect plays an important role in decreasing overall tensile strength of threaded profiled rivets (such as those used in this analysis), in comparison to unthreaded rivets.

Figure 51A presents engineering stress (R) - strain (ε) curves for the joining partners investigated in this work. For the calculation of R from M5-threaded material, a fictitious cross section area (A_s) has been assumed based on tensile testing procedures for screws [249], in order to disregard the multi-axial stress concentration effect (notch effect) caused by the sharp transition between thread external an internal diameters. The values of A_s, are "on the safe side" of design project tolerances and calculated from Equation (29) [249]

$$A_s = \frac{\pi}{4} \cdot \left(\frac{d_2 + d_3}{2} \right)^2 \qquad (29)$$

where:

d_2 is the pitch diameter of the threaded rivet.

d_3 is the minor diameter of the threaded rivet

For a regular threaded M5-screw the value of A_s is 14,2 mm^2 and was used in the stress calculations of AA2024-T351 material in this work [250]. The obtained average tensile strength (R_m) for this rivet was 459,5 ± 11,4 N/mm^2 (Load = 6524,4 ± 162,3 N) and the strain at rupture (ε_r), was 9,0 ± 1,5 %. Examples R x ε -graphs for PEI-base material flat tensile specimens (tested parallel and perpendicularly to extrusion direction) are presented together with AA2024-T351 M5-rivet for comparing their different mechanical behaviour and influence on joint

strength. Although R_m-values of both PEI parallel and perpendicular flat tensile samples are quite similar (for the parallel-samples R_m is slightly higher, see Table 11, Section 3.2.c), ε_r values for the parallel-samples (Figure 51A, number 2) are much higher than the perpendicular samples (Figure 51A, number 3) because of the increased strengthening effect caused by the chain orientation in the extrusion direction [251]. This is specially true for the case of brittle polymers such as PEI, where ductility is higher parallel to extrusion direction as seen in Figure 51B, number 2, for the tested sample with some necking appearing near to the breaking area. Figure 51B illustrates the tested samples of Figure 51A. As it was expected, Al-rivet is the strongest partner in this joint combination.

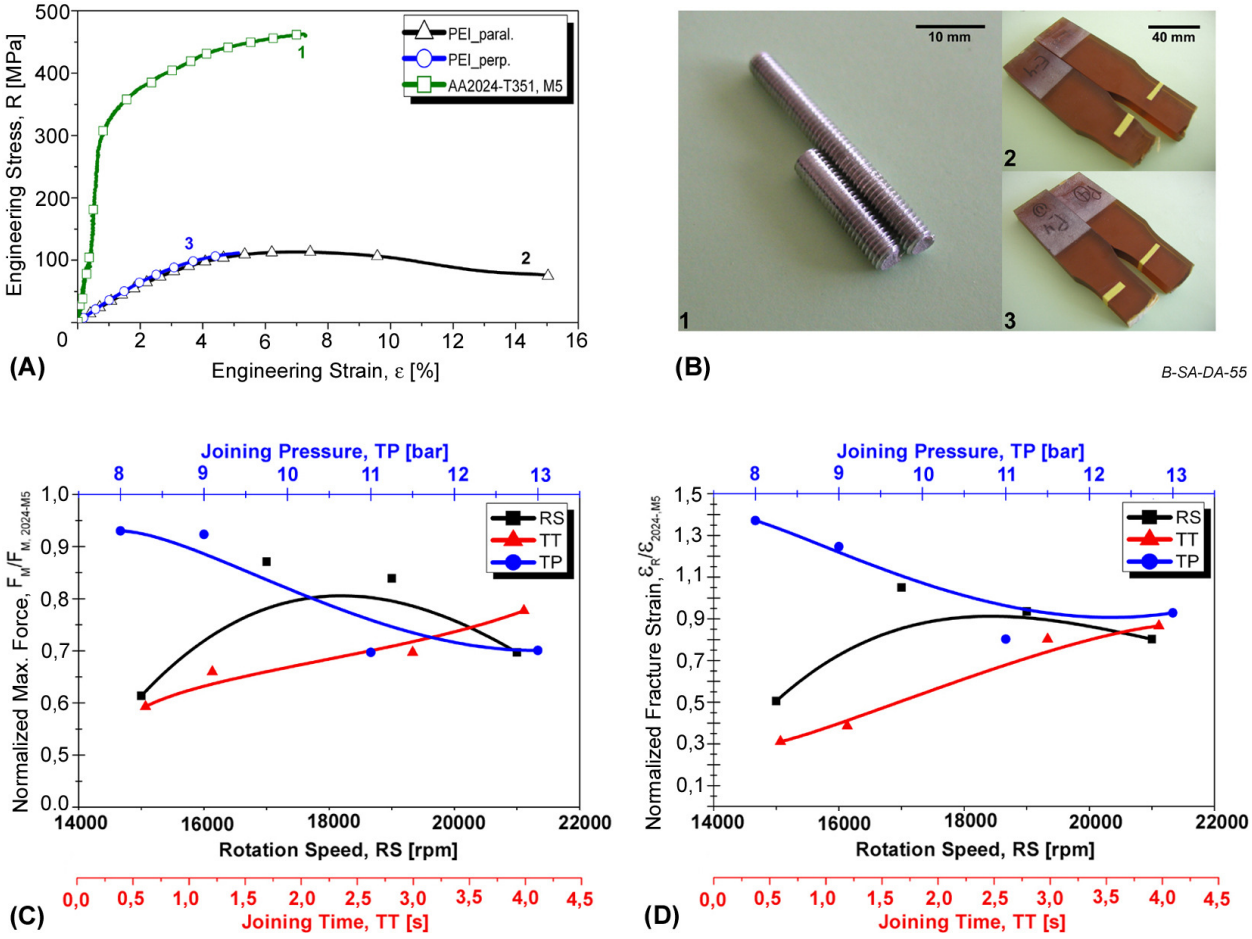

Figure 51. A) Engineering stress-strain example curves for the joining partners PEI and M5-AA2024-T351. B) View of the tested tensile samples in A). C) Normalized maximal force of comparison joints to AA2024-T351. D) Normalized fracture strain at break (or joint's strain at break efficiency) of comparison joints to AA2024-T351.

The influence of RS, TT and TP on the maximum force (F_M) and ε_r is presented in Figure 51C and Figure 51D, respectively, in terms of normalized maximal force to AA2024-T351 M5-rivet, the strongest partner ($F_M/F_{M\ 2024\text{-}M5}$), and the normalized fracture strain to M5 AA2024-T351 rivet, ($\varepsilon_r/\ \varepsilon_{r\ 2024\text{-}M5}$). These are the joint efficiencies. Appendix 5 provides the average force-strain plots for the joined samples.

Three modes of failure were identified for point-on-plate friction riveted joints on PEI/AA2024-T351: Failure on the polymeric base plate (*BP*), failure in the internal rivet shaft at the AZ (*RI*), and failure in the external rivet shaft (*RE)*. Figure 52 shows a schematic representation of these failure types. The fracture type and frequency of occurrence for tested samples are presented in Table 15. Examples of fractured samples of Table 15 are found in Figure 53.

Table 15. Fracture type and frequency of occurrence for RS-, TT-, and TP-T-pull tensile samples (average of 5 tests/param.).

Sample	BP	RI	RE
15000 rpm	100%	–	–
17000 rpm	100%	–	–
19000 rpm	100%	–	–
21000 rpm	57%	43%	–
0,6 s	100%	–	–
1,2 s	100%	–	–
3,0 s	57%	43%	–
4,0 s	–	100%	–
8,0 bar	–	15%	85%
9,0 bar	20%	60%	20%
11,0 bar	57%	43%	–
13,0 bar	–	100%	–

T-SA-DA-13

BP: Base Plate fracture; RI: Rivet-Intern fracture ; RE: Rivet-Extern fracture

For RS-samples the fracture type with the highest occurrence rate was the *BP* (see Table 15 and Figure 53), while in the case of TT samples the *BP* type took place up to the 3,0 sec condition and then changed to the *RI* type for the 4,0 sec condition as observed in Figure 53 . For TP samples, the fracture type was initially *RE* (for sample 8,0 bar) changing to *RI* type at 9,0 bar, subsequently to *BP* type (for sample 11,0 bar) and finally returning to the RI type in condition 13,0 bar (see Figure 53).

Among F_M and ε_r normalized curves (Figure 51C and Figure 51D) it is possible to observe a similar behaviour, where for increasing RS and TT there is a trend in rising strength and strain, and in decreasing stress and strain with rising TP. The weakest joint partner (PEI) did not appear to directly influence the joint efficiency, considering that fracture was observed not only in the PEI base plate but also in the M5-AA2024-T351 rivet (see Table 15). Additionally, the presence of voids in the PTMAZ as well as the amount of thermal degradation appeared to be unrelated to global strength.

It would be expected that higher content of voids/thermal degradation in the PTMAZ would decrease global joint strength. Although void content increases with TT and TP and remained roughly unchanged for RS (see Figure 39A) and thermal degradation level increased with increasing parameters (see Figure 50), tensile strength did not strictly follow the initial assumption of decrease with defects and/or thermal degradation; contrary to that it increased with RS and TT while decreased with TP as previously mentioned.

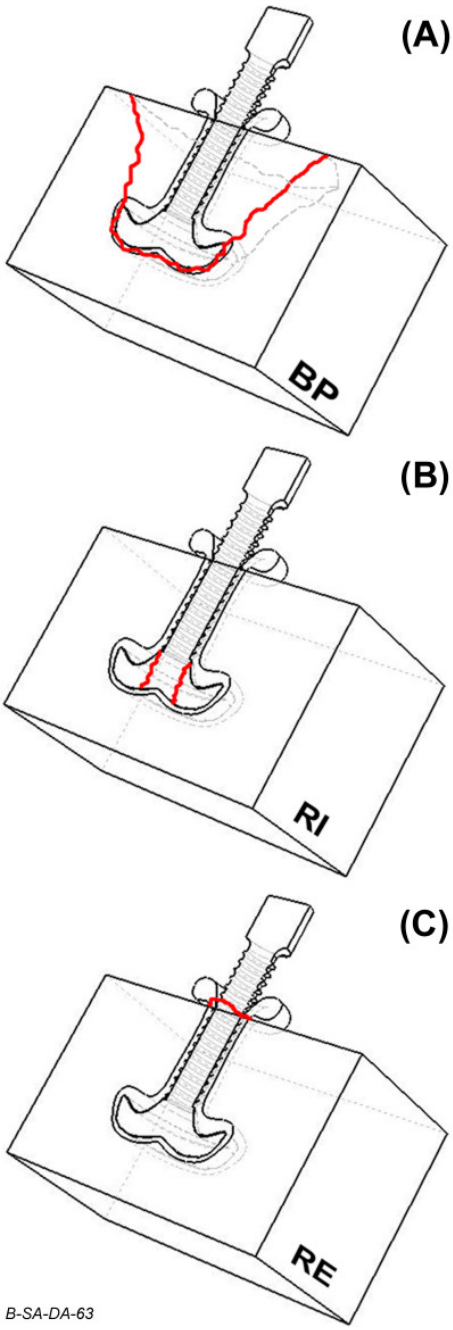

Figure 52. . Scheme of fracture types observed in the T-pull tensile specimens. The red line corresponds to the crack path. BP stays for failure on the polymeric base plate (A). RI for failure in the internal rivet's shaft at the AZ (B) and RE for failure in the external rivet's shaft (C).

On the other hand, the global tensile strength of a joint seemed to be rather related to the geometrical aspects of the AZ. An increase in width, "w" and height, "h", with RS and TT (see Figure 41) seems to be responsible for the increase in strength by improving anchoring (see Figure 51C and Figure 51D). Even in the cases where some cracking at the AZ due to unsteady forging were present, (as for instance in the case of 4,0 sec TT-sample see Figure 38, Section 4.2.c) strength does not seem to be depreciated.

The deterioration of strength with increasing TP appeared to be related to the format of the deformed rivet tip in the AZ: by observing Figure 38, Figure 40, Figure 41, TP samples 8,0 bar and 9,0 bar, which presented the highest stress/strain joint efficiencies ($F_M/F_{M\ 2024\text{-}M5} \cong 0{,}93$ and $\varepsilon_r/\varepsilon_{r\ 2024\text{-}M5} \cong 1{,}4$ /1,25, respectively), had in addition to high "w" and "h" values (w ≅ 9,0/10,5 mm and h ≅ 7,0/7,5 mm), flatter and uniform AZs, which seemed to improve anchoring of the rivet inside the polymeric base plate. This improvement in rivet anchoring for these two samples could also be observed in their fracture behaviour, where failure occurred in the rivet, the strongest partner (*RE* and *RI* fracture types).

Nevertheless when TP levels are too high, the joints experience a changing forging regime; at 13, 0 bar the AZ is virtually pushed off from the polymeric base plate and partially separated from the main AZ body (AZ body is divided in two parts by a crack originated from the unsteady material flow caused by excessive FOP) as seen in Figure 40 and Figure 53. This sort of geometrical feature in the AZ decreases the joint efficiency by decreasing anchoring and rising the notch effect.

If on the one hand threads positively influence the transportation of molten polymer around the shaft of the rivet, the molten temperature distribution, as well as the elimination of volumetric defects (voids) out of the PTMAZ, (and indirectly the polymer-polymer and polymer-metal interface formation in the PHAZ and PTMAZ),on the other hand it leads to reduced strength

owing to stress intensification, as previously discussed. In tensile testing of tough screws ductile failure normally occurs without the typical “cup-and-cone” plastic deformation pattern because of the multi-axial stress state induced on the bottom of the thread [249]. For aluminium screws crack usually initiates at the bottom of a thread flight and follows a 45^{o} up to the middle of the cross section [164, 165]. Appendix 6 shows the fractographic features of the M5 2024-T351 aluminium rivet from Figure 51A and Figure 51B (Nr.1) whose characteristics correspond to the literature, as described above.

The RE fracture type is commonly observed in situations where the anchoring performance of the rivet is high. Figure 54 presents an example of a RE-type fractured sample (TP-sample 8,0 bar). In this case, ductile failure took place at the first loading bearing thread embedded into the polymeric base plate (see Figure 54A). A secondary stable crack front nucleated in the polymeric base plate around the AZ was also observed, pointed out by arrows in Figure 54A and Figure 54B (top and bottom views of the fractured polymeric base plate). This stepwise-crack path following a 45^{o} direction over 2 or 3 flights of threaded components, is associated with the greater amount of elastic/plastic deformation suffered by the initial threads in contact with a nut or a bush, under tensile loading [249, 252]. For this joint the polymeric base plate acts as a nut or a bush, so the stress is concentrated in the first embedded rivet thread, leading to failure (ductile fracture without necking).

The RI fracture type is usually caused by brittle failure in T-pull tensile when rivet anchoring performance is only medium, or when the width and penetration depth of the AZ is high but cracks associated with unsteady forging are present, as exemplified in Figure 55 for the TT sample 4,0 sec. As schematically represented in Figure 52B, the failure happened in the internal portion of rivet at the AZ (see Figure 55B, Figure 55C and Figure 55D). During loading the bottom of the AZ is initially detached from the base plate by mixed cracking of polymer-polymer (the weld line in the PHAZ-PTMAZ) and polymer-metal interfaces (bonded interface between PTMAZ-AZ). Finally the hindering of the AZ increased plastic deformation either in the regions where lower microhardness values were observed or in the thinner sections of the AZ, as pointed by the arrows in Figure 55G. This causes the crack to initiate in the threads placed parallel to the main load direction, and roughly propagate parallel. Figure 55E and Figure 55F show the transgranular cracking path in both left and right sides of the AZ. Generally, secondary cracking around the AZ was not observed in this case.

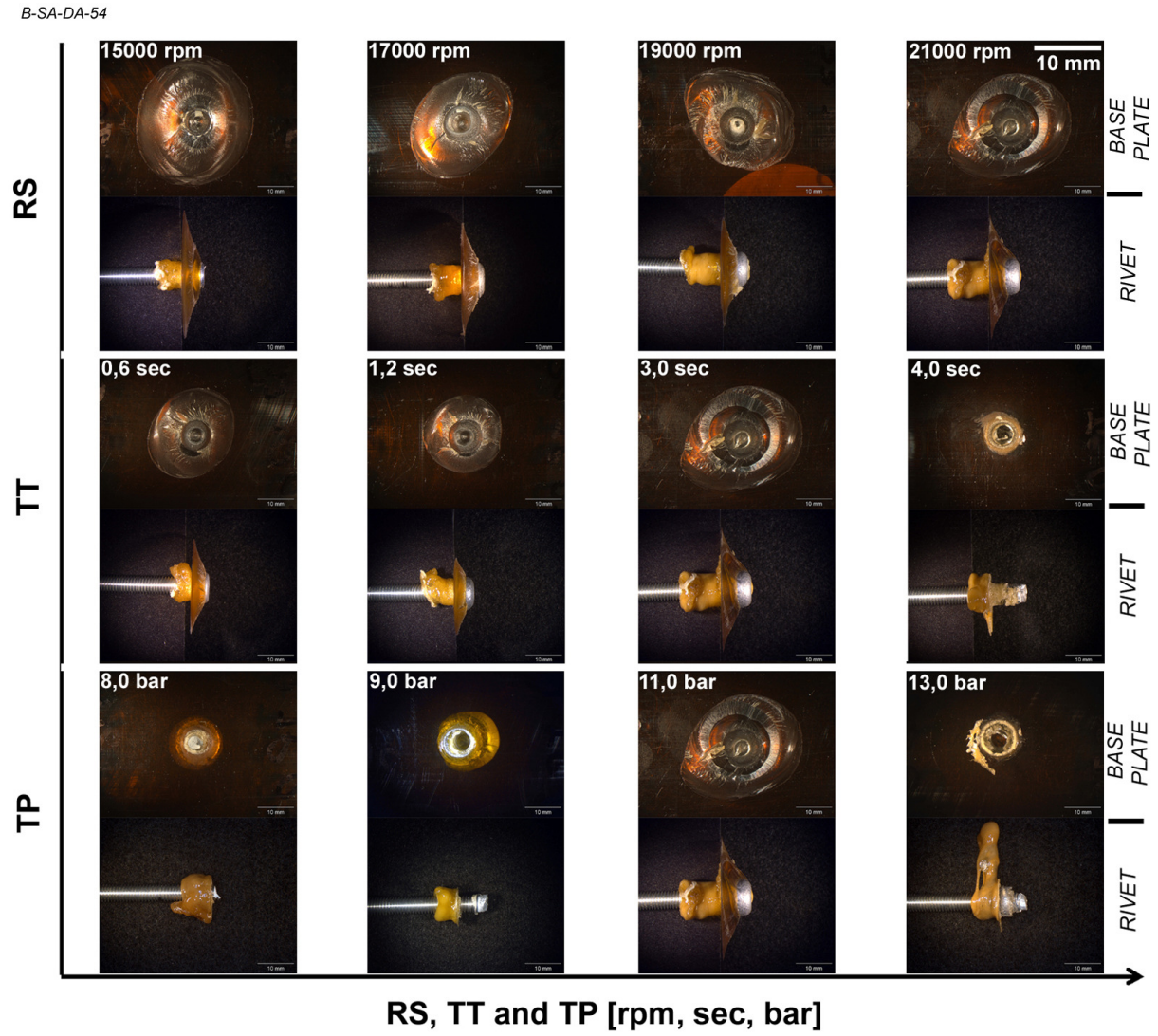

Figure 53. Appearance of fractured T-pull tensile samples of comparative point-on-plate friction riveted joints. For each sample photographs from fractured polymeric base plate (top photo) and from its rivet are presented, 6X.

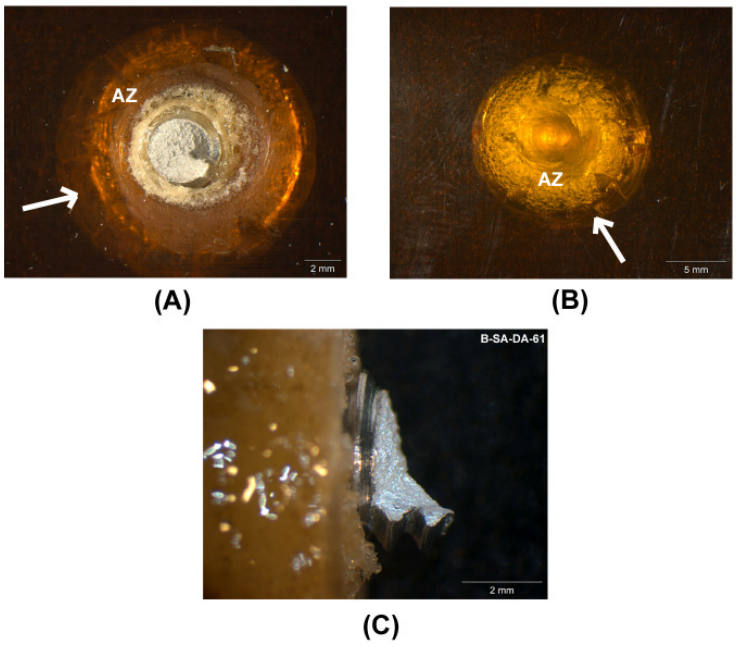

Figure 54. Example of a RE fracture type (TP-sample 8,0 bar). A) Top view of the fractured polymeric base plate, 18X. B) Bottom view of the fractured polymeric base plate, 12X. C) Close-up picture of the fractured rivet, 40X. In A) and B) AZ is the anchoring zone and arrows indicate the secondary stable cracking around AZ.

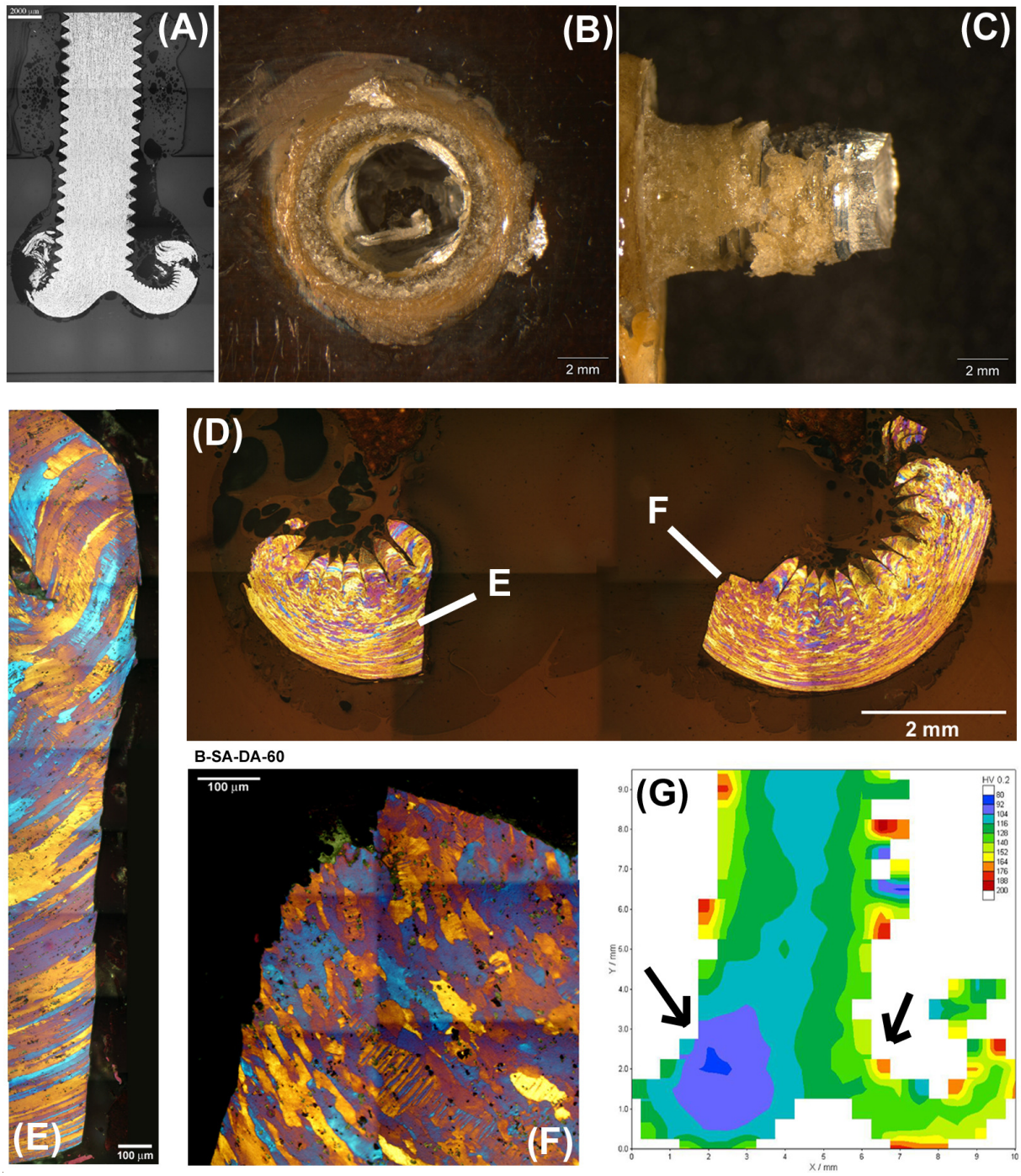

Figure 55. Example of a RI-fracture type (TT-sample 4,0 sec). A)Joint's cross section prior to testing,16X. B) Top view of the fractured polymeric base plate, 18X. C) Appearance of the fractured rivet, 18X. D) Cross section overview of the fractured polymeric base plate, 50X, Barker. E) Magnified view of the region E in D), 500X, Barker. F) Magnified view of the region F in D), 500X, Barker. G) Microhardness map from cross section macrograph in A); the black arrows indicate the crack initiation site in the AZ.

When AZ is not placed deep enough in the polymeric base plate in order to allow the involving polymeric volume to bear the tensile loading, there is an elevation in the strain concentration in the polymeric volume involving the AZ. Local critical stress intensity factor (K_{IC}) in the polymer is overcome and cracks nucleate simultaneously in several sites around the AZ. The crack propagates to the top surface of the polymeric base plate and the joint fails in a brittle way as

schematically represented in Figure 52A. An example for the BP-mode can be observed in Figure 57 and Figure 58.

Brittle fracture in glassy polymers, such as the PEI, normally involves a failure mechanism called “crazing” [113, 114,253]. Crazes are cracking precursor mechanisms; they are micro-fissures originated by microcavitation in high stress concentration areas, which leads to the formation of voids. Nevertheless, the coalescence of these voids is prevented by the stretching of fibrils from the bulk material. The fibrils prevent the widening of the crazes up to the point where their local mechanical strength is superseded and they brake down leading to unstable crack propagation. For a complete approach in crazing mechanisms refer to [253-255]. A scheme of the craze growth mechanism described above, as well as the surface appearance of a multi-crazed fractured PEI-polymer is illustrated in Figure 56.

Figure 57A shows the cross section of the BP type fracture mode prior to testing, where the crack nucleation points around the upper part of the AZ are indicated by white arrows. There are four different fractographic zones, which are typical of brittle failure in PEI plastics [115, 256]. The bottom of the AZ fractured region (region E, Figure 57 and Figure 58); the *initiation zone* or the rough whitened zone (region C in Figure 57 and Figure 58); the *mist zone* (region B_1, Figure 57 and Figure 58) and the smooth area or the *mirror/end zone* (region A, Figure 57 and Figure 58). In the AZ fractured region one observes roughly 50% adhesive and 50% cohesive fractures related, respectively, to the polymer-polymer interface (PHAZ-PTMAZ interface) and the polymer-metal interface (PTMAZ-AZ interface), as seen in Figure 57C and Figure 57D. The cohesive fracture zone is characterized by rests of bonded rough polymeric surface, where fracture probably took place in the weld line by tearing type yielding (localized ductile fracture) [257] of PTMAZ-PHAZ interface. Around the deformed rivet tip, one observes several crack nucleation sites, as illustrated in Figure 57E (region D); crack propagation direction was radial to the rivet shaft.

In the *initiation zone* or also named stable crack propagation zone, *river patterns,* which *are* typical structural features also found in fracture surfaces of brittle metals and ceramics [258], are present. River patterns in PEI are composed of ridges and microflow lines resultant from joining and reorientation of cleavage craze planes from different directions [115]. The river pattern coalescence direction points out the crack propagation direction. Ridges and microflow lines can be observed in Figure 58B (region C).

In Figure 58C (region B) the transition between stable and unstable crack propagation regime is observed; this transition is characterized by an increasing roughening of the fractured surface. In the Mist Zone (Figure 58D, region B_1) one finds the presence of the so called *patch patterns* (see also Figure 56), which are islands of protruded and recessed crazed material forming a complementary structure with their respective fractured half [259]. Patch patterns are

associated with the crack oscillation between the bulk-fibril interfaces during unstable crack propagation [255,260]. There is also the presence of elongated structures displaced parallel to the local crack propagation direction, called *hackles* (marked with a black arrow in Figure 58D). They are found in regions where a change from plain strain (triaxial tension state) in the deeper regions to plain stress (biaxial tension state) [261] takes place, when crack front nears the surface of the polymeric base plate.

The *mirror/end zone* (Figure 58E and F, region A) is composed of *end-banded structures* also known as *striation patterns* [259]. These nearly evenly separated patterns are perpendicularly positioned to the local crack propagation direction. Between bands (marked with black arrows positioned parallel to the image's diagonal in Figure 58E and Figure 58F) islands of crazed material (patch patterns) are seen. It is believed that cracking in this zone is connected with single crazing instead of multiple crazing as for the patch patterns. This assumption is based on the measurement of band's width for several polymers, which indicated that width is similar to the length of a single craze [259].

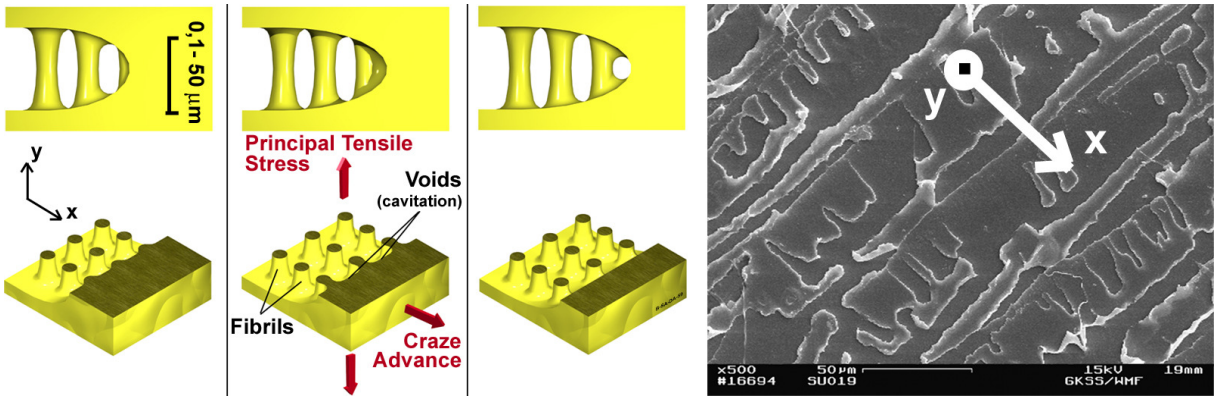

Figure 56. Scheme of crazing growth mechanisms showing cavitation of voids and stretching of fibrils from the bulk material. On the right-hand side of picture the representation of a cracked multi-crazed structure (patch patterns) where x corresponds to the crazing/crack propagation direction and y the direction of fibrils, 500X.

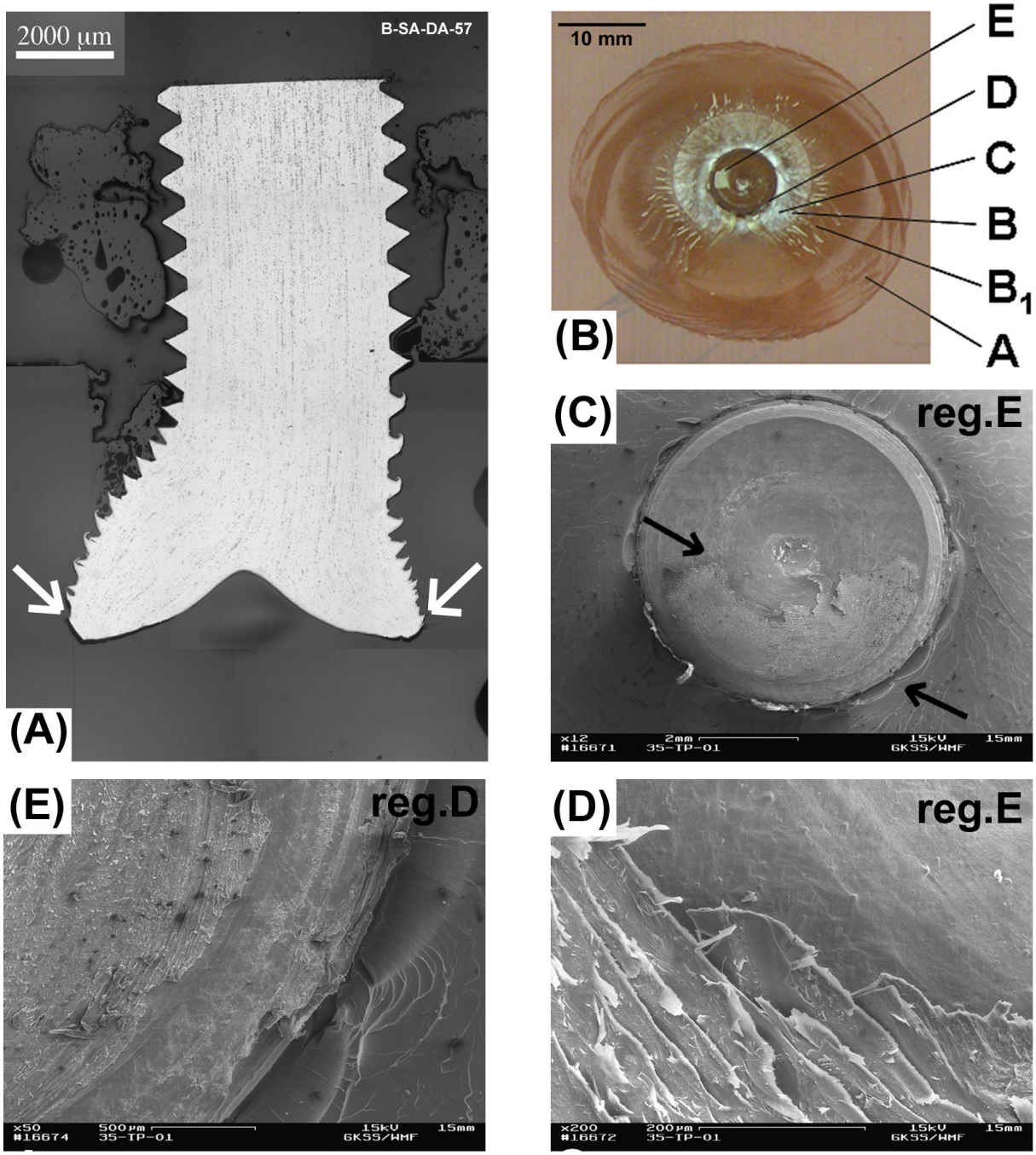

Figure 57. Example of a BP-fracture type (RS-sample 15000 rpm). A) Joint's cross section prior to testing,16X. B) Top-view of the fractured polymeric base plate with the studied fractographic zones marked in capital letters. C) BSE-SEM image showing the fractured AZ correspondent to the region E in B), 12X. D) Magnified BSE-SEM image of region E marked by the black arrow on the left-hand side of C); the polymeric roughened portion regarding the lower half of this picture is an example of cohesive fractured area in the polymer-polymer interface region (PHAZ-PTMAZ), while the upper half regarding the metallic flatter surface is an example of adhesive failure in the polymer-metal interface (PTMAZ-AZ), 200X. E) Magnified BSE-SEM image of crack initiation sites around the AZ (region D in B) correspondent to the place marked with the black arrow on the right-hand side of C), 50X.

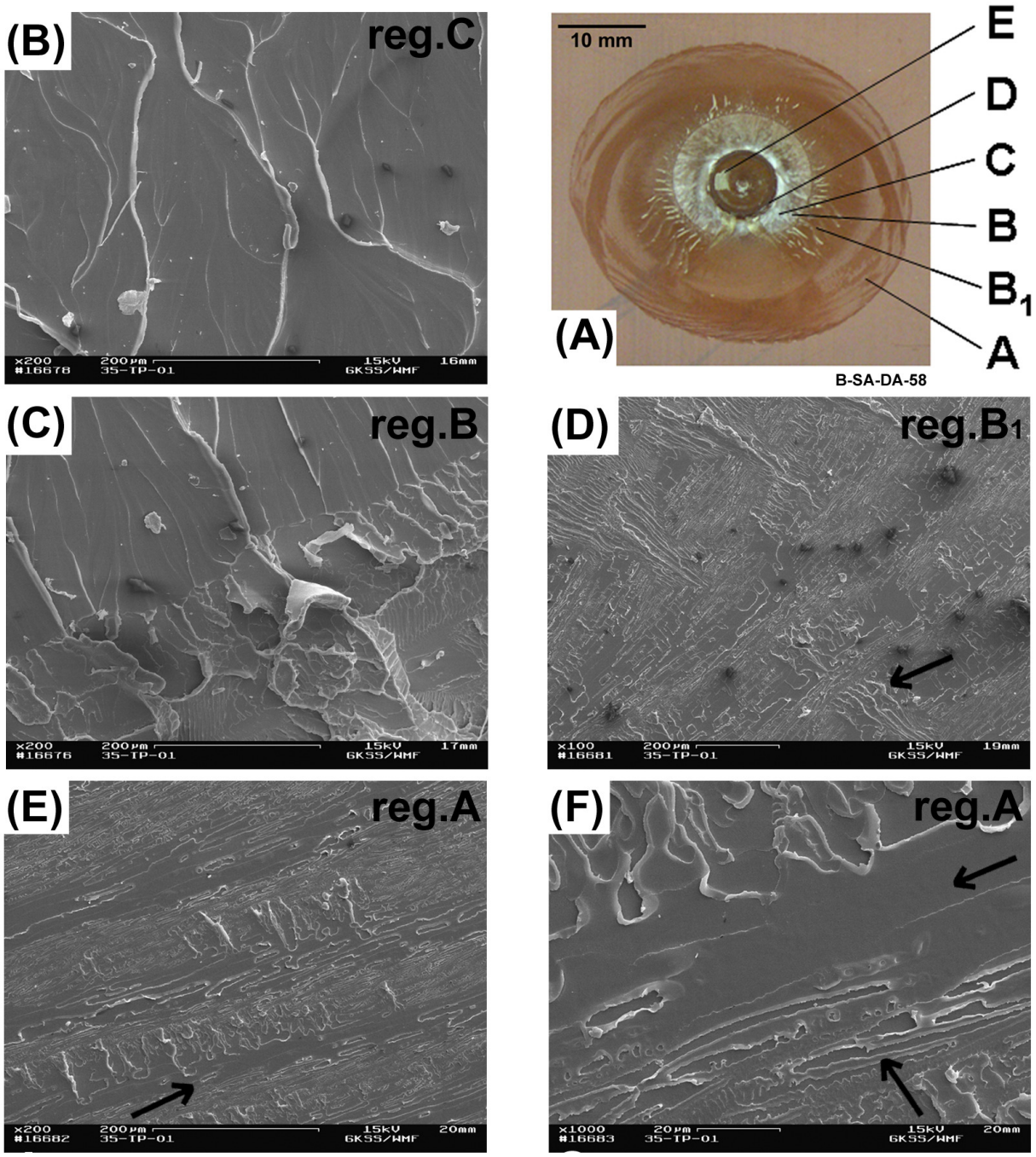

Figure 58. Continuation of Figure 57. A) Top-view of the fractured polymeric base plate. B) BSE-SEM image showing river patterns at the Initiation Zone (Region C in A) formed by ridges and microflow lines; the crack propagation direction follows the coalescence direction of ridges and microflow lines, 200X. C) BSE-SEM image from the transition area separating the stable-slow and unstable-fast crack propagation regimes, 200X. D) BSE-SEM image showing patch patterns and hackles (indicated by the black arrow) in the Mist Zone (region B_1 in A). E) BSE-SEM image of end-banded structures (striations patterns) with islands of patch patterns in the Mirror/End zone (region A in A); the black arrow marks the region magnified in F, 200X. F) Magnified BSE-SEM image of end-banded structures showing the transition between a flat band (marked with the upper black arrow) and the islands of crazed patch pattern material (marked with the lower black arrow), 1000X.

4.2.f. Process variables: heating time (HT), burn-off (BO), burn-off rate (BOR) and frictional torque (M_Z)

Establishing the influence of RS, TT and TP on heating time, burn-off, burn-off rate and frictional torque, by means of evaluating point-on-plate friction riveted joints, is very important in determining operating limits for friction riveting. As already discussed in Section 4.1.d, these four process variables are closely related to heat input, material plasticizing and flow, dictating joint quality and potentially indicating defective joints due to machine mal-function (in this last case given by M_Z). Figure 59A to Figure 59E provide these comparison results for PEI/AA2024-T351 joints.

Calculated HT results are seen in Figure 59A. As it was expected TT had the greatest influence on HT, whereby HT raises with TT. RS seemed also to elevate HT, although its influence is not as strong as in the case of TT. On the other hand an elevation of TP did not sharply change the HT. While in friction welding of metals HT is inversely proportional to TP [139, 262], in this combination of friction riveted materials HT seems to remain unchanged. From those results and considering that HT is assumed to be a direct representative of frictional heat input in the joint, TT and RS appear to induce to higher converted frictional energy than TP.

Figure 59B shows the curves for BO results. Here BO clearly increases with RS, TT and TP, with an accentuated influence of TP in comparison to RS and TT. These results were in accordance with insertion depth (*h*) and width of AZ (*w*), behaviour, as well as with the level of plasticizing in the AZ (see Figure 41A, Figure 41B and Figure 39B), which in turns confirms the importance of BO on rivet plasticizing and forging regimes (see Section 4.1.d). The behaviour of BO with RS, TT and TP in friction riveting is very similar as in spin welding of plastics [263-266], where BO is also involved with level of joining partner's penetration (insertion).

The influence of joining parameters on BOR can be found in Figure 59C. BOR also grows with RS, TT and TP. This is reasonable, since it is calculated from the quotient between BO and HT see Section 4.1.d). As in the case of spin welding, the BOR in friction riveting is directly proportional to these process parameters [86]; in other words the process speed is directly proportional to RS, TT and TP.

The average controlling plots of M_Z versus time are presented in Appendix 7. The values of M_z in Phase-III ($M_{Z\text{-III}}$) (steady state viscous dissipation phase, Figure 24A), and of M_z in Phase-IV ($M_{Z\text{-IV}}$) (rivet forging phase, Figure 24A), are seen in Figure 59D and Figure 59E.

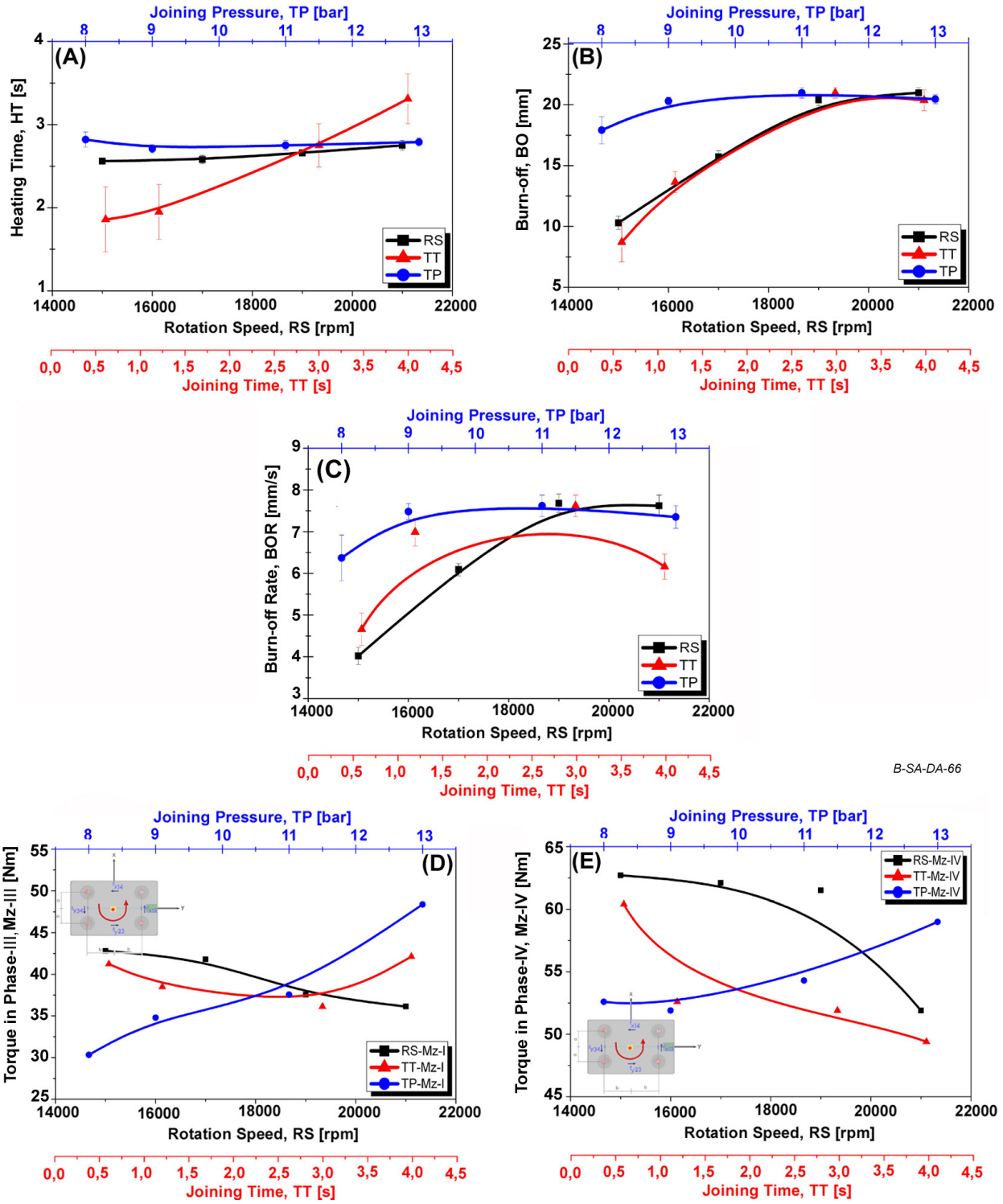

Figure 59. Results of the influence of process parameters on variables in the friction riveting technique. A) On heating time (HT). B) On burn-of, (BO). C) On burn-off rate (BOR). D) On frictional torque in Phase-III (steady state viscous dissipation phase) ($M_{z\text{-}III}$). E) On frictional torque in Phase-IV (rivet forging phase) ($M_{z\text{-}IV}$).

From the M_Z-results, one observes that $M_{Z\text{-}III}$ and $M_{Z\text{-}IV}$ decreases with RS and TT and increases with TP. An exception is found for TT sample 4,0 sec, where initial high temperatures instantly led to a drop in viscosity, so the molten film beneath the rivet tip is reduced in thickness, and a change in the frictional heating conditions is observed; this in turns lead to a decrease in

temperature (see Figure 32B) and associated increased viscosity (thus higher M_z due to opposite forces regarding rivet interaction with colder polymeric volumes, are measured). Measured $M_{Z\text{-}IV}$ was bigger than $M_{Z\text{-}III}$ owing to the higher set up FOP. Bearing in mind that $M_{Z\text{-}III}$ is a representative of softening/melting level in the PTMAZ and $M_{Z\text{-}IV}$ is straight changed by the level of plasticizing in the rivet tip during forging, the decrease of $M_{Z\text{-}III}$ and $M_{Z\text{-}IV}$ with increasing RS and TT results was expected. High values of TT and RS elevate temperature (see Figure 32D), decreasing the polymer's molten viscosity and increasing rivet tip plasticity, in other words reducing M_Z. Although higher values of TP also caused an elevation in temperature (see Figure 32D), the M_Z behaviour is more influenced by the outflow rate of molten polymer in the PTMAZ. The bigger the applied pressure, the higher the molten polymer outflow rate will be. This in turn reduces the molten film thickness in the PTMAZ, making the rotating rivet to be in contact with colder (high viscosity) polymer volumes, increasing frictional torque. This behaviour is also found in spin welding [86,150, 264, 266, 267] and friction welding of metals [140, 141, 262].

4.2.g. Heat input

The proposed analytical heat input model of friction riveting is demonstrated and further analysed in this section, where the results of the influence of RS, TT and TP on total heat input (Q_{total}) (Equation (28), Section 4.1.g) are investigated. For the calculation of viscosity, η (Equations (26) and (27), Section 4.1.g) some simplified assumptions had to be made. The friction coefficient, μ, was assumed as an average constant value of 0,4 (see Appendix 8), although it is known that for plastics such as PEI it decreases with increasing applied pressure, tending to constant values with time [182]. In addition it is well known that for plastics, temperature does not have a strong influence on μ, although this behaviour is usually dependent on structure [218]. In order to evaluate the temperature sensitivity effect on η, without artificially lowering the molten viscosity by lowering η_0 (Equations (27), Section 4.1.g) temperature (T) was kept constant at 400 ^{o}C, an average value corresponding to actual PEI-processing temperatures [101] (see Appendix 8).The other PEI-constants used in the calculation of η are also found in Appendix 8.

Additional required simplifications in order to overcome difficulties associated with the experimental determination of some variables were: the normal pressure distribution ($P(r)$) on the rubbing area (A), the width of the molten zone (H), the maximal tangential velocity (V_{max}) were taken as constants, respectively, from the friction pressure (FP), from an average measured value of 1 mm, and from the calculation with the maximum radius (the external rivet radius). Finally, the maximal axial speed was adopted from the burn-off rate values (BOR) presented in Figure 59C. The single calculated contributions for Q_{total} for the produced samples are presented in Table 16 and the calculated values of Q_{total} are plotted in Figure 60.

Table 16. Calculated values of heat input from frictional (Equation (19) and (22), Section 4.1.g) and normal force (Equations (23) and (25), Section 4.1.g) contributions on the total heat input (Q_{total}) (Eq. (28), Section 4.1.g). For TT-samples, Q_{total} is also provided in W.s/mm^2 units for comparison issues.

Sample	Q_{fr}^{sol} (W/mm^2)	Q_{ax}^{sol} (W/mm^2)	Q_{fr}^{visc} (W/mm^2)	Q_{ax}^{visc} (W/mm^2)	Q_{total} (W/mm^2 ; W.s/mm^2)	
15000 rpm	0,419	0,002	4,091	0,002	4,514	
17000 rpm	0,475	0,002	5,186	0,004	5,668	
19000 rpm	0,531	0,003	6,398	0,006	6,938	
21000 rpm	0,586	0,003	7,724	0,006	8,320	
0,6 s	0,586	0,002	7,724	0,003	8,315	15,466
1,2 s	0,586	0,003	7,724	0,005	8,319	16,221
3,0 s	0,586	0,003	7,724	0,006	8,320	22,879
4,0 s	0,586	0,002	7,724	0,004	8,317	27,530
8,0 bar	0,367	0,002	7,724	0,005	8,097	
9,0 bar	0,440	0,002	7,724	0,006	8,172	
11,0 bar	0,586	0,003	7,724	0,006	8,320	
13,0 bar	0,733	0,004	7,724	0,006	8,467	

T-SA-DA-15

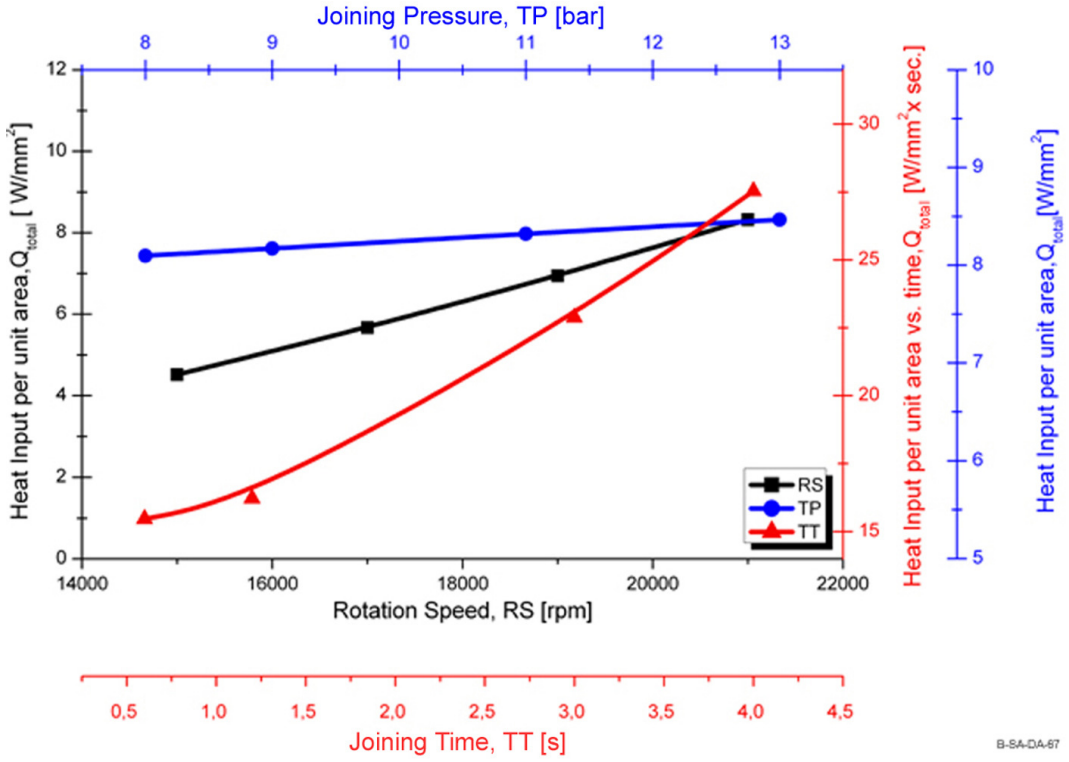

Figure 60. Influence of RS, TT and TP process parameters on the total heat input, Q_{total}, for comparative samples.

In Table 16 and Figure 60 the values of Q_{total} for TT-samples are also provided in terms of energy per unit area, multiplied by unit time (W x s x mm^{-2}). The proposed heat input model determines Q_{total} in terms of energy per unit area, (see Equation (28), Section 4.1.g). Without considering the influence of time, the only varied parameters in the case of TT comparative samples, Q_{total} remains approximately unchanged (about 8,3 W x $mm^{-2,}$ see Table 16). In order to study the real influence of time on the TT-samples, Q_{total} was additionally obtained through multiplying results calculated from Equation (28), Section 4.1.g, by the HT-values (see Figure 59A), a representative of the actual joining duration.

As one can observe in Figure 60, the theoretical heat input data increases with increasing RS, TT and TP; nevertheless, Q_{total} seems to be differently influenced by each single process parameter. From the curve inclinations it can be observed that the Q_{total} increasing rate is steeper for TT-samples, milder for RS-samples and smaller for TP-samples (staying almost unchanged for TP-samples) in this experimental working range. The obtained theoretical Q_{total} behaviour is in accordance with HT-trend to RS, TT and TP, as presented in Figure 59A, which suggests a good model correlation with the experimental data.

Finally, the results presented in Table 16 led to a very important observation. The normal force contributions ($Q_{ax}^{sol}, Q_{ax}^{visc}$ calculated by Equation (23) and Equation (25), Section 4.1.g) on Q_{total} are very small in comparison to frictional contributions ($Q_{fr}^{sol}, Q_{fr}^{visc}$ calculated by Equation (19) and Equation (22), Section 4.1.g), the former assuming average values in order of 0,03% and 0,06%, while the latter average values in order of 99,0% of Q_{total}. Moreover, Q_{fr}^{visc} is in average much higher than Q_{fr}^{sol} (approx. 93% and 7% respectively), showing that the most important mechanism in heat generation in friction riveting happens by internal shearing in the molten polymer (phases P-II and P-III, Figure 24A). This new paradigm calls for an important modification in Q_{total} (Equation (28) of Section 4.1.g), where its second term related to the normal force contributions can be ignored, resulting in the new simplified Equation (30) for the friction riveting analytical model:

$$Q_{total} = \left[\left(\frac{2}{3}\cdot\mu\cdot P(r)\right)+\left(\frac{\eta\cdot V_{\max}}{H}\right)\right]\cdot V_{\max} \quad \left[W/m^2\right] \tag{30}$$

whose variables were described in Section 4.1.g.

Although a limitation of this analytical heat input model is the possibility of only having total average values instead of local heat input values, the proposed model can be further used for temperature regime modelling. In practice a simplified analytical model is very attractive for process optimization, considering that complex mathematical models usually require complex

input data, as well as special programming routines, while in the former case it can be normally implemented by taking simple experimental input data and easily worked within simple statistical data processing software.

4.3. Friction riveted overlap joints

4.3.a. PEI/AA2024-T351 overlap joints

Overlap joints of polymer-metal hybrid structures constitute a very important class in mechanically fastening. Particularly in aircraft structures, mechanically fastened joints play a central role in multi-material components [17], where structural applications require often load transfer in the fastener by shear [268]. In Section 4.2.e, the tensile properties of the friction riveted joints were demonstrated. Additionally to that, the lap shear strength (LSS) of the case study joints on PEI/AA2024-T351 is evaluated in terms of short term (Section 4.3.b) and long term behaviour (Section 4.3.c) in the current section.

The case study “overlap joints” consisted of single-riveted (extruded aluminium AA2024-T351, ∅ 5mm, presented in Section 3.2.b), 5 mm thick PEI-plates (for material description see Section 4.2.c). Based on acquired joining know-how for point-on-plates joints, an experimental process window was designed in order to establish optimized process parameter ranges where good quality overlap joints in terms of volumetric defects and AZ-anchoring could be obtained. The tested joining parameter range was: RS= 19000 – 21000 rpm; TT= 3,0 – 4,5 s and TP= 8,0 – 11,0 bar. Appendix 9 presents the detailed process parameter table for the investigated samples. Within this range of joining parameters, all joints were formed, although with different quality level. Appendix 10 shows the cross section macrographs of samples presented in Appendix 9. The joints with the lowest visual amount of defects plus the greatest *h* and *w* levels were within following ranges: RS= 21000 rpm; TT= 3,0 – 4,5 sec and TP = 8,0 bar; they corresponded to samples PEI2000.51, 60 and 61 (see Appendix 9 and 10). Considering that the visual amount of volumetric defects in the PTMAZ of these samples was comparable, so PEI200.51, the sample with the biggest *h* and *w* values, was chosen for further mechanical characterization. Figure 61 illustrates the optimized samples and their measured *h* and *w*.

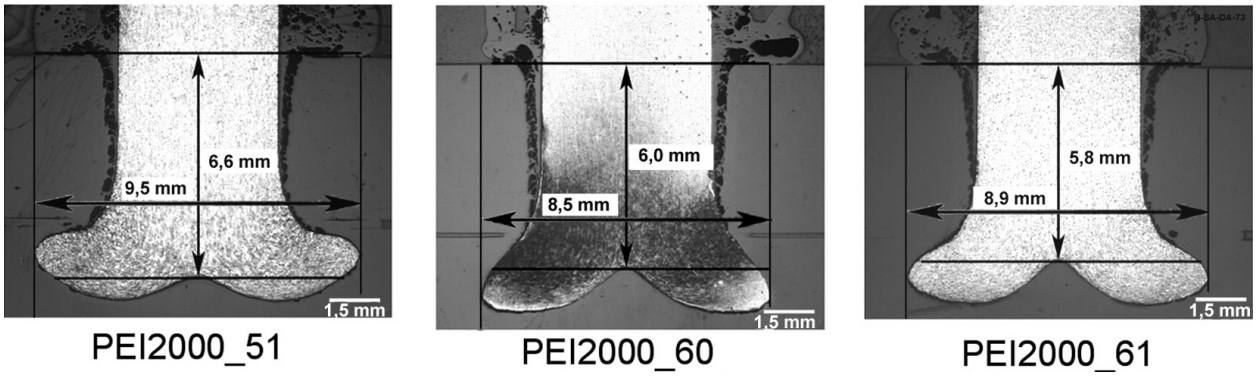

Figure 61. Single-rivet friction riveting joints on PEI/AA2024-T351 (extruded rod), for the optimized joining parameters range. PEI2000.51 was chosen for further mechanical characterization.

4.3.b. Lap shear strength (LSS) of friction riveted overlap joints

The testing procedure and sample geometry for determining LSS, were in accordance with testing procedure described in Section 3.1.f. Results in the current section are provided as the average of at least four experiments. LSS-samples were designed for allowing bearing failure type (compressive forces acting on the border of the hole in contact with the rivet, which crush polymeric material) in the polymeric base elements, which is desired in the mechanical fastening of aircraft structural polymeric matrix composite applications, due to its non-catastrophic nature (occurring progressively with load) [268, 269]. Owing to the stress concentration created by the presence of a hole around the rivet, fracture normally takes place in the polymeric material instead of in the metallic rivet, which strongly decreases the overall joint efficiency [17]. Figure 62 illustrates the course of a typical LSS-test. Usually this sort of test (Bearing Test) is stopped when R_m is reached and a drop of about $0,3*R_m$ is observed, in order to avoid rupture and masking of the true failure mode [270]. Nevertheless, in this study tests were carried out up to rupture, aiming to understand the complete behaviour of friction riveted overlaps under quasi-static loading.

Initially, the joint deforms only elastically (Figure 62A), displaying a linear increase on the stress-strain curve. When plastic deformation begins by bearing at the upper and lower polymeric plate, the curve deviates from linearity and yielding takes place, although without a clearly defined transition point (Figure 62B). After achieving its maximum (at R_m), stress starts dropping to the moment when upper and lower polymeric plates are detached from each other and joint failure takes place (Figure 62C). Just after their detachment, plates slip away a couple of millimetres from each other and then get stuck. This sudden stop leads to a new increase in the stress-strain curve, until the load becomes too severe and catastrophic net-tension failure mode substitutes bearing and rupture takes place in the lower polymeric plate (Figure 62D). A detailed view of a typical ruptured LSS-sample is shown in Figure 63.

The average LSS-results for the mechanical and the laser extensometers are presented in Table 17. Calculations followed the standard procedures of [270] and examples of stress-strain curves for both extensometers with the graphical estimations of the offset lap shear strength at 2,0% strain ($R_{2.0\%}$) (standard representative yielding point for LSS samples), lap shear strength, (R_m) and strain at R_m (ε_m), are found in Appendix 11. From Table 17 one can observe that both results measured by mechanical and laser extensometry are comparable, indicating that no plane rotation around axial rivet direction happened. The average total values, $R_{2.0\%}$ = 75,1 ± 0,7 MPa, R_m = 77,5 ± 0,1 MPa and ε_m = 6,4 ± 0,6 % suggest good mechanical performance of this overlap joint. Although no comparison data on mechanical fastening of PEI were found in the available literature, the joint efficiency of ca. 70% in terms of R_m, in comparison to polymer tensile strength can be considered positive. The decrease in strength of polymeric fastened joints is due to stress concentration associated with the rivet role [48]. Nevertheless in friction riveting the fastener (rivet) does not have to go through the whole joint thickness, a reduced notch-effect in the polymeric base plates is present and an improvement in joint efficiency may also take place comparing to traditional mechanically fastened joints; nonetheless this comparison, which is out of the scope of this study, must still be checked.

Besides, the joint strength of friction riveted overlap joints may be further improved by installing nuts or collars on the free length of the rivet over the upper polymeric plate. It has been reported that the so-called “clamp-up” compressive forces through the thickness of the polymeric base plate is increased by nuts or collars, so the joint static and fatigue strength of the hybrid polymer-metal joint can be improved [271].

Table 17. Average LSS-properties of friction riveted PEI/AA2024-T351 overlap joints calculated according procedure presented in Section 3.1.f.

LSS Properties	$R_{2,0\%}$ (MPa)	R_m(MPa)	ε_m(%)
Avg. Mech. Extensometer	75,6	77,4	6,8
Avg. Laser Extensometer	74,6	77,5	6,0
Mech./Laser Mean	75,1	77,5	6,4
Experim. Error	0,7	0,1	0,6

T-SH-DA-17

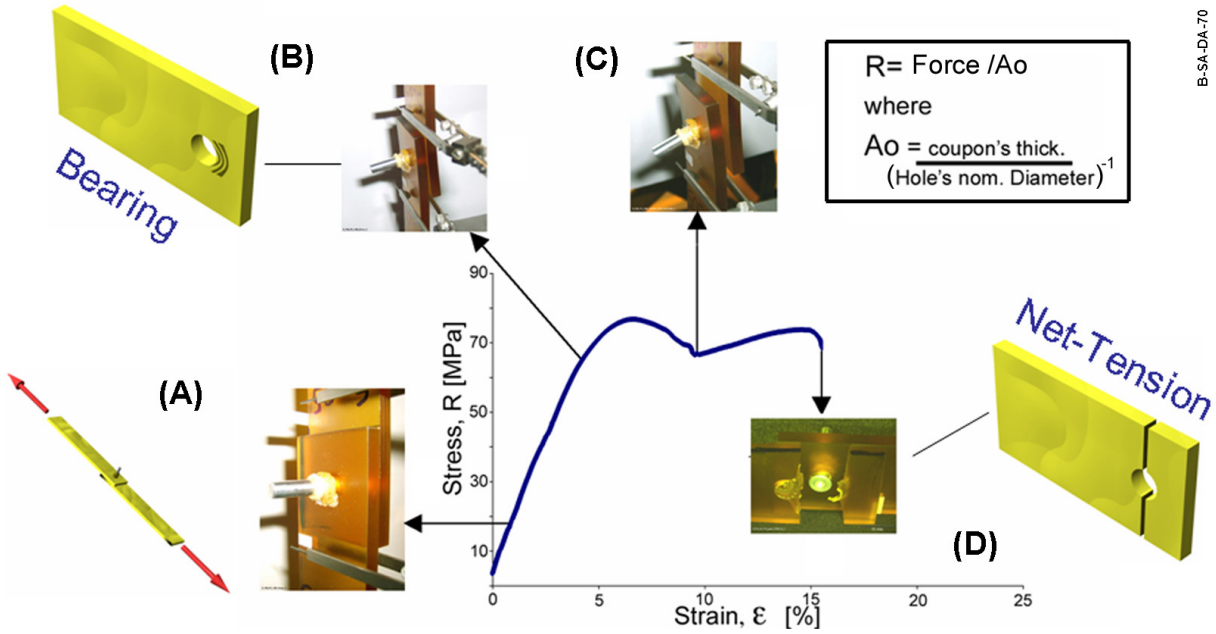

Figure 62.Example of a typical engineering stress-strain curve in a friction riveted overlap joint on PEI/AA2024-T351. A) Beginning of the test. B) Yielding of the joint (bearing). C) Joint actual failure (detachment of polymeric plates). D) Catastrophic final rupture (net-tension).

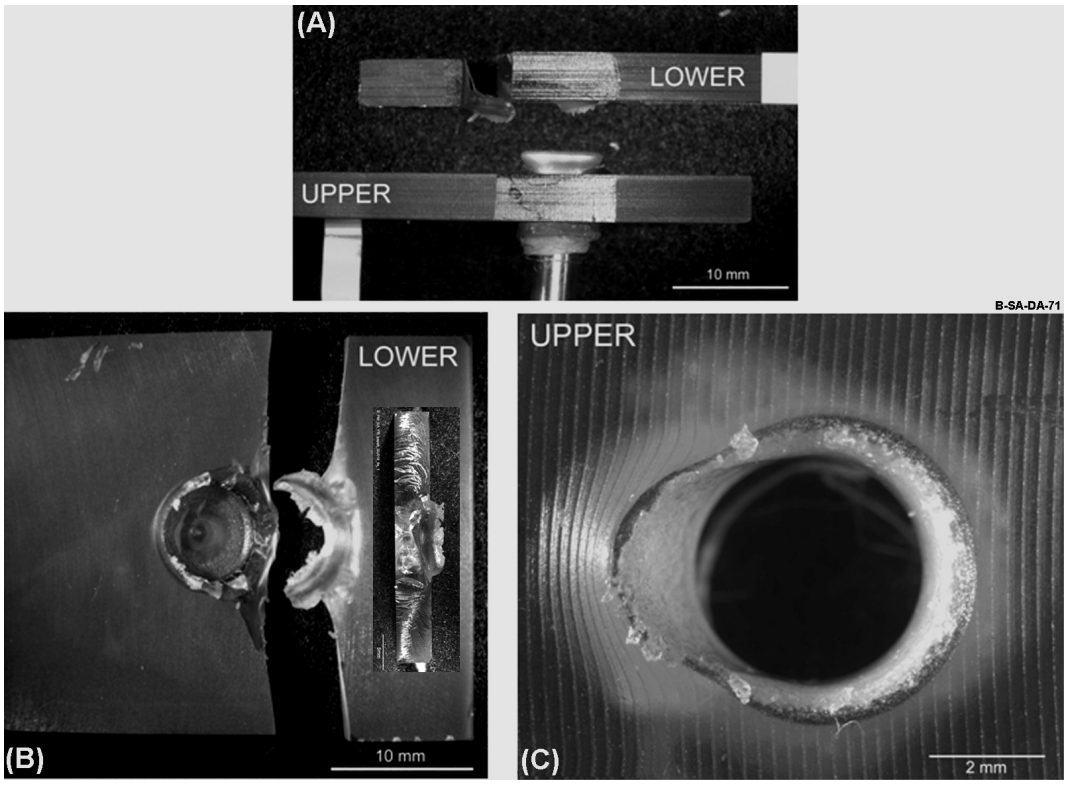

Figure 63. Example of a fractured LSS-sample. A) Side-view, 6X. B) Main-photo: top-view of the lower polymeric plate, with net-tension failure mode as main rupture mechanism, 6X. The detail-photo shows the front view of the cracked half on the right-hand side of main-photo, 9X. C) top-view of the upper polymeric-plate with bearing as the main failure mode 18X.

4.3.c. Stress relaxation of friction riveted overlap joints

Mechanically fastened joints in polymers and polymeric composites can be directly affected by the chain relaxation phenomenon associated with the viscoelastic behaviour of the polymer partner. Undesirable side effects can take place when these joints are placed either under a constant force or deformation. Reduction in fastener tightness (the joint sealing force) and clamp-up force are examples of such negative phenomena [169, 271]. Under constant force testing, the creep properties of the joint are evaluated, while under constant deformation, the stress relaxation properties (the time-dependent decay of stress [272]). Polymeric time-dependent properties, or the viscoelastic behaviour, correspond to mixed mode of elastic and viscous behaviour; while metals can be considered elastic materials (100% deformation recovering), high molecular polymers (plastics) have an important viscous deformation component in addition to the elastic one [251].

Stress relaxation or the disentanglement of chains (for extra information on chain entanglement theories, refer to [146]) in polymers can be represented by the simplified mathematical Maxwell Model [251, 273, 274] composed of a Hookean spring (elastic component) with stiffness modulus, E, connected in series with a viscous dashpot with viscosity, η. This is schematically illustrated in Figure 64.

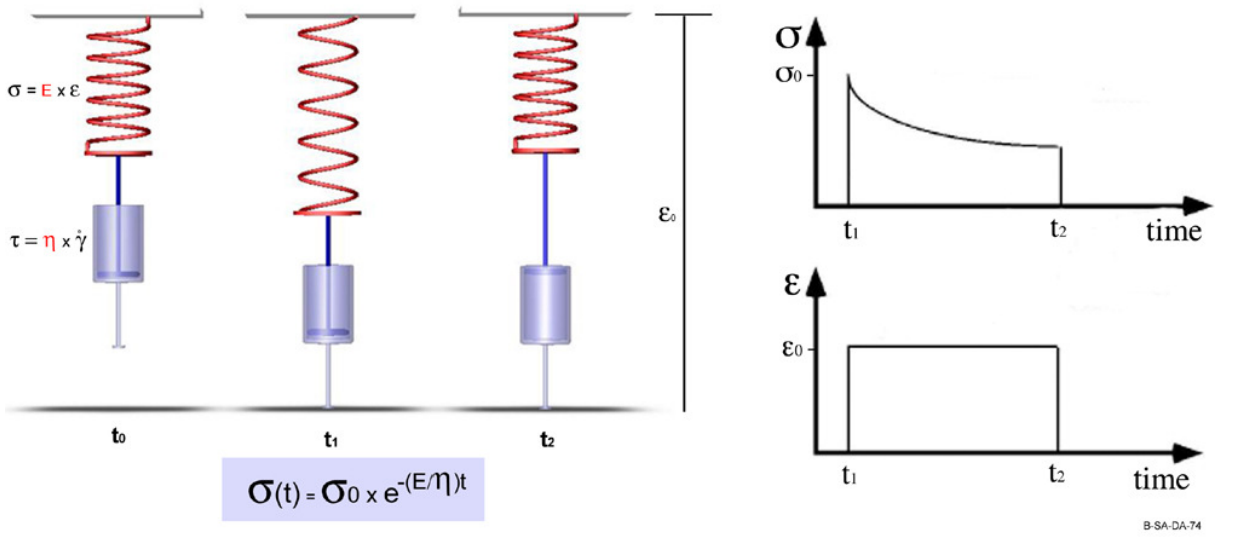

Figure 64. Maxell Model for viscoelastic stress relaxation in plastics. Symbols: σ, is the stress η, the viscosity, τ the shear stress, γ the shear rate, ε the strain and t the time.

Initially, a constant deformation, ε_0 is applied (t_1); the initial deformation fully takes place in the spring element. When time goes on, the dashpot starts to relax and the spring retracts, or in other words the stress decays with time (t_2). The Maxwell Model is represented by an exponential decay [272] given by the equation presented in Figure 64.

Stress relaxation of single-rivet friction riveted joints on PEI/AA2024-T351 was tested in accordance with experimental procedures described in Section 3.1.g. Three different constant deformations, ε_0 = 4,0%, 6,0 % and 8,5% were applied and three specimens tested for each condition at room temperature. Average stress relaxation data is presented in Figure 65. In Figure 65A the results of the time-dependent stress decay (*R(t)*) is shown; in Figure 65B, the calculated stress relaxation modulus (*E(t)*) is presented. The ε_0 conditions were chosen to cover the complete stress-strain behaviour of LSS-samples (see Figure 62), where 4,0% lays in the elastic-linear portion, the 6,0% near to ε_m (see Table 17, Section 4.3.b) and 8,5% prior to joint detachment (see Figure 62).

As expected, increasing ε_0 resulted in higher initial stresses and increased time-dependent stress decay rates, as can be seen in Figure 65A. The initial values of calculated time-dependent modulus (E(t)) on the other hand, diminished with increasing ε_0, as it was also expected; nevertheless, a marked trend in the E(t) decay-rate with ε_0 was not observed. Tests were halted prior to failure and examples of side-views of samples after testing are presented in Figure 66. Note the elevation in the detachment level with increasing ε_0.

Although no available literature data on stress relaxation of PEI could be obtained for comparison purposes, these results have shown the importance of the viscoelastic recovery in metal-polymer multi-material structures. It also provided basic design data for real applications. For further information on viscoelastic behaviour (creep properties) of the PEI-base material used in this work can be found in [275].

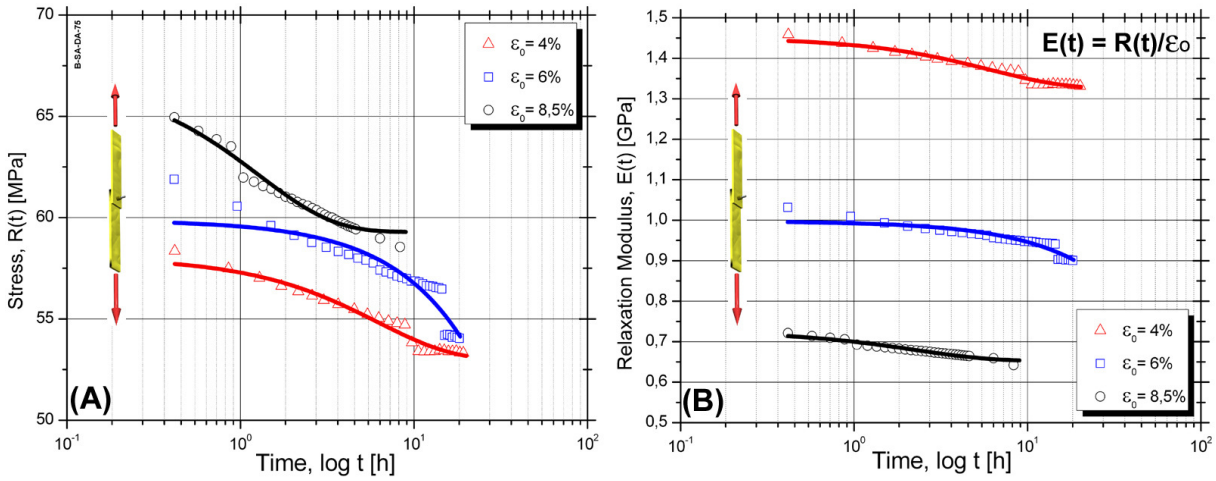

Figure 65. Average results of stress relaxation testing for single-rivet friction riveted joints on PEI/AA2024-T351. A) time-dependent stress decay. B) Calculated time-dependent stress relaxation modulus behaviour.

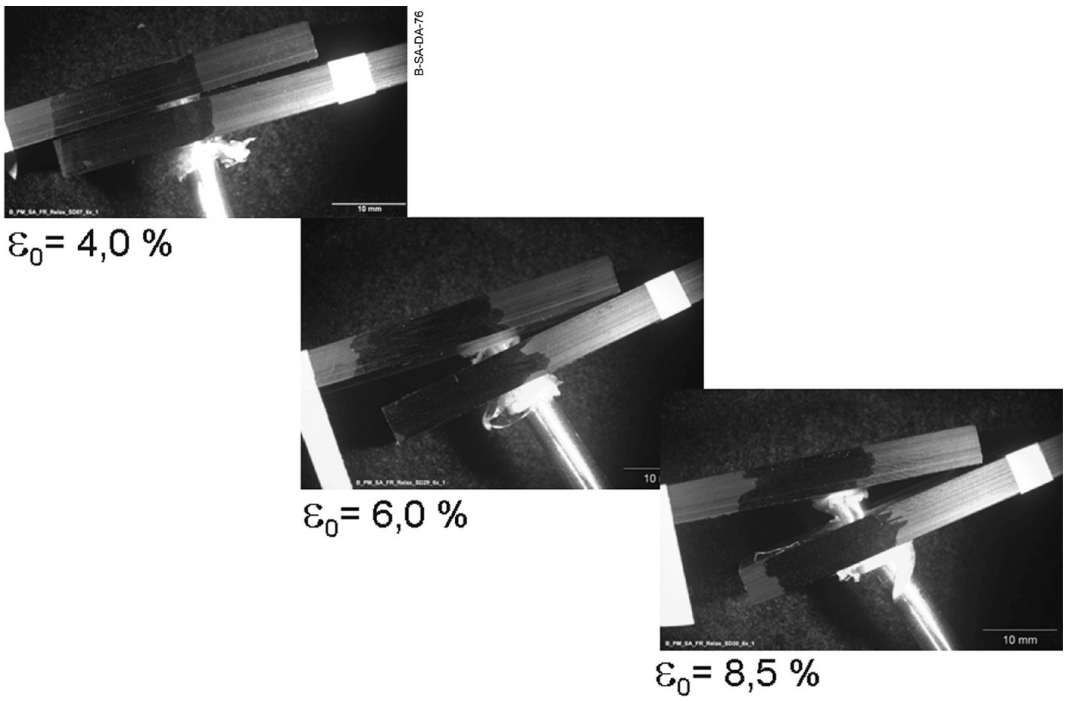

Figure 66. Example of tested stress relaxation samples in this study (PEI/AA2024-T351 overlap joints).

5. SUMMARY OF RESULTS, CONCLUSIONS AND FINAL REMARKS

Bearing in mind the main goals of this work presented in section “Objectives”, which were to develop, demonstrate and characterize the new Friction Riveting joining technique, the results of analysis and experiments carried out in this work provide the following conclusions:

- The selected combination of base materials PEI and aluminium AA2024-T351 were successfully joined in two different joint geometries (“point-on-plate” joints in Section 4.2.a and overlap joints in Section 4.3.a) by friction riveting, where both geometries exhibited good mechanical joint efficiency in comparison to base materials (for point-on-plate joints the tensile strength joint efficiency in terms of the strongest base material AA2024-T351, F_M/F_M 2024-M5, varied in the approximate range of 60% ≤ F_M/F_M 2024-M5 ≤ 93%, and overlap joints with lap shear strength joint efficiency in terms of polymeric coupon tensile strength of roughly 70%, respectively, presented in Section 4.2.e and Section 4.3.b).

- The physical description of the process proposed in Section 4.1.e, where friction riveting is divided into 5 phases, was supported by temperature and M_Z results (presented in Sections 4.2.b and 4.2.f), whose behaviour was in accordance with the proposed physical explanation on frictional regime, thermal history, polymeric melting and metal plasticizing schema, as well as the forging phase.

- The theoretical behaviour of the main process parameters RS, TT and TP and variables HT, BO, BOR, temperature and Mz described in Section 4.1.d, were confirmed with experimental observations: RS, TT and TP were directly involved in temperature development (Section 4.2.b) and related thermo-mechanical phenomena (rheology of molten viscosity, metal plasticizing, volumetric defect formation, thermal degradation, as presented in Sections 4.2.b, 4.2.c and 4.2.d). The process variable HT could be directly correlated with heat input as experimentally shown in Sections 4.2.f and 4.2.g. A correlation between BO/BOR, rivet insertion depth (*h*), rivet width (*w*) (*h* and *w* resembling the AZ deformation level) and rivet plasticizing level was demonstrated in Section 4.2.f. As it was expected temperature behaviour (Section 4.2.b) could be correlated with rheology of molten polymer, polymer thermal degradation and volumetric defect formation, plasticizing level and microhardness (see results from Sections 4.2.c, 4.2.d and 4.2.f); nevertheless, a direct correlation with heat input was not observed (see Section 4.2.g), due to the low polymer thermal conductivity, whose effect inhibits heat dissipation leading to increasing temperatures, although heat input may remain unchanged. Finally M_z-results showed the importance of this variable on rivet plasticizing estimations (Section 4.2.f).

- The proposed joining mechanisms involving structural changes in friction riveting (Sections 4.1.e and 4.1.f) were confirmed by extensive investigations on microstructural features of PHAZ, PTMAZ, MHAZ, MTMAZ and AZ, as well as on microhardness and amount of polymeric thermal degradation (joint local mechanical behaviour) as presented in Section 4.2.d.

- The proposed analytical model presented in Section 4.1.g was experimentally demonstrated in Section 4.2.g. The initial general formulation for total heat input (Q_{total}) given by Equation (28), considered both frictional and normal force contributions (respectively Q_{fr} and Q_{ax}). After heat input validation results indicated that the Q_{ax} contribution to Q_{total} is actually very small (only in the order of 0,1%) Equation (28) was finally rearranged, by dismissing its second member associated with Q_{ax}, resulting in the new Equation (30), where the main source of heat is frictional heating. Additionally, the frictional contribution during the solid friction (Phase P-I, Section 4.1.c) was about 7%, whereas the frictional contribution during molten friction (Phases P-II and P-III Section 4.1.c) was about 93% of Q_{fr}. From this one can conclude that heating develops mainly due to internal shearing in the molten polymer of PTMAZ.

-The influence of process parameters RS, TT and TP on variables was presented in Section 4.2.b to 4.2.g. The summarized conclusions for each variable studied in these joined materials combinations are given below:

Temperature: the results of thermometric and thermographic temperature measurements have shown that increasing RS, TT and TP also yielded increasing temperatures (Figure 31 and Figure 32), where distance to the heat source dependence of temperature was markedly due to the low polymer thermal conductivity. For the analysed materials combination temperature in the PHAZ was within 30-65 ^{o}C, in the PTMAZ within 300-500 ^{o}C and less than 200 ^{o}C in the rivet free length near to the upper surface of the polymeric base plate (Figure 34). Additionally, the calculated heating rate (HR_{TLo1}), which is also important for controlling the nucleation of volumetric defects [276] increased with RS, TT and TP. An exception of these increasing temperature behaviour was observed for TT sample 4,0 sec (the severest joining condition for TT samples) in Figure 31 and Figure 32, where a change in the frictional conditions supported by too extreme initial local temperatures leading to a sharp drop in viscosity, reduction in the molten film thickness in the rubbing area and to a associated reduction of local temperature, was the most probable identified cause .

Microstructure: The presence of volumetric defects in the PTMAZ determined by the ratio V_d/V_{PEI} was found to increase with TT and TP but remained roughly unchanged for increasing RS values (Figure 39A). Although the RS caused an increase in the average temperature, heat input (or local temperature) was not severely changed for this RS working parameter range, as has been shown by the low level of thermal degradation (Figure 50E and Figure 50F), so almost no variations in the volumetric defect amount was observed (Figure 39A) in comparison to

V_d/V_{PEI} in TT- and TP-samples. The deformation level in the paraboloidal volume of AZ evaluated by the ratio V_{Riv}/V_{PEI}, *w* and *h* grows with RS, TT and TP (Figure 39B, Figure 41A, Figure 41B, respectively). The metallic joint microstructure was modified by temperature or/and mechanical deformation being annealed by static and dynamic recovery (in the MHAZ and MTMAZ), and by dynamic recrystallization nucleated by deformation bands (partially in the MTMAZ) as shown in Figure 42 and Figure 43. RS was the only parameter that seems to change the amount of recrystallized grains, which increase with the parameter, while increasing TT and TP did not strongly modify the metallic microstructure in this working parameters range (Figure 44).

Microhardness: Increments in RS, TT and TP induced a general microhardness drop in the MHAZ and MTMAZ regions (Figure 45) due to annealing phenomena, as commented above. However, a trend in microhardness decrease was only identified for increasing RS, which confirms the visual trend in raising the amount of dynamically recrystallized grains with this parameter. In the case of polymer microhardness in the PHAZ and PTMAZ an overall increase could be observed, most likely associated with physical ageing and/or decreased plasticizing thanks to structural water elimination (Figure 46). Nevertheless, neither a dependence of microhardness on RS, TT and TP, nor the precise transition interface between PHAZ and PTMAZ could be defined by this technique. The adopted experimental indentation force (0,98 N) may be too high for the investigated polymer, so the polymer microhardness results should be regarded as qualitative. Nanoindentation testing (with forces in the micro Newton scale) might help for better solving polymer microhardness of friction riveting joints, by inducing lower plastically deformed volumes around the indentations.

Thermal Degradation: Considering the high measured average temperatures within the range of the early stage of PEI thermal degradation temperature (≅ 520 °C), where chain scission is the main degradation mechanism [277], thermal degradation took place, as confirmed as by GPC-results (Figure 50). The broadening of MWD-elugrams to the right-hand side of base material MWD plus the decrease in peak values of normal MWDs (Figure 50A, Figure 50C and Figure 50E) were an indicative of chain scissioning. The dependence of MW with RS, TT and TP was determined by the normalized M_n/M_{nPEI} and M_w/M_{wPEI} molecular weights, showing a decreasing trend with increasing these parameters (Figure 50B, Figure 50D and Figure 50F). The induced maximal MW decrease followed the ordering TP > TT > RS (TP: Mn=-18%, Mw =-26%; TT: Mn= -8,5%, Mw=-10,5%; RS: Mn=-5%, Mw=-10%), what may suggest that present volumetric defects in RS-samples (Figure 36 and Figure 39A) are mainly thanks to volatile evolution (Section 4.1.e), while for TT and TP samples, respectively, a mixed thermal degradation-volatile evolution and dominant thermal degradation volumetric defect nucleation regimes. Although the percentage of MW decrease measured in this study may deteriorate local mechanical performance (in addition to the influence of microhardness decrease), this remained within the

range where PEI global mechanical performance is independent from MW [278]. As expected the resultant MW decrease did not directly affect global mechanical performance of friction riveted joints in this study (Section 4.2.e).

Tensile Strength: The analysis of T-pull tensile testing presented in Section 4.2.e helped establishing the parameters influencing tensile strength. The comparison of joint efficiencies in terms of maximum force ($F_M/F_{M\ 2024\text{-}M5}$) and fracture strain ($\varepsilon_r/\varepsilon_{r\ 2024\text{-}M5}$) (Figure 51C and Figure 51D) with volumetric defects content (V_d/V_{PEI}, Figure 39A) and thermal degradation amount (M_n/M_{nPEI} and M_w/M_{wPEI}, Figure 50) have shown that tensile strength is not directly influenced by these parameters. Nonetheless, tensile strength appears rather to be controlled by AZ-geometry, where high measured strength joint efficiencies are normally associated with high *h* and *w* and more uniform AZs (as for instance for TP-samples 8,0 bar and 9,0 bar with $F_M/F_{M\ 2024\text{-}M5} \cong 93\%$, $w \cong 9{,}0/10{,}5$ mm and $h \cong 7{,}0/7{,}5$ mm, respectively, in Figure 51C and Figure 41). Three types of failure modes were identified for T-pull tensile specimens in this combination of materials (Figure 53, Figure 54, Figure 55, Figure 57 and Figure 58): the ductile fracture in the extern rivet shaft portion, RE-type, for samples where AZ efficiency is high so fracture takes place in the metallic member; the brittle fracture in the internal rivet shaft, RI-type, when medium AZ efficiency or defective (cracked) AZ are observed and the brittle failure in the polymeric base plate, BP-type, in the case where AZ-anchoring is present but *h* is small. Joint Strength ($F_M/F_{M\ 2024\text{-}M5}$) and ductility (represented by $\varepsilon_r/\varepsilon_{r\ 2024\text{-}M5}$) increased with RS and TT (as AZ-anchoring efficiency increased) and decreased with TP (as AZ-anchoring efficiency decreased) as presented in Figure 51C and Figure 51D.

The influence of RS, TT and TP on process variables and properties is summarized in Table 18. The symbol “+” stays for “increasing” and the symbol “-“ for “decreasing”.

- Single rivet overlap joints on 5mm PEI plates and ∅5mm AA2024-T351 rivets, were successfully achieved, showing an optimized working parameter range of RS= 21000 rpm; TT= 3,0 – 4,5 s; TP= 8,0 bar. Static mechanical properties of friction riveted overlap joints were evaluated by lap shear tensile testing, and analysed in terms of lap shear strength results (LSS) ($Rm \cong 77{,}5$ MPa, $R2{,}0\% \cong 75{,}1$ MPa, $\varepsilon_m \cong 6{,}4$ %, Table 17). The failure mechanisms were initially by bearing (mainly on the upper polymeric plate) and final rupture took place catastrophically by net-tension (on the lower polymeric plate). Strength joint efficiency of about 70% of the tensile strength of polymeric coupon plus the fact that the rivet does not pass the whole joint thickness signals a good joint performance of overlap friction riveted joints.

Table 18. Summarized results of the process parameters influence on process variables/properties in friction riveting.

Variable/Property	RS +	TT +	TP +
Temperature	+	+	+
Vol. Defects (PTMAZ), V_d/V_{PEI}	o	+	+
AZ-deformation (by V_{Riv}/V_{PEI}, *h* , *w)*	+	+	+
HV0,2 -Rivet (in MHAZ/MTMAZ)	-	-	-
HV0,1-Polymer. (in PHAZ/PTMAZ)	+	+	+
MW (Mn/Mn_{PEI} and Mw/Mw_{PEI})	-	-	-
Joint Efficiency ($F_M/F_{M\ 2024\text{-}M5}$)	+	+	-
Joint Ductility ($\varepsilon_f/\varepsilon_{f\ 2024\text{-}M5}$)	+	+	-
Heating Time, HT	+	+	o
Burn-off, BO	+	+	+
Burn-off rate, BOR	+	+	+
Rotational Torque, M_z	-	-	+
Heat Input, Q_{total}	+	+	o

T-SA-DA-18

+ : variable/property increases with parameter
- : variable/property decreases with parameter
o: variable/propertty is not/is slightly varied with parameter

- Creep properties were evaluated by stress relaxation testing (Section 4.3.c). Results represented by time-dependent stress (*R(t)*), and stress relaxation modulus (*E(t)*) displayed the typical polymer viscoelastic behaviour with increasingly constant deformation (ε_o): higher initial R(t)-values and R(t)-time-decay rates, and smaller E(t)-values (although clear E(t)-decay rates with ε_m were not identified for testing conditions). This analysis served to substantiate the importance of polymer viscoelasticity for the time-dependent mechanical behaviour of polymer-metal multi-materials friction riveted joints (tightness and clamp-up forces).

The proposed models and mechanisms, as well as the results of joining parameters influence on temperature development, joining mechanisms and mechanical performance of friction riveted joints on commercial available PEI/AA2024-T351 materials provided an important pathway to further exploitation of scientific and technical fields of this new joining technique for polymer-metal multi-materials structures. Although joint features and joining mechanisms may slightly vary within different joining partner combinations owing to individual structural, thermo-physical and mechanical properties of the participating materials, results originated from this

work can be extended to other combinations of engineering thermoplastic and lightweight alloys.

The new alternative joining technique developed, characterized and demonstrated in this work proved itself to be an interesting alternative joining technique for dissimilar polymer-metal joints, with high mechanical performance under tensile and shear loading without further geometrical changes, adaptations or use of filler material (e.g., rivet-bonding and other adhesive-hybrid techniques). It is a great advantage in comparison to other current joining methods, whose joint performance is usually only improved in one of these loading conditions. Furthermore, friction riveting's flexibility, short joining cycles, reduced process steps (absent or reduced obligatory pre-joining and preparative actions) and simple machinery, and possible robotic applications, suggest potential cost savings compared to the current state-of-art, as describe in the literature review of this work (Section 1). In addition to that, the absence of need in developing new joining equipment (friction welding machines commercially available over many years) and the possibility of using adapted industrial machinery for friction riveting, make this new technology highly transferable for industrial applications.

The advantages of this technique in comparison to other current mechanical fastening and adhesive bonding joining methods can be summarized as follow:

- Little or absent surface cleaning or preparation of the joining partners.
- No obligatory need of boring pre-holes.
- Hermetic sealed joints can be obtained by choosing adequate joint geometry.
- Single side accessibility is required.
- Joining is independent of position (either vertically or horizontally).
- Reduced number of process steps and short joining cycles potentially leading to production costs savings.
- A wide range of materials can be joined.
- Simple and low cost machinery, as well as robotic applications are possible.
- Good joint tensile and shear mechanical performance.

On the other hand, some limitations were also identified compared to currently available joining methods:

- Process allows only spot-like joints to be produced.
- The process is not applicable to thermoset polymers without selecting optimized joint configurations.
- Like in weldments, bonded and riveted structures, friction riveted joints are not re-openable, although they are easily recycled.

In the course of this work, the process was demonstrated for several combinations of materials, such as the automotive plastics polyamide 6, polyamide 6.6 reinforced with 30% glass fibres, acryl-butadiene-styrene (ABS); aircraft materials such as polyphenilenesulfide (PPS), reinforced with 40% glass fibres, Polysulphone (PSU) and PEI; and construction materials such as hard polyvinylchloride (PVC-U), with aluminium alloys of 2XXX and 6XXX series, carbon and stainless steels [151, 152, 153]. In real applications friction riveting could be applied for almost all transportation areas, where a weight reduction offensive for fuel saving and emission reduction has being inciting materials designers to develop and construct lightweight structures. These are currently based on materials such as thermoplastics and thermoset engineering plastics and lightweight alloys, such as aluminium and magnesium. Another interesting application field is civil engineering where in the last decade a trend in mixing materials for reducing weight without missing performance, with a extra gain in design freedom and beauty, has led architects and engineers to select for instance, engineering plastics once before only used in cars or airplanes.

In the automotive industry, for example in exterior thermoplastic roof-panels (Smart Roadster, Daimler Chrysler), front-ends and bumper beams made of long fibre reinforced plastics and metal alloys (Mazda 6, Jaguar XJ, BMW M3, among others), in super cars carbon reinforced-lightweight structures (Porsche Carrera GT), in underhood parts such as water pump (Peugeot, Audi, VW, Opel), intake manifolds made of thermoplastic and magnesium (BMW), are only some of the vast polymer-metal multi-material structures currently in use [279]. In the aircraft industry, where earlier only fighting airplanes were fabricated with composites and modern lightweight alloys, civil airplane designers are currently adopting the weight saving advantages of designing with polymers, composites and advanced alloys; current examples are Boeing 787-Dreamliner and the Airbus 350, where multi-material structures will be used not only in structural parts but also in interior and exterior panelling. Shipbuilding and railway are also following this trend by using lightweight polymer-metal sandwich materials in passenger and leisure vehicles, composite bridges and façade elements. The increasing demand in joining those polymer-metal multi-material structures can make the friction riveting method an interesting industrial process in the coming years.

Moreover, the technique has potentially a wide scientific field to be further exploited and understood in the next years. Therefore, the innovative scientific-technological approach hereby provided a new alternative to join the important class of polymer-metal multi-materials structures.

6. RECOMMENDATIONS FOR FUTURE WORK

The recommendations for future work were divided into *Scientific* and *Technical*:

Scientific:

- In addition to investigated static and creep properties, fatigue, impact resistance (joint toughness) and influence of natural/accelerated weathering and/or environmental fluids on friction riveted joint strength, would provide further design information on joint durability and performance, which would help accelerating the transition from lab- to industrial-scale.

- A supplementary study of polymer-polymer (PHAZ/PTMAZ) and polymer-metal interfaces (PTMAZ/AZ) would allow further understanding of the joining mechanisms (material flow, rivet forging), microstructure and local mechanical properties. For this, specific analytical techniques would be meaningful, such as transmission electron and atomic force microscopy (for interface examination), spectroscopic analytical techniques, like for instance infrared scanning and X-ray photoelectron spectroscopy (for chain orientation analysis and adhesion mechanisms in the polymeric volume) and nanoindentation testing for precise characterization of local mechanical behaviour and/or detailed investigation of microstructural zones (in cases when microscopy is insufficient or inadequate, e.g. for amorphous polymers where only poor contrast under optical and electronic microscopy is obtained).

Technical:

- Further development in design of improved geometry of the joining partners and improvement of adhesion properties of base materials would assist improving joint mechanical performance. Examples of such actions are the implementation of new rivet profile geometries for increasing anchoring and rivet surface treatments for increasing metal-polymer adhesion, such as by chemical etching, anodizing, surface coating and/or mechanical abrasion [38, 46].

- The investigation of the joinability of new advanced lightweight materials, such as thermoplastic carbon fibre reinforced composites and sandwich metallic-polymeric materials used in the transportation industry, is an important action to be taken in order to increase the technical added value of the friction riveting technique, considering the increasing importance of these classes of materials.

- Aiming to reduce costs by saving time and materials, to develop computer-based models for thermal development, forging regime, microstructural development, as well as for the mechanical behaviour of friction riveted joints.

7. APPENDIXES

APPENDIX 1.

RSM200 High-Speed Friction Welding Machine, Harms & Wende GmbH.

The summarized technical data regarding the friction riveting equipment used in this work consisted of:

Type:	RSM200
Manufacture:	Harms+Wende GmbH & Co. KG
DriveType:	induction motor
Power:	1.85 kW
Supply voltage:	3 x 400 V/N/PE 50 Hz
Control voltage:	24 VDC
Speed:	6000 rpm – 23 400 rpm
Friction force/forging force	
(pneumatic):	F_{max} = 5 kN at p = 10 bar
Spindle:	double-row angular contact ball bearing mount
	encapsulated on separate carriage
Axial feed:	isolated from drive
Pneumatic system	
Supply:	p_{max} = 10 bar cleaned and oiled
Connection:	1/4” quick connector
Feed:	pneumatic, stroke 50 mm
Dimensions	
RSMG20:	Diameter = 280 mm

	Length = 540 mm
	Weight approx. 31 kg
RSMS20:	760 mm x 600 mm x 350 mm
RSMGV20:	300 mm x 400 mm x 210 mm
RSMP20:	380 mm x 300 mm x 100 mm
Chuck Type:	manually operated
Holding capacity:	∅ = 3 mm to 16 mm
Length:	10 mm to 100 mm
Ambient temperature:	+10 °C to +40 °C

APPENDIX 2.

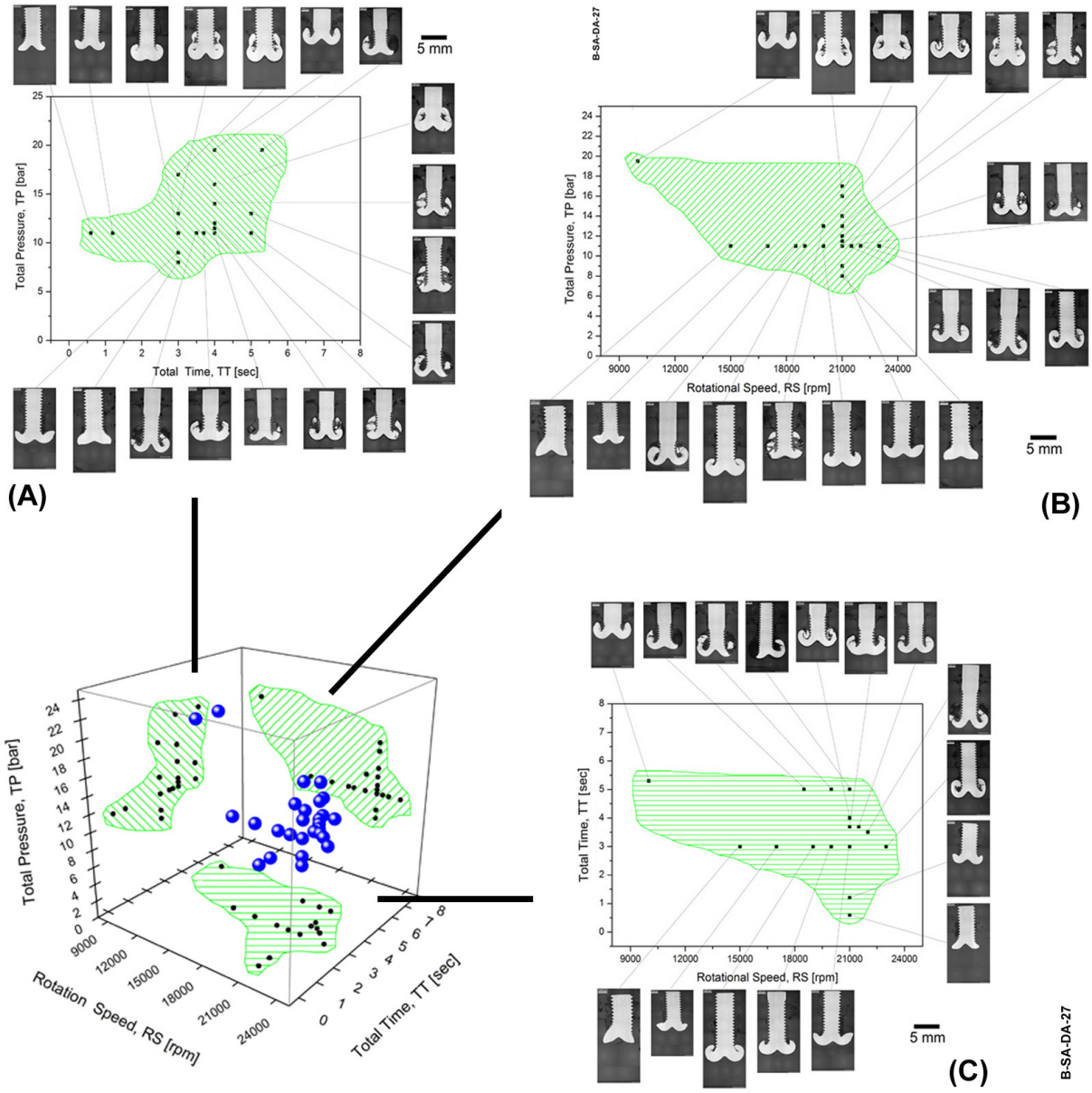

Figure A- 1. Process parameter window for PEI/AA2024-T351 point-on-plate joints. A) TP vs. TT 2D-projection graph. B) TP vs. RS 2D-projection graph. C) TT vs. RS 2D-projection graph.

APPENDIX 3.

The calibration procedure of the infrared thermocamera was carried out as following: type-K thermocouples were embedded in the joining partners (approximately in the mid-thickness of the PEI-base plate and about 5 mm deep in the axial direction of AA2024-T351 rivet); samples were heated in an electric resistance furnace up to 200 ºC and thermometric and IR-thermographic temperatures were collected during cooling. After comparing both results the corrections in the temperature controlling software of the camera were implemented.

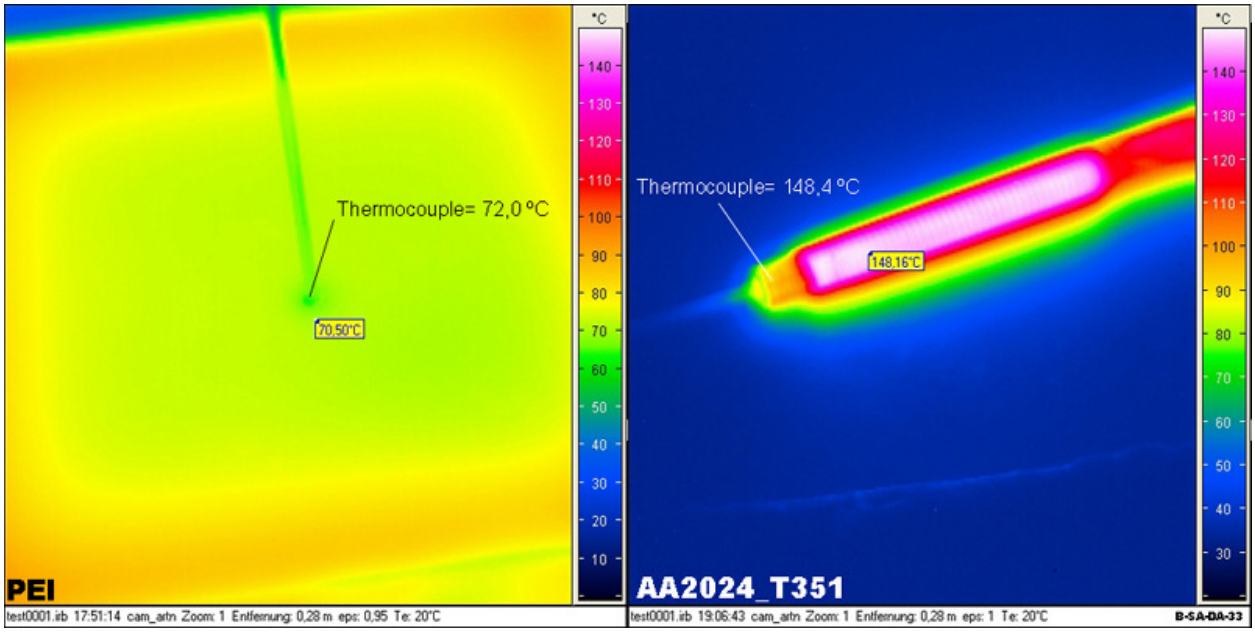

Figure A- 2. IR-temperature equipment calibration results for for PEI base plate (on the left-hand side) and AA2024-T351 rivet (on the right-hand side), by Type-K (Cr.Ni) thermocouple measurements.

APPENDIX 4.

Table A- 1. X-ray µCT quantitative volume segmentation of friction riveting comparison samples.

Sample	V_{PEI} (mm^3)	V_d (mm^3)	V_{Riv} (mm^3)
15000 rpm	43,5	0,4	4,6
17000 rpm	38,8	0,1	8,8
19000 rpm	49,4	0,1	10,6
21000 rpm	38,9	0,3	13,7
0,6 s	35,3	0,3	3,7
1,2 s	33,8	0,1	6,0
3,0 s	38,9	0,3	13,7
4,0 s	66,7	5,6	13,9
8,0 bar	57,2	1,0	7,5
9,0 bar	48,4	1,8	8,6
11,0 bar	38,9	0,3	13,7
13,0 bar	42,0	4,8	10,7

T-SA-DA-12

APPENDIX 5

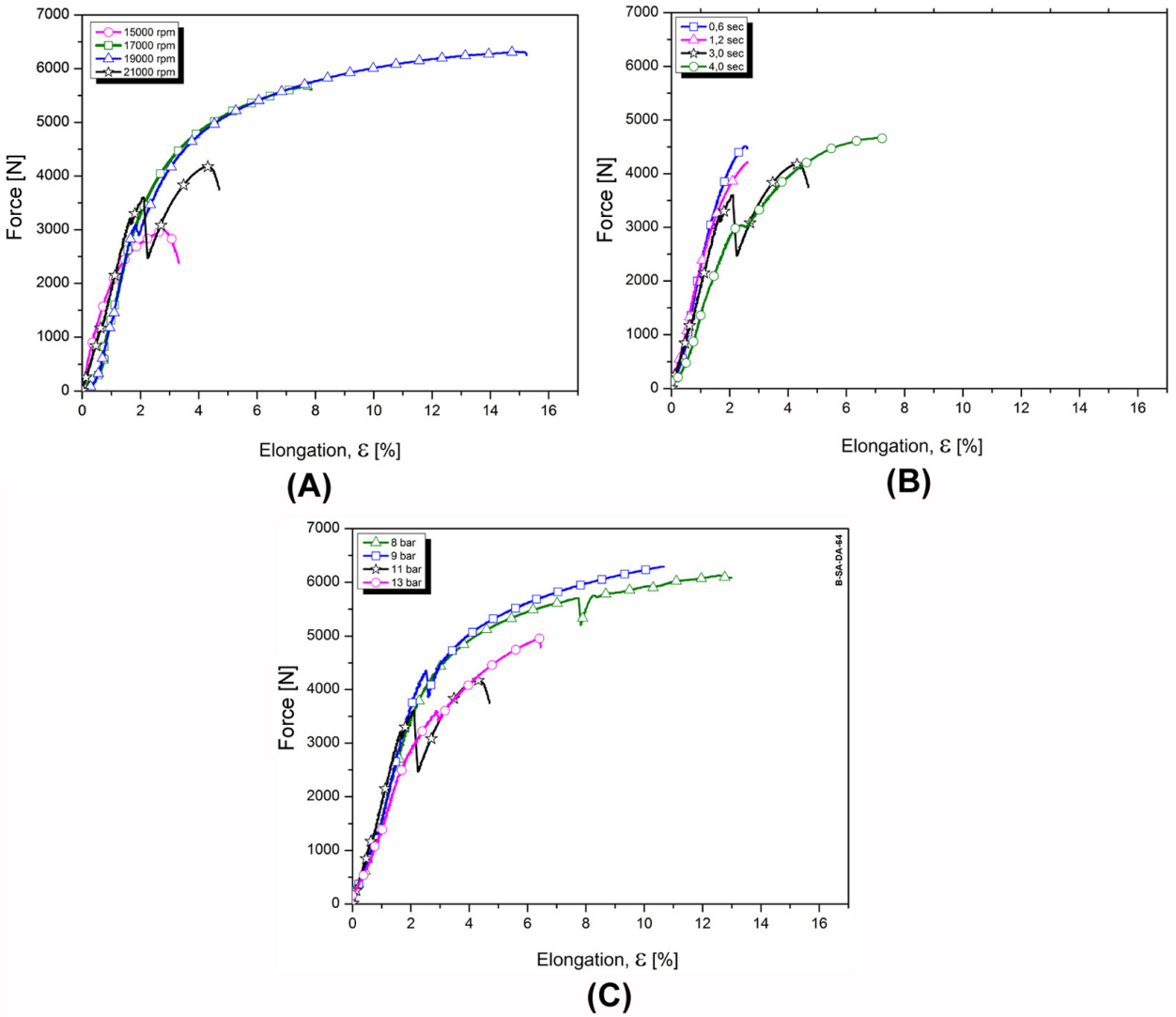

Figure A- 3. Average plots of force vs. elongation for friction rivet comparison samples: A) RS-Samples. B) TT-samples. D) TP-samples.

APPENDIX 6.

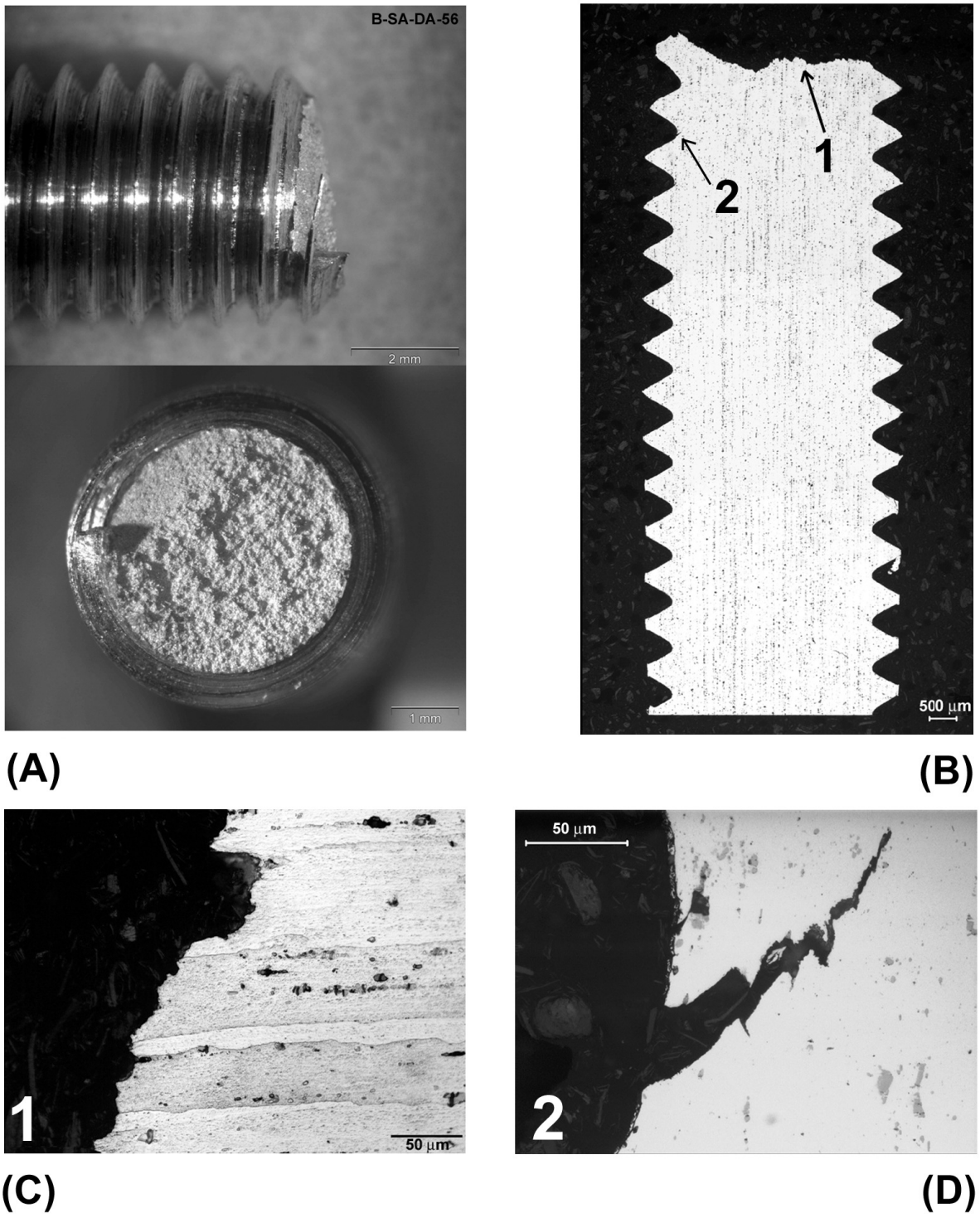

Figure A- 4. A) Stereo macrographs of a broken M5-2024-T351 tensile specimen, 50X. B) Cross section of the fractured sample on A). Note the 45^{o} crack path typical for screws tested under tensile loading, 16X. C) Detail-photo showing the area marked with Nr.1 in B); the transgranular crack path can be identified, 500X, Kroll. D) Secondary cracking at the bottom of the thread-flight marked with Nr.2 in A), 500X, Kroll.

APPENDIX 7.

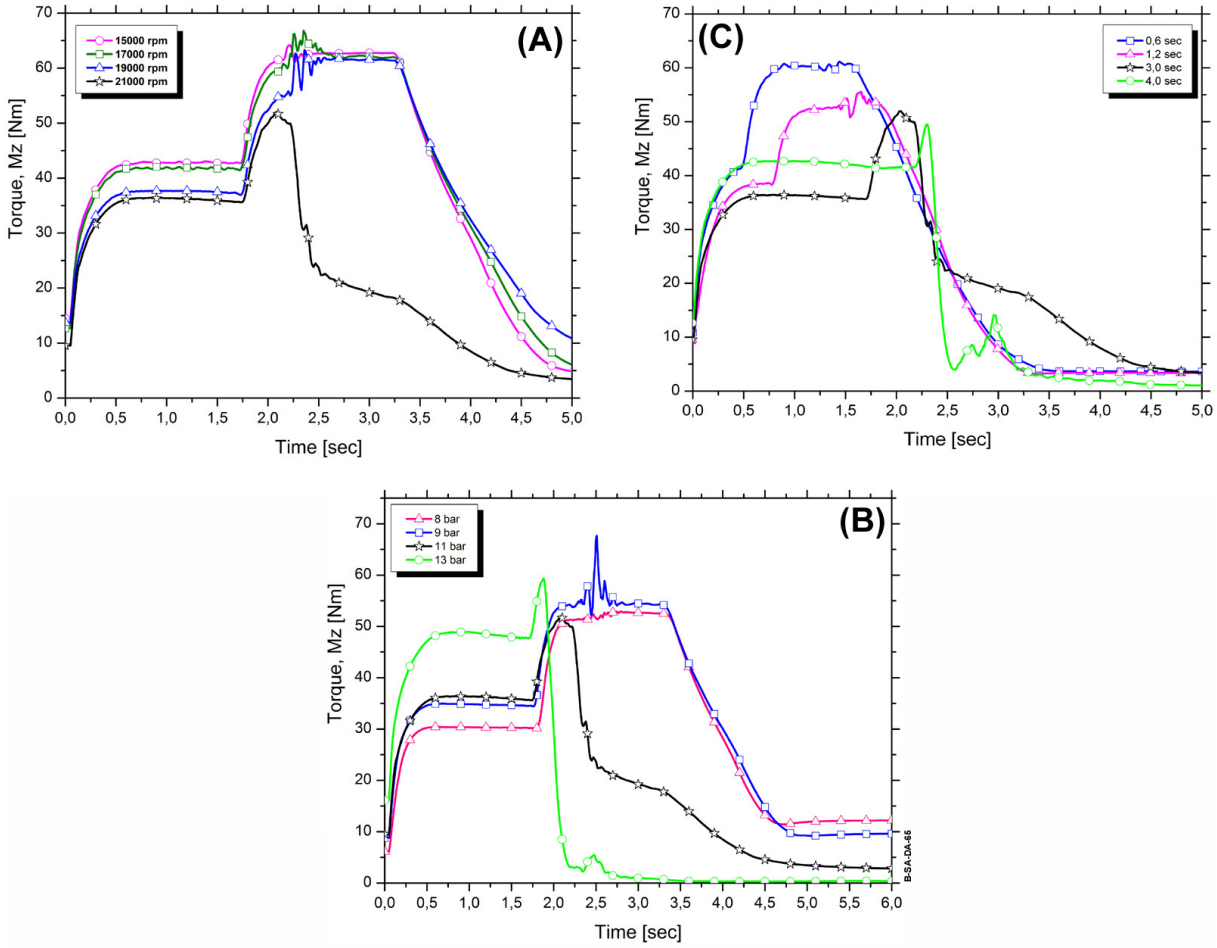

Figure A- 5. Average plots of frictional torque (M_Z) versus. time for point-on-plate friction riveting samples. A) RS-samples. B) TT-samples. C) TP-samples.

APPENDIX 8.

Table A- 2. Values of constants used for calculating viscosity in heat input calculations.

Viscosity Constants	PEI
τ^* [Pa] (1)	$1{,}02 \times 10^6$
α (1)	0,68
n (2)	0,32
C_1 [Pa.s] (1)	$1{,}84 \times 10^3$
C_2 (1)	31,96
β (2)	2×10^{-8}
T_g (3)	221,2
μ (4)	0,4
H [m]	0,001
T_{proc} [ºC] (5)	400,0

T-SA-DA-14

(1) Stokes V.K, Poslinski A.J., Pol. Eng. Sci. 35(5), pp. 441-459 1995.
(2) Dealy J.M., Wissbrun K.F., Kluwer Academics Publishers, Dordrecht, NL, 1999, ISBN: 0-412-73910-0,
(3) DSC experimental result.
(4) Bijwe J. et. al., J. Mat. Sci., 25, pp. 548-556, 1990.
(5) Domininghaus, H., Springer-Verlag, Berlin, Germany, 1998, ISBN: 3-540-62659-X

APPENDIX 9.

Table A- 3. Produced single rivet friction riveted overlap joints on PEI/AA2024-T351 in this study..

Sample	RS (rpm)	FT (ms)	FOT (ms)	FP (bar)	FOP (bar)
PEI2000.51	21000	1500	1500	2,5	5,5
PEI2000.52	21000	1500	1500	3	6
PEI2000.54	21000	1500	1500	4	7
PEI2000.55	19000	1500	1500	4	7
PEI2000.56	19500	1500	1500	4	7
PEI2000.58	19000	1500	1850	4	7
PEI2000.59	21000	1500	1800	4	7
PEI2000.60	21000	1500	1800	2,5	5,5
PEI2000.61	21000	1500	2000	2,5	5,5

T-SA-DA-16

APPENDIX 10.

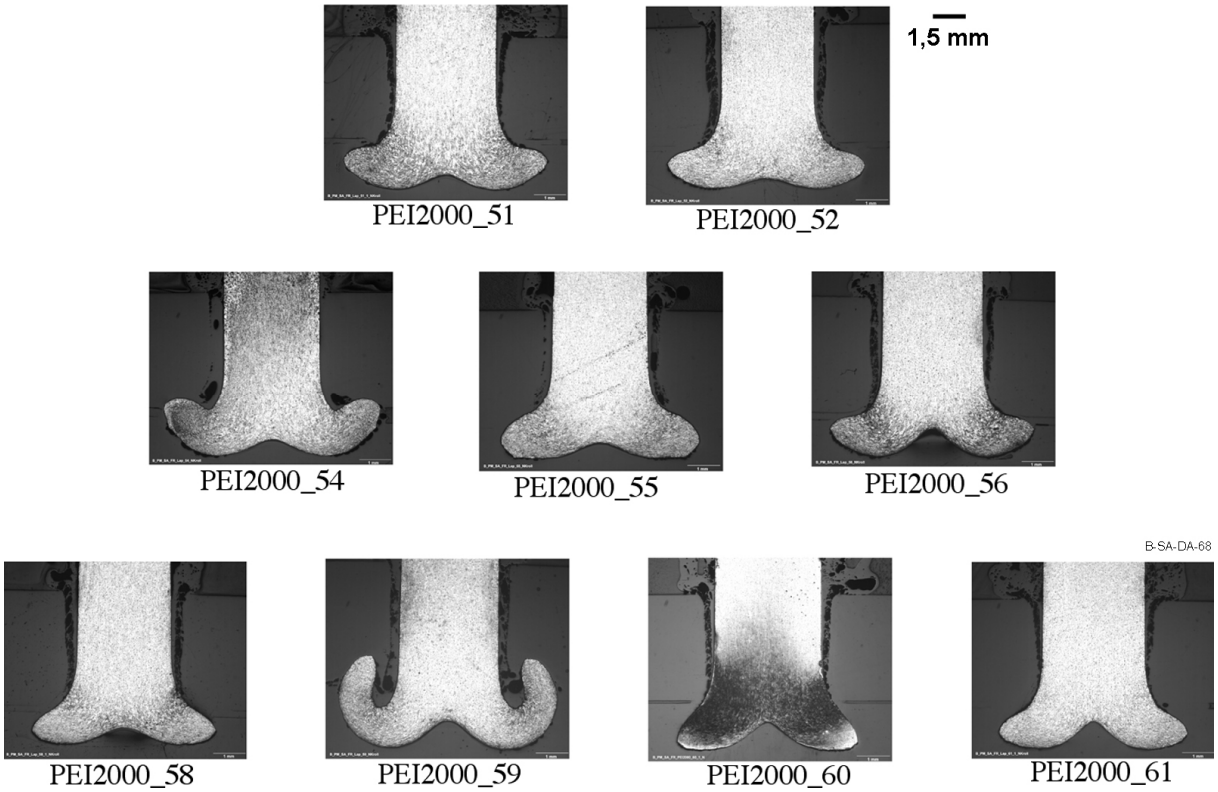

Figure A- 6. Cross-section macrographs of joints from Annex 9, Table A-3, Kroll etching.

APPENDIX 11

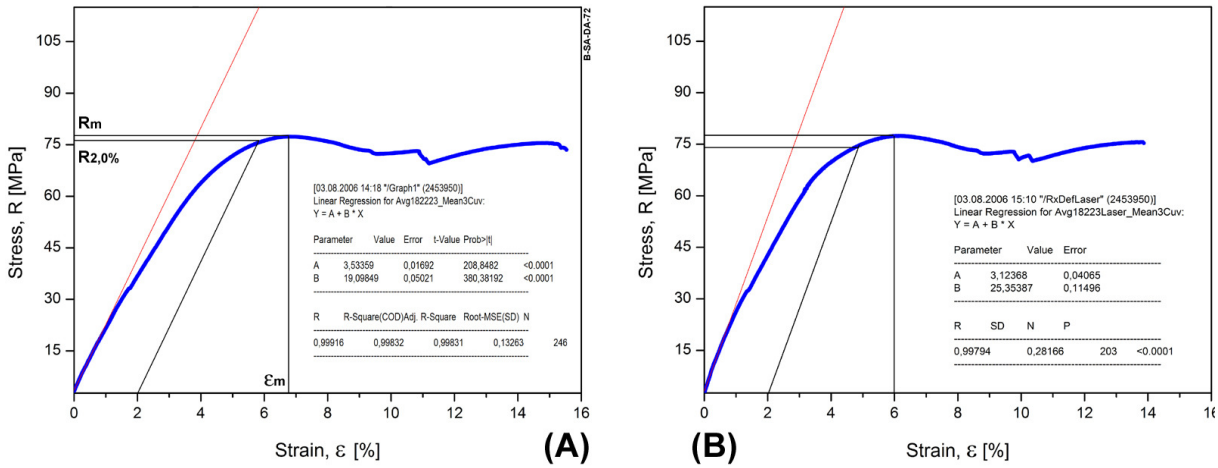

Figure A- 7. Examples calculated Lap Shear Strength parameters for an overlap friction riveted joint on PEI/AA2024-T351. A) Stress-strain results from mechanical extensometer. B) Stress-strain results from laser extensometer.

8. BIBLIOGRAPHY

1. CHAWLA, KK, *Composite Materials Science and Engineering*, Berlin: Springer-Verlag , 1987.

2. HECHT, J. L., *Macrocomposites made by Injection Molding.* Polymer Composites, 7 (3), pp. 186-190, 1986.

3. CAFARO, H., HOFFNER, J., *World's first metal/plastic composite car seat debuts on Mercedes-Benz minivan in Europe*. Bayer Polymer Division Report Nr. 07004, Germany, 1998, pp. 1-4.

4. *ASM International, Automotive Materials*. Advanced Materials & Processes, 2000. 158(2), pp.50-52.

5. FISCH, H., *Plastics – A material of choice for the automotive industry.* In Proc.: Automotive Tooling Seminar, Uddelholm, Germany, 2003.

6. *Volkswagen AG Environmental Report 2003-2004: Partners in Responsibility*. Wolfsburg, Germany, 2004, pp.1-122.

7. *Composites in… Automotive: SPE awards auto innovators*. Composites Technology, December 2005, p.13.

8. BARSOUM, R.G.S., *The best of both worlds: hybrid ship hulls use composite and steel.* AMPTIAC-Quarterly (Adv. Materials and Process Technology Information Analysis Center), 2003. **7**(3).

9. *Environmentally Sound Ship of the Future* At: http://www.marinetalk.com/articlesmarine-companies/art/Environmentally-Sound-Ship-of-the-Future-WAL00694307TU.html. February 2005.

10. GAVINE, A., *Dream Team: An efficient test programm is underway to create an efficient aircraft*. Aerospace Testing International, March 2005, pp. 39-43.

11. WRIGHT, N., LUTZ, M., *Bolt out of the blue.* Aerospace Testing International, June 2005, pp.76-78.

12. MASON, K. F., *Composites aboard high-speed trains.* In Composites Technoloby at http://compositesworld.com/ct/issues/2004/December/685/1, August 2006.

13. *Composite Materials for the Rail Industry.* At http://www.hexcel.com/Markets/Rail/RailMatrl.htm. September 2006.

14. CHALAYE, H., *Composite Materials, drive and innovation.* Le 4 Pages des statistiques industrielles (Sessi-Digitip, Min. de l´Economie des Finances et de l´Industrie). 158, pp.1-4, 2002.

15. KELLY, A., *Composite Materials after seventy years.* Journal of Material Science., 41(2006, pp. 905-912.

16. HERGENROTHER, P. M., *The use, design, synthesis and properties of high performance/high temperature polymers: an overview*. High Performacne Polymers, 15 (2003), pp. 3-45.

17. NIU, M.C.-Y., *Composite Airframe Structures, practical design information and data*. 2nd ed., Hong Kong: Hong Kong Conmilit Press Ltd., 2000.

18. *High-Temperature Plastics 2001, the 5th edition of Klines's in-depth study on the global markets for high-temperatures plastics*. Kline & Company, Inc. at: http://www.klinegroup.com, March 2006.

19. *Thermoplastic composites in Europe to 2025 – Foresight study into future research needs, Output from Task 3.2: foresight activity, Final Version*. Thermoplastic Composites Infrastructure Cooperation Network - Coronet at http://www.coronet.eu.com , April 2004.

20. BUDD, G. *Resources and Production of Aluminium*. Aluminium Federation. Brussels: European Aluminium Association, 1999, pp.1-25.

21. MILLER, W.S., ZHUANG, L., BOTTEMA, J., WITTERBROOD, A.J., DE SMET, P., HASZLER, A., VIEREGGE, A. *Recent development in alloys for the automotive industry*. Materials Science & Engineering, 280(2000), pp.37-49.

22. VASILASH, G. S., *Aluminum Studies – In which we look at a material that is finding use in some of the more interesting vehicles that are beginning to emerge as well as vehicles that we may be driving some day.* Automotive Design and Production at http://www.autofielguide.com/articles/050303.html, June 2006.

23. AMANCIO FILHO, S.T., BEYER, M., DOS SANTOS, J.F., *Verfahren zum Verbinden eines metallischen Bolzens mit einem Kunststoff-Werkstück - Akt. Nr. DE10 2005 056 606.5*, in Deutsches Patent- und Markenamt. Germany, 2005.

24. AMANCIO FILHO, S.T., BEYER, M., DOS SANTOS, J.F., Verfahren zum Verbinden eines metallischen Bolzens mit einem Kunststoff-Werkstück – Appl.. Nr. EP06024429 in European Patent Office, Munich, Germany, 2006.

25. CATSMAN, P, *Polyetherimide (PEI): Metall substituiren*. Kunststoffe, 10/2005, pp. 143-147.

26. GARDINER, G., *Thermoplastic composites gain leading edge on the A380.* High Performance Composites, March 2006, pp. 50-55.

27. IMMARIGEON, J.P. et al. *Light Weight Materials for Aircraft Applications*. Materials Characterization, 35 (1995), pp. 41-67.

28. HEINZ, A. et al. *Recent development in aluminium alloys for aerospace applications*. Materials Science and Engineering, A280 (2000), pp. 102-107.

29. MEYER, A., *US2714746 Method of joining plastic and metal*. US Patent Office, USA,1955.

30. MESSLER Jr., R. W., *Trends in key joining technologies for the twenty-first century.* Assembly Automation, 20(2)pp. 118-128, 2000.

31. MESSLER Jr., R. W., *Joining composite materials and structures: some thought-provoking possibilities*. Journal of Thermoplastic Composite Materials, 17(2004), pp. 51-75.

32. RINK, M., *US005940949 – Device for producing bonded parts*. US Patent Office, USA, 1999.

33. *Hybrid joining- the best of both worlds*. TWI, the welding institute at http://www.twi.co.uk/j32k/protected/band_8/spejcksept2002.html, June 2002.

34. *Hybridtechnik.* Bayer AG at http://plastic.bayer.de/AG/DE/technology/1012/59/index.jsp, January 2003.

35. KWEON J.- H et al., *Failure of carbon composite-to-aluminum joints with combined mechanical fastening and adhesive bonding*. Composite Structures, 75 (2006), pp. 192-198.

36. JOHNSON, W.S., *Adhesively Bonded Joints: Testing, Analysis, and Design.* ASTM - American Society for Testing and Materials. Baltimore, USA,1986.

37. REITZ, W. E., *How to join plastics*. Advanced Materials and Processes, 158 (3), pp. 49-52, 2000.

38.WEGMAN, R. F., *Surface Preparation techniques for adhesive bonding*. Noyes Publications, New Jersey USA, 1989.

39. NIU, M.C.-Y., *Airframe structural design 2nd ed.*., Hong Kong Conmlit Press Ltd.. Hong Kong, China, 1999.

40. KELLY, A., *Concise Encyclopedia of Composite Materials, Revised Edition*. Pergamon, Elservier Science Ltd.. Cambridge, England, 1994.

41. TONG, L., SHEPPARD, A., KELLY, D., CHALKLEY, P., *Effect of joint flexibility in adhesively bonded composite panel-to-flange joints.* Composites Part B, 29B (1998), pp. 287-298.

42. FERABOLI, P. M. A., *Development of carbon/epoxy structural components for a high performance vehicle*. Composites Part B: Engineering, 35 (2004), pp. 323-330.

43. BOUCHET, J.E., HAMELIN, P., *Static and dynamic behaviour of combined composite aluminium tube for automotive applications*. Composites Science and Technology, 60 (2000), pp. 1891-1900.

44. SHIN, K. C., KIM, Y. G., LEE, D. G., *Adhesively bonded lap-joints for the composite-steel shell structure of high speed vehicles*. Composite Structures, 38 (1-4), pp. 215-227, 1997.

45. CAO, J., GRENESTEDT, J. L., *Test of a redesigned glass-fiber reinforced vinyl ester to steel joint for use between a naval GRP superstructure and a steel hull*. Composite Structures. 60 (2003), pp. 439-445.

46. KINLOCH, A. J., *Adhesion and Adhesives, Science and Technology.* Chapman and Hall Ltd., London, England, 1987.

47. LEE, L.-H., *Fundamentals of Adhesion.* Plenum Press, New York, USA, 1991.

48. ROTHEISER, J., *Joining of Plastics- Handbook for designers and engineers*. Munich: Carl Hanser Verlag, Munich, Germany, 1999.

49. POCIUS, A. V., *Adhesion and Adhesives technology: an introduction.* Carl Hanser Verlag, Munich, Germany, 2002.

50. VENABLES, J. D., *Review Adhesion and durability of metal-polymer bonds.* Journal of Materials Science 19 (1984), pp. 2431-2453.

51. BOIZIAU, C., LECAYON, G*., Adhesion of polymers to metals: a review of the results obtained studying a model system*. Surface and Interface Analysis, 12 (1988), pp. 475-485.

52. WATTS, J.F., *The application of surface analysis to studies of the environmental degradation of polymer-to-metal adhesion*. Surface and Interface Analysis, 12 (1988), pp. 497-503.

53. BISCHOF, C., et al., *Zur Adhäsion in Metall-Polymer-Grenzschichten und ihrer praktischen Nutzung*. Acta Polymerica, 40 (3), pp. 214-221, 1988.

54. OWENS, J. F. P., LEE-SULLIVAN, P., *Stiffness behaviour due to fracture in adhesively bonded composite-to-aluminium joints.* International Journal of Adhesion & Adhesives, 20 (2000) 39-45.

55. ZAPOROJTCHENKO, V., et al., *Metal/polymer interfaces with designed morphologies.* Journal of Adhesions Science and Technology, 14 (13), pp. 467-490, 2000.

56. BALDAN, A., *Review adhesively-bonded joints and repairs in metallic alloys, polymers and composite materials: Adhesives, adhesion theories and surface pre-treatmen*t. Journal of Materials Science, 39 (2004), pp. 1-49.

57. BALDAN, A., *Review adhesively-bonded joints and repairs in metallic alloys, polymers and composite materials: Mechanical and environmental durability performance*. Journal of Materials Science, 39 (2004), pp. 4729-4797.

58. LINCOLN, B. et al., *Mechanical Fastening of Plastics - An Engineering Handbook*., Marcel Dekker, Inc.. New York, USA, 1984.

59. SHIGLEY, J. E., *Fastening, Joining and Connecting - A Mechanical Designers' Workbook*. McGraw-Hill, New York, USA, 1986.

60. PARMLEY, R. O., *Standard handbook of Fastening and Joining*, 3rd ed.. McGraw-Hill, New York, USA, 1996.

61. SPECK, J. A., *Mechanical fastening, joining, and assembly*. Marcel Dekker Inc., New York , USA, 1997.

62. RUTHEMBERG, R., *Mit Leichtigkeit fest verbunden.* Konstruktion, Zeitschrift für Produktentwicklung und Ingenieur-Werkstoffe, 1-2 (2005), pp. 22-23.

63. HARPER, E. J. C., *Modern Plastics Handbook, 1st ed.*. McGraw-Hill, New York, USA, 2000.

64. HAHN, O., TAN, Y., *Using a neural network in order to predict the load-bearing behaviour of clinched joints subjected to quasi-static tensile shear loads*. Welding and Cutting, 4 (2003), pp. 226-230.

65. TOX PRESSOTECHNIK GmbH & CO.KG, *Servo-Spindelantrieb – Standard-Kraftkomponenten für Produktionslösungen.* Konstruktion, Zeitschrift für Produktentwicklung und Ingenieur-Werkstoffe, 1-2 (2005), pp.14-15.

66. Leaversuch, R., *Collar Joining method makes Plastic-Metal Hybrids. In* Plastic Technology at http://www.plasticstechnology.com/articles/200210cu2.html, 2002.

67. BASF AG, *Collaring new plastic applications.* At http://www2.basf.de/basf2/html/plastics/englisch/pages/presse/04_251.htm, February 2006.

68. McCONNELl, P., *Joining Composites.* Reinforced Plastics, 06-1999: p. 26-32.

69. RAMAKRISHNA S., et al., *Bolted joints of pultruded sandwich composite laminates.* Composite Structures, 32 (1995), pp. 227-235.

70. BILLMEYER Jr, F.W., *Textbook of Polymer Science 2nd ed.*. Willey-Interscience. New York, USA, 1971.

71. CAHN, R. W., HAASEN, P., *Physical metallurgy.* Elsevier, Amsterdam, Holland, 1996.

72. FAUPEL, F., WILLECKE, R., THRAN, A., *Diffusion of metals in polymers.* Materials Science and Engineering Reports, R22 (1998), pp. 1-55.

73. TADMOR, Z., GOGOS, C. G., *Principles of polymer processing.* John Wiley & Sons, New York, USA, 1979.

74. AWS, *Welding Handbook Vol.2, 8th ed..* American Welding Society, USA, 1991.

75. ASM, *Welding Handbook Vol. 6.* American Society of Metals, USA, 1993.

76. WISE, R., *What really happens-current theories for welding plastics.* Bulletin, the technical journal for industrial members of TWI. 38(3): p. 52-55, 1997.

77. DIN 16960, *Schweißen von thermoplastischen Kunststoffen, in Kunststoffe Mechanische und thermische Eigenschaften*. D.D.I.f.N. e.V., Beuth Verlag GmbH, Berlin, Germany, 1974.

78. DIN 1910, *Schweissen von Kunststoffen Verfahren, in Kunststoffe Mechanische und thermische Eingeschaften, Taschenbuch 18*. D.D.I.f.N. e.V., Beuth Verlag GmbH, Berlin, Germany, 1977.

79. MISTRY, K., *Plastic welding technology for the industry.* Assembly Automation. 17 (3), pp. 196-200, 1997.

80. HABERSTROH E., W. L., STEGMAIER, M., *Kunststoffschweißen - Teil 1: Handwerkliche Verfahren.* Schweissen & Schneiden, 4 (2000). pp. 214-224.

81. HABERSTROH, E., et al., *Kunststoffschweißen - Teil 2: Industrielle Serienfertigung.* Schweissen & Schneiden, 5 (2000), pp. 272-276.

82. WATSON, M. N., et al., *Plastics – an industrial and literature survey of joining technique.* TWI-Industrial Report, The Welding Institute, Cambridge, England, 1986.

83. YARLAGADDA P. K. D. V., TAN, C. C., *An investigation into welding of engineering thermoplastics using focused microwave energy.* Journal of Materials Processing Technology, 74 (1998), pp. 199-212.

84. JONES, I.A., *Laser welding of plastics film and sheet.* Technology Briefing of The Welding Institute, 519/1995. p. 4.

85. *Infrared welding of plastics*. TWI, The Welding Institute at http://www.twi.co.uk/j32k/protected/band_3/ksfc001.html, April 2004.

86. CRAWFORD, R. J., TAM, Y., *Friction welding of plastics.* Journal of Materials Science, 16 (1981), pp. 3275-3282.

87. THEWS, H., *Zeitgemäße Kunststoff-Verbindungstechnik*. Infotip Verlag, Limeshain, Germany. 1986.

88. NORTH, T. H., et al., *Welding of plastics.* ASTM Handbook vol. 6 – Welding, Brazing and Soldering, ASTM International, USA, 2000

89. STOKES, V. K., *Joining Methods for Plastics and Plastic Composites: An Overview.* Polymer Engineering and Science, 29 (19), pp.1310-1324, 1989.

90. SCHLARB, A. K., EHRENSTEIN, G. E., The *impact strength of butt welded vibration welds related to microstructure and welding history*. Polymer Engineering and Science, 29 (23), pp. 1677-1682, 1989.

91. AGEORGES, C., LIN, Y., MENG, H., *Advances in fusion bonding techniques for joining thermoplastics matrix composites: a review*. Composites Part A, 32 (2001), pp. 839-857.

92. MCKNIGHT, S. H., et al., *Scaling issues in resistance welded thermoplastic composite joints.* Advances in Polymer Technology, 16(4), pp. 279-295, 1997.

93. AGEORGES, C., LIN, Y., MENG, H., *Experimental investigation of the resistance welding for thermoplastic-matrix composites. Part I: heating element and heat transfer*. Composites Science and Technology, 60 (2000), pp. 1027-1039.

94. AGEORGES, C., LIN, Y., MENG, H., Experimental investigation of the resistance welding for thermoplastic-matrix composites. Part II: optimum processing window and mechanical performance. Composites Science and Technology, 60 (2000), pp. 1191-1202.

95. RUDOLF, R., et al., *Induktionsschweißen gewebeverstärkter Faser-Kunststoff-Verbunde.* Schweissen & Schneiden, 53(10), pp. 690-695, 2001.

96. KAMPMANN L., GLOOR P., *Welded composite panels, US005580636*. US Patent Office, USA, 1996.

97. WENDISCH, K. -H., *Verfahren zum Verbinden einer thermoplastichen Folie mit einer Metallfolie sowie ein mit dem Verfahren hergestelltes Mehrschicht-Material DE19721731C1*. Deutsches Patent- und Markenamt, Germany, 1999.

98. WIRTH, J. G., HEATH, D. R., *US Patent 3.730.946.* USA, 1973.

99. ASM, *Engineering Plastics 1st ed.* Engineered Materials Handbook Vol. 2. ASM International, 1988.

100. SERFATY, W., *Polyetherimide: a versatile, processable thermoplastic.* In Polyimides, synthesis, characterization, and applications, ed.: MITTAL, K. L., Plenum Press, New York, USA, 1984.

101. DOMININGHAUS, H., *Die Kunststoffe und ihre Eigenschaften*. Springer-Verlag, Berlin, Germany, 1998.

102. BRYDSON, J. A., *Plastics Materials. 7 ed.*. Butterworth Heinemann, USA, 1999.

103. LONG Jr., E. R., COLLINS, W. D., *The effects of fluids in the aircraft environment on a polyetherimide.* Polymer Engineering and Science, 28 (12), pp. 823-828, 1988.

104. STOKES, V. K., *Experiments on the hot-tool welding of three dissimilar thermoplastics*. Polymer 39 (12), pp. 2469-2477, 1998.

105. STOKES, V. K., A *phenomenological study of the hot-tool welding of thermoplastics, Part 3. Polyetherimide.* Polymer, 42 (2001), pp. 775-792.

106. AGEORGES, C., et al., *Characteristics of resistance welding of lap shear coupons. Part I: Heat transfer*. Composites Part A, 29A (1998), pp. 899-909.

107. HOU, M., et al., *Resistance welding of carbon fibre reinforced thermoplastics composite using alternative heating element*. Composite Structures, 47 (1999), pp. 667-672.

108. HOU, M., YE, L., MAI, Y.-W., *An experimental study of resistance welding of carbon fibre fabric reinforced polyetherimide (CF Fabric/PEI) composite material*. Applied Composite Materials 6 (1999), pp. 35-49.

109. STAVROV, D., BERSEE, H. E. N., *Thermal aspects in resistance welding of thermoplastic composites (HT2003-47222).* In Proc. : ASME Summer Heat Transfer Conference, Las Vegas, Nevada, USA, 2003, pp.151-156.

110. STOKES, V. K., *Vibration weld strength data for glass-filled polyetherimide.* Journal of Adhesion Science and Technology, 15 (14), pp. 1763-1768, 2001.

111. *ULTEM 1000 – GE product data sheets.* GE Plastics at http:// www.geplastics.com, May 2005.

112. PECHT, M., WU, X., *Characterization of polyimides used in high density interconnects.* IEEE Transactions on Components, Packaging, and Manufacturing Technology – Part B, 17 (4), pp. 632-639, 1994.

113. IKEDA, R. M., *Shear yield and crazing stresses in selected glassy polymers.* Journal of Applied Polymer Science, 47 (1993), pp. 619-629.

114. LINCOLN, J. J., MORGAN, R. J., SHIN, E. E., *Effect of thermal history on the deformation and failure of polyimides.* Journal of Polymer Science: Part B, 39 (2001), pp. 2947-2959.

115. KIM, K.-Y., YE, L., Effects *of thickness and environmental temperature on fracture behaviour of poyletherimide (PEI)*. Journal of Materials Science, 39 (2004), pp. 1267-1276.

116. FRASSINE, R., PAVAN, A., *Viscoelastic effects on the interlaminar fracture behaviour of the thermoplastic matrix composites: I. rate and temperature dependence in unidirectional PEI/carbon-fibre laminates*. Composites Science and Technology, 54 (1995), pp. 193-200.

117. FUKUHARA, M., *Temperature dependency of elastic moduli an internal dilatational and shear frictions of polyetherimide*. Journal of Applied Polymer Science, 90 (2003), pp. 759-764.

118. SEPE, M. P., *The effect of absorbed moisture on the elevated temperature properties of polyetherimide*. In Proc.: ANTEC 2004, Chicago, Illinois, USA, 2004, pp. 2236-2240.

119. TROTIGNON, J. P., et al., *Fatigue behaviour of some temperature-resistant polymers.* Journal of Materials Science, 28 (1993), pp. 2207-2213.

120. NIMMER, R. P., WOODS, J. T., *An investigation of brittle failure in ductile, notch-sensitive thermoplastics.* Polymer Engineering and Science, 32 (16), pp. 1126-1137.

121. *Keeping technology moving, Lexan and Ultem film and sheet: Advanced engineering materials for the transportation industry.* GE Plastics Specialty Film & Sheet at http:// www.geplastics.com, January 2006.

122. *GE Plastics launches new aircraft interior materials at Aircraft Interiors Expo – May 2006*. at http://www.composites world.com/news/cwweekly/2006/May.htm, May 2006.

123. *Westland 30-300 thermoplastic tailplane.* Plastics and Rubber International, 12 (1), pp. 23-24, 1987.

124. DUTHIE, T., *Saving weight and cost with thermoplastic composites.* Engineering Materials and Design, January, 1988.

125. GRIFFITHS, G. R., HILLIER, W. D., WHITING, J. A. S., *Thermoplastic composite manufacturing technology for a flight standard tailplane.* SAMPE Journal, 25 (3), pp. 29-33, 1989.

126. GINGER, G., *Thermoplastic composites gain leading edge on the A380*. High Performance Composites, March 2006, pp.50-55.

127. HATCH, J. E., *Aluminum, properties and physical metallurgy.* American Society for Metals, ASM, Metals Park, Ohio, USA, 1984.

128. ASM, *Aluminum and aluminium alloys, 3rd ed.* ASM International, USA, 1996.

129. MONDOLFO, L.F. *Aluminum Alloys: Structure and Properties.* London: Butterworths, London, England, 1976.

130. COBDEN, R. *Physical Properties, Characteristics and Alloys*. Brussels: European Aluminium Association, Brussels, Belgium, 1999.

131. ZHANG, C. B., SUN, W., YE. H. Q., *Investigation of the crystallography and morphology of the S' precipitate in an Al(CuMg) alloy by HREM.* Philosophical Magazine Letters, 59 (6), pp. 265-271, 1989.

132. KACAR, H., ATIK, E., MERIC, C., *The effect of precipitation-hardening conditions on wear behaviours at 2024 aluminium alloy*. Journal of Materials Processing Technology, 142 (2003), pp. 762-766.

133. GENEVOIS, C. et al., *Quantitative investigation of precipitation and mechanical behaviour for AA2024 friction stir welds*. Acta Materialia, 53 (2005), pp. 2447-2458.

134. YAN, J., *High-resolution electron microscopy on the morphology of S' – and S-phases in Al-Cu-Mg alloy*. Journal of Materials Science Letters, 10 (1991), pp. 591-593.

135. MAZZINI, S. G., CARETTI, J.C., *Effect of deformation at elevated temperature before age-hardening on the mechanical properties of 2024 commercial aluminium alloy*. Scripta Metallurgica et Materialia, 25 (1991), pp. 1987-1990.

136. IRVING, B., *Why aren't airplanes welded?.* Welding Journal, 76 (1), pp. 31-41, 1997.

137. MENDEZ, P.F. *New trends in welding in the aeronautic industry*. in Proc.: "New Trends for the Manufacturing in the Aeronautic Industry" , Hegan Inasmet, San Sebastian, Spain 2000.

138. RYKALIN, N. N. et al., The heating and cooling of rods butt welded by the friction process. Welding Production, 10 (1959) pp. 42-52.

139. VILL, V. I., *Friction welding of metals*. American Welding Society, New Yorlk, USA, 1962.

140. SCHAEFER, R., *Beitrag zum Reibschweißen von Metallen unter besonderer Berücksichtigung der Energieumwandlung während des Schweißprozesses*. Ph.D. thesis at RWTH-Aachen, Germany, 1971.

141. SCHOBER, D., *Qualitätssicherungssystem für das Reibschweißen von Stahlwerk*stoffen., Ph.D thesis at Technische Hochschule Karl-Marx-Stadt, Germany, 1986.

142. NEUMANN, A., SCHOBER, D., *Reibschweißen von Metallen 1.Auflage*. Verlag Technik GmbH, Berlin, Germany, 1991.

143. CROSSLAND, B., *Friction Welding*. Contemporary Physics, 12 (6), pp. 559-574, 1971.

144. NA, S.-J., *Das Reibschweißen ungleichartiger Metalle*. Ph.D.dissertation at Technische Universität Carolo-Wilhelmina zu Braunschweig, Germany, 1982.

145. MIDLING, O.T., GRONG, ∅., *A process model for friction welding of Al-Mg-Si alloys and Ali-SiC metal matrix composites – I. HAZ temperature and strain rate distribution*. Acta Metall. Mater., 42(5), pp. 1595-1609, 1994.

146. DEALY, J.M., WISSBRUN, K.F., *Melt rheology and its role in plastics processing, theory and applications*. Kluwer Academic Publishers, Dordrecht, Holand, 1999.

147. POTENTE, H., REINKE, M., *Welding parameters and properties of polyolefin parts*. Plastics and Rubber and Applications, 1 (1981), pp. 149-160.

148. TAPPE, P., POTENTE, H., *New results on the spin welding o plastics*. Polymer Engineering and Science, 29 (23), pp. 1655-1660, 1989.

149. STOKES, V.K., *Analysis of the friction (spin)-welding process for thermoplastics*. Journal of Materials Science, 23 (1988), pp. 2772-2785.

150. STOKES, V.K., POSLINSKI, A.J., *Effects of variable viscosity on the steady melting of thermoplastics during spin welding*. Polymer Engineering and Science, 35 (5), pp. 441-459, 1995.

151. AMANCIO-FILHO, S.T., *DAAD-CNPq GDE-Programme Annual Report Nr.1*. Brazil-Germany Bilateral Scientific Cooperation, Brasilia, Brazil, 2003.

152. AMANCIO-FILHO, S.T., *DAAD-CNPq GDE-Programme Annual Report Nr.2*. Brazil-Germany Bilateral Scientific Cooperation, Brasilia, Brazil, 2004.

153. AMANCIO-FILHO, S.T., *DAAD-CNPq GDE-Programme Annual Report Nr.3*. Brazil-Germany Bilateral Scientific Cooperation, Brasilia, Brazil, 2005.

154. *RSM200 Reibschweißsystem – Betriebsanleitung.* Harms & Wende GmbH & Co. KG, Hamburg, Germany, 2002.

155. *B06.9366BB, d 5.01 – Betriebsanleitung Kistler Piezo-Instrumentation*. Kistler Instrumenten AG, Winterthur, Switzerland.

156. PETZOW, G., *Metallographic etching, techniques for metallography, ceramography and plastography, 2nd ed.*. ASM International, USA, 1999.

157. ASTM E384-992e1, *Standard Test Method for Microindentation Hardness of Material.* ASTM International, 2005.

158. CALLEJA, F. J. B., FAKIROV, S. *Microhardness of polymers*. Cambridge University Press, Cambridge, England, 2000.

159. *UT 100 – der automatische Härteprüfer (Produktprosket)*. BAQ GmbH – Automatisierung und Qualitätssicherung, 2004.

160. DIN 53455, *Prüfung von Kunststoffen, Zugversuch.* DIN – Deutsches Institut für Normung e. V., 1981.

161. DIN EN ISO 898-1, *Mechanische Eigenschaften von Verbindungselementen aus Kohlenstoffstahl und legierten Stahl – Teil 1: Schrauben*. DIN – Deutsches Institut für Normung e. V., 1999.

162. VDI 2230 – PART 1, *Systematic calculation of high duty bolted joints; Joints with one cylindrical bolt.* Verein Deutscher Ingenieure, VDI, 2003.

163. DIN EN 10002, *Tensile testing of metallic materials, method of test at ambient temperature*. DIN – Deutsches Institut für Normung e. V., 1999.

164. KAISER, B., *Ermittlung der Gebrauchseigenschaften von Schrauben aus Aluminiumwerkstoffen*. Final Report AiF Nr.12574 B “Aluminiumschrauben”, Technische Universität Darmstadt, Germany, 2002.

165. ARZ, U., *Beitrag zur Ermittlung der Beanspruchbarkeit von Schrauben aus Aluminium-Legierungen*. Ph.D. thesis, Technische Universität Darmstadt, Darmstadt, Germany, 2003.

166. D 5961/DD 5961M-05, *Standard test method for bearing response of polymer matrix composite laminates*. ASTM International, USA, 2005.

167. DIN 53 441, *Prüfung von Kunststofen – Spannungsrelaxationsversuch.* DIN – Deutsches Institut für Normung e. V., 1984.

168. BECKMANN, F., et al., *New developments for synchrotron-radiation-based microtomography at DESY.* In Proc.: SPIE conference, paper 6318, USA, 2006.

169. SHA, V., *Handbook of plastics testing technology, 2nd ed..* John Wiley & Sons, Inc, New York, USA, 1998.

170. ALTGELT, K. H., SEGAL, L., *Gel permeation chromatography.* Marcel Dekker, Inc., New York, USA, 1971.

171. CAMPBELL, D., PETHRICK, R. A., WHITE, J. R., *Polymer Characterization, physical techniques, 2nd ed..* Stanley Thornes (Publishers) Ltd., Cheltenham, U.K., 2000.

172. OTTO, M., *Analytische Chemie, Zweite, vollständig überarbeitete Auflage*. Wiley-VCH, Weinheim, Germany, 2000.

173. SVEHLA, G., *Comprehensive analytical chemistry, vol. VI: Analytical Infrared Spectroscopy.* Elsevier Scientific Publishing Company, Amsterdam, Holland, 1976.

174. EHRENSTEIN, G. W., *Kunststoff-Schadenanalyse, Methoden und Verfahren.* Carl Hanser Verlag, München, Germany,1992.

175. SCHMIEDEL, H., *Handbuch der Kunststoffprüfung.* Carl Hanser Verlag, München, Germany, 1992.

176. EHRENSTEIN, G., RIEDEL, G., TRAWIEL, P., *Thermal analysis of plastics, theory and practice*. Carl Hanser Verlag, München, Germany, 2004.

177. ISO 11357-1, *Plastics – Differential scanning calorimetry (DSC) – Part 1: General principles*. 1997.

178. MEYER, A., *Friction hydro pillar processing: bonding mechanisms and properties.* Ph.D. thesis, Technische Universität Carolo-Wilhelmina zu Braunschweig, 2003.

179. *VarioTherm - Einführung in Theorie und Praxis der Infrarot-Thermografie*. Infra Tec GmbH, Dresden, Germany, 2005.

180. AMANCIO FILHO, S. T., *Preliminary Study on the Microstructure and Mechanical Properties of Dissimilar Friction Stir Welds in Aluminium Alloys used in the Aircraft Industry*. M.Sc. thesis, Federal University of Sao Carlos, Brazil, 2002.

181. SAWYER, L. C., GRUBB, D. T., *Polymer microscopy, 2nd ed..* Chapman & Hall, London, England, 1996.

182. BIJWE, J., TEWARI, U. S., VASUDEVAN P., *Friction and wear studies of bulk polyetherimide*. Journal of Materials Science, 25 (1990), pp. 548-556, 1990.

183. MUSTO, P., KARASZ F. E., MAcKNIGHT, W. J., *Fourier transform infra-red spectroscopy on the thermo-oxidative degradation of polybenzimidazole and of a polybenzimidazole/polyetherimide blend*. Polymer, 34 (13), pp. 2934-2945, 1993.

184. GARDNER, S. H., *An investigation of the structure-property relationships for high performance thermoplastics matrix, carbon fiber composites with a tailored polyimide interphase*. D. Ph. Dissertation, Virginia Polytechnic Institute and State University, Blacksburg, USA, 1998.

185. CHIEFARI, J., et al., *Water as solvent in polyimide synthesis: thermoset and thermoplastic examples*. High Performance Polymers, 15 (2003), pp. 269-279.

186. KURODA, S. –I., MITA, I., *Degradation of aromatic polymers – II. The crosslinking during thermal and thermo-oxidative degradation of a polyimide*. European Polymer Journal, 25 (6), pp. 611-620, 1989.

187. LAMBERT, J. B., et al., *Introduction to organic spectroscopy.* Prentice Hall, USA, 1987.

188. SUNDAR, S. et al., *Aqueous dispersions of polyurethane cationomers: a new approach for hydrophobic modification and crosslinking*. Colloid Polymer Science, 283 (2004), pp. 209-218.

189. GUERRA, G., et al., *Fourier Transform Infrared Spectroscopy of some miscible polybenzidazole/polyimide blends*. Macromolecules, 21 (1998), pp. 231-234.

190. HUMMEL, D. O., et al., *Linear-temperature programmed pyrolysis of thermoresistant polymers – mass and FT-IR spectrometries; Part 3. poly(1,4-phenylene terephthalamide) and aromatic polyimides*. Journal of Analytical and Applied Pyrolysis, 33 (1995), pp. 195-212.

191. SEO, Y., et al., *Compatibilizing effect of a poly(esterimide) on the properties of the blends of poly(ether imide) and a thermotropic liquid crystalline polymer: 1. Compatibilizer synthesis and thermal and rheological properties of the in situ composite system*. Polymer, 36 (3), pp.515-523, 1995.

192. PRAMODA, K. P., et al., *Characterization and thermal degradation of polyimide and polyamide liquid crystalline polymers*. Polymer Degradation and Stability, 67 (2000), pp. 365-374.

193. VORA, R. H., et al., *Preparation and characterization of 4,4´-bis(4-aminophenoxy)diphenyl Sulfone based fluoropoly(ether-imide)/organo-modified clay nonocomposites*. Macromolecular Materials and Engineering, 288 (2003), 337-356.

194. KURDI, J., KUMAR, A., *Structuring and characterization of a novel highly microporous PEI/BMI semi-interpenetrating polymer network*. Polymer, 46 (2005), pp. 6910-6922.

195. CHOUKOUROV, A., et al., *Thin polymer films from polyimide vacuum thermal degradation with and without a glow discharge.* Vacuum, 80 (8), pp. 923-929, 2006.

196. SUNDAR, S., et al., *Crosslinked sulfonated polyimide networks as polymer electrolyte membranes in fuel cells.* Journal of Polymer Science: Part B: Polymer Physics, 43 (2005), pp. 2370-2379.

197. PRYDE, C. A., *IR studies of polyimides. I. Effects of chemical and physical changes during cure.* Journal of Polymer Science: Part A. Polymer Chemistry, 27 (1989), 711-724.

198. MENGES, G., *Werkstoffkunde der Kunststoffe, 2. Auflage.* Carl Hanser Verlag, München, Germany, 1985.

199. MENNING, G., *Wear in plastics processing, how to understand, protect and avoid*. Hanser Publishers, Munich, Germany, 1995.

200. DVS 2909, *Teil 1: Reibschweißen von metallischen Werkstoffen Verfahren, Begriffe, Werkstoffe*. Deutscher Verband für Schweisstechnik e.V., Düsseldorf, Germany, 1989.

201. EN ISO 15620:1999, *Schweißen – Reibschweißen von metallischen Werkstoffen.* Comité Européen de Normalisation, CEN. Brussels, Belgium, 1999.

202. ASM, *Welding, Brazing and Soldering Handbook Vol. 6*. ASM International, USA, 1994.

203. BETHLEHEM, W. F., *Geeignet zur Prozesßüberwachung: Störungen des Momentenverlaufes lassen fehlerhafte Reibschweißungen erkennen*. Schweißen und Schneiden, 36 (1), pp. 23-28, 1984.

204. STRUIK, L. C. E., *Physical aging in amorphous polymers and other materials.* Elsevier Scientific Publishing Co., Amsterdam, Netherlands, 1978.

205. BROSTOW, W., CORNELIUSSEN, R. D., *Failure of Plastics.* Hanser Publishers, Munich, Germany, 1986.

206. MALLOY, R. A., *Plastic part design for injection molding, an introduction.* Hanser Publishers, Munich, Germany, 1994.

207. JONES, R. L., RICHARDS, R. W., *Polymer at surfaces and interfaces*. Cambridge University Press, Cambridge, U.K., 1999.

208. WOOL, R. P., *Polymer interfaces, structure and strength*. Hanser Publishers, Munich, Germany, 1995.

209. BASTIEN, L. J., GILLESPIE Jr., J. W., *A non-isothermal healing model for strength and toughness of fusion bonded joints of amorphous thermoplastics*. Polymer Engineering and Science, 31 (24), pp. 1720-1730, 1991.

210. BUCKLEY, C. P., WU, J., HAUGHIE, D. W., *The integrity of welded interfaces in ultra high molecular weight polyethylene: Part 1: Model*. Biomaterials, 27 (2006), pp. 3178-3186.

211. CHUNG, F. H., *Unified theory and guidelines on adhesion*. Journal of Applied Polymer Science, 42 (1991), pp. 1319-1331.

212. FOURCHE, G., An *overview of the basic aspects of polymer adhesion. Part I: fundamentals*. Polymer Engineering and Science, 35 (12), pp. 957-967, 1995.

213. TIAN, W. J., ZHANG, H. Y., SHEN, J. C., *Some properties of interfaces between metals and polymers*. Surface Review and Letters, 4 (4), pp. 703-708, 1997.

214. ATANASOSKA, L., et al., *XPS study of chemical bonding at polyimide interfaces with metal and semiconductor overlayers*. Vaccum, 40 (1/2), pp. 85-90, 1988.

215. PIREAUX, J. J., et al., *The aluminium-polyimide interface: an electron-induced vibrational spectroscopy approach*. Journal of Chem. Phys., 88 (5), pp. 3353-3362, 1988.

216. VERHOEVEN, J. D., *Fundamentals of Physical Metallurgy.* John Wiley and Sons, New York, USA, 1975.

217. D'AMORE, A., et al., *Long-term behaviour of PEI and PEI-based composites subjected to physical aging.* Composites Science and Technology, 59 (1999), pp. 1993-2003.

218. BOWDEN, F. P., TABOR, D., *The friction and lubrication of solids*. Oxford University Press, London, England, 1954.

219. MERDAS, I., THOMINETTI, F., VERDU, J., *Humid Aging of Polyetherimide. II. Consequences of water absorption on thermomechanical properties.* Journal of Applied Polymer Science, 77 (2000), pp. 1445-1451.

220. ROYCHOWDHURY, S., GILLESPIE Jr., J. W., ADVANI, S. G., *Volatile-induced void formation in amorphous thermoplastic polymeric materials: I. Modelling and parametric studies*. Journal of Composite Materials, 35 (4/2001), pp. 340-366.

221. SMALLMANN, R. E., *Modern physical metallurgy, 4th ed.*. Butterworths, London, England, 1985.

222. UEKI, M., HORIE; S., NAKAMURA, T., *Factors affecting dynamic recrystallization of metals and alloys.* Materials Science and Technology, 3 (1987), pp. 329-337.

223. BELYAYEV, S. P. et al., *Dynamic recrystallization of aluminium*. Physics of Metals and Metallurgy, 52 (3), pp. 143-152, 1981.

224. FRATINI, L., BUFFA, G., *CDRX modelling in friction stir welding of aluminium alloys.* International Journal of Machine Tools & Manufacture, 45 (2005), pp. 1188-1194.

225. DOHERTY, R. D., et al., *Current Issues in recrystallization: a review*. Materials Science and Engineering, A238 (1997), pp. 219-274.

226. KABYSHEV, R., MAZURINA, I., *Mechanisms of grain refinement in aluminium alloys during severe plastic deformation.* Materials Science Forum, 467-470 (2004), pp. 1251-1260.

227. SWISHER, D. L., *Deformation banding and grain refinement in FCC materials*. Dissertation from Naval Postgraduate School, U.S. Navy, Monterey, CA, USA, 2003.

228. KORBEL A., et al., *Microstructural aspects of strain localization in Al-Mg alloys*. Acta Metallurgica, 34 (10), pp. 1999-2009, 1986.

229. LIU, J., *Shear banding in rolled dispersion hardened Al-Mg_2Si alloys.* Scripta Metallurgica, 23 (1989), pp. 1811-1816.

230. KULKARNI. S. S., STARKE, E. A., KUHLMANN-WILLSDORF, D., *Some observations on deformation banding and correlated microstructures of two aluminium alloys compressed at different temperatures*. Acta Materialia, 46 (15), pp. 5283-5301, 1998.

231. McNELLEY, T. R., SWISHER, S. L., PÉREZ-PRADO, M. T., *Deformation Bands and the formation of grain boundaries in a superplastic aluminium alloy.* Metallurgical and Materials Transactions A, 33A (2002), pp.279-290.

232. PÉREZ-PRADO, M. T., et al., *Texture analysis of the transition from slip to grain boundary sliding in a continuous recrystallized superplastic alloy*. Materials Science and Engineering A, A342 (2003), pp. 216-230.

233. DUGGAN, B. J., LEE, C. S., *Deformation banding, original grain size and recrystallization in FCC intermediate-to-high SFE metals*. Scripta Metallurgica et Materialia, 27 (11), pp. 1503-1507, 1992.

234. GOURDET, S., MONTHEILLET, F., An experimental study of the recrystallization mechanism during hot deformation of aluminium. Materials Science and Engineering, A283 (2000), pp. 274-288.

235. LI, Y., MURR, L. E., McCLURE, J. C., *Flow visualization and residual microstructures associated with friction stir welding of 2024 aluminum to 6061 aluminum*. Materials Science and Engineering A, A271, (1999), pp. 213-223.

236. ASM, *Metals Handbook, 3rd ed.*. ASM International, Materials Park, OH, USA, 1993.

237. NICHOLSON, L. M., WHITLEY, K. S., GATES, T. S., *The role of molecular weight and temperature on the elastic and viscoelastic properties of a glassy thermoplastic polyimide*. International Journal of Fatigue, 24 (2002), pp. 185-195.

238. SANNER, M. A., HARALUR, G., MAY, A., *Effect of molecular weight on brittle-to-ductile transition temperature of polyetherimide.* Journal of Applied Polymer Science, 92 (2004), pp. 1666-1671.

239. KURODA; S. –I., et al., *Degradation of aromatic polymers – I. rates of crosslinking and chain scission during thermal degradation of several soluble aromatic polymers.* European Polymer Journal, 25 (1), pp. 1-7, 1989.

240. TORRECILLAS, R., et al., *Thermal degradation of high performance polymers – influence of structure on polyimide thermostability*. Polymer Degradation and Stability, 54 (1996), pp. 267-274.

241. CAROCCIO, S., PUGLISI C., MONTAUDO,G., *Thermal degradation mechanisms of polyetherimide investigated by direct pirolysis mass spectroscopy*. Macrom. Chem. Phys., 200 (1999), pp. 2345-2355.

242. PERNG, L. H., *Thermal Degradation Mechanisms of Poly(ether imide) by stepwise Py-GC/MS*. Journal of Applied Polymer Science,79 (2001), pp. 1151-1161.

243. AUGH, L., GILLESPIE Jr., J. W., FINK, B. K., *Degradation of continuous carbon-fiber reinforced polyetherimide composites during induction heating.* Journal of Thermoplastic composite materials, 14 (2001), pp. 96-115.

244. BARBOSA-COUTINHO, E., SALIM, V. M. M., Borges, C. P., *Preparation of carbon hollow fiber membranes by pyrolysis of polyetherimide.* Carbon, 41 (2003) 1707-1714.

245. HARINAHT, V. A., LOU, J., *Characterization of the thermo-oxidative stability of filled thermoplastic polyetherimide.* In Proc.: IMECE`03, 2003 ASME International Mechanical Engineering Congress, 15-21 November, Washington, D.C., USA, 2003.

246. CAROCCIO, S., PUGLISI C., MONTAUDO,G., *New vistas in polymer degradation. Thermal oxidation processes in poly(ether imide).* Macromolecules, 38 (2005), pp. 6849-6862.

247. SCHNABEL, W., *Polymer Degradation, principles and practical applications*. Akademie-Verlag, Berlin, Germany, 1981.

248. CAROCCIO, S., PUGLISI C., MONTAUDO,G., *Comparison of Photooxidation and thermal oxidation processes in poly(ether imide).* Macromolecules, 38 (2005), pp. 6863-6870.

249. ILLGNER, K. H., ESSER, J., *Schrauben Vademecum, 9. Auflage.* RASCH Verlag, Bramsche, Germany, 2001.

250. VDI 2230, *Systematische Berechnung hochbeanspruchter Schraubenverbindungen - Zylindrische Einschraubenverbindungen Blatt 1*. Verein Deutscher Ingenieure, VDI, Beuth Verlag , Berlin, Germany, 2003.

251. NIELSEN, L. E., *Mechanical Properties of Polymers and Composites, Volume 2*. Marcel Dekker, Inc., New York, USA, 1974.

252. TURLACH, G., *Höchstfeste Schrauben für den Leichtbau.* In Proc.: "2. Fachtagung Schraubenverbindungen, Berechnung, Gestaltung und Anwendung", VDI Verlag. Würzburg, Germany, September 2001.

253. BROSTOW, W., *Performance of plastics*. Hanser Publishers, Munich, Germany, 2000.

254. MICHLER, G. H., *Kunststoff-Mikromechanik, Morphologie, Deformations- und Bruchmechanismen*. Carl Hanser Verlag, Munich, Germany, 1992.

255. KINLOCH, A. J., YOUNG, R. J., *Fracture Behaviour of Polymers*. Applied Science Publishers, London, U.K., 1983.

256. KIM, K. –Y, YE, L., YAN, C., *Fracture behaviour of polyetherimide (PEI) and interlaminar fracture of CF/PEI laminates at elevated temperatures*. Polymer Composites, 26 (1), pp. 20-28, 2005.

257. CHANG, F. –C., CHU, L. –H., *Co-existence of ductile, semi-ductile, and brittle fractures of polycarbonate*. Journal of Applied Polymer Science, 44 (192), pp. 1615-1623, 1992.

258. ASM HANDBOOK, *Volume 12, Fractography*. ASM International, Metals Park, OH, USA, 1987.

259. ROULIN-MOLONEY, A. C., *Fractography and failure mechanisms of polymers and composites*. Elsevier Applied Science, London, U.K., 1989.

260. AGRAWAL, C. M., PEARSAL, G. W., *The fracture morphology of fast unstable fracture in polycarbonate*. Journal of Materials Science, 26 (1991), pp. 1919-1930.

261. ASM ENGINEERED MATERIALS HANDBOOK, *Engineering plastics Vol.2*. ASM International, Metals Park, OH, USA, 1988.

262. ELLIS, C. R. G., *Continuous drive friction welding of mild steel*. Welding Research Supplement, April 1972, pp. 183-s – 197-s.

263. POTENTE, H., UEBBING, M., *Friction welding of polyamides*. Poylmer Engineering and Science, 37 (4), pp. 726-737, 1997.

264. FESTA, D., CAKMAK M., *Spin welding behaviour and structure development in a thermotropic liquid crystalline polyme*r. In Proc.: ANTEC`92, SPE Annual Technical Conference, Society of Plastic Engineers (US), USA, 1992, pp. 344-348.

265. SCHAIBLE, S., CAKMAK, M., *Instrumented spin welding of polyvinylidene fluoride*. In Proc.: ANTEC`92, SPE Annual Technical Conference, Society of Plastic Engineers (US), USA, 1992, pp.893-895.

266. RAJARAMAN, H., CAKMAK, M., *The effect of glass fiber fillers on the welding behaviour of poly p-phenylene sulphide*. In Proc.: ANTEC`92, SPE Annual Technical Conference, Society of Plastic Engineers (US), USA, 1992, pp. 896-899.

267. TAPPE, P., POTENTE;, H., *New results on the spin welding of plastics*. Polymer Engineering and Science, 29 (23), pp. 1655-1660, 1989.

268. HART-SMITH, L. J., *Mechanically-fastened joints for advanced composites – phenomenological considerations and simple analyses*. In Prod.: Conference on Fibrous Composites in Structural Design. Plenum Press, New York, USA, 1978, pp. 543-574.

269. LAWLOR, V. P., STANLEY, W. F., McCARTHY, M. A., *Characterisation of damage development in single-shear bolted composites*. Journal of Plastics, Rubber and Composites., 31 (3), pp. 126-133, 2002.

270. D 5961/D 5961M-05, *Standard test method for bearing response of polymer matrix composite laminates*. ASTM International, USA, 2005.

271. HORN, W., SCHMITT, R. R., *Relaxation in bolted thermoplastic composites, paper AIAA-93-1350-CP*. In Proc.: Structures, Structural Dynamics and Materials Conference, American Institute of Aeronautics and Astronautics, April 19-22, 1993, Washington DC., USA, 1993, pp. 485-494.

272. BIRLEY, A. W., HAWORTH B., BATCHELOR, J., *Physics of plastics, processing, properties and materials engineering*. Hanser Publishers, Munich, Germany, 1992.

273. WARD, I. M., *Mechanical properties of solid polymers 2nd ed.*. J. W. Arrowsmith Ltd., Bristol, U.K., 1983.

274. VAN KREVELEN, D. W., *Properties of polymers, their correlation with chemical structure: their numerical estimation and prediction fro additive group contributions, 3rd ed.*. Elsevier, Amsterdam, Holland, 1990.

275. PLASTICS DESIGN LIBRARY, *The effect of creep and other time related factors on plastics, Vol.I-Book A and B*. William Andrew, Inc., New York, USA, 1991.

276. ROYCHOWDHRY, S., GILLESPIE Jr, J. W., ADVANI, S.G., *Volatile-induced void formation in amorphous thermoplastic polymeric materials: I. Modelling and parametric studies*. Journal of Composite Materials, 35 (4/2001), pp. 340-366.

277. CAROCCIO, S., PUGLISI, C., MONTAUDO, G., *Thermal degradation mechanisms of polyetherimide investigated by direct pyrolisis mass spectroscopy*. Macrom. Chem. Phys., 200 (1999) pp. 2345-2355.

278. SANNER, M. A., HARALUR, G., MAY, A., *Effect of molecular weight on brittle-to-ductile transition temperature of polyetherimide*. Journal of Applied Polymer Science, 92 (2004), pp. 1666-1671.

279. HAZEN, J. R., MUSSELMAN, M., *Automotive composites, a design and manufacturing guide, 2nd ed.*. Ray Publishing Inc., Wheat Ridge, USA, 2006.

Dedicated to my wife Gisele, my parents, Sara and Daniel

“I will lift up mine eyes unto the hills, from whence cometh my help? My help cometh from the LORD, which made heaven and earth”

“Ich hebe meine Augen auf zu den Bergen. Woher kommt mir Hilfe? Meine Hilfe kommt vom HERRN, der Himmel und Erde gemacht hat.”

“Elevo os meus olhos para os montes: de onde me virá o socorro? O meu socorro vem do SENHOR, que fez o céu e a terra.”

Psalms, Psalm, Salmos 121:1-2.